ELECTRON-TRANSFER IN COVALENTLY COUPLED DONOR-ACCEPTOR COMPLEXES

Thesis by

Max Bachrach

In Partial Fulfillment of the Requirements

for the Degree of

Doctor of Philosophy

California Institute of Technology

Pasadena, California

1996

(Submitted July 21, 1995)

Acknowledgements

Numerous people have helped make this work possible, and I wish to thank them all: Harry Gray, Jay Winkler, Seth Marder, David Wiedenfeld, Mark McCleskey, Chin-Ti Chen, Patrick Farmer, Adrian Ponce, Chris Kenyon, and members of the Gray Group, past and present.

I especially wish to thank my parents for their love and support. I am sure I owe a large part of my interest in science to my father, whose curiosity encouraged the development of my own. My wife Chelsea has also affected my life greatly, giving me love, companionship and a great deal of encouragement during the past five years. I must also thank her family for their constant support.

Abstract

A picosecond transient absorption experiment has been constructed and used for the study of intramolecular electron-transfer (ET) in three molecular systems. The first of these is a donor-bridge-acceptor (D(br)A) complex composed of a d^8-d^8 iridium core covalently coupled to two pyridinium acceptors with flexible phosphonite spacers. Varying the pyridiniums' substituents allows control of the driving-forces ($\Delta G°$) of the photoinduced ET reactions from the core's singlet and triplet states. The rates of these reactions have been determined from steady-state and time-resolved emission experiments. Picosecond transient absorption has been used to measure the rates of subsequent charge-recombination, and determine their dependencies on $\Delta G°$. The reorganization energy accompanying intramolecular electron-transfer within this system ($\lambda \approx 0.86$ eV) has been determined by fitting the rates of photoinduced and thermal reactions to a single-mode quantum-mechanical ET model.

The rates of all the photoinduced and thermal ET reactions have been measured as a function of temperature (200° K - 280° K). These data show that the charge-recombination reactions, which lie within the Marcus inverted region ($-\Delta G° > \lambda$), have rates (k_{BET}) that are strongly dependent on temperature. Deuteration of the pyridinium acceptor has a temperature independent effect ($k_H/k_D = 1.2$) on k_{BET}, indicating that, although the inverted region reactions within these complexes exhibit behavior that is remarkably classical, quantum-mechanical effects do need to be considered. Both temperature and isotope effects suggest that

the molecules' low internal reorganization energies ($\lambda_{in} \approx 0.006$ eV) account for their ET behavior.

Less comprehensive studies of two other electron-transfer systems are also reported. Unlike the iridium system, in which the donor-acceptor electronic coupling H_{AB} is less than 100 cm^{-1}, the couplings within these are over 2000 cm^{-1}. It has been found that despite the large amount of coupling between the metals of $[(bpy)(tpy)Ru^{II}CNRu^{II}(NH_3)_5]^{2+}$ (bpy = 2,2'-bipyridine; tpy = 2,2',2"-terpyridine), our transient absorption experiment is able to detect formation of a charge-separated state following excitation into the Ru→immine charge-transfer band. It is proposed that this species can be described as $[(bpy)(tpy\bullet^-)Ru^{II}CNRu^{III}(NH_3)_5]^{2+}$, and that unusually low coupling between the tpy ligand and the oxidized ruthenium leads to slow (1×10^{10} s^{-1}) charge-recombination.

The ground-state absorption features and excited-state decay kinetics of a series of ferrocene-based D(br)A complexes have also been measured. It is proposed that H_{AB} is much larger than 2000 cm^{-1} for these complexes, and plays an important role in determining their nonlinear optical properties.

Table of Contents

List of Figures

List of Tables

To my parents and Chelsea

Chapter I

Introduction

Electron-transfer is intimately involved in the conversion of light and chemical energy into forms useful for biological functions. For example, lithotrophic bacteria obtain energy from the oxidation of inorganic material, such as nitrate or ferrous ions, and store it in carbohydrates formed from the reduction of carbon dioxide. Other bacteria, like plants, are able to convert light to chemical energy. Photosynthesis has been studied for several decades with the hope that by understanding this remarkable process, highly efficient artificial means of harnessing solar energy could be constructed.

Photosynthesis is a combination of a series of processes, all involving electron-transfer (ET). The first step occurs within the reaction center, which contains light-absorbing pigments that vary among organisms. Three classes of pigments have been identified: chlorophylls, bilins and carotenoids.[1] Chlorophylls are tetrapyrrole rings containing a coordinated magnesium ion, and bilins are linear tetrapyrroles. Carotenoids are hydrocarbons, usually 40 carbons in length, which can both serve as pigments and sinks for chlorophyll triplet states. Whether in plant or animal, the reaction center's optically induced excited-state is a powerful reductant, capable of transferring an electron to a neighboring electron acceptor with a temperature-independent rate that is typically faster than 1×10^{11} s^{-1}.[2] From there, the electron is transferred down a chain of acceptors. In purple bacteria, the electron moves to a quinone known as Q_A in approximately 200 ps to form its radical anion.[3] This, in turn, reduces a second quinone Q_B, which continues the chain. In green sulfur bacteria, the acceptors are iron-sulfur (bound ferrodoxin) centers. By

contrast, the excited-state of photosynthetic reaction center I reduces ferrodoxin, a polypeptide capable of diffusing through the cell. The reaction scheme of photosystem II is shown in Figure I.1.

It is clear that the events following a reaction center's absorption of light vary greatly among photosynthetic plants and bacteria. What all these systems have in common, however, is a very large difference between the amount of productive charge-transfer and unproductive charge-recombination.[4] For each ET step in the long chain that eventually leads to energy storage, the reduced electron acceptor can, instead of transferring the electron to the next link, return it to its predecessor. The efficiency of an ET reaction is thus dependent on the charge-recombination to charge-transfer ratio, or the ratio of the rates of the two processes.

One of the primary problems facing the design of artificial light-harvesting systems is the reduction of this ratio. It is relatively easy to synthesize a chromophore that can act as a powerful reductant upon optical excitation, but it is more difficult to control the rate at which it reacts with an acceptor, and to then prevent the oxidation of the reduced acceptor by the now electron-deficient chromophore. A large body of research has addressed this problem by studying the general mechanism of electron-transfer.

The advantages of such fundamental studies lie not only in their encouragement of rational approaches to the design of artificial photosynthetic systems, but also in the fact that ET is fundamental to other processes that do not involve chemical reactivity. For example, nonlinear optical behavior depends on the

Figure I.1 An electron-transport scheme of Photosystem IIα, showing estimated and measured reaction times involved in each transfer. Alternate names for each of the intermediates are shown below the major components. (Taken from reference 5.)

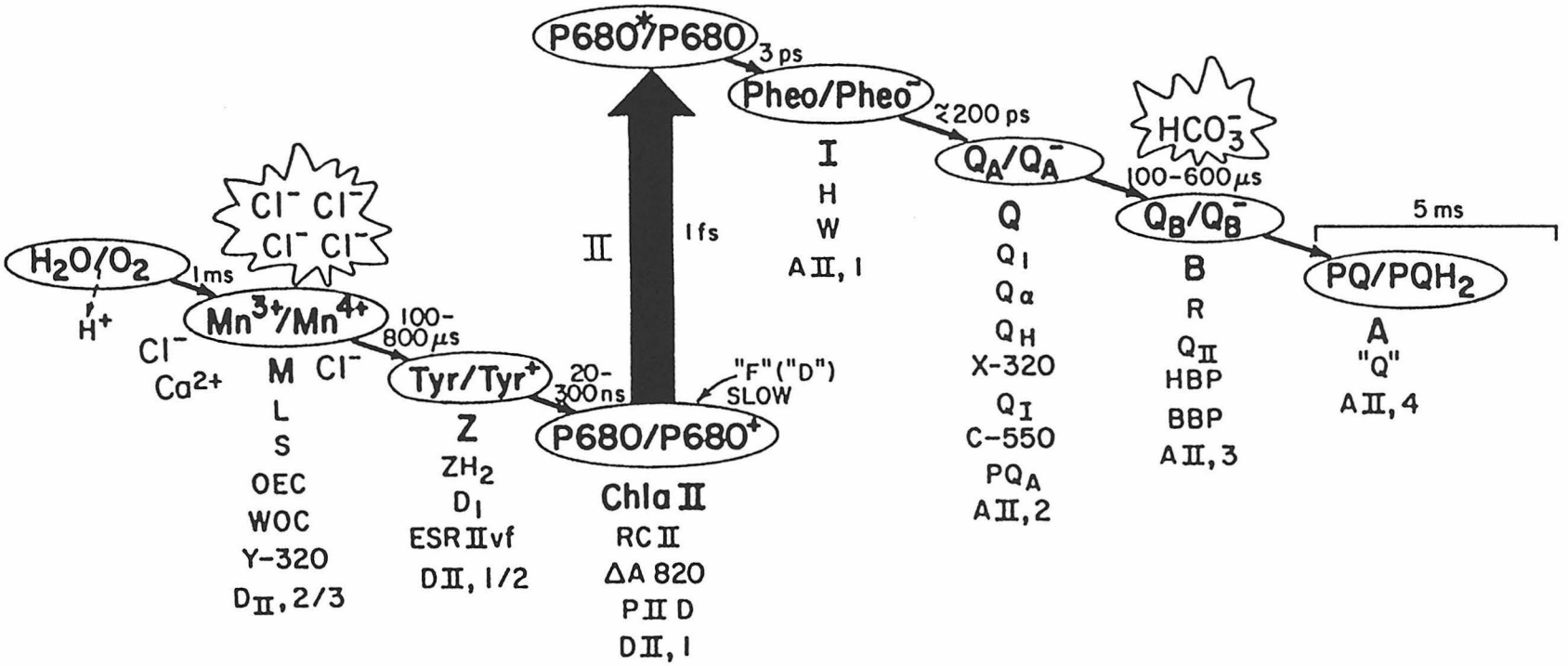
P680*/P680
3 ps
Pheo/Pheo⁻
≈200 ps
Q_A/Q_A^-
HCO_3^-
100-600 μs
Q_B/Q_B^-
5 ms
PQ/PQH_2
A
"Q"
AII, 4
B
R
Q_{II}
HBP
BBP
AII, 3
Q
Q_I
Q_α
Q_H
X-320
Q_I
C-550
PQ_A
AII, 2
I
H
W
AII, 1
II
1 fs
H_2O/O_2
1 ms
H^+
Cl^- Cl^-
Cl^- Cl^-
Mn^{3+}/Mn^{4+}
100-800 μs
Cl^-
Ca^{2+}
M
L
S
OEC
WOC
Y-320
D_{II}, 2/3
Cl^-
Tyr/Tyr⁺
20-300 ns
"F" ("D")
SLOW
Z
ZH_2
D_1
ESR IIvf
DII, 1/2
P680/P680⁺
Chla II
RC II
ΔA 820
P II D
DII, 1

interaction between charge and light, but does not lead to the formation of chemical products.

The work described within this thesis is directed at understanding in greater detail some of the factors that affect ET. Its purpose is manifold: First, it is aimed at resolving an apparent conflict between theory and experiment, and in doing so provide some insight into how the charge-recombination/charge-transfer ratio might be reduced within artificial light-harvesting systems. Second, it contributes to a very limited body of experimental work concerning ET between strongly interacting electron donor/acceptor pairs. Finally, it seeks to provide an experimental basis for the establishment of a quantitative relationship between molecules' electron-transfer properties and nonlinear optical susceptibilities.

Experiment is meaningless without a theoretical framework with which to rationalize its findings. In turn, the accuracy of theory can only be tested by experimentation. Thus, the results reported in Chapters III, IV and V are explained within the context of classical ET theory; more sophisticated theory is then used to help explain why some data deviate from its predictions.

Electron Transfer Theory

The numerous mathematical electron-transfer models published during the past few decades all stem from the pioneering work of Marcus.[6] The classical physics underlying his theory give it an appealing simplicity and a starting point for investigations directed at understanding the factors which affect the process. As the field has grown, these factors have been dealt with in greater detail and

sophistication by Marcus and others. Theory that originally was used to explain simple outer-sphere self-exchange rates[7] has grown to include ET within and between molecules of varying complexities and sizes, from small organics to large metallo-proteins.[8]

Because of the complexity of these newer models, many researchers turn first to semiclassical Marcus theory to understand their findings. While it does not accurately predict the rate of ET in certain limits, it still provides a first-order approximation that is very useful in the formulation of coherent research.

Classical Marcus Theory

In Figure I.2, simplified potential surfaces corresponding to a reactant and product are shown. Energy is plotted as a function of nuclear geometry. Fluctuations in the reactant's nuclear configuration can move it to a point which corresponds to a possible nuclear configuration of the product. In the late 1950s, Marcus derived a classical expression for the rate of outer-sphere ET k_{ET} that can occur at such transition state geometries with probability κ:

Equation I.1

$$k_{ET} = \kappa A \sigma^2 \exp\left(\frac{-\Delta G^*}{RT}\right)$$

The transmission coefficient κ is a function of the distance between the electron donor and acceptor. When $\kappa \approx 1$, a reaction is called adiabatic. Bimolecular reactions depend on the collision frequency of the donor and acceptor, considered in $A\sigma^2$. The free energy of activation ΔG^* is itself a function of the standard free energy of the charge-transfer reaction ΔG° and its reorganization energy λ:

Figure I.2 Nuclear potential energy curves for the reaction and product states considered in classical electron-transfer theory, plotted as a function of nuclear coordinates: (**A**) relative energies of the states when $-\Delta G^\circ = 0$, (**B**) relative energies of the states when $-\Delta G^\circ \approx \lambda$ and (**C**) relative energies of the states when $-\Delta G^\circ > \lambda$. The assumptions on which these pictures are based yield a parabolic $\ln(k_{ET})$ *vs.* $-\Delta G^\circ$ curve.

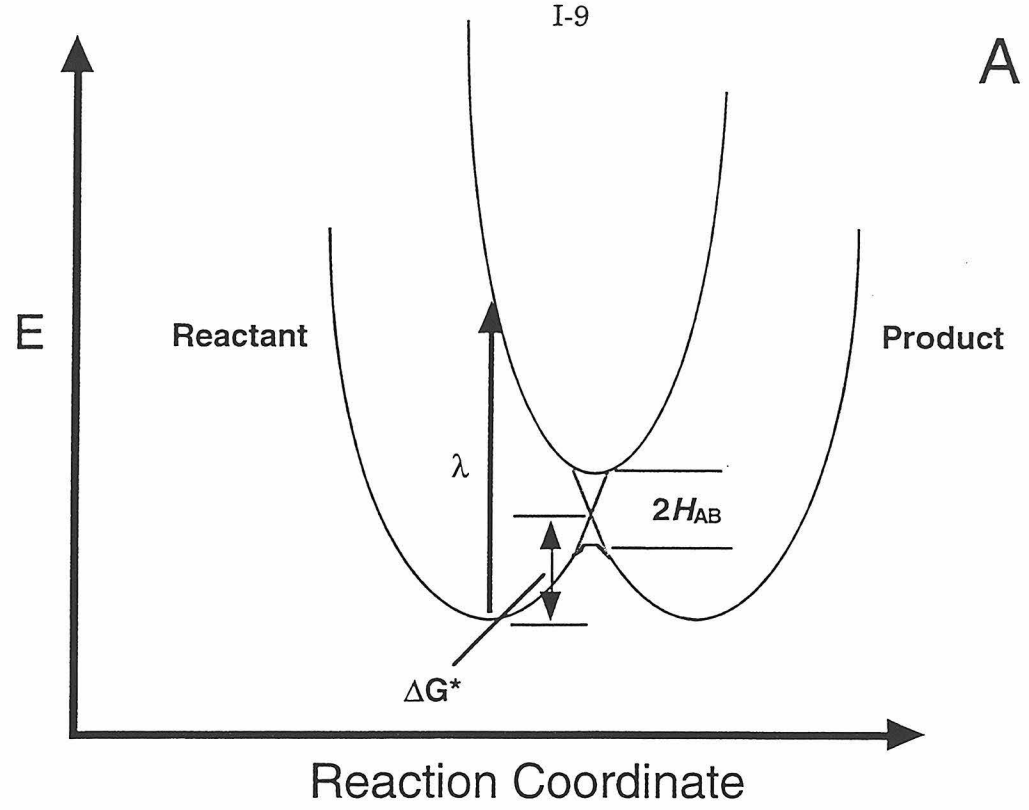
A
E
Reactant
Product
λ
2H_{AB}
ΔG*
Reaction Coordinate

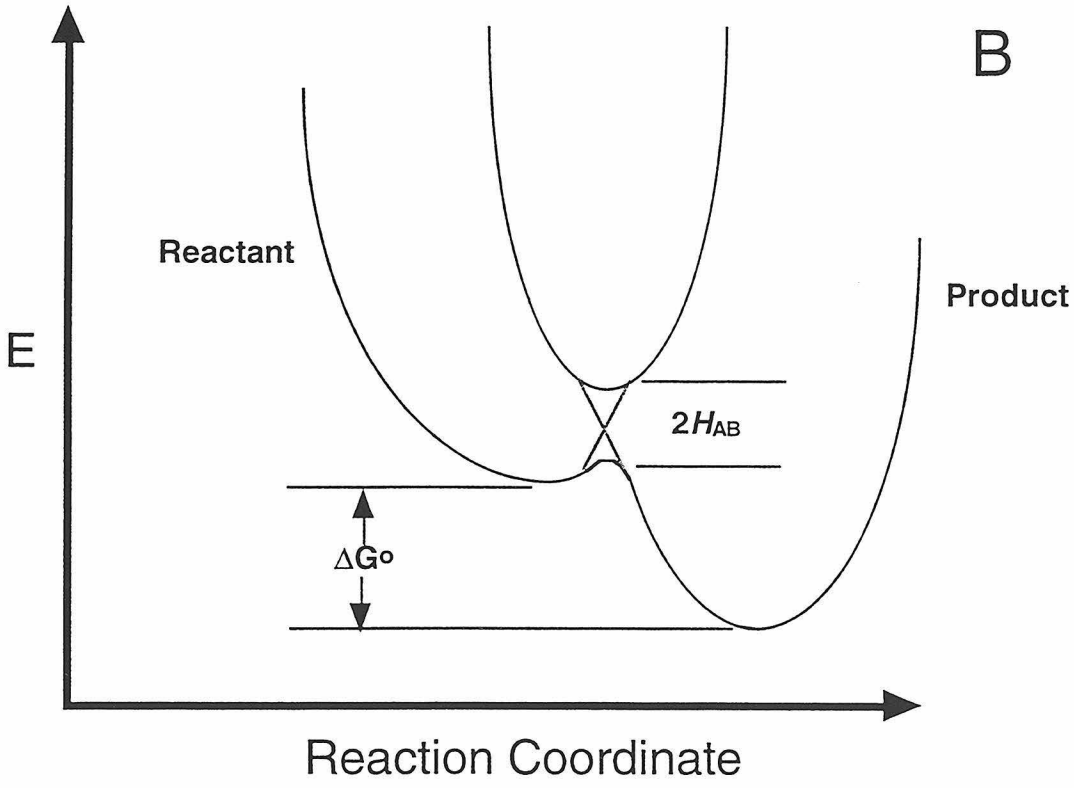
B
E
Reactant
Product
2H_{AB}
ΔG°
Reaction Coordinate

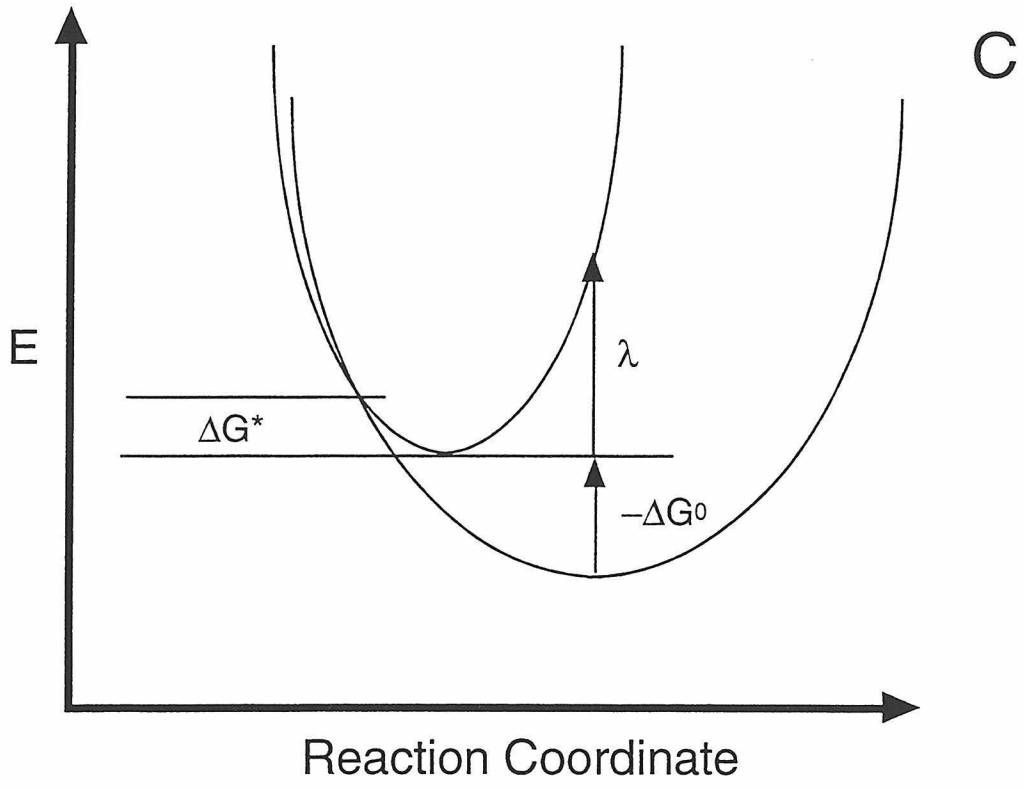
C
E
λ
ΔG*
−ΔG0
Reaction Coordinate

Equation I.2 $$\Delta G^{*} = \frac{\left(\lambda + \Delta G^{\circ}\right)^{2}}{4\lambda}$$

Following ET, the reactants' nuclear vibrational coordinates will change to accommodate the new charge distribution. The orientations of solvent molecules will also shift to stabilize the product. Treating the former as harmonic oscillators yields λ_{in}, while dielectric continuum theory provides an estimate for λ_{out}. The overall reorganization energy is the sum of these two:

Equation I.3 $$\lambda = \lambda_{in} + \lambda_{out}$$

A cursory examination of this model reveals that it predicts k_{ET} will increase as a function of ΔG° until $-\Delta G^{\circ} = \lambda$: This region of a rate versus driving-force plot is called the "normal" region (Figure I.2). In the "inverted" region, $-\Delta G^{\circ}$ becomes greater than λ and Equation I.1 predicts a slowing of k_{ET}. This prediction has been put to considerable test during the past two decades.

Quantum Mechanical Electron Transfer Models

One reason the inverted region has gained so much attention is that it provides an explanation for the efficiency of biological electron-transfer reactions. If a productive charge separation reaction occurs when $-\Delta G^{\circ} \approx \lambda$, its rate will be close to the maximum of $\kappa A \sigma^{2}$. If the driving-force of the reverse, energy-wasting charge-recombination is much greater than λ, its rate would be much slower, and the amount of productive ET would far exceed the amount of unproductive ET. Such rate differences have been observed in the reaction centers of several photosynthetic systems.[4]

Although there are a few examples in which the inverted region has been observed in synthetic donor-acceptor systems, most exhibit substantially weaker slowing of k_{ET} as $-\Delta G^{\circ}$ increases beyond λ than classical Marcus theory predicts. These observations can be reconciled with electron-transfer models that include quantum-mechanical effects.

Consideration of Quantum-Mechanical Effects

Theoretical ET models run the gamut from the fully classical to the fully quantum-mechanical. Most lie somewhere between these two limits, and consider only inner-sphere reorganization quantum-mechanically, leaving λ_{out} unchanged. Until recently, most of these treatments applied only to nonadiabatic reactions, in contrast to the original work of Marcus, which assumed ET is an adiabatic process ($\kappa \approx 1$ in Equation I.1). They are all of the general form:

Equation I.4 $$k_{ET} = \frac{2\pi}{h} H_{AB}^2 (FC)$$

The electronic interaction between the reactant and product potential surfaces is considered in H_{AB}, the electronic matrix element. The Frank-Condon factor FC is the sum of the products of the vibrational and solvational wavefunctions of the reactant and product, and is weighted by Boltzmann factors. In the high temperature limit, where the energies of nuclear vibrations are much smaller than kT and can be treated classically, this becomes:[9]

Equation I.5 $$k_{ET} = \frac{4\pi^2}{h} H_{DA}^2 \frac{1}{\sqrt{(4\pi RT)}} \exp\left(-\frac{\Delta G^*}{RT}\right)$$

In reality, many inner sphere vibrations have energies greater than kT, so the high-temperature limit no longer applies; Equation I.4 must include vibrational Frank-Condon terms to yield rates close to those observed by experiment. Their consideration has two effects. First, the possibility now exists that a system may move from its reactant surface to a vibrationally excited-state of its product surface, effectively reducing the reaction's activation barrier. This effect has been used to explain the excited-state behavior of the dye betaine-30.[10] Originally, it was also used to account for the absence of an inverted effect in the k_{ET} *vs.* -ΔG° plots obtained from the study of bimolecular systems.[11,12] Now, it is recognized that changes in the inverted effect are instead due to nuclear tunneling.

Classical Marcus theory predicts that as -ΔG° becomes greater than λ, an activation barrier begins to grow which slows k_{ET} in the same way it is slowed in the normal region. When quantum-mechanical interactions between reactant and product wavefunctions are considered, k_{ET} undergoes little change in the normal region, where the potential surfaces of the two are well separated. In the inverted region, however, the two are nested, substantially increasing the wavefunctions' overlap (Figure I.3). This allows movement -- or tunneling -- from one surface to the other without the necessity of surmounting an activation barrier. In such cases, the observed reaction rates are thus faster than what is predicted by classical theory and lead to a flattening of the k_{ET} *vs.* -ΔG° curve at high driving-forces (Figure I.4).

Figure I.3 Quantum mechanics allows nuclear tunneling between the product and reactant surfaces to occur. Although it can occur for reactions in which $-\Delta G^\circ < \lambda$ (**A**), its probability is increased for those in the inverted region (**B**).

A

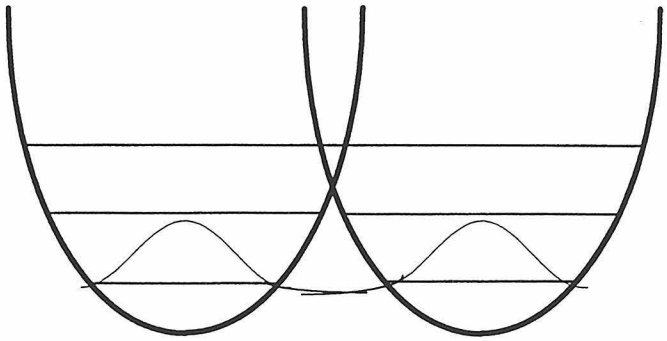

B

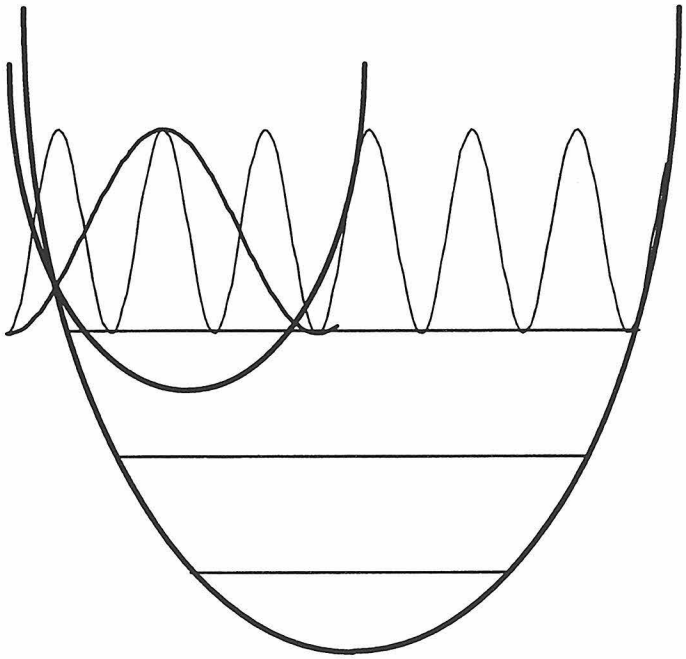

Figure I.4 A plot of $\ln(k_{ET})$ *vs.* $-\Delta G°$ in the high-temperature limit as predicted by Equation I.5 with λ = 1 eV and H_{AB} = 26 cm^{-1} (**A**) substantially changes in appearance upon consideration of a 1500 cm^{-1} (λ_{in} = 0.1 eV and λ_{out} = 0.9 eV) that can couple the reactant and product potential surfaces (**B**).

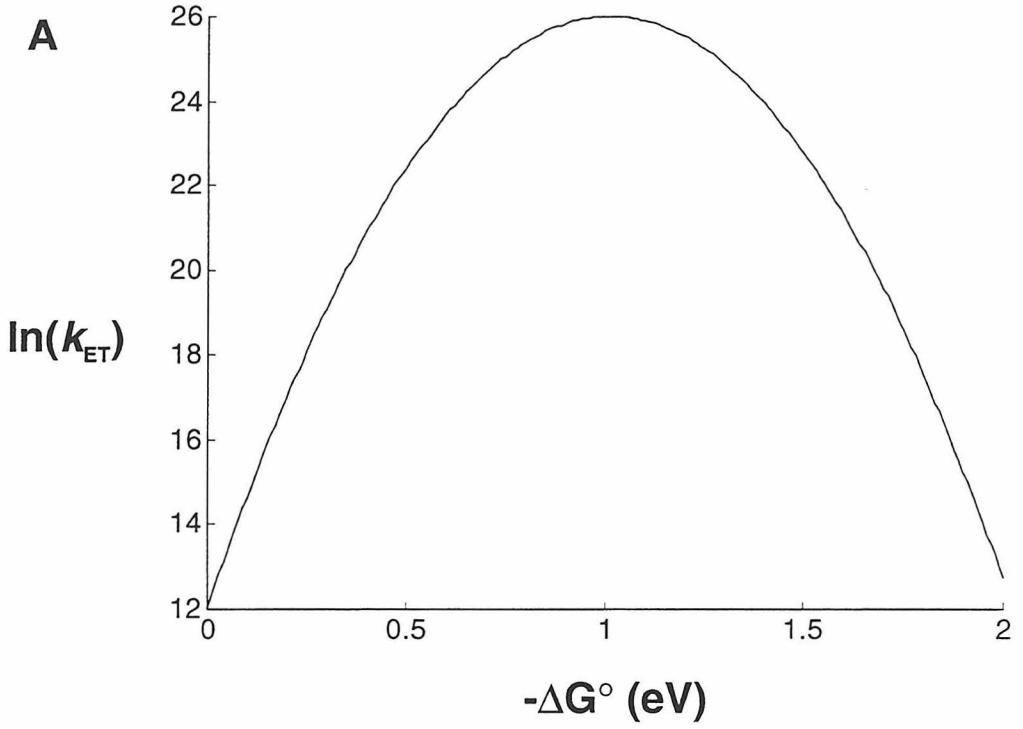
A
ln(k_{ET})
26
24
22
20
18
16
14
12
0
0.5
1
1.5
2
-ΔG° (eV)

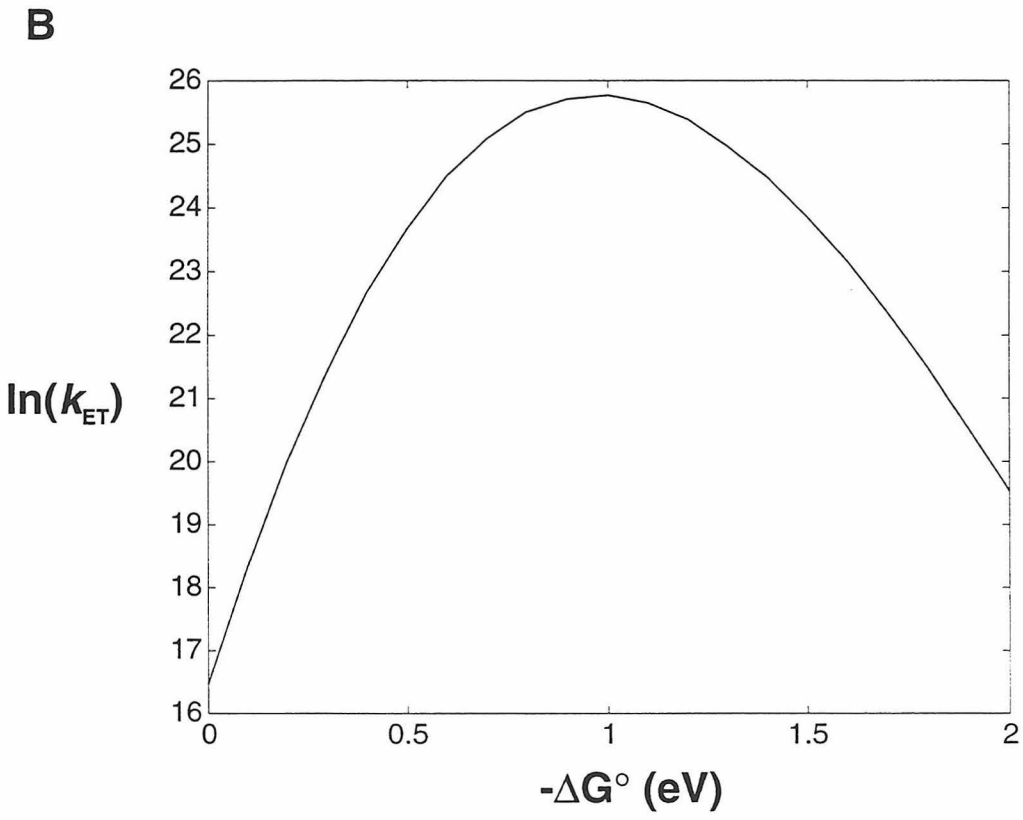
B
ln(k_{ET})
26
25
24
23
22
21
20
19
18
17
16
0
0.5
1
1.5
2
-ΔG° (eV)

Variations of Equation I.4 have been used to explain the behavior of many high driving-force reactions. They do not, however, accurately predict the rates of adiabatic -- and some inverted region -- reactions.

Consideration of Adiabaticity and Solvent Dynamics

An assumption often made by ET models is that dielectric relaxation of the medium surrounding a redox couple is much faster than the electronic relaxation accompanying the reactions within it. This assumption is not always valid. With suitable values of H_{AB}, adiabatic reactions can occur on the picosecond or subpicosecond timescale. As technology advanced to make measurements of such reactions possible, theoreticians were forced to extend quantum-mechanical ET theory to provide for a smooth transition between the nonadiabatic and adiabatic regimes, and to address the possibility that dielectric relaxation may occur at a rate slower than electronic relaxation.

The transition between the nonadiabatic and adiabatic limits has been addressed with Landau-Zener theory,[13] and is closely tied to the behavior of the solvent. Zusman was the first to consider diffusive, rather than uniform, reaction coordinates in a theoretical treatment of electron-transfer. In the adiabatic limit, his model reduces to a result obtained by Kramers over 50 years ago that relates reaction rates to solvent viscosity.[14,15] His approach allows the connection of the nonadiabatic limit, where a reaction's probability is determined by H_{AB}, to the adiabatic limit, where it is determined by reaction coordinate dynamics. In the

latter case, the maximum reaction rate is proportional to the inverse of the solvent relaxation time τ_L.

Since this work, several ET models utilizing the diffusive motion assumption have been developed.[16,17,18] The data reported in the following chapters have been analyzed with a model developed by Jortner and coworkers:[17]

Equation I.6 $$k_{ET} = \frac{k_{NA}}{1 + \mathcal{K}_A}$$

The reaction rate is dependent on a nonadiabatic rate k_{NA}, which is a function of temperature T, activation energy E_A, solvent reorganization energy E_r and electronic coupling:

Equation I.7 $$k_{NA} = \frac{2\pi H_{AB}^2}{\hbar\sqrt{4\pi E_r kT}} \exp\left(\frac{-E_A}{kT}\right)$$

The adiabatic parameter is also a function of the coupling, as well as the solvent longitudinal relaxation time:

Equation I.8 $$\mathcal{K}_A = \frac{4\pi H_{AB}^2 \tau_L}{\hbar E_R}$$

The transition from the nonadiabatic to the adiabatic regime occurs as $\mathcal{K}_A$ grows from much less than 1 to much greater than 1.

Recent work by Barbara and others has shown that the rate of some activationless and inverted is not limited by $1/\tau_L$.[10,19] This has since been addressed by Bixon and Jortner,[20] but has little bearing on the reactions studied here.

This Work

The electron-transfer reactions which are considered in this thesis are described in three chapters. These follow Chapter II, which contains a detailed description of the picosecond transient absorption experiment constructed for this research. In Chapter III, the behavior of a series of molecules containing an iridium chromophore bound to different pyridinium cations is discussed. The electronic interaction between these molecules' electron donor and acceptor moieties is much weaker than the very large metal-metal coupling within the cyanide-bridged bis-ruthenium complexes described in Chapter IV. In Chapter V, a description of the ground- and excited-state behavior of a series of ferrocene derivatives is presented. Conclusions are drawn in each chapter that will be helpful in the rational design of both photochemical (light-harvesting) and photophysical (non-linear optical) materials.

REFERENCES AND NOTES

[1] Gregory, R. P. F. Photosynthesis. Chapman and Hall: New York. **1989**.

[2] Kirmaier, C.; Holten, D. *Isr. J. Chem.* **1988**, *28*, 79: Wasielewski, M. R.; Tiede, D. M. *FEBS Lett.* **1986**, *204*, 368: Fleming, G. R.; Martin, J. L.; Breton, J. *Nature*, **1988**, *333*, 190.

[3] Holten, D.; Windsor, M. W.; Parson, W. W.; Thornber, J. P. *Biochim Biophys. Acta* **1978**, *501*, 112.

[4] Netzel, T. L.; Bergkamp, M. A.; Chang, C.-K. *J. Am. Chem. Soc.* **1982**, *104*, 1952: Fujita, I.; Fajer, J.; Chang, C.-K.; Wang, C.-B.; Bergkamp, M. A.; Netzel, T. L. *J. Phys. Chem.* **1982**, *86*, 3754: Maiti, S.; Walker, G. C.; Cowen, B. R.; Pippenger, R.; Moser, C. C.; Dutton, P. L.; Hochstrasser, R. M. *Proc. Natl. Acad. Sci. USA* **1994**, *91*, 10360.

[5] Govindjee; Wasielewski, M. R. *Photosystem II: From a Femptosecond to a Millisecond* in Plant Biology Volume 8: Photosynthesis, Briggs, W. R. ed. Liss: New York: **1989**.

[6] Marcus, R. A. *J. Chem. Phys.* **1956**, *24*, 966: Marcus, R. A. *J. Chem. Phys.* **1957**, *26*, 867: Marcus, R. A. *J. Chem. Phys.* **1957**, *26*, 872.

[7] Brunschwig, B. S.; Creutz, C.; Macartney, D. H.; Sham, T. K.; Sutin, N. *Faraday Disc. Chem. Soc.* **1982**, *74*, 113.

[8] Winkler, J. R.; Gray, H. B. *Chem. Rev.* **1992**, *92*, 369: Gunner, M. R.; Robertson, D. E.; Dutton, P. L. *J. Phys. Chem.* **1986**, *90*, 3783: Siddarth, P.; Marcus, R. A. *J. Phys. Chem.* **1993**, *97*, 13078.

[9] Marcus, R. A.; Sutin, N. *Biochim. Biophys. Acta* **1985**, *811*, 265.

[10] Åkesson, E.; Johnson, A. E.; Levinger, N. E.; Walker, G. C.; DuBruil, T. P.; Barbara, P. F. *J. Chem. Phys.* **1992**, *96*, 7859.

[11] Efrima, S.; Bixon, M. *Chem. Phys. Lett.* **1974**, *25*, 34: Efrima, S.; Bixon, M. *Chem. Phys.* **1976**, *13*, 447.

[12] Rehm, D.; Weller, A. *Israel J. Chem.* **1970**, *8*, 259.

[13] Levich, V. G. *Adv. Electrochem. Eng.* **1965**, *4*, 249.

[14] Zusman, L. D. *Chem. Phys.* **1980**, *49*, 295.

[15] Kramers, H. A. *Physica* **1940**, *7*, 284.

[16] Friedman, H. L.; Newton, M. D. *Faraday Discuss. Chem. Soc. London* **1982**, *74*, 73: Sumi, H.; Marcus, R. A. *J. Chem. Phys.* **1986**, *84*, 4894.

[17] Rips, I.; Jortner, J. *J. Chem. Phys.* **1987**, *87*, 2090.

[18] Jortner, J.; Bixon, M. *J. Chem. Phys.* **1988**, *88*, 167.

[19] Kobayashi, T.; Takagi, Y.; Kandori, H.; Kemnitz, K.; Yoshihara, K. *Chem. Phys. Lett.* **1991**, *180*, 416: Pöllinger, F.; Heitele, H.; Michel-Beyerle, M. E.; Anders, C.; Futscher, M.; Staab, H. A. *Chem. Phys. Lett.* **1992**, *198*, 645.

[20] Bixon, M.; Jortner, J. *Chem. Phys.* **1993**, *176*, 467.

Chapter II

A Picosecond Transient Absorption Experiment

Transient Absorption

A molecule can move from one electronic state to another by the absorption or emission of a photon. Positions of features in its ground-state optical absorption spectrum are thus determined by the energies of its higher-lying states. Their intensities are determined by the selection rules governing the transitions. A molecule in an excited-state also has an absorption spectrum, due to the absorption of photons with energies equal to the difference between it and higher lying excited-states (Figure II.1).

The transient absorption (TA) experiment relies on the fact that spectral features are unique to particular electronic states, meaning a molecule that absorbs a certain frequency of light in its ground-state will not necessarily absorb it in an excited-state. This makes it possible to determine the nature of an excited-state by measuring its absorption spectrum, and to determine its lifetime by measuring the intensity of a transition unique to it as a function of time. A TA experiment can obtain both kinds of information by first exciting a sample, and then measuring its absorption at an individual wavelength or over a range of wavelengths. The transmittance of the sample is obtained at different times after excitation and is compared to that of the sample's ground-state by taking the logrithm of the ratio of the two. This optical density change (ΔOD) is 0 at a particular wavelength if the sample absorbs the same amount of it in both states. A ground-state absorption feature is said to *bleach* upon excitation if it disappears or weakens in intensity in

Figure II.1 A cartoon representation of transient absorption showing the relative energies of molecules (represented as circles) as they are probed in their ground and excited states (**A**). The absorption spectrum obtained with the probe light is dependent on the relative energies of the transitions between the current and a higher lying state (**B**).

A

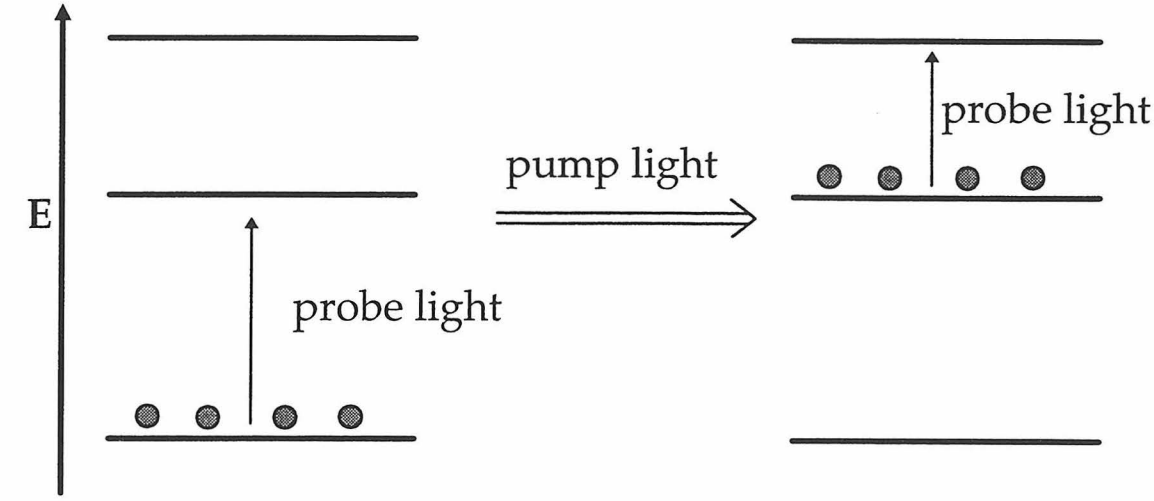

B

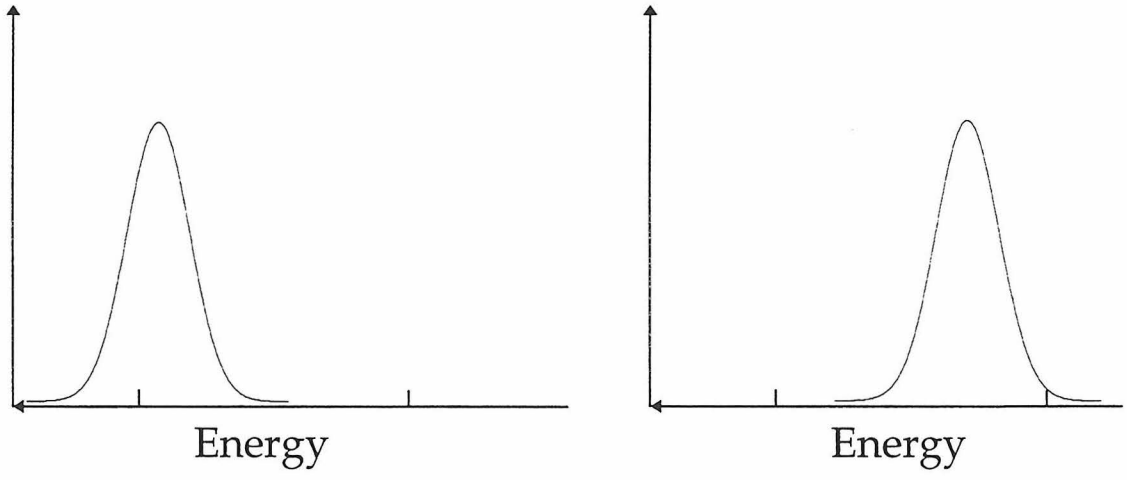

the excited-state ($\Delta OD < 0$). If absorption increases at a particular wavelength upon excitation, $\Delta OD > 0$.

Although an excited -- or transient -- state of a molecule can be prepared in a number of ways, it is formed in this experiment by the absorption of a laser pulse. Transient absorption experiments on the nanosecond and longer timescales typically use a continuous-wave (CW) light source, such as an arc-lamp or CW laser, to probe the sample, and electronically measure the amount of light that passes through it at specific times. It is difficult to build digitizers and amplifiers that function on faster timescales, however, so experiments with subnanosecond resolutions use a second laser pulse as, or to generate, the probe light. Temporal variation between the two pulses is then achieved by varying the relative distances they must travel before reaching the sample.

The general mechanism of the picosecond transient absorption (PTA) experiment is simple, but its implementation is not. The description of this particular experiment is divided into five parts: pulse generation, detection optics, data acquisition, sample handling, and software control.

The Experiment

This experiment was constructed to examine the photoinduced excited-state behavior of the compounds discussed in the following chapters. It was designed, however, to also be effective in the study of other molecules. It is capable of measuring rates as fast as 5×10^{10} s^{-1}, but can achieve pump-probe delays of up to 33 ns, longer than the system response of the nanosecond TA experiment currently used by our group. In addition, it allows the collection of transient spectra as wide as 300 nm in one laser shot, greatly simplifying the investigation of short-lived transient species with unknown spectral characteristics.

Pulse Generation

A Coherent Antares mode-locked Nd:YAG laser and a Continuum RGA-60 regenerative amplifier are used in the experiment. The Antares generates 1064 nm pulses at 38 Mhz with full-width at half-maximum (FWHM) values of approximately 90 ps. Originally intended as a dye amplifier pump source, the RGA-60 runs at 10 Hz, and can easily generate 50 mJ 1064 nm (FWHM $\approx$ 90 ps) pulses when seeded with the unmodified output of the Antares. In this experiment, however, its output directly generates the pump and probe pulses, and so its pulses' temporal widths affect the experiment's temporal response. The combination of two 90 ps pulses (one for the probe and one for the pump) yields an instrument response of ~180 ps if their temporal profiles are roughly gaussian. This limits the experiment's usefulness to measuring the kinetics of processes with lifetimes greater than 0.5 ns. Because many of the excited-states we are interested in decay

within this amount of time, the amplifier's output pulses must be shortened before their kinetics can be measured. This is done by chirped pulse amplification and compression.

Chirped Pulse Compression: Theory

The method of pulse shortening we have employed relies on the nonlinear optical effect self-phase modulation (SPM). When a suitably intense optical pulse passes through a medium, it can induce transient changes in its index of refraction. These changes are dependent on the pulse's time-dependent intensity I(t) and the optical Kerr coefficient of the medium n_{2I}:

Equation II.1 $$\Delta n(t) \equiv n(t) - n_0 = n_{2I}\mathrm{I(t)}$$

Intensity variations in the pulse thus induce a phase modulation that is dependent on its center wavelength λ and the distance L it has traveled through the medium:[1]

Equation II.2 $$\Delta\omega(t) = \exp\left(\frac{-j2\pi n_{2I}\mathrm{I(t)L}}{\lambda}\right)$$

If $n_{2I} > 0$, the modulation lowers the pulse's optical frequency during its leading edge where $dn/dt > 0$, and raises it during its trailing edge, giving the pulse a frequency chirp that increases with L. As the pulse travels through the medium, both its spectral and temporal widths are increased (Figure II.2).

Once a pulse has been chirped, its temporal width can be substantially shortened by compression. A compressor can be thought of as a delay line with a frequency dependent delay. By moving all the frequencies within the chirped pulse into phase, the pulse's temporal width is reduced by a factor that is dependent on

Figure II.2 A qualitative representation of the frequency (**A**) and temporal (**B**) broadening that occurs upon propagation of a short (~6-ps) pulse through an optical fiber. The wavelength of the light is a function of its phase relative to the pulse's temporal center (**C**), so that linear dispersive compression can yield significant pulse shortening (**D**). (Taken from reference 1.)

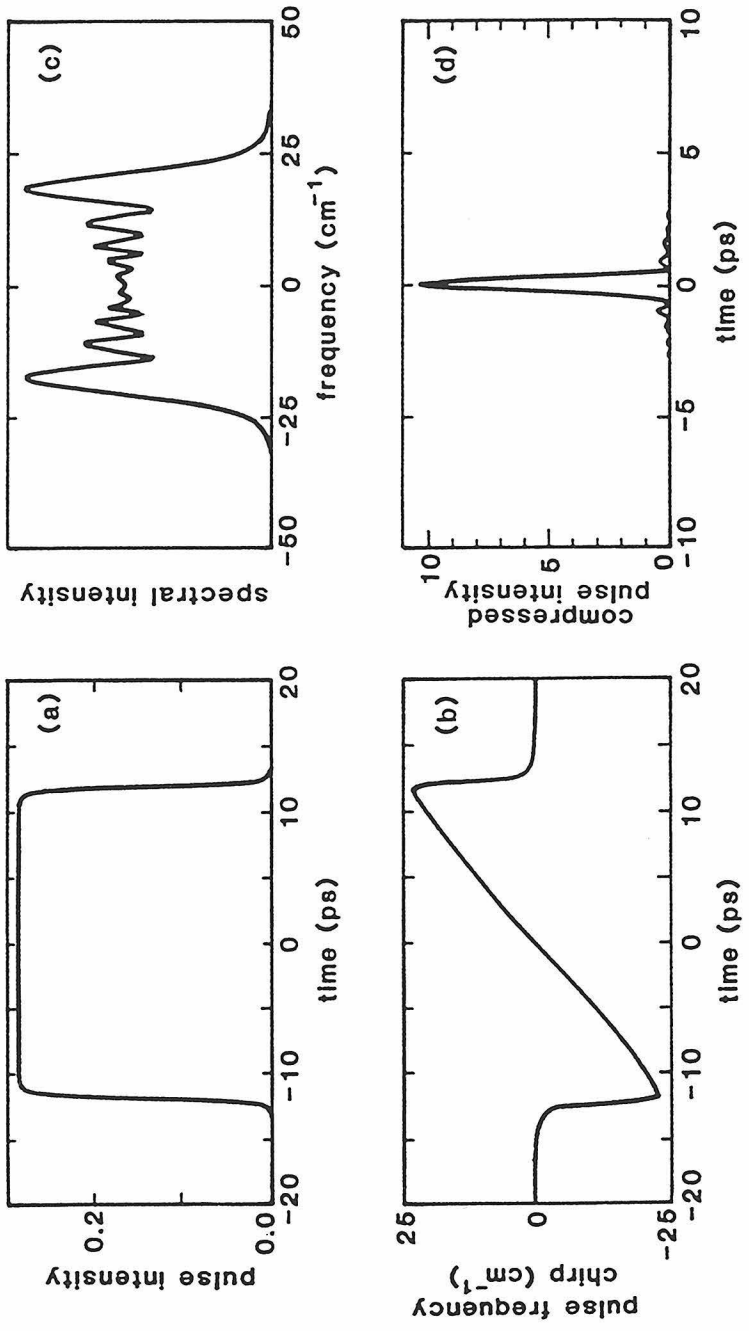
(a)
pulse intensity
0.0
0.2
−20
−10
0
10
20
time (ps)
(b)
pulse frequency chirp (cm⁻¹)
25
0
−25
−20
−10
0
10
20
time (ps)
(c)
spectral intensity
−50
−25
0
25
50
frequency (cm⁻¹)
(d)
compressed pulse intensity
0
5
10
−10
−5
0
5
10
time (ps)

the spectral bandwidth of the input pulse. So, ideally, the more a pulse is chirped, the shorter its temporal width will be after compression.

Chirped Pulse Amplification and Compression: Practice

Although any medium with a sizable optical Kerr coefficient can be used to chirp laser pulses, practical considerations reduce the number of options. Most applications use optical fibers because of their low loss and freedom from detrimental nonlinear processes such as self-focusing.[2] Still, fibers add group-velocity dispersive (GVD) elements to the pulses that are not as significant in bulk media. These can limit the bandwidth imposed by the chirp, but can also linearize it, increasing compression efficiencies. Approximately 100-m of single-mode 1.064 μM optical fiber are used in this experiment to chirp a fraction of the Antares' fundamental output. The amount of light fed into the fiber is adjusted to provide the 1 watt of output used to seed the amplifier.[3]

The seed's spectral profile is highly dependent on both the amount of light fed into the fiber and the cavity length of the Antares. At high input powers, the spectrum loses symmetry and develops large spikes attributable to SPM, GVD and stimulated Raman scattering.[4] These inhomogenaities do not exist at the powers used during the experiment. As anticipated by Equation II.2, the width of the spectrum is dependent on the cavity length of the Antares, which affects the temporal widths of the pulses fed into the fiber. Because of this, drifts in the Antares cavity length can substantially affect the experiment's temporal response.

Pulses are compressed between the laser's oscillator and amplifier stages

(Figure II.3). They are compressed here because the powers necessary (~25 mJ at 1064 nm) to generate adequate pump and probe light intensities would burn any dispersive optics used after the laser. The 10 mJ pulses from the oscillator are directed out of the RGA-60 and onto a 1200 groove/mm gold grating (Milton-Roy). Compression is achieved by reflecting them off of the grating three more times with a retroreflecting prism.[5] Before they enter the amplifier stage, their powers have been attenuated to approximately 1 mJ.[6] Their widths, however, have been reduced from ~45 ps with chirped-pulse amplification alone to ~10 ps (Figure II.4).[7]

Overcoming Regenerative Amplifier Problems

As Figure II.4 indicates, chirped pulse amplification and compression leads to the generation of near transform-limited Nd:YAG pulses, but the RGA-60's design as a dye amplifier pump source allows behavior that must be controlled before it can be used for this experiment. Problems that have been encountered during construction of this experiment typically involve the Pockels cells within the laser's oscillator stage.

The basic design of the RGA-60 is described in detail elsewhere.[8] It is centered around an oscillator composed of two high reflecting mirrors, some polarizers and polarization rotators, and two Pockels cells. Pockels cells are electro-optic modulators capable of electric-field-induced birefringence changes. When the laser is not running, seed pulses enter the oscillator cavity, make one round trip, and are then rejected by the polarizers within it. When 1200 V is applied across the first Pockels cell, it rotates the seed's polarization, allowing it to remain in the

Figure II.3 Schematic representation of the chirped pulse amplification scheme currently used to generate near transform-limited Nd:YAG pulses with energies of ~25 mJ.

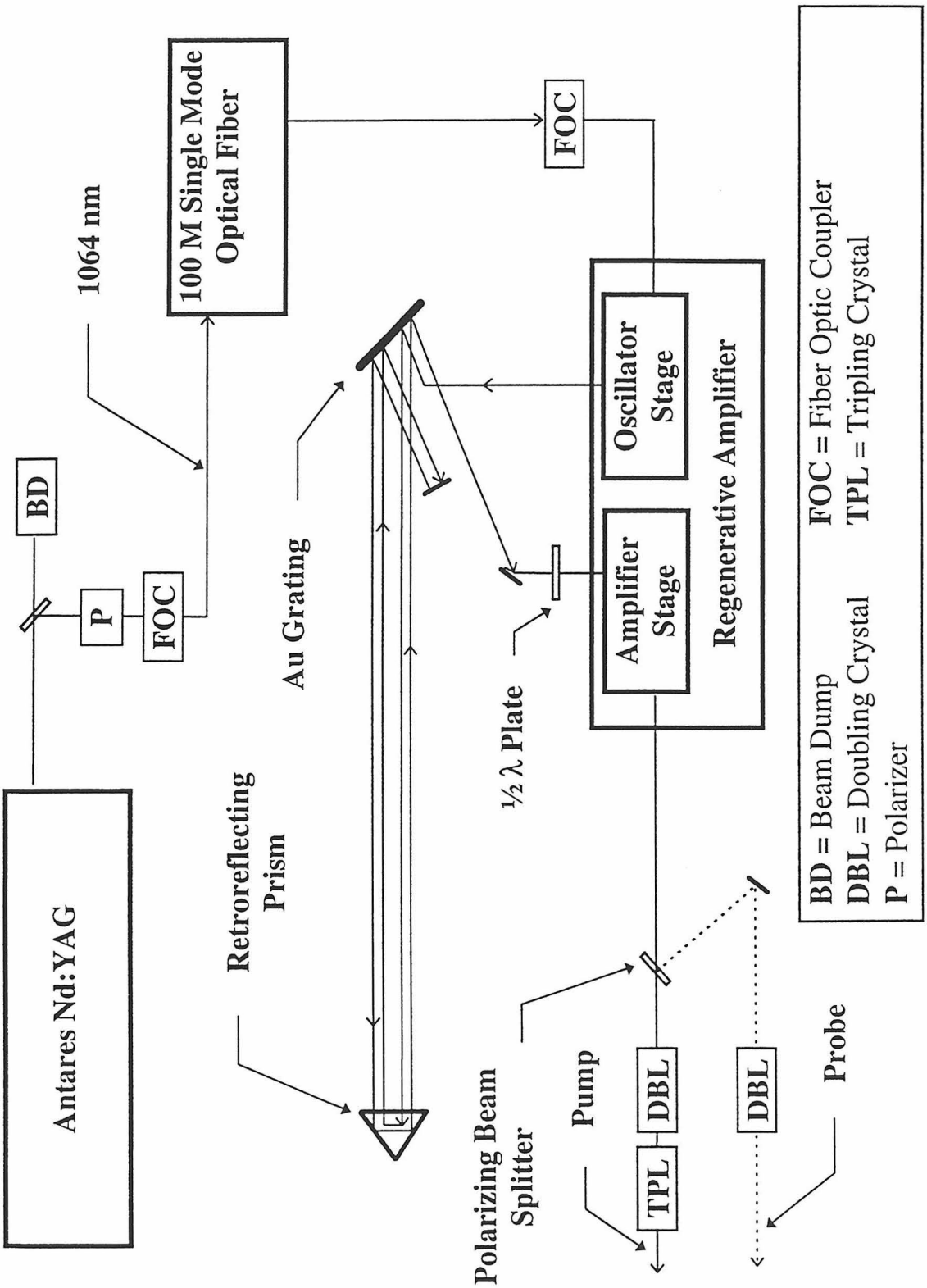
Antares Nd:YAG
BD
P
FOC
1064 nm
100 M Single Mode Optical Fiber
FOC
Au Grating
Retroreflecting Prism
½ λ Plate
Oscillator Stage
Amplifier Stage
Regenerative Amplifier
Polarizing Beam Splitter
Pump
TPL
DBL
DBL
Probe
BD = Beam Dump
DBL = Doubling Crystal
P = Polarizer
FOC = Fiber Optic Coupler
TPL = Tripling Crystal

Figure II.4 Pulses from the regenerative amplifier following compression have autocorrelation signals that can typically be fit to a Gaussian function FWHM ≈ 10 ps.

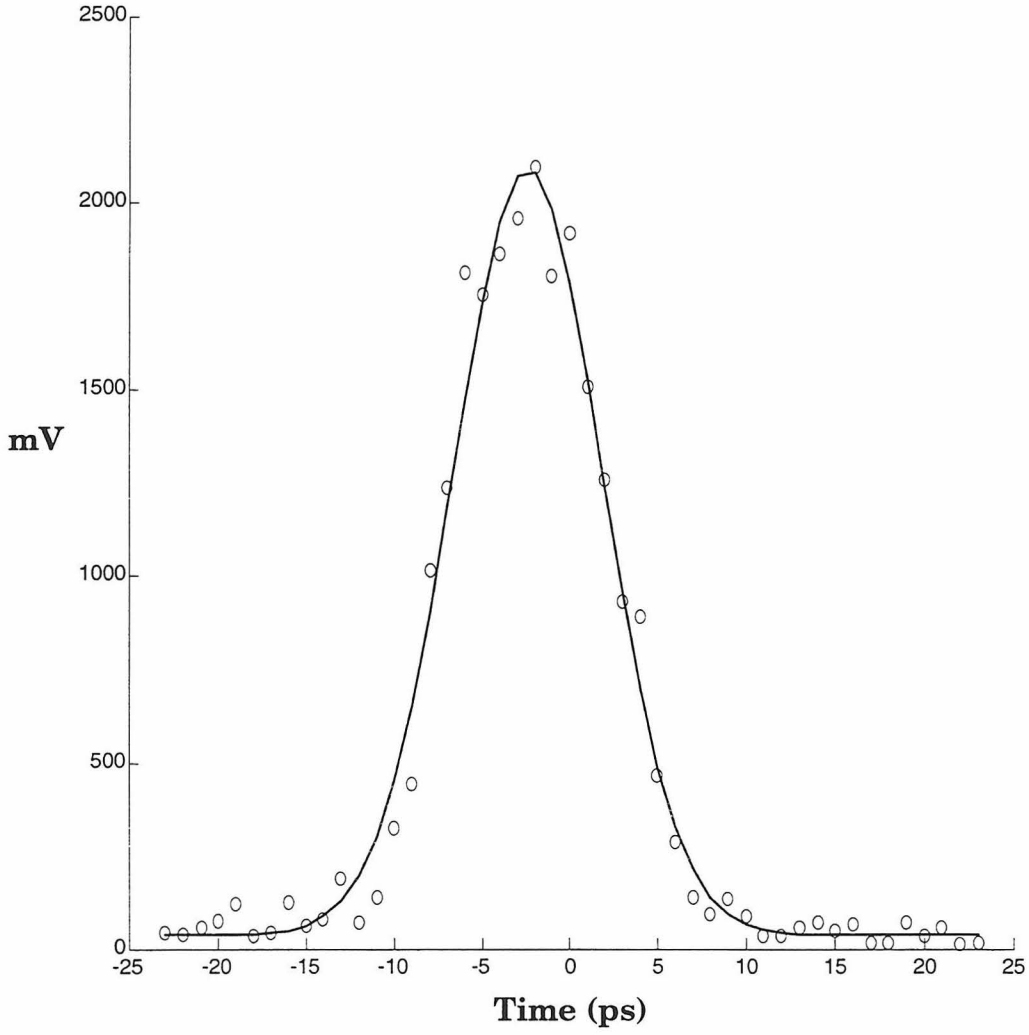
2500
2000
1500
1000
500
0
mV
-25
-20
-15
-10
-5
0
5
10
15
20
25
Time (ps)

cavity for amplification. Activation of the second Pockels cell ejects an amplified pulse from the cavity. The cells' polarization efficiencies depend on their alignment within the cavity and the amount and risetime of the voltage applied across them. Because the pulses in the oscillator cavity are separated by 7 ns, it is important that the birefringence of the switch-out Pockels cell undergoes a complete change within 2 or 3 ns.

The RGA-60's reliance on outdated Marx bank technology to generate the quarter-wave voltage has proved problematical. The Marx banks are series of 15 2N5551 transistors that fail in a cascade when the first is triggered, generating a 1200 V pulse from a 350 V power supply. Their performance is highly dependent on all of the transistors': If one cannot hold the steady-state voltage, the full 1200 V will never be generated. If one does not react quickly, the risetime of the pulse can be severely compromised. Unfortunately, extended use results in both slow and catastrophic failure of the transistors, especially the first in the chain. The complete failure of one halts the laser output entirely, but the partial failure of one -- a more common occurrence -- can lead to longer pulse widths and poor pulse selection. Because these problems can be caused by other factors, such as poor seed pulse stability, they are difficult to diagnose. Drifts in the timing of the switch-out Pockels cell can also dramatically affect the output pulses' widths. These problems are currently avoided by close monitoring of the lasers' behavior during experiments. Replacement of the Marx banks with ones of newer design will be done in the future. Many alternatives exist, some of which utilize MOSFETs[9] or

spark-gap switches,[10] and others of which simply use modifications of the linear transistor design.[11]

Another problem arises from the amplifier's unstable resonator design. While yielding very high gain, the design also allows the amplification of stray reflections within the laser. In our particular case, some orientations of the switch-out Pockels cell can cause the generation of a second output pulse 230 ps after the first. It appears that reflections between surfaces inside the cell cause the problem. The presence of the second pulse is constantly monitored during experiments by feeding some of the amplifier's 1064 nm output into a home-built autocorrelator. It is eliminated with small adjustments to the Pockels cell's orientation.

Generation of Pump Colors

After leaving the amplifier, the ~25 mJ 1064 nm (~10 ps FWHM) pulses are divided with a polarizing beamsplitter. A half-wave plate placed before the RGA-60's amplifier stage allows control over division of the light. One portion generates the probe light, and the other generates the pump. Harmonic generation is done after the beamsplitter to reduce chances of burning the doubling crystals. The continuum probe light is generated with 532 nm pulses, but both 532 nm and 355 nm pulses have been used for sample excitation. Other wavelengths are generated by focusing either harmonic through a 3-ft long tube containing gases at various pressures. First Stokes Raman-shifted light has been created with efficiencies as high as 40% using 150 psi of methane or 850 psi of hydrogen.[12] The high powers and good spatial characteristics of the first Stokes lines permit their

immediate use as pump light. Both 416 nm (355 nm in H_2) and 683 nm (532 nm in H_2) have been used. Higher-order Stokes lines, and anti-Stokes lines, have also been generated, but have yet to be used in an experiment: Their low powers and ring-like shape mean amplification is necessary before they can be used for sample excitation. This could be accomplished with a Raman amplifier,[13] but a flashlamp-pumped dye amplifier would be a more practical solution.

When Raman-shifted light is used to excite samples, a pellin-boca prism placed after the gas tube helps remove the fundamental and other Raman-shifted colors from the desired one (Figure II.5). The light is highly polarized, so a half-wave plate placed before the tube is adjusted to minimize surface losses at the prism. When Nd:YAG harmonics are used for sample excitation, the shift tube is removed and the prism is replaced with a mirror.

The system response depends on the pump light. If a Nd:YAG harmonic is used, it can be fit to a 30 ps-wide (FWHM) gaussian function.[14] When Raman-shifted light is used, the width narrows to ~18 ps (Figure II.6).[15]

The pump pulses travel a fixed distance to the sample. The timing of the probe pulses is adjusted by reflecting them off of mirrors mounted on an 8-ft delay stage.[16] A retroreflector then raises the beam's height, and sends it back down the stage. By traveling the stage four times, the probe light can arrive at the sample over 30 ns after it has been excited. The positioning error of the stage is negligible.

Figure II.5 In addition to containing the detection optics, the second table used by the experiment contains the delay stage and the Raman shift pipe. When Nd:YAG harmonics are used for sample excitation, the pipe is removed, and the pellin-boca prism used to separate its colors is replaced with a mirror. The detection optics are arranged to allow a counter-propagating collinear pump-probe geometry.

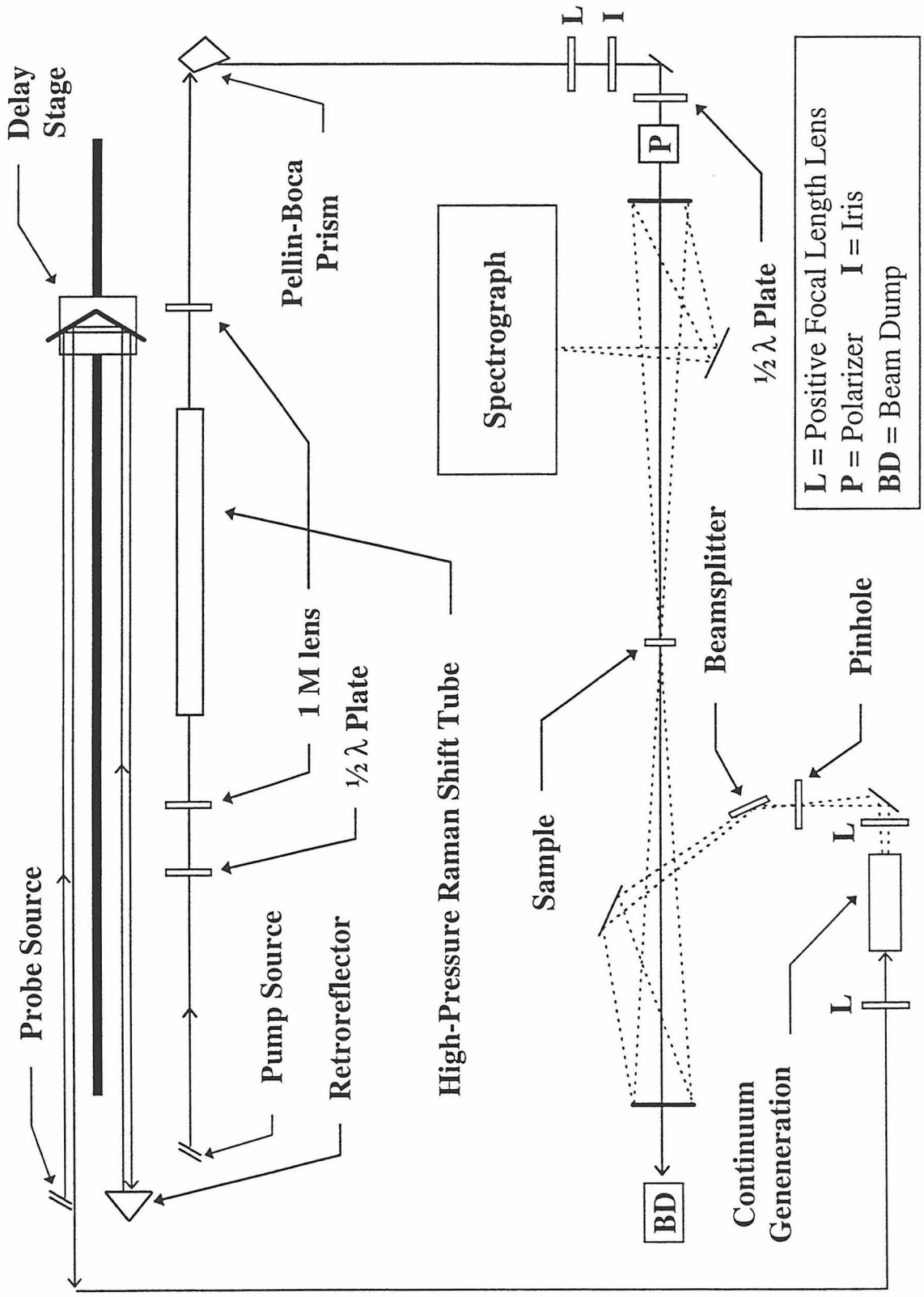
Delay Stage
Probe Source
Pump Source
Retroreflector
1 M lens
½ λ Plate
Pellin-Boca Prism
High-Pressure Raman Shift Tube
Spectrograph
Sample
Beamsplitter
Pinhole
Continuum Genereration
½ λ Plate
L
I
P
BD
L = Positive Focal Length Lens
P = Polarizer I = Iris
BD = Beam Dump

Figure II.6 The system response for 532 nm excitation experiments can be determined by fitting the shifted Soret of Fe(octaethyl porphyrin) to a Gaussian (**A**: FWHM = 30 ps). The Soret bleach of horse heart cytrochrome c is used to determine the system response when 416 nm excitation is used (**B**: FWHM = 17.5 ps).

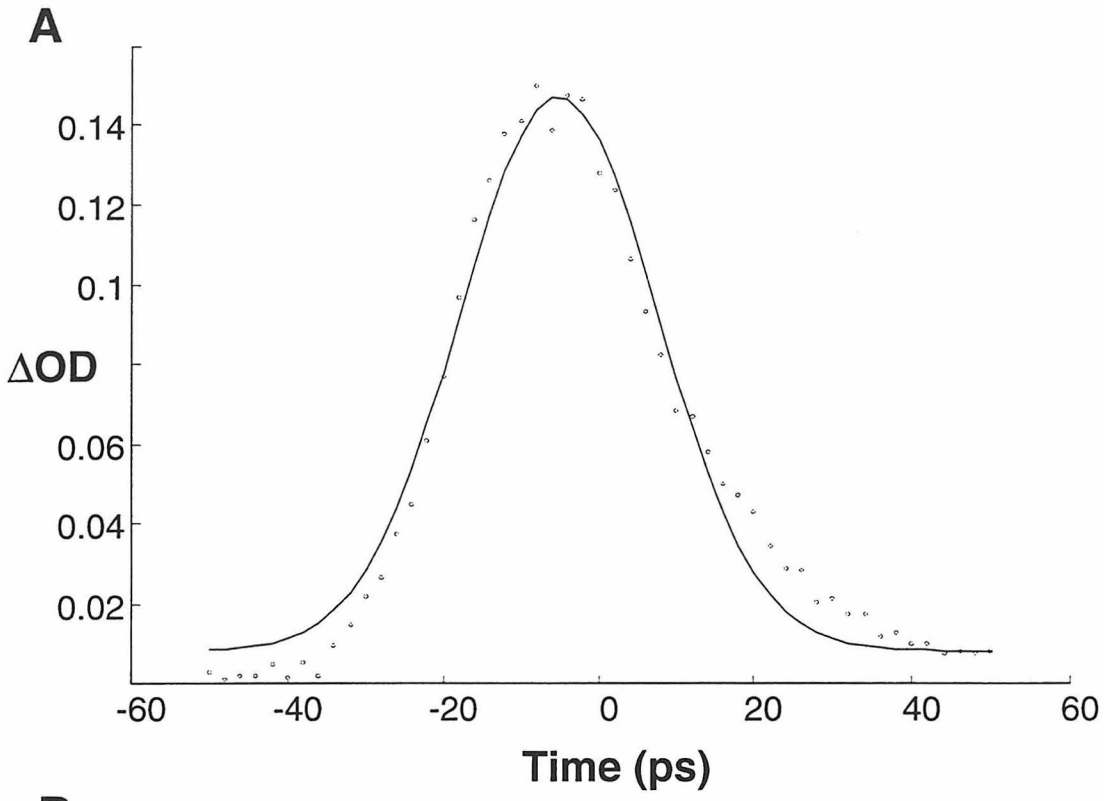
A
0.14
0.12
0.1
ΔOD
0.06
0.04
0.02
-60
-40
-20
0
20
40
60
Time (ps)

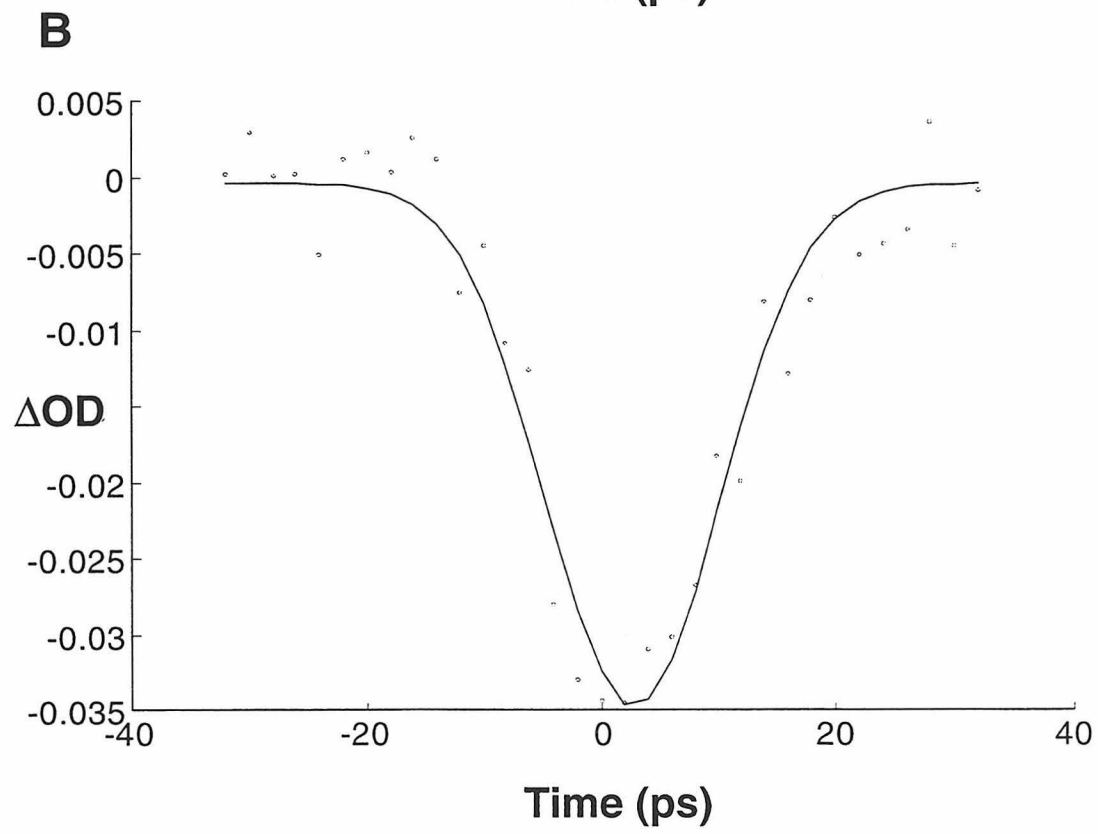
B
0.005
0
-0.005
-0.01
ΔOD
-0.02
-0.025
-0.03
-0.035
-40
-20
0
20
40
Time (ps)

Detection Optics

The optics used to direct the probe light onto the sample and into the detector all work at *f*15. They are separated from the rest of the experiment by a 400-μm pinhole (Figure II.7). The continuum probe light is generated by focusing ~1.5 mJ 532 nm pulses through a 10-cm path-length cell containing a mixture of D_2O, H_2O and H_2SO_4. The spectrum of the resulting light is highly dependent on the powers and width of the pulses used to generate it, as well as the components of the mixture and their ratios (Figure II.8). Pure H_2O produces a large amount of red light dominated by the first Stokes-line. A series of anti-Stokes lines to the blue of 532 nm are generated with pure D_2O. The combination of these, with some strong acid to reduce the intensities of Raman scattering from O-H stretches, allows 532 nm pulses to produce light suitable for probing the sample anywhere between 360 nm and 800 nm. The residual green is removed with a dielectric mirror, and the resulting light is collected by a lens and focused through the pinhole. After passing through a polarizer, the light is divided with a beamsplitter into sample and reference portions. The reference optics exist simply to focus the light into the spectrograph. The sample optics focus and collect the probe light while providing for a collinear pump/probe geometry: The 2-inch diameter mirrors that direct the light onto the sample and then collect it each have a 1-cm hole drilled in their centers. The pump light is directed through these holes. The amount of scattered pump light that enters the detector is minimized by a counter-propagation arrangement, in which the pump and probe pulses travel in opposite directions.

Figure II.7 The detection optics are composed of both curved and flat UV aluminum mirrors. The polarization of the probe light is vertical. Its sample and reference portions are both focused into the spectrograph, one on top of the other. The 1-mm space between the two diode arrays is large enough to ensure that with proper alignment no crosstalk occurs.

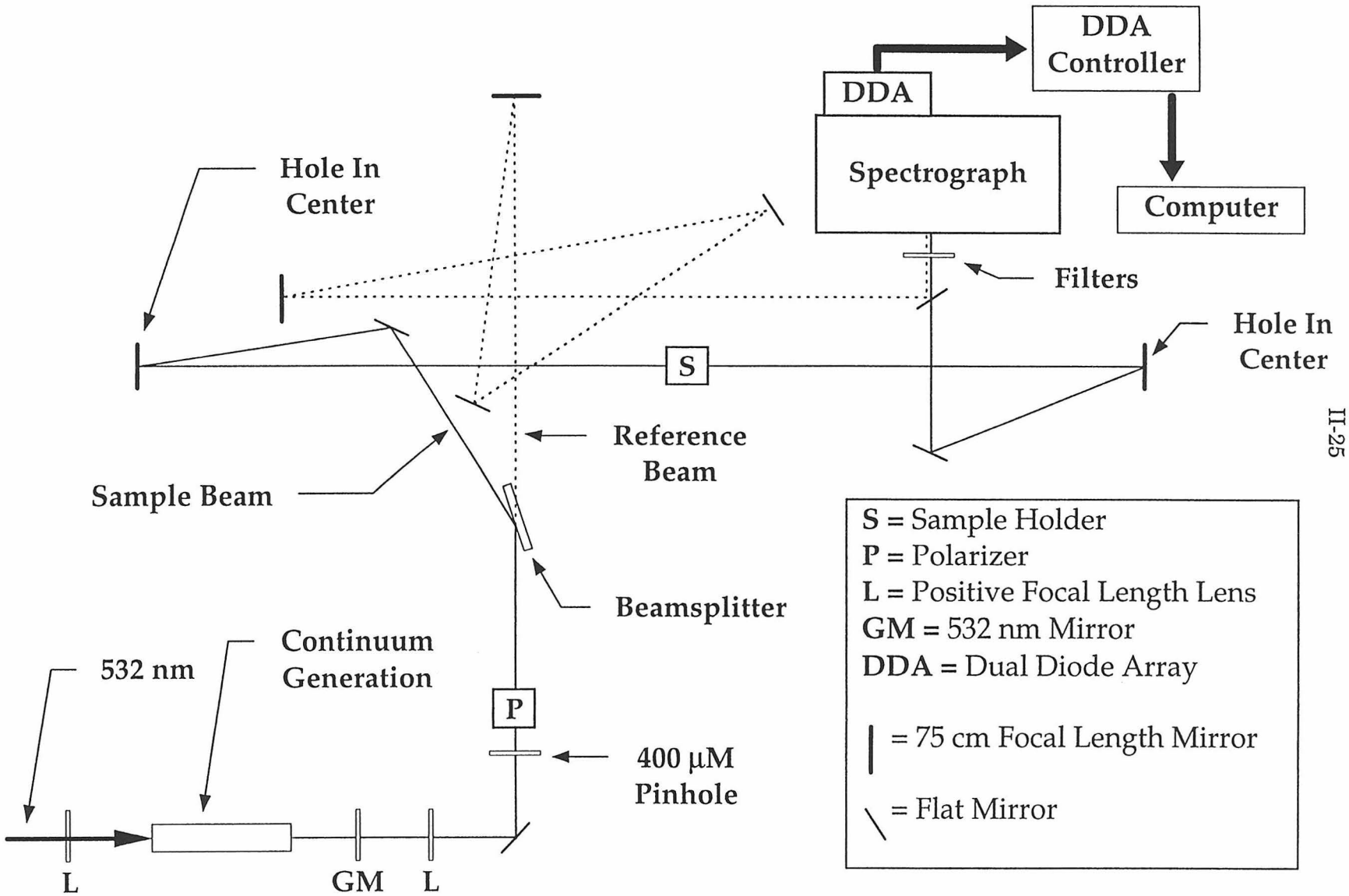
DDA
Controller
DDA
Spectrograph
Computer
Hole In
Center
Filters
Hole In
Center
S
Reference
Beam
Sample Beam
Beamsplitter
Continuum
Generation
532 nm
P
400 μM
Pinhole
L
GM
L
S = Sample Holder
P = Polarizer
L = Positive Focal Length Lens
GM = 532 nm Mirror
DDA = Dual Diode Array
= 75 cm Focal Length Mirror
= Flat Mirror

Figure II.8 Probe light is generated by focusing ~1.5 mJ 532 nm pulses (FWHM ~10 ps) into a 10-cm path-length cell containing a mixture of D_2O, H_2O and H_2SO_4. Residual green light is removed with filters. The shape of the continuum spectra in the red (**A**) and the blue (**B**) depend on the mixture's components and their ratios.

A

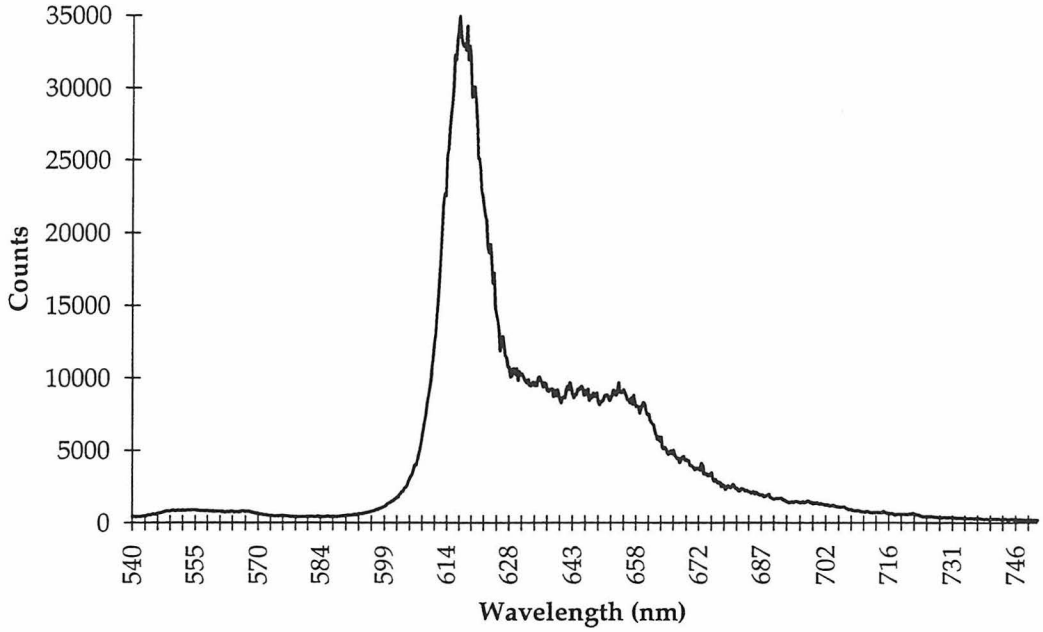
35000
30000
25000
20000
15000
10000
5000
0
Counts
540
555
570
584
599
614
628
643
658
672
687
702
716
731
746
Wavelength (nm)

B

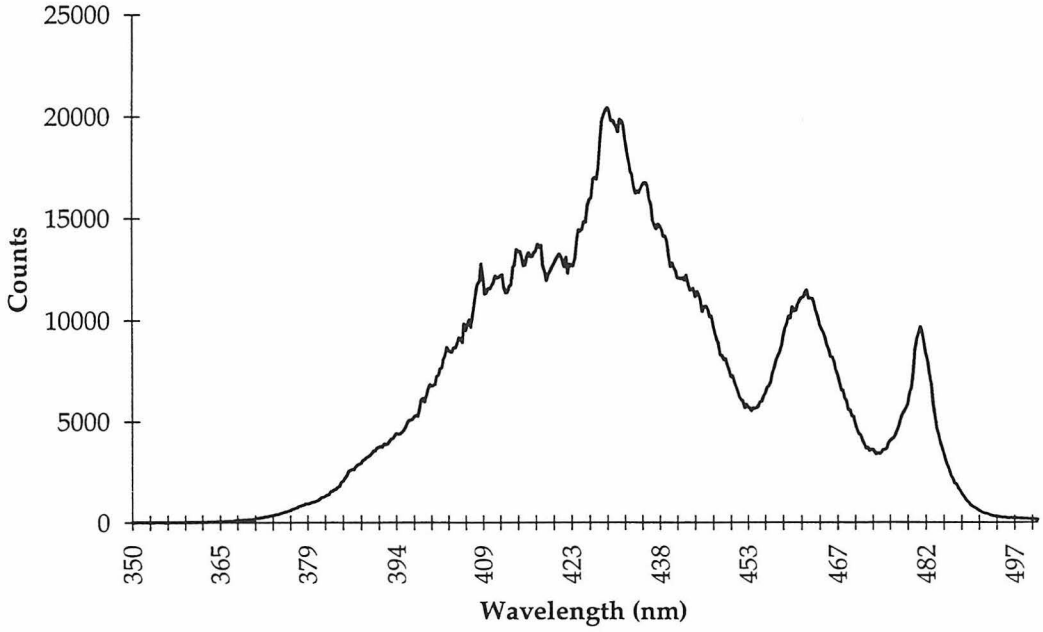
25000
20000
15000
10000
5000
0
Counts
350
365
379
394
409
423
438
453
467
482
497
Wavelength (nm)

The collinearity of the two beams simplifies experiments in which molecular rotational dynamics occur at rates comparable with the decay of the excited-states under study. By rotating of the pump light's polarization to the magic angle relative to the probe light's, such effects can be removed from the transient data.

Data Acquisition

Data acquisition involves the cooperative use of several devices, most of which are controlled by software described below. The lasers, however, run continuously throughout the experiment. At its start, the pump and probe beams are initially blocked by pneumatic shutters controlled by an array of solenoids. The solenoids determine in what direction the nitrogen gas used to drive them flows, and hence their orientations (Figure II.9). When the shutter after the delay stage is opened, probe light is generated, split into sample and reference portions, and finally focused into the spectrograph and detected with the dual diode array (Figure II.7).[17] A grating turret in the spectrograph allows the selection of two 300 groove/mm gratings -- one blazed for 500 nm and the other for 300 nm -- or a 1200 groove/mm holographic grating. Every time the regenerative amplifier fires, it sends a -15 V synchronization pulse to an inverter and voltage divider, the +5 V output of which triggers the diode array detector to read the arrays. Each diode array contains 1024 diodes, and is long enough to allow spectral regions as wide as 300 nm to be viewed at one time with the lower resolution gratings. The holographic grating allows regions approximately 90 nm wide to be viewed at one time.

Figure II.9 Pneumatic shutters control the sample's exposure to both pump and probe pulses.

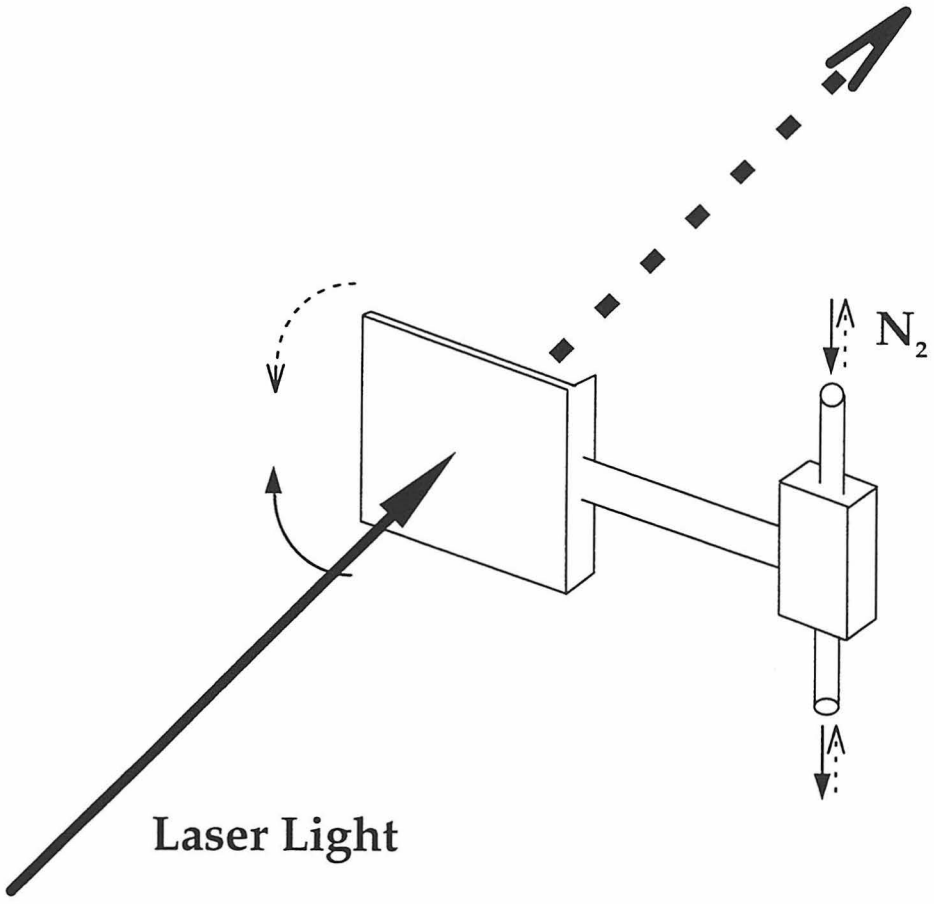
N_2
Laser Light

Data collection is performed by the software in units called runs. A run contains a number of cycles, each of which corresponds to one delay stage position. Each cycle includes background, ground-state and excited-state data. If multiple runs are collected, this data is averaged. At the start of each cycle, both shutters are closed and background noise is collected. A shutter then opens to allow the generation of continuum probe light and the collection of ground-state absorption data. Finally, the second shutter opens, exposing the sample to the pump beam and allowing the collection of excited-state spectra.

If an experiment consists only of the collection of a transient spectrum at a single delay, collection is continued until its signal-to-noise ratio is acceptable. If decay kinetics are being acquired, a single wavelength is selected at the start of the experiment, and after each run the data acquisition software plots the ΔOD at it *versus* time. The experiment is continued until the signal-to-noise ratio of the kinetic trace is acceptable.

By collecting the data in multiple runs of cycles containing information acquired with only a few -- typically five or six -- laser shots, drifts in beam quality and pump/probe overlap have little effect on the quality of the data. Random power fluctuations are spread over all the delay points, and so also have little effect on the quality of the kinetic data.

Sample Handling

The quality of data collected with this experiment is dependent on a number of factors. One of them is the way in which the sample is treated during an

experiment. It is important, particularly in experiments that use laser pulses shorter than a nanosecond, that new sample is excited with each shot. Many compounds will begin to decompose after they are repeatedly exposed to laser pulses' high peak powers. In picosecond experiments, other factors, such as multiphoton-induced degradation, can also decrease the quality of data. In order to obtain the best data possible, it is important to ensure that a new sample volume is excited with each laser shot.

In nanosecond experiments, this can be accomplished by stirring the solution sample within its cuvette, which is typically 1-cm square. For low time resolution experiments, this technique can also be used in this experiment. For the study of fast kinetics, however, a 1-cm long path-length is unacceptable: The longer the path-length, the slower the system response. With the pulse widths used here, an optical path-length of longer than 2-mm can have a detrimental effect on the system's temporal response. Clearly, a stirbar will not fit within a 2-mm cuvette, and so an alternative method for refreshing the sample volume is used.

Most experiments performed with this PTA system use quartz 1-mm path-length cells, through which the solution sample is flowed. The top and bottom of a cell are attached to the side and bottom of a flask. Stirring the solution (typically 25 mL) generates a velocity gradient within the flask, forcing the sample to flow through the cell, top to bottom.

Software Control

Except the lasers, all the devices in the experiment are controlled with home-written software running on an IBM PC-compatible computer under MS-DOS. Additional software was written to analyze the data after the completion of an experiment. All the programs were written in a mixture of C and C++ using a Borland C++ compiler (version 4.0). The data collection program can be divided into four parts: device control, data acquisition, data storage and the graphical interface.

When the delay stage is first turned on, it executes an initialization program that turns on the stage motor and tells the stage to seek its physical end. Once there, the logical stage position is set to zero tics.[18] The PC software displays the stage position in picoseconds from this position.[19] To move the stage, the operator enters a desired time, and the program converts it to tics, couches it in the appropriate delay stage controller commands, and sends the information to the controller *via* an RS-232 serial interface.

Communication with the spectrograph utilizes a GPIB interface, and so is much less prone to error. The grating and center wavelength can both be set with the controlling software.

The shutters are also controlled by software, although their settings can be manually overridden. The solenoids that control the flow of gas operate on 115 V A/C which is controlled by switches operated with TTL logic. Auxiliary outputs on diode array controller are used to operate the switches.

Direct memory access (DMA) is used to transfer data between the computer and the controller. DMA is a means by which an external device can put data directly into the computer's memory, without the involvement of the CPU. The software uses modifications of functions provided by Princeton Instruments that program the two Intel 8237 chips on the PC system board which control DMA transfers. These modifications include a memory routine that allocates the contiguous, single-page memory blocks necessary for DMA transfers.[20]

The data transferred to the computer is composed of two arrays of 16-bit integers, each corresponding to the intensity of one diode.[21] The top array measures the light transmitted through the sample, and the bottom measures the reference light. Background noise is subtracted from each before their ratio is calculated. The log of this ratio yields an absorption spectrum. Currently, every four pixels are summed in software[22] before the optical density calculation is made, yielding a floating point array 256 elements long. The ratio of two such calculations, one each for the sample's ground- and excited-states, provides the ΔOD data stored to disk. A complete experiment is stored as a file that contains a header followed by blocks of data, each of which contains the optical density information and the position of the delay stage for one collection cycle. The data is stored at the end of each run, so that new, averaged data replaces the old.

Finally, to enable the facile collection of good data, an interface has been written that allows graphical representation of the data as it is collected. The raw output from the diodes can be read and displayed for alignment purposes. When a single excited-state spectrum is collected, it is displayed and updated at the end of

each run. The display is different for the collection of transient kinetics: At the end of each cycle, the transient at that delay stage position is displayed on the bottom half of the screen. At the end of each run, the ΔOD value at one wavelength chosen at the start of the experiment is plotted against time on the top half of the screen, allowing observation of the kinetics during the course of the experiment. After the experiment, additional software allows the extraction of kinetics at any wavelength in the region for which data was collected.

Conclusion

Without the use of dye lasers, a picosecond transient-absorption system has been built that is very flexible: It can generate a variety of different pump wavelengths by Raman-shifting the Nd:YAG harmonics, and can probe optical absorption changes within a sample throughout the visible and near UV. It will be clear from the following chapters that this experiment provides high quality data useful for the study of a large number of different molecules.

REFERENCES AND NOTES

[1] Siegman, A. E. Lasers, University Science Books. Mill Valley, CA. **1986**.

[2] W. J. Tomlinson, R. H. Stolen and C. V. Shank, *J. Opt. Soc. Am. B* **1**, 139 (1984).

[3] Losses due to the fiber and its optic couplers are approximately 60%.

[4] J. M. Hickmann, J. F. Martins-Filho and A. S. L. Gomes, *Optics Com.* **84**, 327 (1991).

[5] The single grating/prism combination was used in the first example of chirped pulse recompression: Nakatsuka, H.; Grischkowsky, D.; Balant, A. C. *Phys. Rev. Lett.* **1981**, *47*, 910.

[6] Losses of roughly 25% are suffered at the grating.

[7] Autocorrelation of the pulses is performed with an Inrad 5-14B autocorrelator.

[8] Dawson, M. D.; Schroeder, W. A.; Norwood, D. P.; Smirl, A. L.; Weston, J.; Ettelbrick, R. N.; Aubert, R. *Optics Lett.* **1988**, *13*, 990.

[9] Baker, R. J.; Johnson, B. P. *Elect. Lett.* **1993**, *29*, 56.

[10] Beverly, R. E.; Campbell, R. N. *Rev. Sci. Instrum.* **1994**, *65*, 259.

[11] Rai, V. N.; Shukla, M. *Rev. Sci. Instrum.* **1994**, *65*, 2134: Christiansen, J.; Frank, K.; Hartmann, W. *Nucl. Inst. Meth. Phys. Res.* **1987**, *A256*, 529.

[12] Varying the pressures of the gasses results in changing the intensity ratios of first Stokes to other Stokes Raman lines.

[13] Meier, B.; Penzkofer, A. *Appl. Phys. B* **1991**, *53*, 65.

[14] The system response for 532 nm and 355 nm pump wavelengths has been determined by observing the transient kinetics of Fe^{III}(octaethyl porphyrin).

[15] The system response for 416 nm pump light has been determined by observing the bleach of the Soret absorption of horse heart cytochrome *c*.

[16] Anorad Anorail.

[17] The dual diode array is a Princeton Instruments model DPDA-1024. The spectrograph is an Acton Research SpectraPro 275.

[18] For the 8-ft long stage, 1 tic = 1/6400 mm.

[19] It should be noted that the physical end of the stage generally does not correspond to the point at which the probe pulse travels a distance equal to that traveled by the pump pulse.

[20] Nolan, T. *Dr. Dobbs Journal* **1990**, *1*, 28.

[21] This controller contains a 16 bit D/A converter.

[22] Binning can be performed by the hardware before the data is transferred to the computer, but Princeton Instruments never completed the code that enables the use of this feature.

Chapter III

Intramolecular Electron-Transfer in Weakly Coupled Donor-Acceptor Systems

Introduction

The excited-state properties of iridium dimers have long been of interest to our group. Their study grew out of work addressing the spectroscopic characteristics of binuclear rhodium(I) and iridium(I) isocyanide complexes.[1,2] The $^1A_{1g}$ $(d\sigma^*)^2$ (D_{4h}) ground-states of these and other d^8-d^8 dimers, such as $[Pt_2(P_2O_5H_2)_4]^{4-}$, have weakly bonding metal-metal interactions due to mixing between the molecules' filled $d\sigma$ and $d\sigma^*$ orbitals and their unoccupied $p\sigma$ and $p\sigma^*$ orbitals.[3] Vibration and low-temperature optical spectroscopy indicate the metal-metal bonding within these face-to-face metal dimers increases substantially in their singlet ($^1A_{1u}$) and triplet ($^3A_{1u}$) excited-states (Figure III.1). For example, an absorption feature centered at 670 nm in the low temperature optical spectrum of $Rh_2(1,3\text{-diisocyanopropane})_4^{2+}$, which has been assigned to the $d\sigma^* \rightarrow p\sigma$ transition, shows a vibrational progression consistent with the Rh-Rh stretching frequency.[4]

The spectroscopy of these compounds was studied concurrently with the chemical properties of their optically accessible excited-states. It was quickly observed that they are capable of reacting with a variety of substrates. For example, the $^3(d\sigma^*p\sigma)$ state of $[Pt_2(P_2O_5H_2)_4]^{4-}$ reacts with aromatics such as toluene to produce H_2 and organic radicals.[2] The rates of these reactions increase as the C-H bond energies of the substrates decrease, indicating they occur *via* a hydrogen atom-transfer mechanism. In contrast, the reaction which occurs upon irradiation of $Ir_2(2,5\text{-diisocyano-}2,5\text{-dimethylhexane})_4^{2+}$ in 1,2-dichloroethane occurs *via* an

Figure III.1 The metals in square planar d^8-d^8 dimers such as $[Pt_2(P_2O_5H_2)_4]^{4-}$ interact weakly in their $^1A_{1g}\,(d\sigma^*)^2$ ground-states, but more strongly in their excited $(d\sigma^*)^1(p\sigma)^1$ ones.

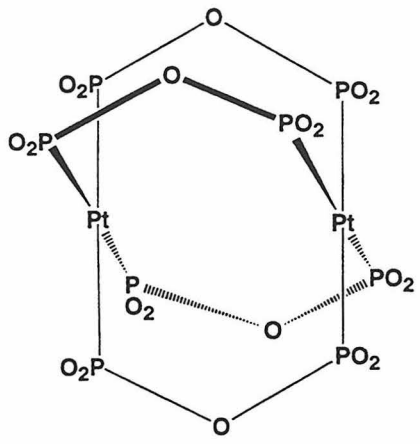
O
O2P
O
PO2
O2P
PO2
Pt
Pt
P
O2
PO2
O
O2P
PO2
O

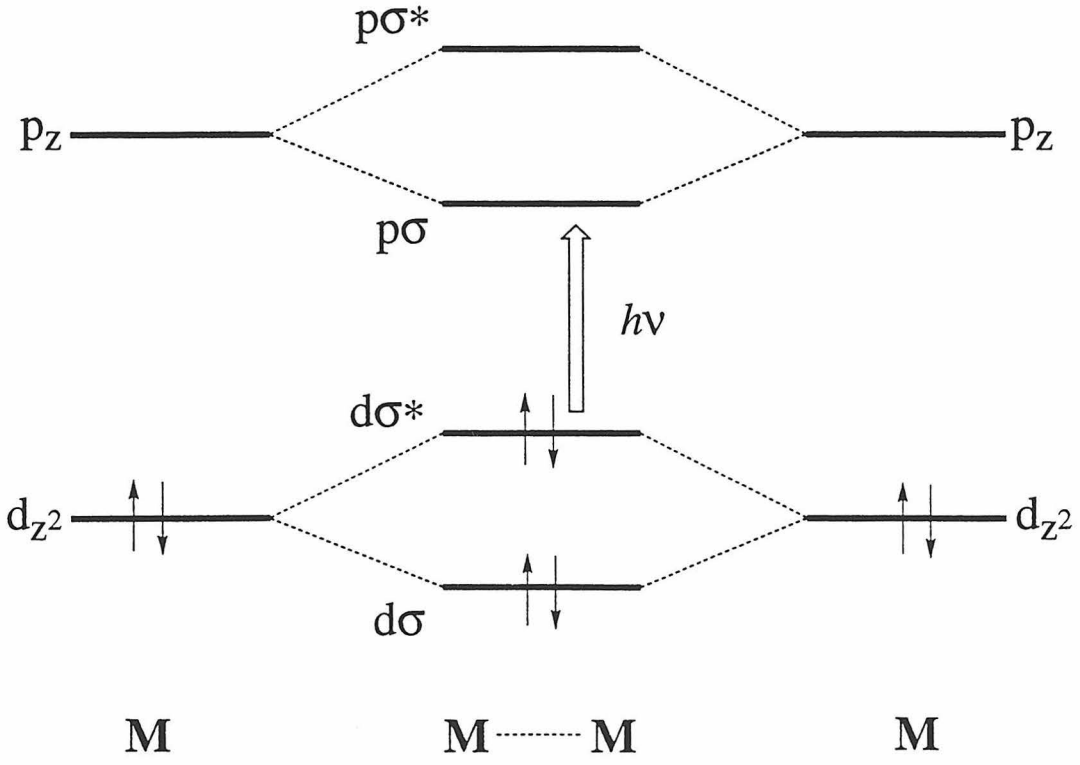
pσ*
pz
pz
pσ
hν
dσ*
dz2
dz2
dσ
M
M
M
M

electron-transfer mechanism.[5] The final product of this reaction is the chlorine adduct Ir_2(2,5-diisocyano-2,5-dimethylhexane)$_4Cl_2^{2+}$.

Observation of these excited-state reactivities led to the realization that similar compounds could be made that would act as efficient photo-active catalysts for hydrogenation and other reactions. Consequently, consideration was given to how the reactivities of these molecules could be improved, and attention turned to lower symmetry (C_{2v}) pyrazolyl-bridged iridium complexes. These allow more facile substrate-metal binding and the potential for a substrate to bind to both metals simultaneously (Figure III.2).

Like their more symmetric counterparts, [Ir(μ-pyrazolyl)(COD)]$_2$ (**1**), [Ir(μ-3-methylpyrazolyl)(COD)]$_2$ (**2**) and [Ir(μ-3,4,5-trimethylpyrazolyl)(COD)]$_2$ (**3**) (COD = 1,5-cyclooctadiene) all exhibit metal-metal interactions between the filled d_{z^2} orbitals of the iridium atoms. The degree of interaction depends strongly on the bridging ligand: Metal-metal distances vary from 3.216 Å for **1**, to 3.073 Å for **3**.[6] These differences manifest themselves in the compounds' spectroscopic and catalytic behavior; **2** acts as a hydrogenation catalyst, while **1** does not. Their visible absorption spectra are dominated by the singlet $d\sigma^* \rightarrow p\sigma$ transition centered near 500 nm ($\varepsilon \approx 9{,}000\ M^{-1}cm^{-1}$) which moves to lower energy as more methyl groups are added to the bridging pyrazolyl ligand. A weak shoulder to lower energy ($\varepsilon \approx 200\ M^{-1}cm^{-1}$) is assigned to the triplet transition.[7] Analysis of the photoelectron spectra of **1**, **2** and **3** indicates that their spectroscopic and reactive differences are due more to electronic inductive effects than to steric ones.[8] This finding is consistent with IR

Figure III.2 Pyrazoyl-bridged iridium dimers such as [Ir(μ-pyrazolyl)(COD)]$_2$ have lower symmetries than the square planar complexes, but their metals interact in the same way.

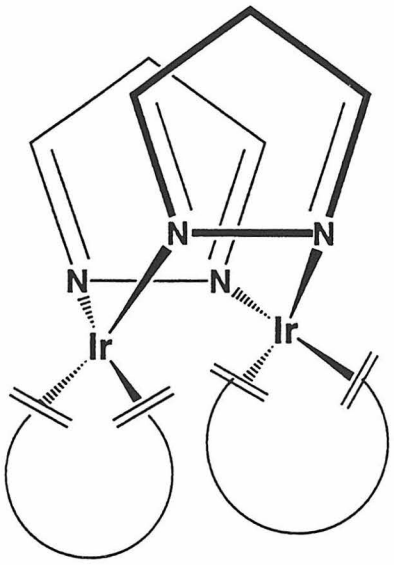
N
N
N
N
Ir
Ir

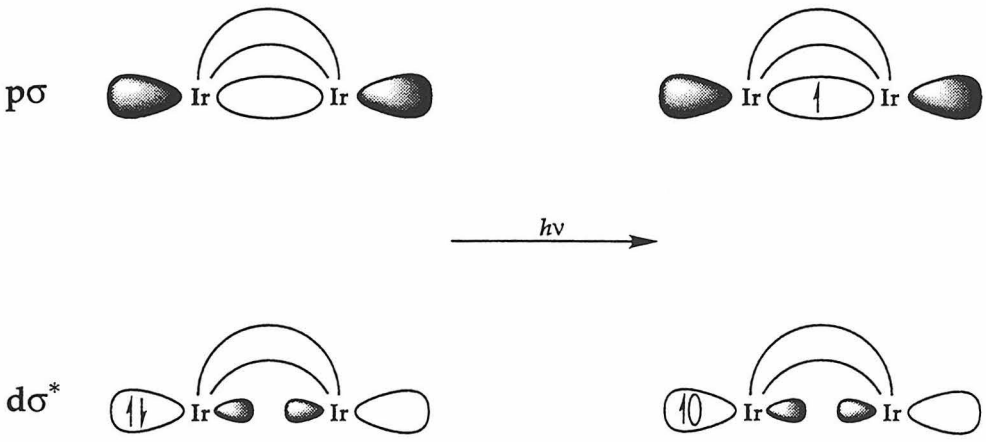
pσ
Ir
Ir
Ir
1
Ir
hν
dσ*
1
Ir
Ir
0
Ir
Ir

absorption data which suggests the $d\sigma^* \rightarrow p\sigma$ transition contains some metal-ligand charge-transfer character.[9]

The emission spectra of the iridium dimers consist of weak fluorescence from the singlet $^1B_2$ excited-state centered near 580 nm, and phosphorescence from the triplet state centered near 700 nm. The lifetimes of these features correspond to their relative intensities: The $^1B_2$ state of **1** has a lifetime of less than 20 ps, and the $^3B_2$ excited-state a lifetime of 250 ns in acetonitrile at room temperature.[10] The singlet quantum yields are almost independent of temperature, but the phosphorescence yields increase significantly as the solvated sample is cooled.[9] The nature of its thermally activated nonradiative decay pathway has yet to be determined.

These molecules have rich photochemistries: Their $^3B_2$ excited-state is a powerful reductant ($Ir_2^+/^3Ir_2^*$ $E_{½}$= -1.7 V *vs.* SSCE in acetonitrile). At room temperature, the triplet state of **1** reduces methyl-viologen with a diffusion-limited rate in acetonitrile. With this finding, it quickly became apparent that these complexes can be used to address the accuracy of Marcus' classical electron-transfer model (Equation I.1). This would be accomplished by measuring the rate of ET k_{ET} from the $^3B_2$ state of **1** to a series of substrates with different reduction potentials.

The dependence of k_{ET} on the driving-force of the reaction $\Delta G°$ has been measured using several different pyridinium cations.[7] It was found for these bimolecular reactions that as $-\Delta G°$ increases, k_{ET} increases from 1.1×10^6 s^{-1} (for 2,6-dimethyl-4-methoxy-*N*-methylpyridinium) to eventually plateau near the diffusion limit when $-\Delta G° \approx 1$ V (for 4-cyano-*N*-methylpyridinium). Similar behavior had been

observed by Rehm and Weller in their pioneering studies of the driving-force dependence of photoinduced intermolecular ET:[11] The inverted effect predicted by Marcus theory was not observed. Recently, the bimolecular iridium/pyridinium system underwent reexamination.[12,13] This work confirmed that the photoinduced reactions (Figure III.3) do not slow even as $-\Delta G°$ greatly exceeds any reasonable estimate of the reorganization energy λ. In contrast, the rates of the subsequent recombination reactions do slow considerably as $-\Delta G°$ grows larger than 1 eV. This difference between charge-separation and recombination reactions is an important one that has bearing on the work described below. It is believed that the high driving-force photoinduced reactions involve an excited pyridinyl radical anion state instead of the ground-state most likely involved in the low driving-force reactions.[14] Although the formation of an excited-state is thermodynamically less favorable than the formation of the pyridinyl ground-state, it can occur at a much greater rate if its driving-force is closer to λ. Similar reasoning has been used to explain ET rates in ruthenium-modified cytochrome *c*.[15]

The diffusion barrier clearly hampers determination of a number of important factors affecting k_{ET}, such as the reactivity of the compounds' $^1B_2$ excited-states and the adiabatic limiting rate. Consequently, a method was found to covalently attach pyridinium acceptors to the 3,5-dimethyl pyrazolyl-bridged iridium core (Figure III.4). The studies of $[Ir_2(\mu\text{-}pz^*)_2(CO)_2(Ph_2PO(CH_2)_2A^+)_2]$ ($Ir_2(A)_2$: pz^* = 3,5-dimethylpyrazolyl; Ph = C_6H_5; A^+ = pyridinium electron acceptor) which began in the mid-1980s are concluded with this work.

Figure III.3 Marcus plot of forward (open circles) and recombination (filled circles) ET rates between compound **1** and various pyridinium acceptors. (Taken from reference 16.)

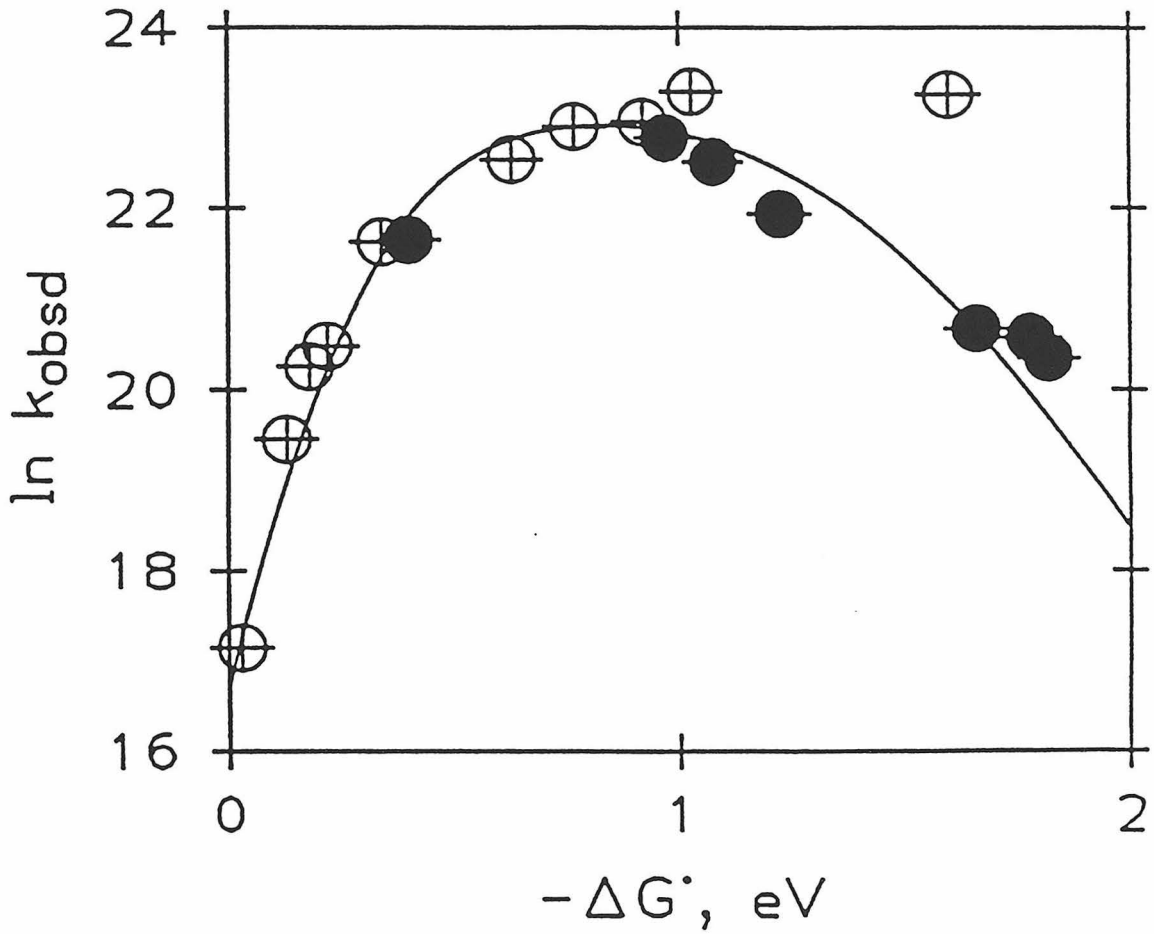
24
22
20
18
16
ln k_{obsd}
0
1
2
$-\Delta G^{\circ}$, eV

Figure III.4 $[Ir_2(\mu\text{-}pz^*)_2(CO)_2(Ph_2PO(CH_2)_2pyridinium)_2]$

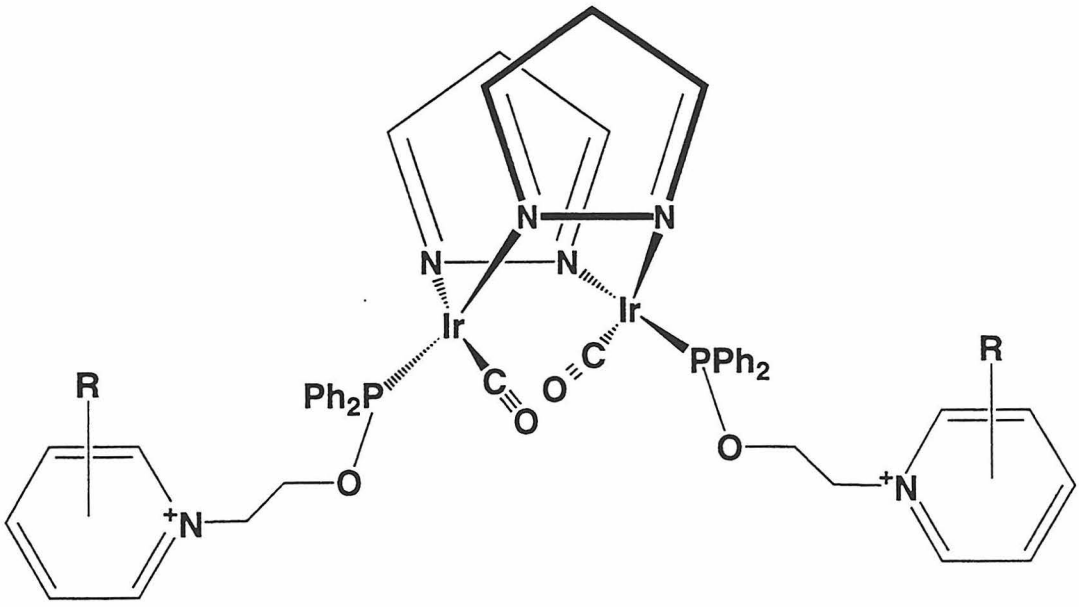
N
N
N
N
Ir
Ir
Ph2P
PPh2
C
O
C
O
R
R
O
O
+N
+N

Pyridiniums are connected to the metals with flexible phosphonite bridges. The absorption spectra of the resulting compounds vary little from the sum of their two components, indicating the donor-acceptor coupling is weak. Their emission spectra are also little changed: The molecules luminesce from both singlet and triplet dσ*pσ states at roughly the same energies as the simple iridium complexes **1**, **2** and **3**. The lifetimes of these states are different, however. Compounds containing poor electron acceptors, such as the model complex Ir_2(triethyl ammonium)$_2$, have singlet lifetimes of approximately 100 ps, and triplet lifetimes of about 1.1 μs.[17,18] Those with good electron acceptors such as pyridinium or 4-phenylpyridinium have dramatically shorter excited-state lifetimes. Confirmation that deactivation of the iridium core's excited-state occurs *via* ET came from picosecond transient absorption measurements of Ir_2(4-phenylpyridinium)$_2$.[17] Its transient spectrum contains the absorption at 390 nm and bleach at 460 nm shown by the model complex, in addition to a strong absorption increase at 350 nm characteristic of the *N*-alkyl-4-phenylpyridinyl radical anion.

Fox and coworkers measured the driving-force dependence of k_{ET} with three compounds; Ir_2(2,4,6-trimethylpyridinium)$_2$, Ir_2(4-methylpyridinium)$_2$ and Ir_2(pyridinium)$_2$. Their photoinduced rates were determined from quantum-yield and time-resolved luminescence measurements, while the recombination rates were measured by transient absorption.[19] Although the number of acceptors used in these studies was far fewer than what had been used in the bimolecular ones, both the singlet and triplet states of the iridium core are viable electron donors in the covalent systems: Bimolecular experiments were limited to ET from the triplet

state because of the iridium dimers' short singlet lifetimes. Now, the diffusion barrier is circumvented, so that for every acceptor, two photoinduced reactions can -- in principle -- be measured (Figure III.5). Quenching of the compounds' fluorescence at ~520 nm provides information about the rates of ET from their singlet states, and quenching of their phosphorescence at ~710 nm yields information about those from their triplets.

The rates of the subsequent high driving-force charge-recombination (^{b}ET) reactions were measured by transient absorption. When combined with the photoinduced rates and plotted as a function of $-\Delta G°$, excellent agreement was found with semiclassical Marcus theory. The charge-separation rates rise from 3.5×10^{6} s^{-1} ($^{3}Ir_2$* $\rightarrow$ 2,4,6-trimethylpyridinum) to greater than 5×10^{11} s^{-1} ($^{1}Ir_2$* $\rightarrow$ 4-phenylpyridinum). The recombination reactions, all of which have $-\Delta G° > 1$ eV, slow dramatically as their driving-forces increase. The fact that both singlet and triplet photoinduced ET and ^{b}ET all fit so well to a single inverted parabola suggest that their donor-acceptor coupling is similar, and can be considered together in a fit to Equation I.5 which yields values of 30 cm^{-1} for H_{AB} and 1.06 eV for λ in acetonitrile. When these results were reported, it was pointed out that not only do they bode well for the rational synthesis of artificial photosynthetic systems, but that this amount of electronic coupling is very close to that estimated for the primary donor-acceptor pair within the bacterial photosynthetic reaction center ($H_{AB} \approx 25$ cm^{-1}).[20]

Comparison of the driving force dependence of k_{ET} in the intra- and intermolecular iridium/pyridinium systems appeared to be the logical conclusion to years of research. As more studies of high driving-force intramolecular ET reactions

Figure III.5 Absorption of light by the iridium/pyridinium molecules' core produces both singlet and triplet excited states which can decay by radiative and nonradiative decay in addition to the electron-transfer pathway. Reduction of a covalently bound pyridinium acceptor can occur from either state with rates $^{1}k_{ET}$ and $^{3}k_{ET}$, respectively. Following photoinduced ET, thermal charge-recombination returns the molecules to their ground states at a rate k_{BET}.

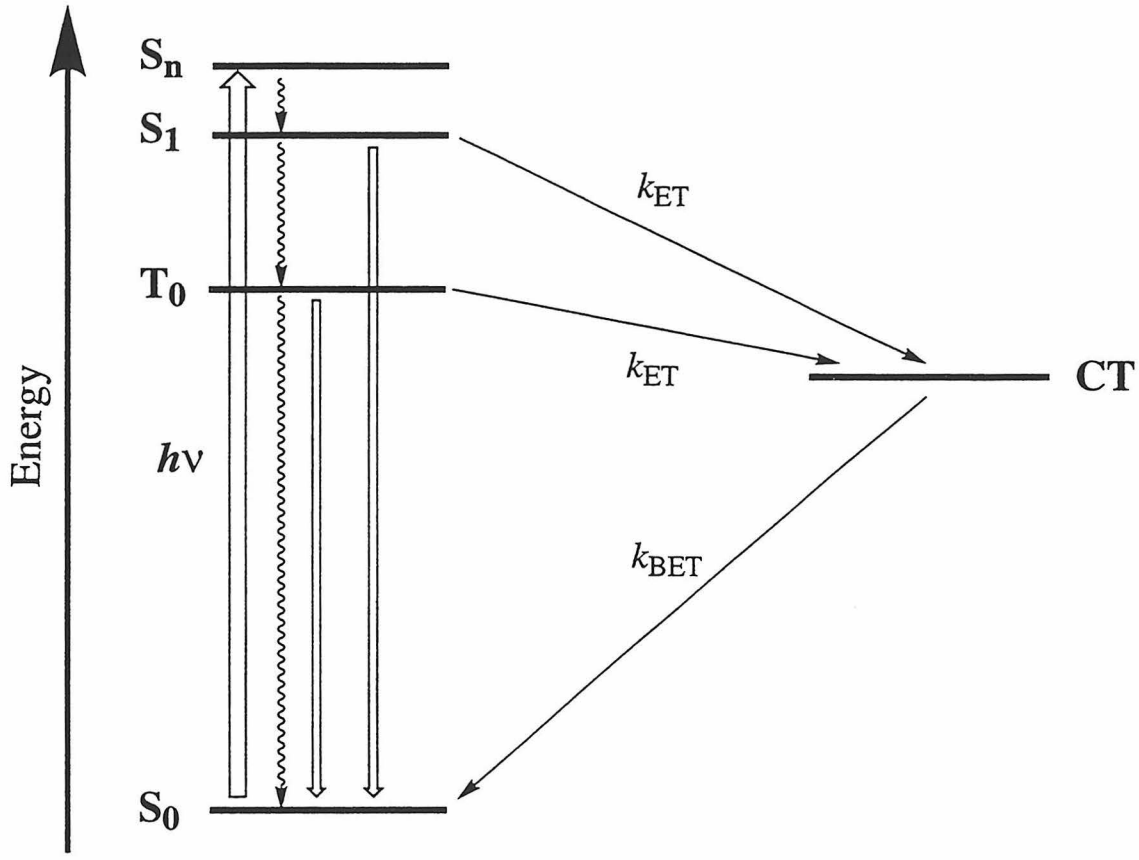
Energy
S_n
S_1
T_0
$h\nu$
S_0
k_{ET}
k_{ET}
CT
k_{BET}

have emerged in the literature, however, it has become clear that inverted effects as strong as those predicted by Equation I.5 are rarely observed.[21] The iridium system's apparently excellent agreement with semiclassical Marcus theory appears to be an oddity. Its more detailed study is therefore important in understanding how highly inverted effects can be built into artificial light-harvesting systems.

Current Studies

The more detailed work is reported here. The early experiments have been repeated and augmented with additional studies all aimed at determining if this ET system behaves classically. We have added an additional acceptor (3,4-dimethylpyridinium) to the series to increase the density of points forming the driving-force curve. More important, the rates of charge-separation and recombination within all the complexes have been measured as a function of temperature. If the reactions behave classically, they should exhibit similar Arrhenius behavior in both the Marcus normal and inverted regions. The effect deuteration of the pyridiniums has on the rates of photoinduced and thermal ET has also been determined: The rates should have little dependence on nuclear vibrational frequencies if the system behaves classically.

Experimental

All solvents were rigorously degassed before any experiments were performed. UV-grade acetonitrile was refluxed over CaH_2 before use, and butyronitrile was distilled and dried over CaH_2 before use. All room-temperature samples, whether used for steady state or transient absorption, emission or Raman

experiments, were degassed with five freeze-pump-thaw cycles. Samples prepared for temperature dependence studies were prepared under an inert atmosphere with dry, degassed solvent. All sample cells were made of UV-grade quartz, and were cleaned with aqua-regia, methanol and acetone before use.

During all the steady state emission, time-resolved emission and transient absorption experiments, sample temperatures were controlled with a CTI Cryogenics model 22 refrigerator.

Synthesis

The natural abundance compounds were synthesized as previously described by Dr. T. M. McCleskey and Dr. D. Weidenfeld.[18] Synthesis of the deuterated isomers was accomplished in the same manner using deuterated pyridine, 4-methylpyridine and 4-phenylpyridine.

Optical Absorption

Absorption spectra obtained prior to steady state and transient experiments were measured with a Hewlett Packard 8452A diode array UV-Vis spectrometer.

Electrochemistry

Electrochemical experiments were conducted by Dr. Michael G. Hill.

Conventional electrochemical experiments were performed with either a Bioanalytical Systems (BAS) Model 100 electrochemical analyzer or a Princeton Applied Research (PAR) Model 173 potentiostat/galvanostat, driven by a PAR 174 Universal Programmer. Cyclic voltammetry was performed with a normal three-

electrode configuration consisting of either a glassy-carbon or platinum working electrode (BAS), a AgCl/Ag reference electrode, and a platinum-wire auxiliary electrode. The working compartment of the electrochemical cell was separated from the reference compartment by a modified Luggin capillary. All three compartments contained a 0.25 M solution of supporting electrolyte.

Variable-temperature electrochemistry was carried out using a non-isothermal cell arrangement.[22] Data were collected for the $[Ir(pz)(CO)(PPh_2OCH_2CH_2\text{-}4\text{-phenylpyridinium})]_2[PF_6]_2$ salt over the temperature range +30° to -30° C. A plot of $E^{o\prime}$ (py^+/py) - $E^{o\prime}$ (Ir_2^+/Ir) in 0.25 M $TBA^+PF_6^-$ / CH_2Cl_2 *vs.* temperature gave a straight line with slope equal to +0.16 mV/°C.

Butyronitrile (Aldrich) and dichloromethane (Fischer, HPLC grade) were distilled from P_2O_5 prior to use. Tetrabutylammonium hexafluorophosphate ($TBA^+PF_6^-$) (Southwestern Analytical) was used as received. Electrolyte solutions were prepared and stored over 80 - 200 mesh activated alumina (Fischer Scientific) and activated 4 Å molecular sieves.

Potentials are reported *vs.* aqueous AgCl/Ag and are not corrected for the junction potential.[23] Under conditions identical to those employed here, the ferrocenium/ferrocene (Fc^+/Fc) couple has an $E^{o\prime}$ of 0.397 V with $E_{pa} - E_{pc} = 64$ mV.[24]

Fast-scan microelectrode voltammetry (ν = 500 - 20,000 V/s) was carried out using a home-built potentiostat based on the design of Wightman.[25] I-V curves were captured on a Tetronix Model DSA602 digitizing oscilloscope, and transferred to a PC for analysis. Working electrodes were constructed from carbon or platinum fibers (8 μm^2 d^2 100 μm) encased in glass tips. Experiments were performed in a

one-compartment cell, employing a $AgNO_3$/Ag quasi-reference electrode separated from the working solution by a small piece of vicon tubing. Working solutions consisted of 0.25 M $TBA^+PF_6^-$ electrolyte and ~0.5 mM sample in butyronitrile. In each case, ferrocene was added as an internal standard. Potentials are reported *vs.* NHE using our measured value of E^o (Fc^+/Fc) = +0.129 V *vs.* SCE in 1.0 M aqueous KCl.

Steady State Emission and Resonance Raman

Emission spectra were acquired with a Hamamatsu R928 photomultiplier tube (PMT) attached to a Spex model 1403 double monochrometer, and powered by a Pacific Photometric model 204 power supply. The PMT output was fed to an EG&G Ortec model 9320 sampling/control unit and model 9315 photon counting unit. The monochrometer was controlled, and the data stored, with home-written software. Samples were excited with the 441.7 nm line of a Liconix HeCd laser (~20 mW at the sample). The laser light was passed through a pellin-boca prism and then focused onto a 100 μm slit to eliminate flourescence, after which it was collected with a lens and focused through the sample (1-cm path-length). Emission and Raman scattering was collected at 90° to the excitation light path. Absorption at the excitation wavelength was typically 0.1.

Spectra were obtained at least three times for each temperature. Their areas were determined by numerical integration (Matlab), and the average used to calculate ET rates.

Nanosecond Time-Resolved Emission

In the time-resolved emission experiments, samples were excited with the 460 nm (~20 ns FWHM, ~1 mJ at the sample) output of a Lambda Physic FL 3002 dye laser (Coumarin 480 dye in methanol) pumped by a Lambda Physic LPX 200 excimer laser (XeCl: 308 nm). Light was collected with a LeCroy 5-stage PMT attached to an ISA monochrometer. Signals were amplified with a custom built amplifier designed at Brookhaven National Laboratories and sent to a Sony/Tektronix RTD 710 digitizer. Data was then transfered to an IBM-compatible PC for storage and analysis with home-written software.

A dual sample holder was constructed so that both natural abundance and deuterated samples could be placed in the cryocooler at the same time, ensuring that both were at the same temperature during each experiment. Samples were contained in quartz NMR tubes, cut to fit the dimensions of the sample holder.

Picosecond Transient Absorption

This experiment was performed as described in Chapter II. All compounds were excited at 355 nm (~750 μJ per pulse at the sample) except Ir_2(4-phenylpyridinium)$_2$, which was excited at 532 nm.

Most data was collected with the cryocooler described above. Samples were contained in quartz 5-window fluorescence cells (Helma: 1-cm by 1-cm outer dimensions, ~ 0.9 mm by 2-mm inner dimensions) that allow an optical path-length of 2 mm. Samples were closely watched during data collection, and their x or y

positions (where z is along the light path) moved slightly between collection cycles to reduce the effects of sample decomposition.

After each experiment, absorption spectra of the samples were measured to ensure that decomposition did not occur during data collection. Only data collected with samples that showed no decomposition were used.

Measurements were repeated for each temperature and compound at least three times with fresh samples. Each data set was fit to a single exponential decay function with Matlab running on an IBM-compatible PC. The rates reported are the averages of these measurements.

Time-Correlated Single Photon Counting

Time-correlated single photon counting experiments were performed on samples prepared under an inert atmosphere in quartz NMR tubes. Tetraphenylethylene (Aldrich) was recrystallized from THF, washed with acetone and vacuum dried before use.

Samples were excited at 330 nm. Transient kinetics were determined by monitoring their 460 nm emission.

Excitation light was generated from the output of a Coherent 701-2 dye laser pumped with the doubled output of a Coherent Antares 76-s Nd:YAG laser. The dye laser operated with DCM (Kodak) laser dye dissolved in an ethylene glycol: benzyl alcohol solution. The repetition frequency of the laser's output was set to 0.76 MHz with a Coherent 7200 cavity dumper. The red pulses were doubled in a phase-

matched BBO crystal, and the intensity of the resulting 330 nm light was used to optimize the dye laser's cavity length.

Data was collected at right-angles to the path of the excitation light, and the sample was imaged 2:1. A Melles Griot film polarizer ensured fluorescence was collected at the magic angle to the excitation light's polarization. Emission was detected with a Hamamatsu microchannel plate PMT cooled to -40° C and biased at -3030 V with a Benton 205-05R power supply. A McPherson Model 270 monochrometer (1-mm slit-width) was used to select the observation wavelength. Signals from the PMT were amplified with an HP 8447F amplifier, and sent to a modified EG&G Ortec constant fraction discriminator. The discriminator's start signals were generated with a Thorlabs fast photodiode, and the data timing was delayed with a Tennelec TC864 time-amplitude converter and biased amplifier. The data were collected with an EG&G Ortec Spectrum Ace 4K mutichannel analyzer, and stored with the provided software on an IBM-compatible PC.

The system response was determined by scattering the pump light off of a suspension of nondairy creamer in water, and convoluted with a single or multiple exponential decay functions to fit complex, fast kinetics. Most data was simply fit to a single exponential function. Fitting was done with Matlab on an IBM RISC6000 workstation.

Molecular Mechanics

Calculations were performed in the labs of Professor William Goddard by Ben Ramirez with Biosym version 3.2.1 running on a Silicon Graphics 4D/480

workstation. Conformational analysis utilized the Dreiding II force field, with the initial sample temperature set to 600° K. The temperature was decreased in 25° increments during which 5 ps were allowed for equilibrium. Final conformations at 300° K were determined after the model was allowed to equilibrate for 200 ps.

Results

Electrochemistry

All of the iridium complexes exhibited reversible 1e- iridium-centered oxidations in dichloromethane, and irreversible 2e- oxidations in butyronitrile. As previously described, the irreversible 2e- response likely results from a ligand-induced (butyronitrile) disproportionation of the d^7-d^8 radical species.[26] In butyronitrile, the oxidations remained irreversible up to scan rates of ~5000 V/s (above which the heterogeneous ET rates were too slow to yield well resolved CV's).[27] Because ample work on similar systems has indicated that the *reversible* 1e- oxidations of d^8-d^8 complexes are medium independent,[28] the 1e- potentials recorded in dichloromethane were used to calculate thermodynamic driving forces for the photoinduced ET reactions.

With the exception of Ir_2(4-phenylpyridinium)$_2$, all of the complexes showed irreversible 2e- pyridinium-centered reductions up to scan rates as high as 20,000 V/s. Plots of E_{pc} *vs.* log(ν) gave slopes of 30 mV, consistent with a fast unimolecular homogeneous reaction following initial electron-transfer.[29] Given that pyridinyl radicals are known to dimerize at the 4-position,[30] we propose that the 2e- reductions (one for each pyridinium of the dimer) are followed by an intramolecular coupling of the pyridium units. In contrast, Ir_2(4-phenylpyridinium)$_2$ showed an electrochemical response consistent with subsequent bimolecular dimerization (*e.g.*, E_{pc} *vs.* log(ν) plots gave slopes of 19.6 mV).[31] At moderately fast scan rates (> ~10

V/s) and relatively low concentrations (~0.1 mM) the compound showed a reversible reduction, from which we calculate a dimerization rate constant of 7.4×10^6 M^{-1} s^{-1}.

To estimate the potentials of the pyridinium reductions for the other complexes, measurements were carried out on the analogous *n*-methylpyridinium salts. Each of these compounds exhibited characteristics indicative of a fast dimerization reaction following initial electron-transfer. Using fast scan rates and dilute solutions, it was possible to measure the reversible 1e- couples for *N*-methylpyridinium hexafluorophosphate and *N*-methyl-4-methylpyridinium hexafluorophosphate. Limits for the reversible couples of the other compounds were estimated from their irreversible peak potentials, according to reference 31 and assuming that the dimerization constants were greater than 1×10^7 $M^{-1}s^{-1}$ (a value that would yield reversible electrochemistry) but less than the diffusion controlled limit (1×10^{10} $M^{-1}s^{-1}$).

The electrochemical data are shown in Table III.1. It should be noted that these differ slightly from previous results. In particular, the reduction potential of 2,4,6-trimethylpyridinium has changed by ~0.08 eV, making the driving-force of the photoinduced reduction from the iridium core's triplet state close to zero. This may explain the multiphasic kinetics of the time-resolved phosphorescence data collected by Fox and coworkers.[18] Those measurements were not repeated here.

The reduction potentials of both the pyridinium and iridium couples are temperature dependent, decreasing slightly as the temperature is increased. The Ir_2(+/0) couple shows a dependence of -0.822 mV/°C, and the 4-phenylpyridinium acceptor shows one of -0.66 mV/°C. The total effect of +0.19 mV/degree is too small

Table III.1 Differences between the iridium core and pyridinium acceptors' reduction potentials determined in butyronitrile.

Acceptor	Reduction Potential (V *vs.* $Ir_2^{+/0}$)
4-phenyl pyridinium	-1.52
pyridinium	-1.66
4-methyl pyridinium	-1.82
2,4-dimethyl pyridinium	-1.92
2,4,6-trimethyl pyridinium	-2.03

to have an effect greater than the error of the combined electrochemical and kinetic data, and so is not considered further.

The reduction potentials of natural-abundance, partially and fully deuterated 4-phenyl pyridinium PF_6 salts are identical (-1.224 V *vs.* AgCl/Ag).

Resonance Raman

The iodide salt of 4-phenylpyridinium has a charge-transfer absorption band centered at 358 nm in acetonitrile. Excitation of the salt on the red edge (441.7 nm) of this transition yields enhanced Raman scattering that provides information about the structure of the pyridinyl radical. When nuclear distortions along a particular coordinate occur in its excited-state, the Raman scattering from these vibrations will be enhanced when the excitation wavelength is in resonance with the ground-to-excited-state transition. The intensity of a feature in the nonresonant spectrum will increase in the resonant spectrum by an amount related to the difference between the excited- and ground-state nuclear distortions along that vibrational coordinate.[32] It is thus possible to determine from these spectra how the pyridinium nuclear coordinates change upon its reduction, and quantitative analysis of the data can reveal the amount of nuclear reorganization λ_{in} that occurs within the electron acceptor during reduction.

The resonance Raman (RR) spectrum of natural-abundance 4-phenylpyridinium shows six distinctive features between 1000 cm^{-1} and 1800 cm^{-1} (Figure III.6). No scattering at higher energies was observed. Those between 1350 cm^{-1} and 1700 cm^{-1} can be assigned to ring skeletal modes, while those at lower

Figure III.6 Resonance Raman spectrum of 4-phenylpyridinium iodide in CD_3CN excited into its I- $\rightarrow$ pyridinium charge-transfer band at 441.7 nm. The full scan between 200 cm^{-1} and 3500 cm^{-1} is shown in (**A**), and the region in which enhanced scattering is observed is shown in (**B**). Stars indicate solvent peaks.

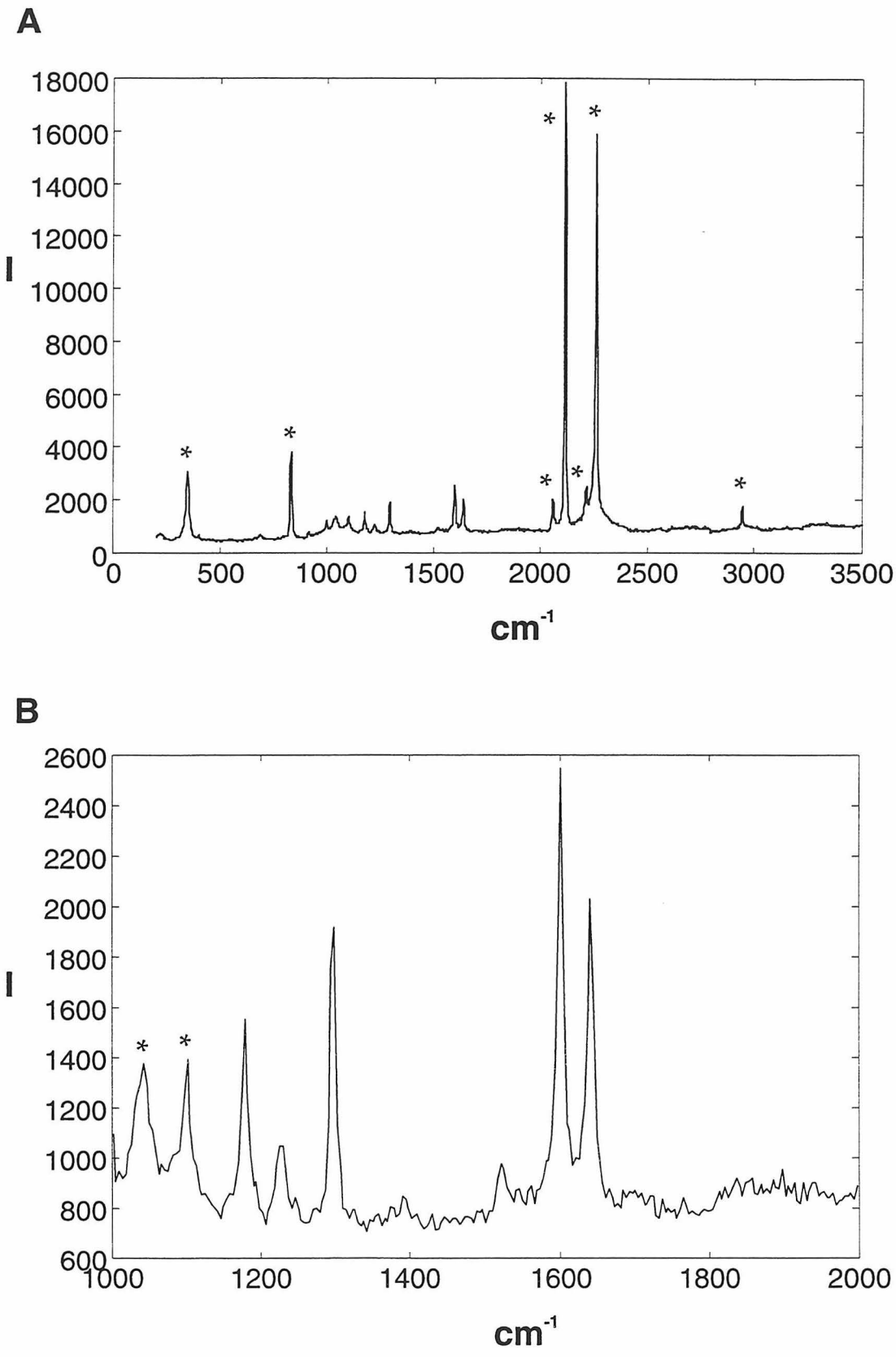
A
18000
16000
14000
12000
10000
8000
6000
4000
2000
0
I
0
500
1000
1500
2000
2500
3000
3500
cm-1
B
2600
2400
2200
2000
1800
1600
1400
1200
1000
800
600
I
1000
1200
1400
1600
1800
2000
cm-1

energies are probably due to a mixture of the aliphatic C-N stretch and in-plane C-H bends.[33] To help in the assignment of these vibrations, two isomers of the complex have been made: The RR spectrum of the partially deuterated 2,6-dideutero-4-phenyl-pyridinium iodide salt shows a disappearance -- or large shift -- of the bands at 1228 cm^{-1} and 1641 cm^{-1} (Figure III.7). This suggests the higher energy one is due to a C-N skeletal stretch. The band at 1601 cm^{-1} may be the C-C ring breathing mode. These assignments are supported by the RR spectrum of the 2,3,5,6-tetradeutero-4-phenyl-pyridinium iodide salt (Figure III.8).

Steady State Emission

Although the rates of electron-transfer from the iridium core's singlet state to the pyridinium acceptors are too fast to measure by picosecond transient absorption, they can be determined from quantum yield measurements.

The singlet excited-states of the $Ir_2(A)_2$ complexes in solution are deactivated in part by emission. The fluorescence quantum yield Φ_f of the model complex Ir_2(triethyl ammonium)$_2$, in which ET does not occur, is 0.0015 in acetonitrile at room temperature.[18] The quantum yield is defined as the ratio of fluorescence to absorbed light. In other model complexes, Φ_f becomes larger as the bridge is shortened: Φ_f = 0.0023 for $PPh_2OCH_2CH_3$ and Φ_f = 0.0027 for PPh_2OCH_3, suggesting that much of the molecules' nonradiative decay is due to the flexibility of the phosphonite ligand.

When the iridium core is connected to an electron acceptor, Φ_f decreases by an amount related to the driving force for ^{1}ET. If the only process causing the

Figure III.7 Resonance Raman spectrum of 2,6-dideutero-4-phenyl-pyridinium in CD_3CN excited at 441.7 nm (**A**) compared to that of the natural-abundance compound (**B**).

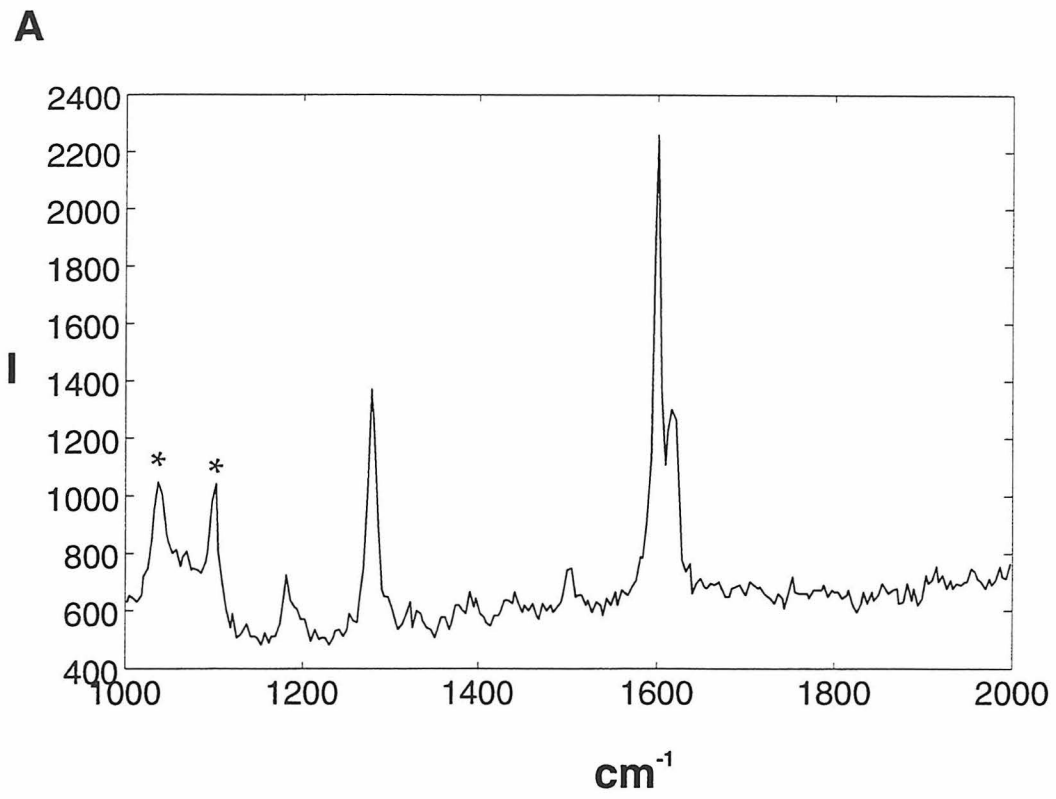
A
I
2400
2200
2000
1800
1600
1400
1200
1000
800
600
400
1000
1200
1400
1600
1800
2000
cm-1
*
*

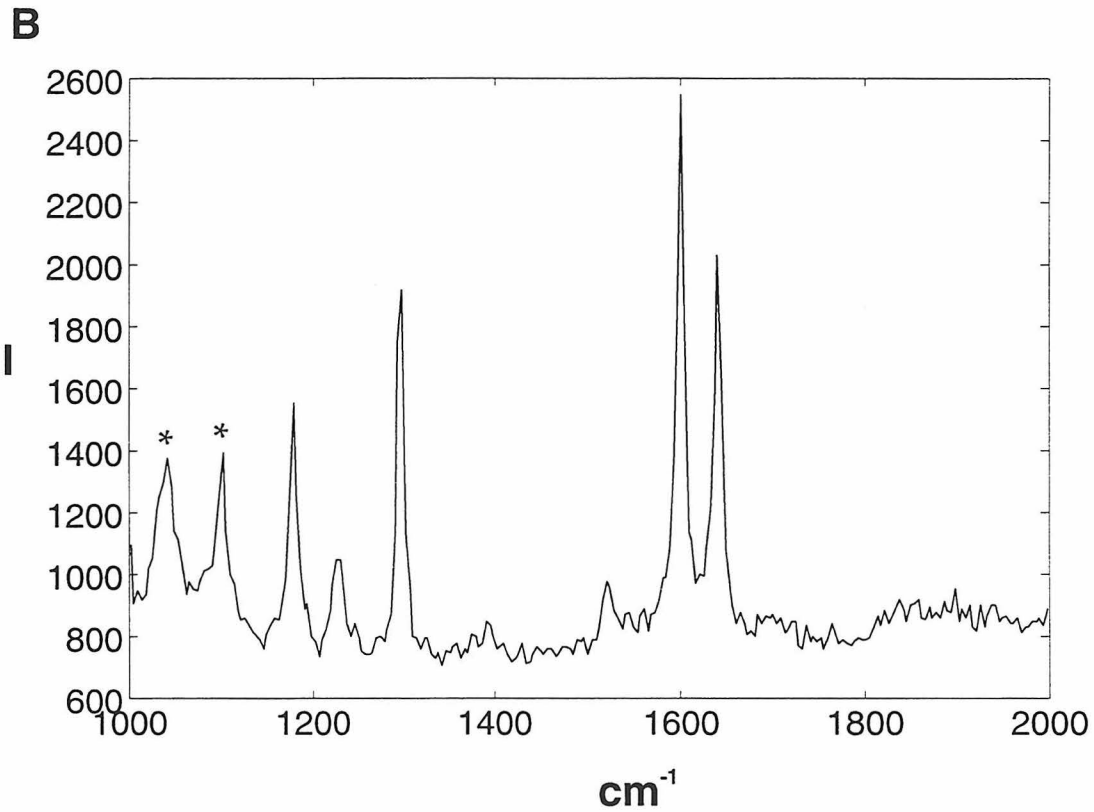
B
I
2600
2400
2200
2000
1800
1600
1400
1200
1000
800
600
1000
1200
1400
1600
1800
2000
cm-1
*
*

Figure III.8 Resonance Raman spectrum of 2,3,5,6-tetradeutero-4-phenyl-pyridinium in CD_3CN excited at 441.7 nm (**A**) compared to that of the natural-abundance compound (**B**).

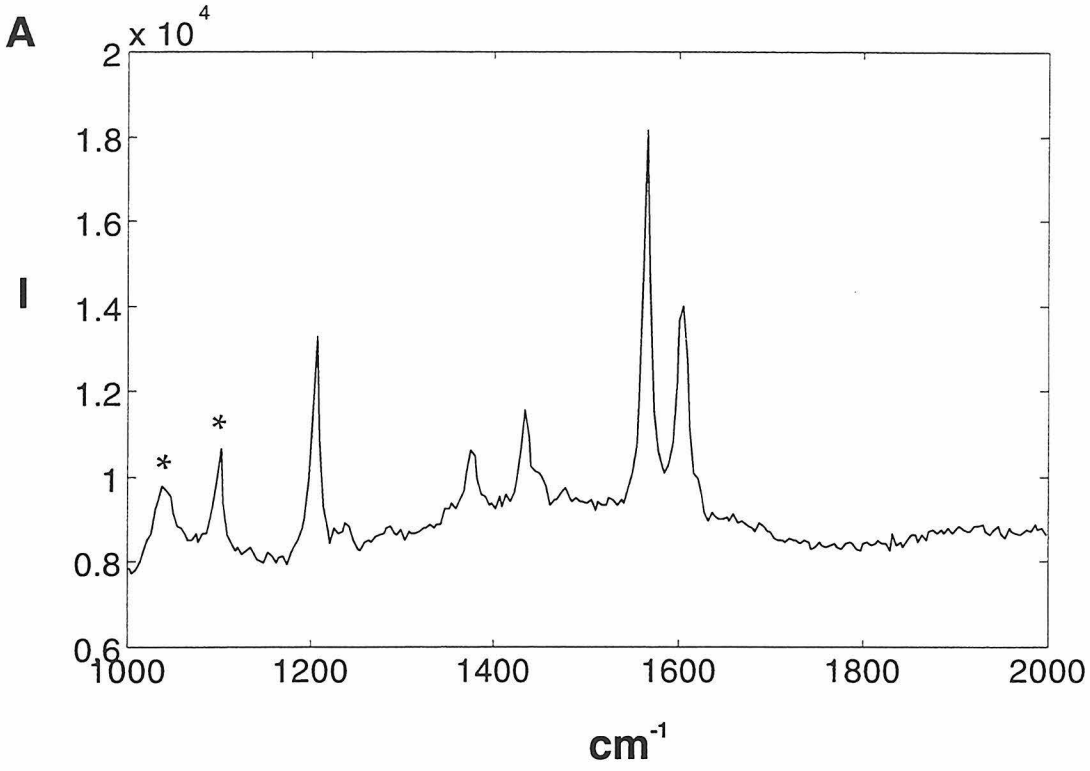
A
x 10^4
2
1.8
1.6
I
1.4
1.2
1
0.8
0.6
*
*
1000
1200
1400
1600
1800
2000
cm-1

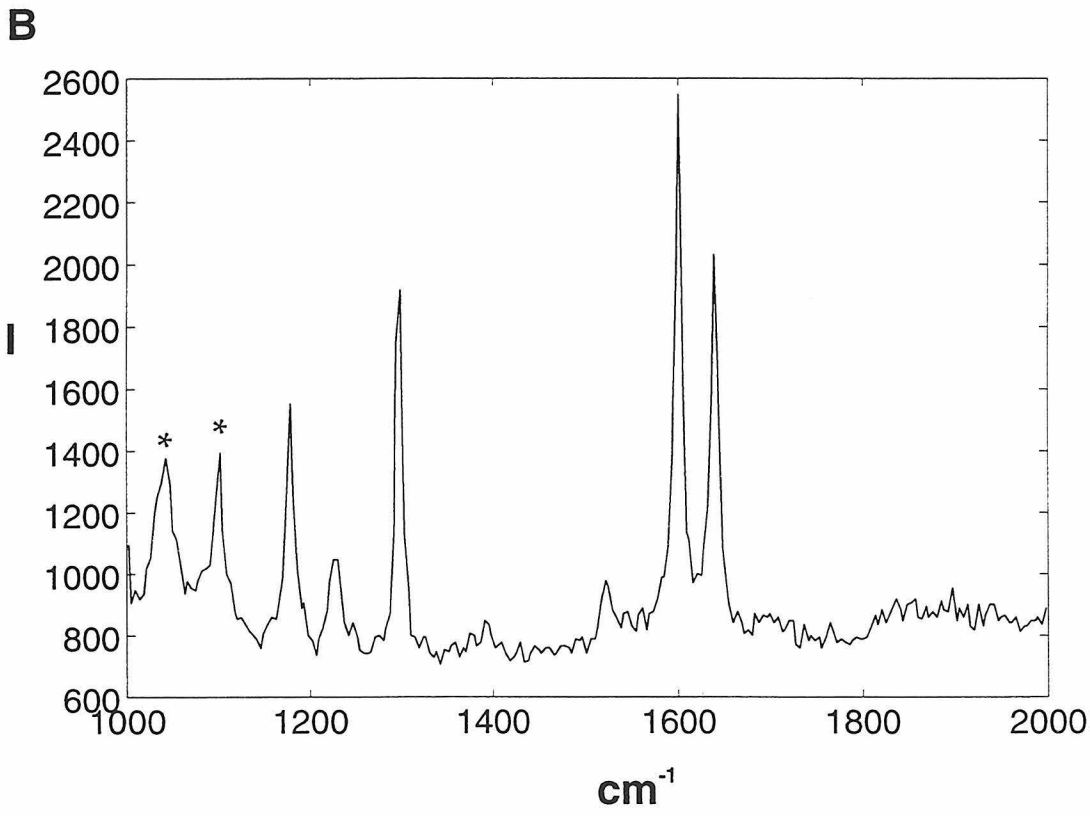
B
2600
2400
2200
2000
I
1800
1600
1400
1200
1000
800
600
*
*
1000
1200
1400
1600
1800
2000
cm-1

decrease in the quantum yield of 0.0015 is electron-transfer, then k_{ET} can be determined from the excited-state lifetime τ by:

Equation III.1 $$\tau = \frac{1}{\left(k_r + k_{nr} + k_{ET}\right)}$$

in which k_r is the radiative decay rate and k_{nr} is the nonradiative rate.

Temperature Dependence

The electron-transfer rates are strongly dependent on temperature, spanning two orders of magnitude between 200° K and 330° K (Table III.2). A strong driving-force dependence is also apparent. Emission from Ir_2(4-phenylpyridinium)$_2$ ($-\Delta G°$ = 0.98 eV) cannot be detected at any temperature above the freezing point of butyronitrile, indicating that the reaction may be an activationless one.

The activation energy E_A of each ^{1}ET reaction can be determined from an Arrhenius plot, in which it should equal the slope of the line formed by plotting $\ln(k_{ET} \times \sqrt{T})$ *vs.* 1/T. The data for each reaction, when presented in this way, does indeed appear to be linear (Figure III.9). The values determined for E_A are discussed below.

Isotope Dependence

Pyridinium deuteration affects the singlet rates of Ir_2(pyridinium)$_2$ and Ir_2(4-methylpyridinium)$_2$ differently. Electrochemical data indicates this is not a thermodynamic effect. For ^{1}ET from the iridium core to 4-methylpyridinium at 200°

Table III.2 [1]ET rates as a function of temperature and driving force.

Temperature (°K)	-ΔG° (eV)			
	0.47	0.58	0.68	0.84
200	8.85×10^{9}	2.46×10^{10}	8.18×10^{10}	1.22×10^{11}
210	1.74×10^{10}	4.82×10^{10}	1.18×10^{11}	1.78×10^{11}
220	1.68×10^{10}	6.22×10^{10}	1.58×10^{11}	2.13×10^{11}
230	2.89×10^{10}	1.09×10^{11}	2.32×10^{11}	2.82×10^{11}
240	2.93×10^{10}	1.15×10^{11}	3.12×10^{11}	3.46×10^{11}
250	5.11×10^{10}	1.72×10^{11}	4.83×10^{11}	4.55×10^{11}
260	4.79×10^{10}	1.83×10^{11}	4.21×10^{11}	4.84×10^{11}
270	5.74×10^{10}	2.68×10^{11}	6.80×10^{11}	6.63×10^{11}
280	7.77×10^{10}	2.72×10^{11}	6.46×10^{11}	7.44×10^{11}
290	8.78×10^{10}	3.89×10^{11}	8.81×10^{11}	8.02×10^{11}
300	1.28×10^{11}	4.35×10^{11}	8.20×10^{11}	9.24×10^{11}
310	1.53×10^{11}	4.91×10^{11}	1.12×10^{12}	--
320	1.94×10^{11}	5.73×10^{11}	1.20×10^{12}	--
330	2.21×10^{11}	6.88×10^{11}	--	--

Figure III.9 The reductions of the pyridinium acceptors by the iridium core's singlet excited-state have activation energies that can be determined from Arrhenius plots: 'o' = 2,4,6-trimethylpyridinium, '*' = 3,4-dimethylpyridinium, '+' = 4-methylpyridinium and 'x' = pyridinium.

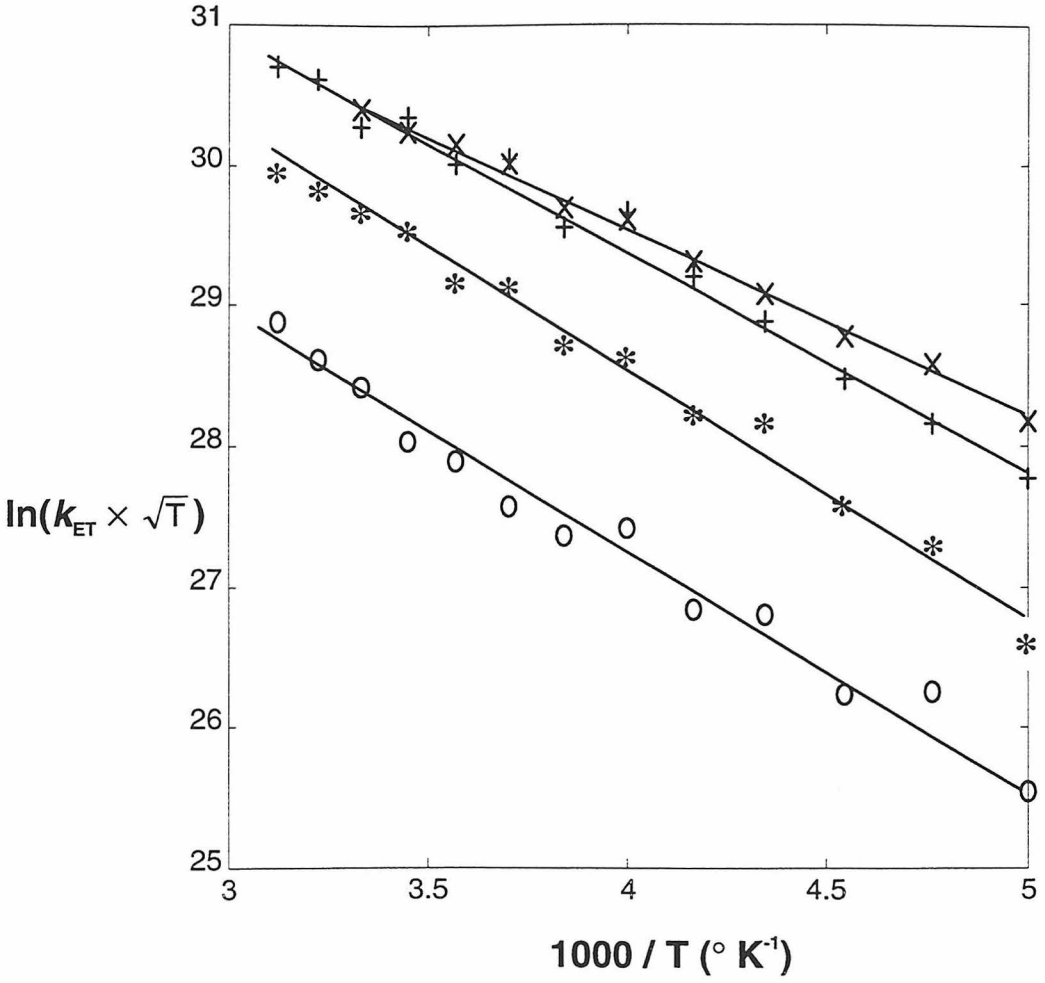
31
30
29
28
27
26
25
3
3.5
4
4.5
5
ln($k_{ET} \times \sqrt{T}$)
1000 / T (° K^{-1})

K ($-\Delta G°$ = 0.68 eV), k_H/k_D = 1.17. For the higher driving force ($-\Delta G°$ = 0.89) photoinduced reduction of pyridinium, k_H/k_D = 1.27 at 200° K.

Nanosecond Time-Resolved Emission

The iridium core's triplet state is 0.5 eV lower in energy than its singlet, and is thus a weaker reductant.[18] The relative decrease in driving-forces is enough to reduce the reaction rates to the point where their effect on the complexes' phosphorescence lifetimes can be determined by nanosecond time-resolved emission. The triplet emission lifetime[18] (1.1 μs) of the model complex Ir_2(triethyl ammonium)$_2$ is significantly reduced in the electron-transfer complexes. As above, the assumption can be made that differences between the phosphorescence lifetimes of the substituted pyridinium complexes and the model complex are due solely to ET, and thus the rates of ^{3}ET rate can be determined from the quenching data.

Temperature Dependence

These reactions lie deep within the Marcus normal region, and their rates are thus strongly temperature dependent (Table III.3). Their activation energies have been determined in the manner described above (Figure III.10), and are considered in the discussion below.

Isotope Dependence

Synthetic difficulties prevented study of the deuterated 2,4,6-trimethylpyridinium and 3,4-dimethylpyridinium complexes. However, the effect deuteration has on the rate of ^{3}ET within Ir_2(4-methylpyridinium)$_2$ confirms that

Table III.3 ^{3}ET rates as a function of temperature and driving force.

Temperature (°K)	-ΔG° (eV)	
	0.08	0.18
200	7.43×10^5	5.35×10^6
210	1.46×10^6	1.03×10^7
220	2.86×10^6	1.82×10^7
230	5.43×10^6	--
240	9.57×10^6	--
250	1.64×10^7	--
260	--	--
270	--	--
280	--	--
290	--	--
300	--	--
310	--	--

Figure III.10 The reductions of the pyridinium acceptors by the iridium core's triplet excited-state have activation energies that can be determined from Arrhenius plots: 'o' = 3,4-dimethylpyridinium, '*' = 4-methylpyridinium.

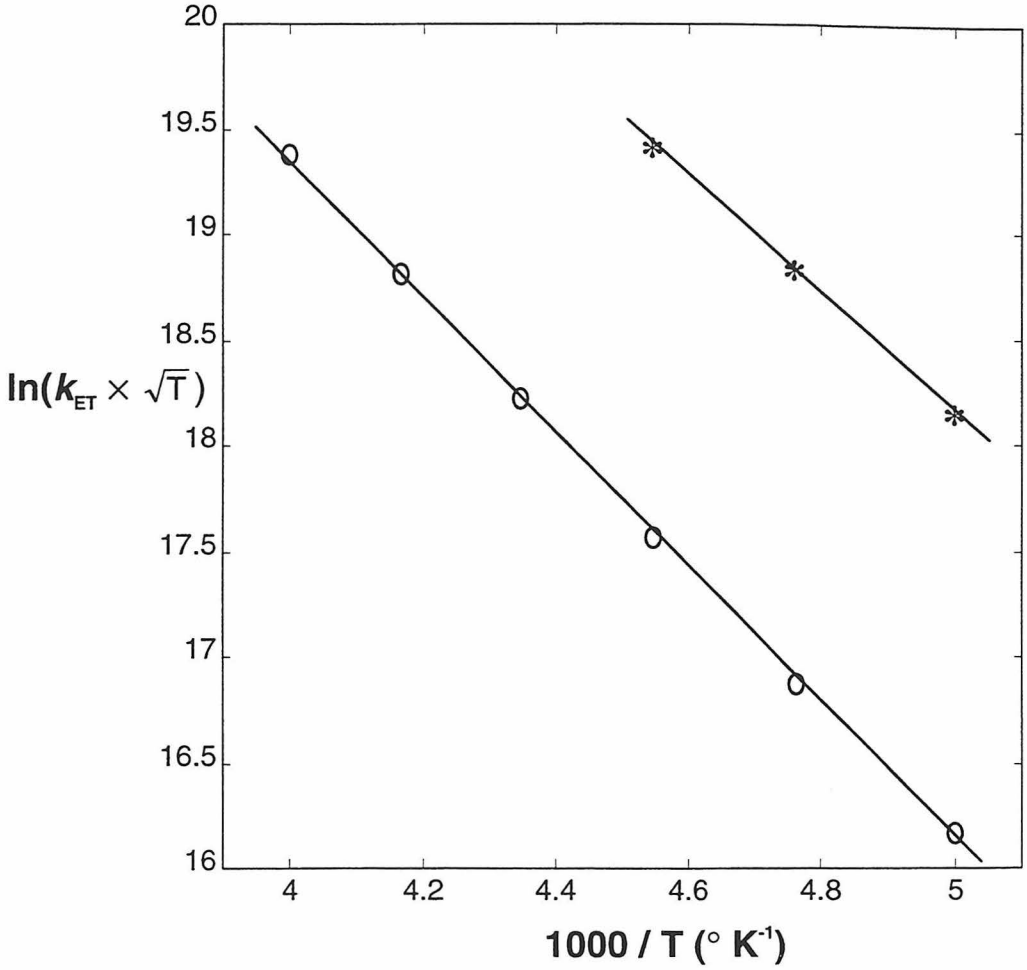
20
19.5
19
18.5
18
17.5
17
16.5
16
ln($k_{ET} \times \sqrt{T}$)
4
4.2
4.4
4.6
4.8
5
1000 / T (° K^{-1})

these reactions are sensitive to pyridinium nuclear vibrations. In fact, the isotope effect in this compound is large enough to be apparent in its emission decay kinetics (Figure III.11). Because of the strong temperature dependencies of the triplet reactions, great care was taken to ensure that the temperatures of the different isotopes were identical: When two samples were held in the cryocooler at the same time, the observed isotope effect is substantial: $k_H/k_D = 1.43$ at 200° K.

Picosecond Transient Absorption

The rates of charge-recombination k_{BET} following reduction of the pyridinium acceptors have been determined by picosecond transient absorption (PTA). Rates were measured for all the complexes except Ir_2(4-methylpyridinium)$_2$.[34]

Photochemistry

Before these studies were begun, there was concern that the sample degradation observed during the initial PTA work would make temperature dependent studies impossible. Those room temperature measurements employed flowcells, ensuring that fresh sample was excited every time the laser was fired, and yet the formation of black deposits on the incident faces of the sample cells was still observed. Samples cannot be flowed or stirred while in the cryocooler. Before attempting the temperature dependence studies, the earlier work was repeated. Sample decomposition was again observed, and its rate was found to be dependent on laser power, but not on the nature of the pyridinium.

Once a black deposit forms, sample degradation proceeds rapidly. It is unclear if the degraded product catalyses further degradation *via* a different

Figure III.11 Replacement of the pyridinium aromatic hydrogen atoms with deuteriums has a pronounced effect on the phosphorescence decay rate of Ir_2(4-methylpyridinium)$_2$: Excitation λ = 460 nm, observation λ = 710 nm.

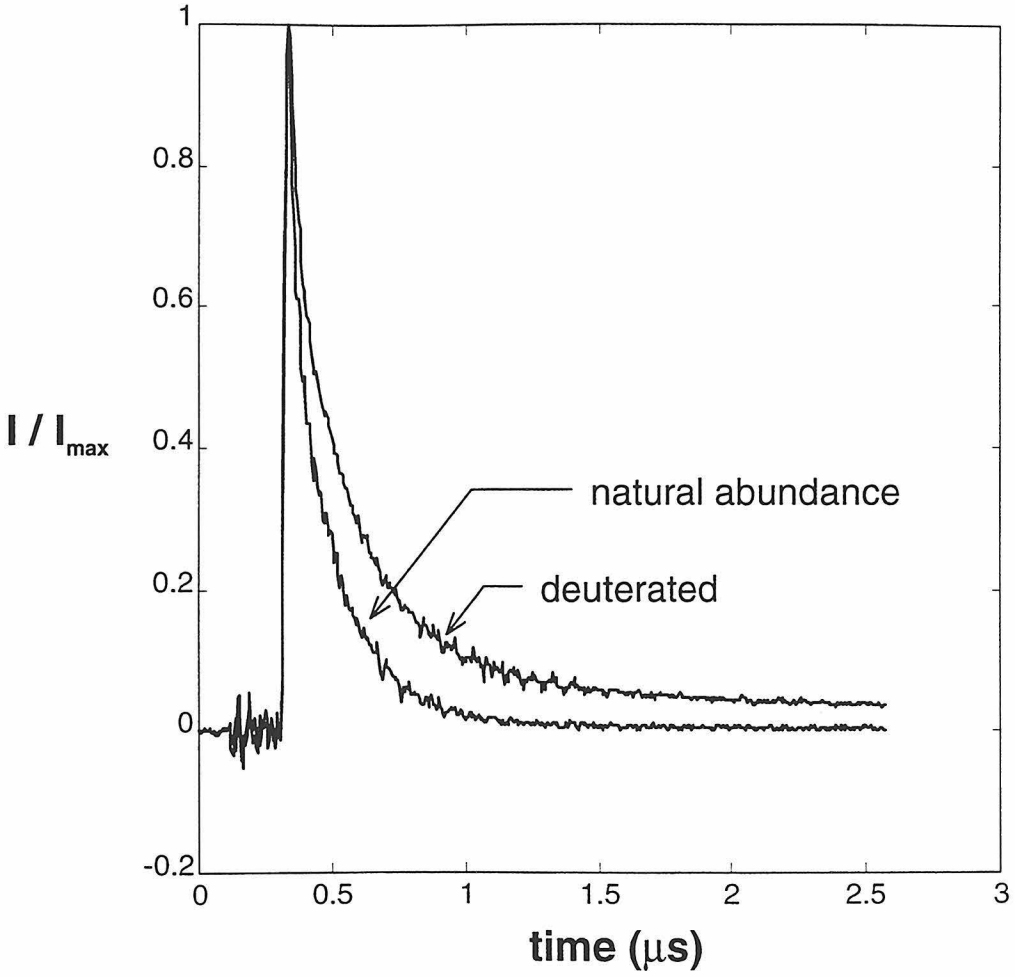
1
0.8
0.6
0.4
0.2
0
-0.2
I / I max
natural abundance
deuterated
0
0.5
1
1.5
2
2.5
3
time (μs)

pathway, or if its absorbance of light creates the heat necessary to cause decomposition. Whatever the case, two pieces of evidence support the hypothesis that the initial photoinduced decomposition is caused by two-photon absorption leading to ligand dissociation. First, its rate qualitatively appears dependent on pulse energies in a manner that is consistent with the $(\text{power})^2$ dependence of two-photon processes. Second, we have noted that the iridium complexes undergo more rapid photoinduced decomposition in acetonitrile than in butyronitrile. This observation indicates that ligand loss, followed -- or assisted -- by coordination of solvent molecules, is a principle step in the decomposition process.

Although the compounds do decompose more quickly during an experiment if they are not stirred or flowed, the experiments could still be performed with the cryocooler without much difficulty. One reason is the use of butyronitrile instead of acetonitrile. Of greater interest, however, is the observation that the decomposition is highly temperature dependent, and is rarely observed at temperatures lower than 260° K.

Temperature Dependence

The transient spectra of the $Ir_2(A)_2$ compounds contain a bleach of the $d\sigma^* \rightarrow p\sigma$ transition centered near 460 nm and an OD increase at higher energies (Figure III.12). The excited-state decay kinetics can be obtained by following either feature as a function of time; both decay with the same rate. Unlike those of most high-driving force ET reactions found in the literature,[21] the rates of these are strongly temperature dependent (Table III.4). For example, k_{BET} within Ir_2(4-

Figure III.12 Transient spectrum of Ir_2(4-phenylpyridinium)$_2$ in butyronitrile at 210° K immediately following excitation at 532 nm.

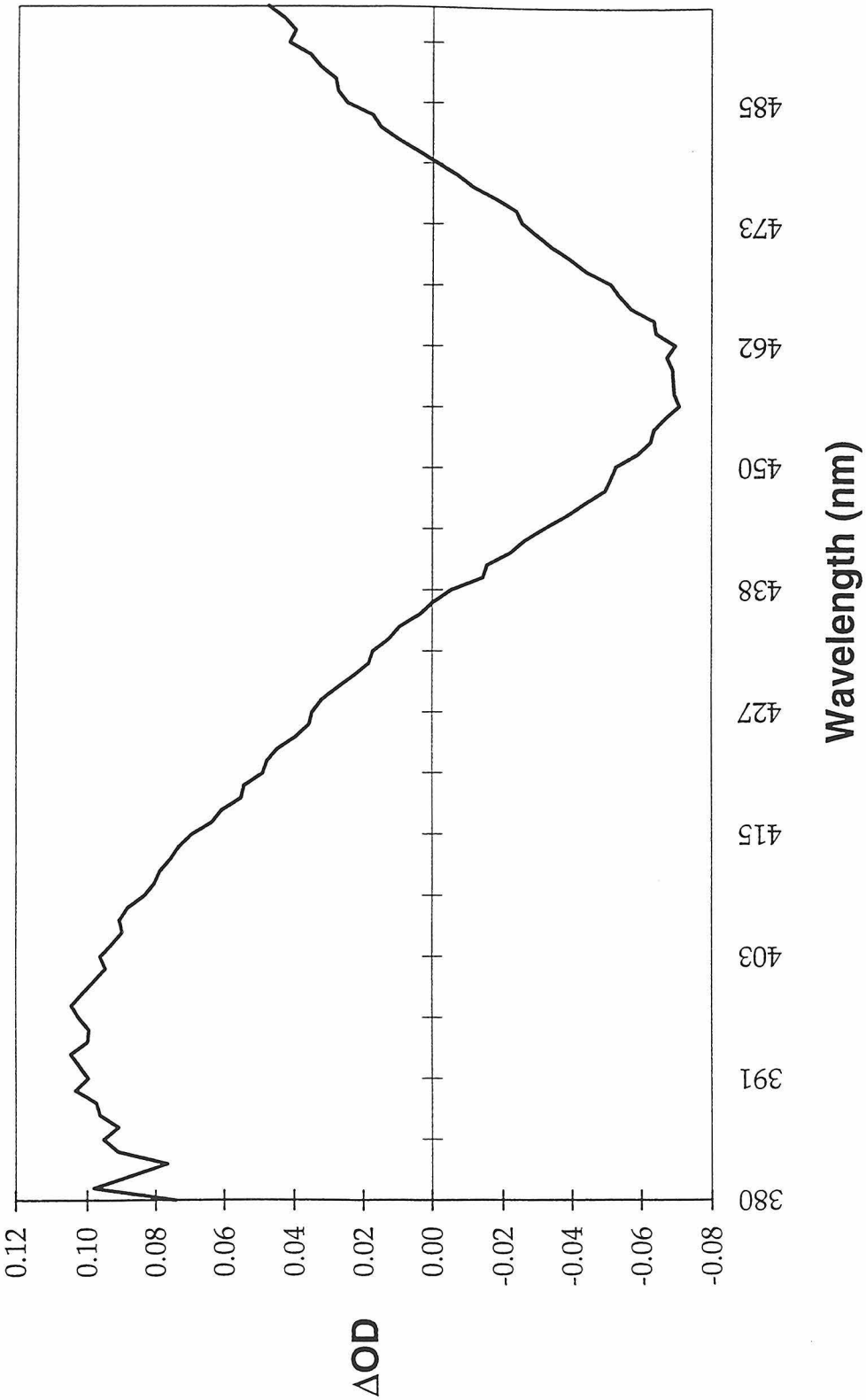
ΔOD
0.12
0.10
0.08
0.06
0.04
0.02
0.00
-0.02
-0.04
-0.06
-0.08
380
391
403
415
427
438
450
462
473
485
Wavelength (nm)

Table III.4 Thermal charge-recombination rates as a function of temperature and driving-force.

Temperature (°K)	-ΔG° (eV)			
	1.52	1.66	1.92	2.03
200	5.04×10^{9}	6.25×10^{8}	--	--
210	5.78×10^{9}	8.60×10^{8}	--	--
220	7.81×10^{9}	1.23×10^{9}	--	--
230	1.00×10^{10}	1.69×10^{9}	--	--
240	1.10×10^{10}	2.33×10^{9}	--	--
250	1.08×10^{10}	3.54×10^{9}	--	--
260	1.19×10^{10}	4.90×10^{9}	2.63×10^{8}	--
270	1.59×10^{10}	6.05×10^{9}	3.75×10^{8}	--
280	1.88×10^{10}	6.51×10^{9}	3.81×10^{8}	8.33×10^{7}

phenylpyridinium)$_2$ at 200° K in butyronitrile is 5.04×10^9 s^{-1}; at 280° K, k_{BET} = 1.88×10^9 s^{-1}. The effect temperature has upon the Ir$_2$(pyridinium)$_2$ rates is clear from an examination of some of the data (Figure III.13). The values of k_{BET} extracted from the data can be used to determine the activation energies of these reactions in the same way E_A for the forward reactions was determined (Figure III.14).

The unusually large dependence of the rates on temperature can be compared to the their strong dependence on driving-force (Figure III.15).

It is important to note that the kinetic data shown in both these figures are representative of all that was collected: The data sets fit well to a single exponential function that typically decays to an offset baseline. The baseline, which appears flat on these timescales, can be attributed to complexes' triplet states, which have very similar transient spectra.

Isotope Dependence

The recombination reactions within Ir$_2$(pyridinium)$_2$ slow upon deuteration of pyridinium rings. The rates for the natural-abundance isomer are consistently 1.2 times faster than those in the deuterated isomer over the entire temperature range 200° - 280° K. This indicates that despite the strongly inverted behavior exhibited by these reactions, nuclear vibrations do affect their behavior.

Time-Correllated Single-Photon Counting

It was noted above that the recombination kinetics fit well to single exponential decay functions. Because ET within these systems can occur through flexible bridges, it important to consider how the molecules' flexibility changes as

Figure III.13 The rate of thermal charge-recombination in $Ir_2(pyridinium)_2$ is highly dependent on temperature: (**A**) T = 210° K, k_{ET} = 8.6×10^8 s^{-1}, (**B**) T = 240° K, k_{ET} = 2.3×10^9 s^{-1} and (**C**) T = 270° K, $k_{ET} = 6.1 \times 10^9$ s^{-1}.

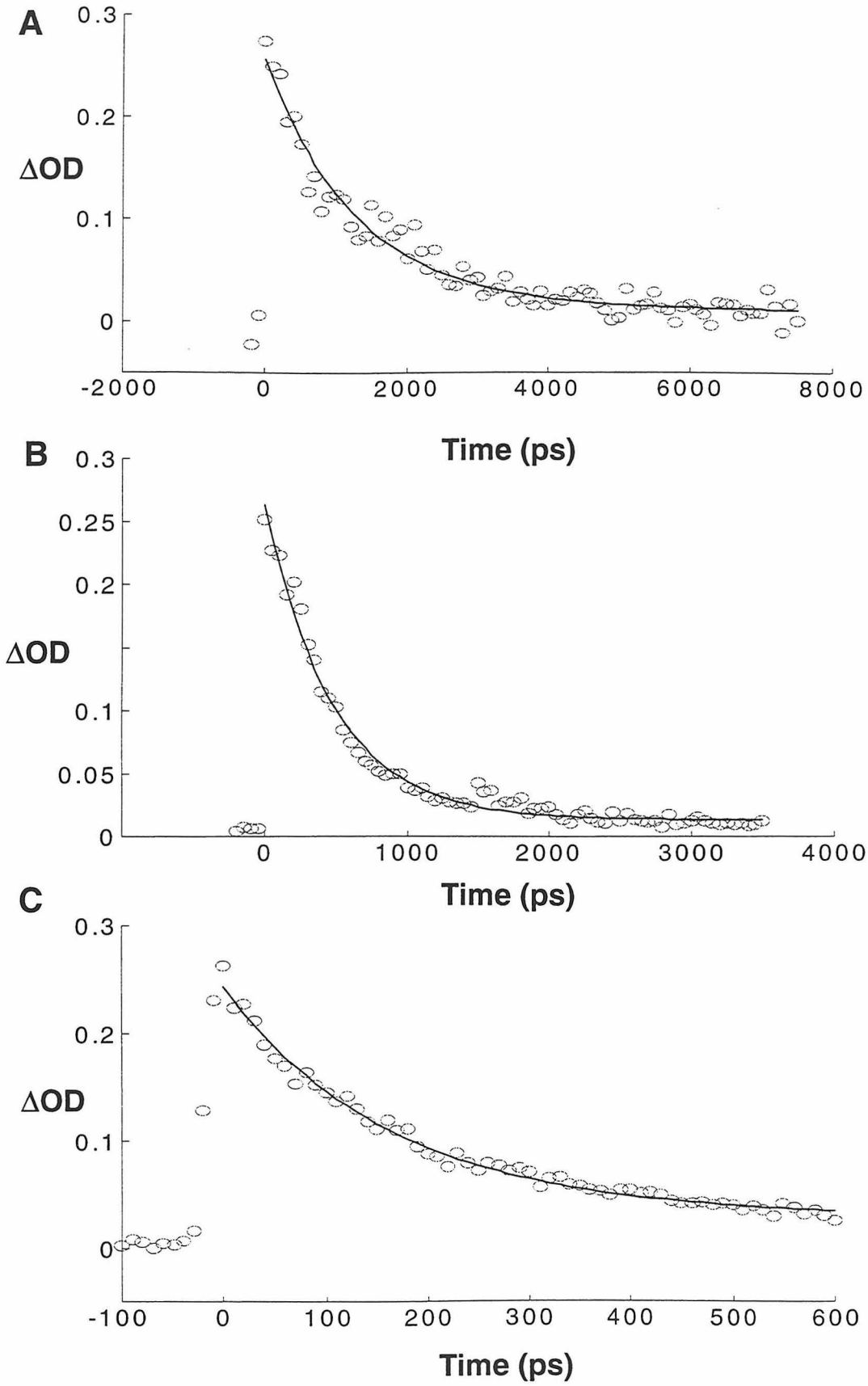
A
0.3
0.2
ΔOD
0.1
0
-2000
0
2000
4000
6000
8000
Time (ps)
B
0.3
0.25
0.2
ΔOD
0.1
0.05
0
0
1000
2000
3000
4000
Time (ps)
C
0.3
0.2
ΔOD
0.1
0
-100
0
100
200
300
400
500
600
Time (ps)

Figure III.14 The charge-recombination reactions have activation energies that can be determined from Arrhenius plots: 'o' = 4-phenylpyridinium, '*' = pyridinium and '+' = 3,4-dimethylpyridinium.

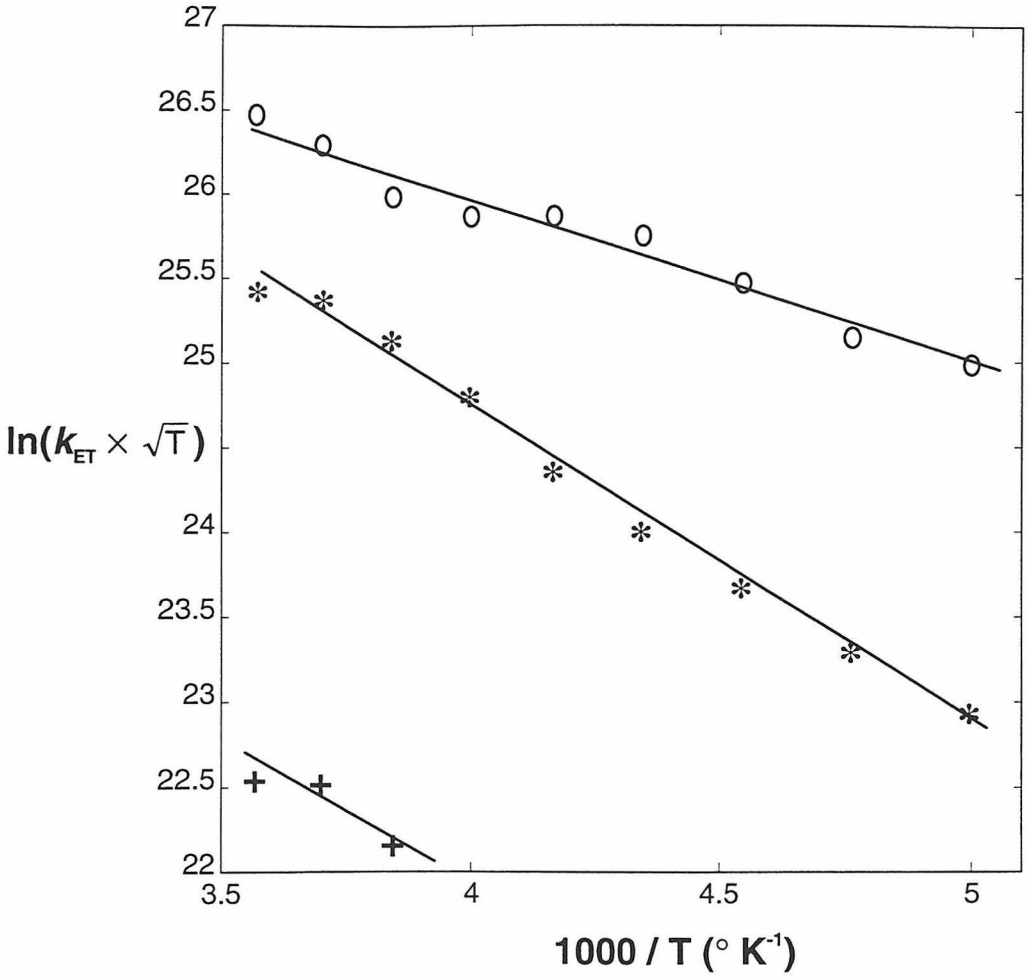
27
26.5
26
25.5
25
24
23.5
23
22.5
22
3.5
4
4.5
5
ln($k_{ET} \times \sqrt{T}$)
1000 / T (° K^{-1})

Figure III.15 The rates of thermal charge-recombination in the $Ir_2(A^+)_2$ compounds are highly dependent on $\Delta G°$: (**A**) A^+ = 3,4-dimethylpyridinium ($-\Delta G° = 1.92$ eV), $k_{ET} = 4.4 \times 10^8$ s^{-1}, (**B**) A^+ = pyridinium ($-\Delta G° = 1.66$ eV), $k_{ET} = 4.9 \times 10^9$ s^{-1} and (**C**) A^+ = 4-phenylpyridinium ($-\Delta G° = 1.52$ eV), $k_{ET} = 1.3 \times 10^{10}$ s^{-1}.

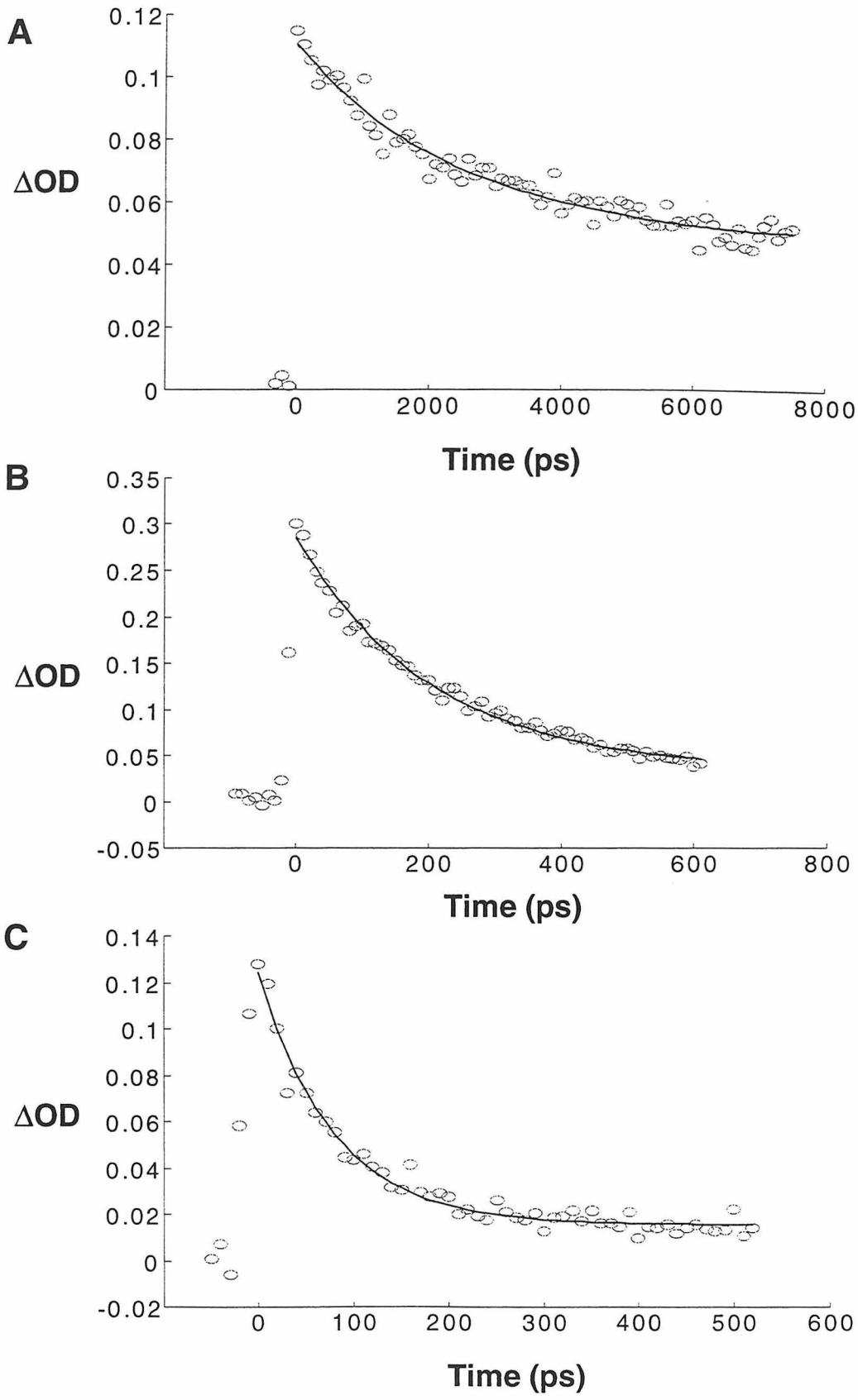
A
ΔOD
0.12
0.1
0.08
0.06
0.04
0.02
0
0
2000
4000
6000
8000
Time (ps)
B
ΔOD
0.35
0.3
0.25
0.2
0.15
0.1
0.05
0
-0.05
0
200
400
600
800
Time (ps)
C
ΔOD
0.14
0.12
0.1
0.08
0.06
0.04
0.02
0
-0.02
0
100
200
300
400
500
600
Time (ps)

the temperature is lowered, and how such changes might affect the rate of both charge-separation and recombination. There are many examples of electron-transfer reactions though flexible amino acid bridges, and kinetics of most are multiphasic.[35] Modeling suggests this is due to ET through different bridge conformers. Although the iridium system's kinetics are all best fit to single exponential decay functions, conformation changes that occur within a few picoseconds prior to ET are still possible. We have conducted experiments to elucidate whether such changes are possible in butyronitrile at 200° K, where monophasic kinetics are still observed.[36]

Conformational changes that may occur would probably involve rotation about the single bonds within the phosphonite spacer. To mimic this, we have chosen to examine the excited-state decay of tetraphenylethylene (TPE). Its phenyl groups might be considered analogous to those on the spacer, and its dominant nonradiative excited-state deactivation pathway involves rotation about the ethylene bond.

TPE was chosen for the large body of information on its excited-state behavior, some of which specifically address the effects of solvent viscosity.[37,38] Like stilbene,[39] optical excitation of the molecule's $\pi \rightarrow \pi^*$ transition forms a singlet excited-state, which can decay either by emission or adoption of a twisted form from which it thermally relaxes (Figure III.16). The rates at which these processes occur depend highly on the polarity and viscosity of the solvent.[40]

When considered in detail, the decay of TPE's excited-state is actually somewhat complex. Its emission is largely multiphasic and dependent on

Figure III.16 Following optical excitation, tetraphenylethylene can return to its ground-state through a number of pathways. Emissive relaxation can occur from its vertically excited state (^{1}V) and from a relaxed one (^{1}R). Nonradiative decay can occur from both states, as well as from a highly twisted one (^{1}p*). In low dielectric solvents, the molecule can return to the ^{1}R state from the ^{1}p* state. (Adapted from reference 38.)

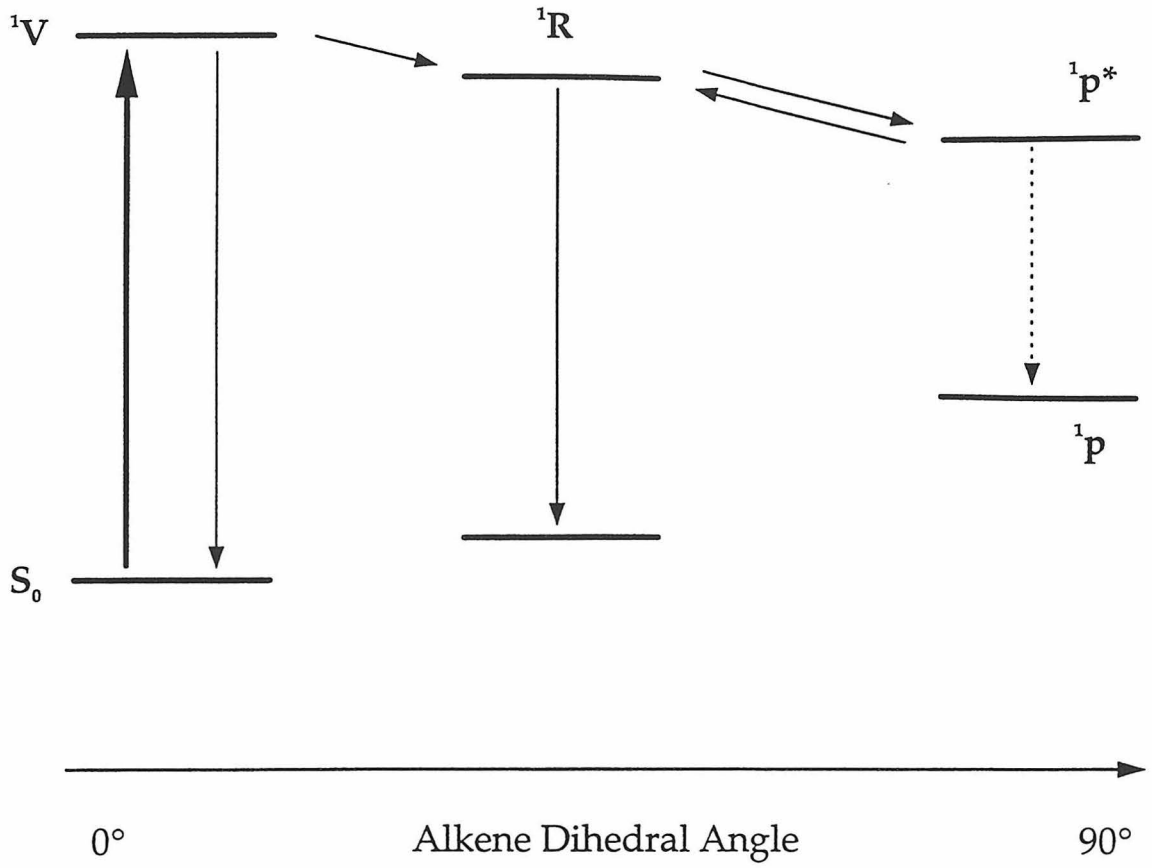
^1V
^1R
$^1p^*$
^1p
S_0
0°
Alkene Dihedral Angle
90°

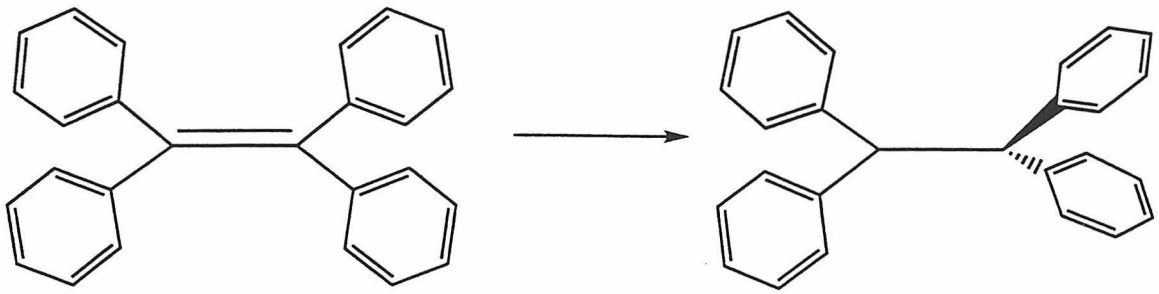

the observation wavelength. This behavior is attributed to luminescence from a conformationally relaxed state somewhat lower in energy than the ^{1}V vertical state.[38] Recent work has provided a map of the singlet photoisomerization potential energy surface of TPE in alkane solvents, placing this relaxed state (^{1}R in Figure III.16) 8 kcal/mol lower in energy than the vertical excited-state, or 69 kcal/mol above the molecule's S_0 state.[38] This state can luminesce, but can also further twist to form a species (^{1}p* in Figure III.16) in which the orientation of the phenyl groups on one half of the molecule are orthogonal to those on the other half. The energy of this twisted state is highly dependent on solvent polarity, but is 2 kcal/mol lower than the ^{1}R state in alkanes. This energy difference is probably significantly higher in buytronitrile, as the twisted state is zwitterionic.[38]

At room temperature, very weak emission from both the ^{1}V and ^{1}R states can be observed at 460 nm. Their quantum yield ratio ϕ_V/ϕ_R is approximately 4×10^5. The rate of emission cannot be resolved with our SPC experiment (system response FWHM $\approx$ 70 ps). This is in agreement with predictions that the $^1V \rightarrow {}^1R$ transition occurs at a rate of 2.4×10^{11} s^{-1}, while the $^1R \rightarrow {}^1p^*$ transition occurs at a rate of 3.3×10^{11} s^{-1} in MCH at 295° K.[37,38] When the sample temperature is lowered to 220° K, the emission profile is unchanged (Figure III.17): It is dominated by a response-limited component assignable to emission from the vertical state, and a very weak, longer-lived tail corresponding to emission from the ^{1}R state, in agreement with published findings. As the temperature is lowered to 200° K, the rate of the ^{1}V emission finally becomes slow enough to resolve with our experiment. Only when the solvent has frozen does the $^1R \rightarrow {}^1p^*$ quantum yield approach zero.

Figure III.17 Time-correllated single-photon counting data collected from the excitation of tetraphenylethylene in butyronitrile at 330 nm (λ_{obs} = 460 nm).

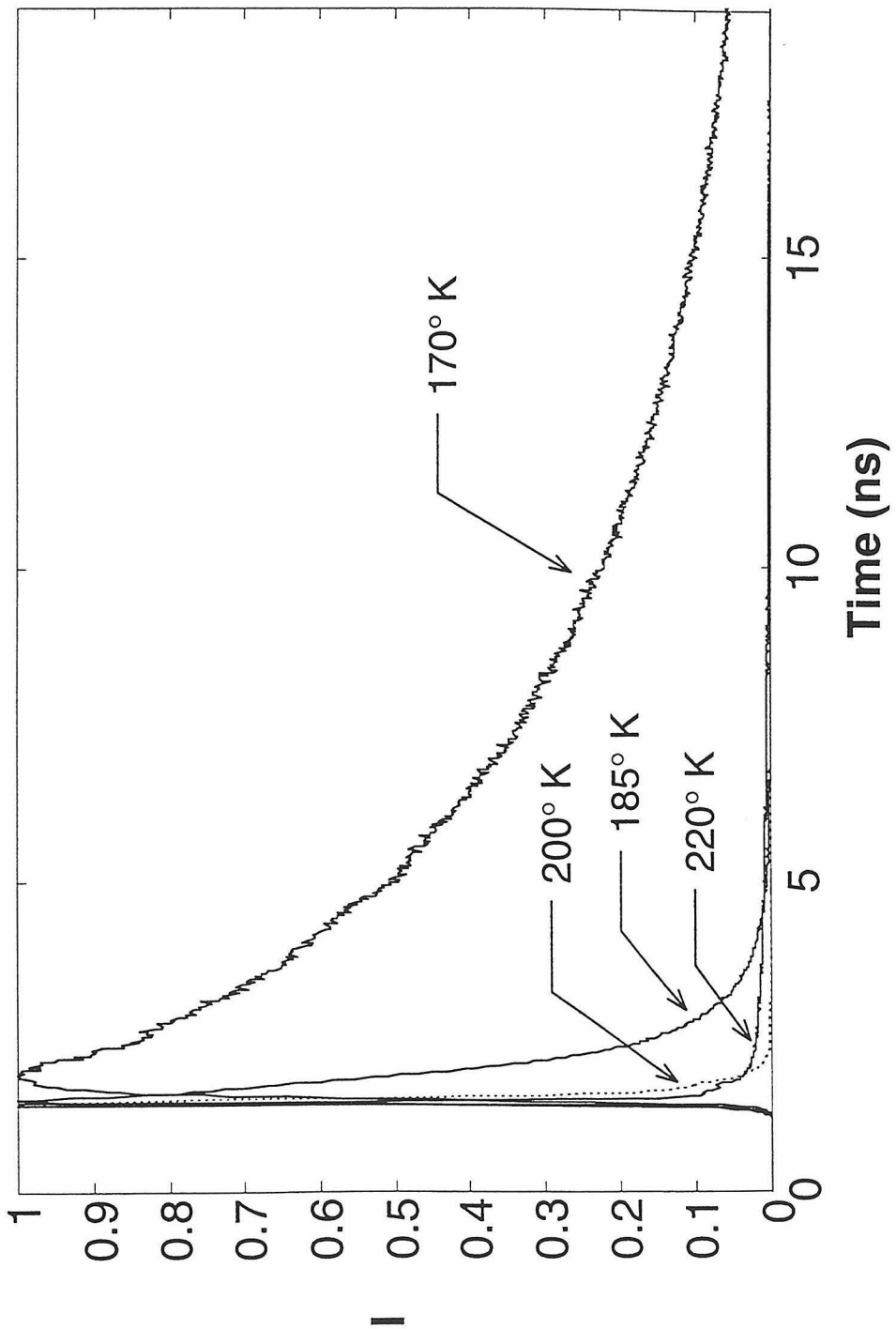
170° K
200° K
185° K
220° K
I
Time (ns)
0
0.1
0.2
0.3
0.4
0.5
0.6
0.7
0.8
0.9
1
5
10
15

Because of the bathochromic nature of TPE emission, the light measured at 460 nm becomes increasingly dominated by emission from the ^1R state as the temperature is lowered: The kinetics at 170° K clearly show a rise corresponding the $^1V \rightarrow {}^1R$ process, and a decay corresponding to the $^1R \rightarrow S_0$ process.

These data indicate that the rotation of adjacent phenyl groups in butyronitrile can occur very rapidly over the entire temperature range used to measure the rates of electron-transfer within the iridium complexes. Convolution of the SPC system response with a single exponential decay indicates that conformational changes at 200° K in butyronitrile occur at rates greater than $1 \times 10^{11}\ s^{-1}$.

Discussion

These studies make $Ir_2(A)_2$ one of the best characterized electron-transfer systems to date. The rates of both photoinduced and thermal charge-transfer reactions have been determined as functions of driving-force, temperature and isotopic composition. The compounds' visible spectroscopy has been rigorously assigned, and crystal structures have been determined. The dependence of k_{BET} on the nature of the bridge connecting the iridium core and pyridinium acceptors was even considered in earlier work.[41] This body of data allows detailed consideration of the ET processes within the $Ir_2(A)_2$ molecules.

Driving-Force Dependencies of Electron-Transfer Reactions

At each ten-degree interval between 200° and 280° K, the rates of all the photoinduced and recombination reactions can be combined and fit to the semiclassical Marcus expression (Figure III.18). Even with revised estimates of $\Delta G°$ for some of the reactions, it is clear that the data behave in much the same way the model predicts. Early studies fit data collected in acetonitrile at room temperature to Equation I.5, yielding values for H_{AB} (24 cm^{-1}) and λ (1.06 eV). Using the same equation to fit the data collected at 200° K in butyronitrile, similar values are obtained: H_{AB} = 26 cm^{-1}, λ = 1.01 eV. These values, however, are different from those determined from fits of the data at other temperatures (Figure III.18). The best fits yield a consistent increase in H_{AB} as the temperature is raised (Table III.5).

The differences between the low and high temperature results indicate that the photoinduced charge-separation and thermal recombination reactions may

Figure III.18 For every temperature, the rates of charge-separation and recombination can be combined and fit to the classical Marcus equation: (**A**) T = 200° K, (**B**) T = 210° K, (**C**) T = 220° K, (**D**) T = 230° K, (**E**) T = 240° K, (**F**) T = 250° K, (**G**) T = 260° K, (**H**) T = 270° K and (**I**) T = 280° K. The results of these fits are listed in Table III.5.

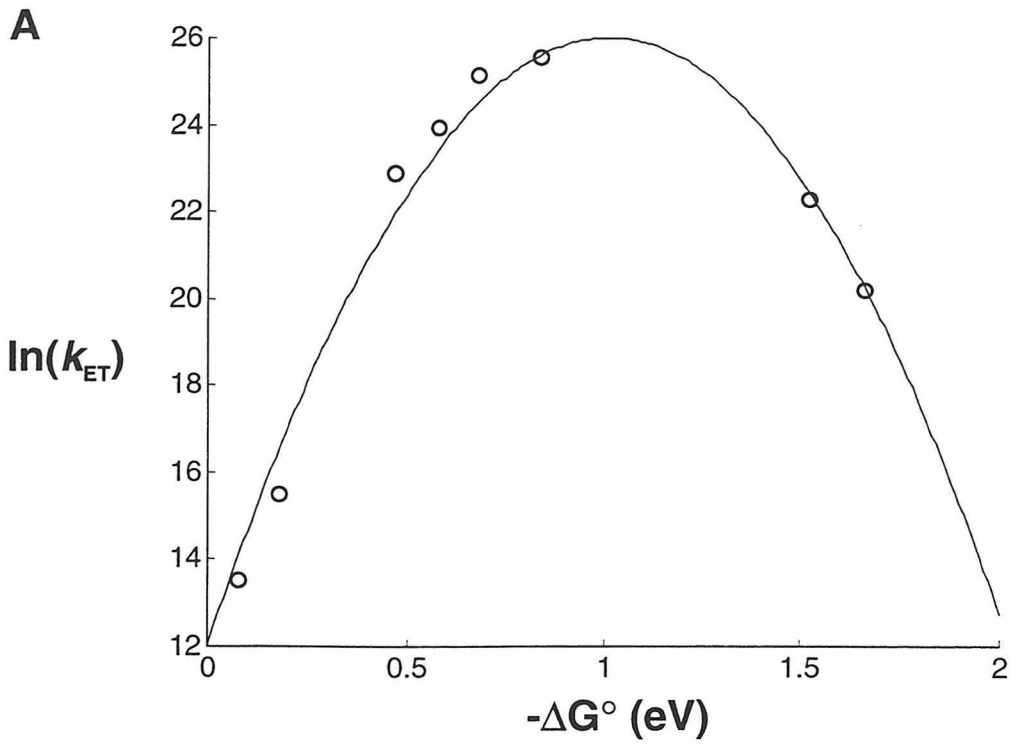
A
ln(k_{ET})
26
24
22
20
18
16
14
12
0
0.5
1
1.5
2
-ΔG° (eV)

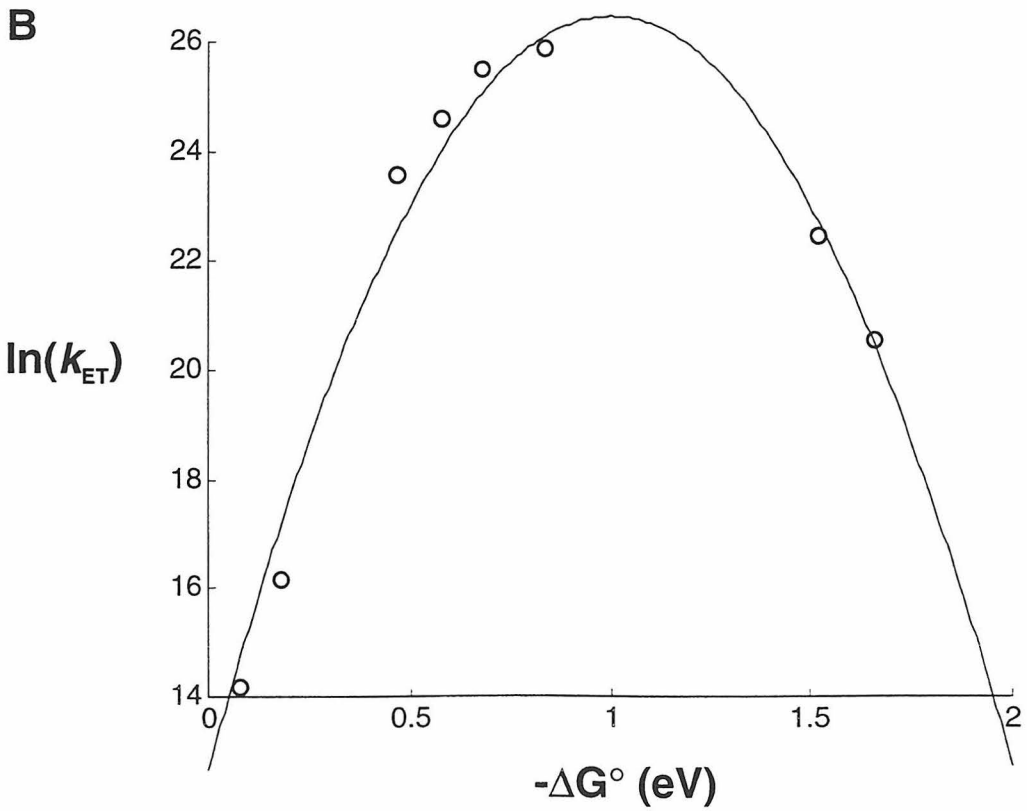
B
ln(k_{ET})
26
24
22
20
18
16
14
0
0.5
1
1.5
2
-ΔG° (eV)

C

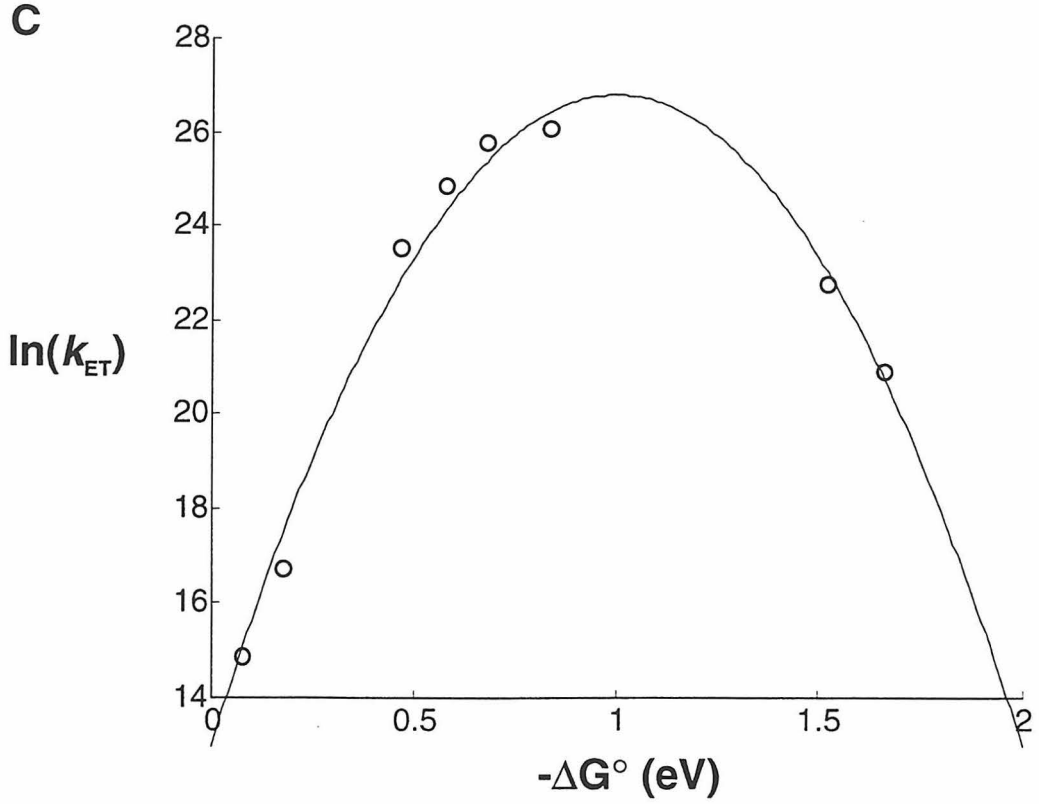
28
26
24
22
20
18
16
14
0
0.5
1
1.5
2
ln(k_{ET})
-ΔG° (eV)

D

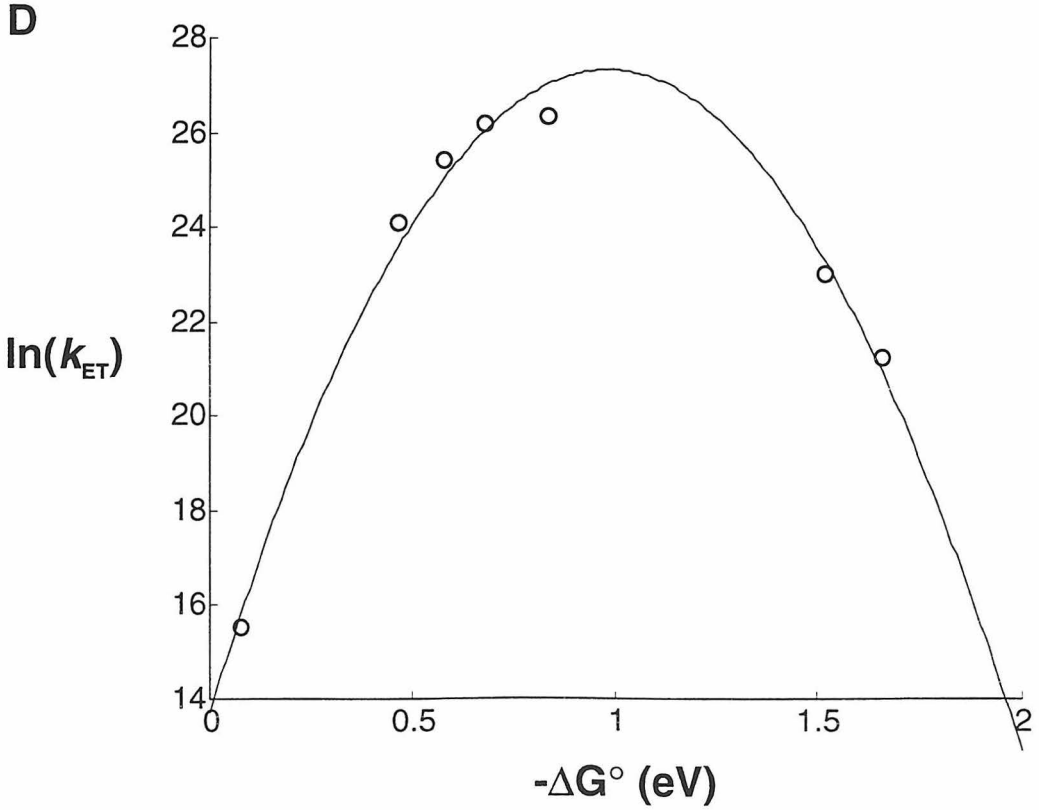
28
26
24
22
20
18
16
14
0
0.5
1
1.5
2
ln(k_{ET})
-ΔG° (eV)

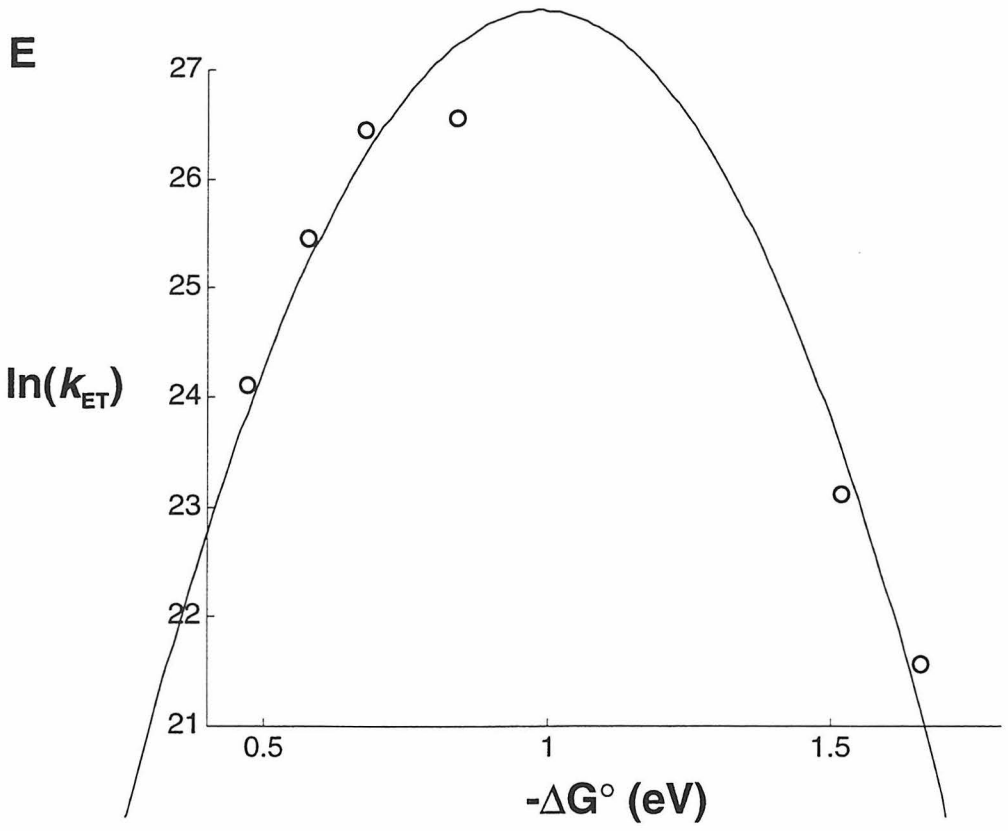
E
27
26
25
24
23
22
21
ln(k_{ET})
0.5
1
1.5
-ΔG° (eV)

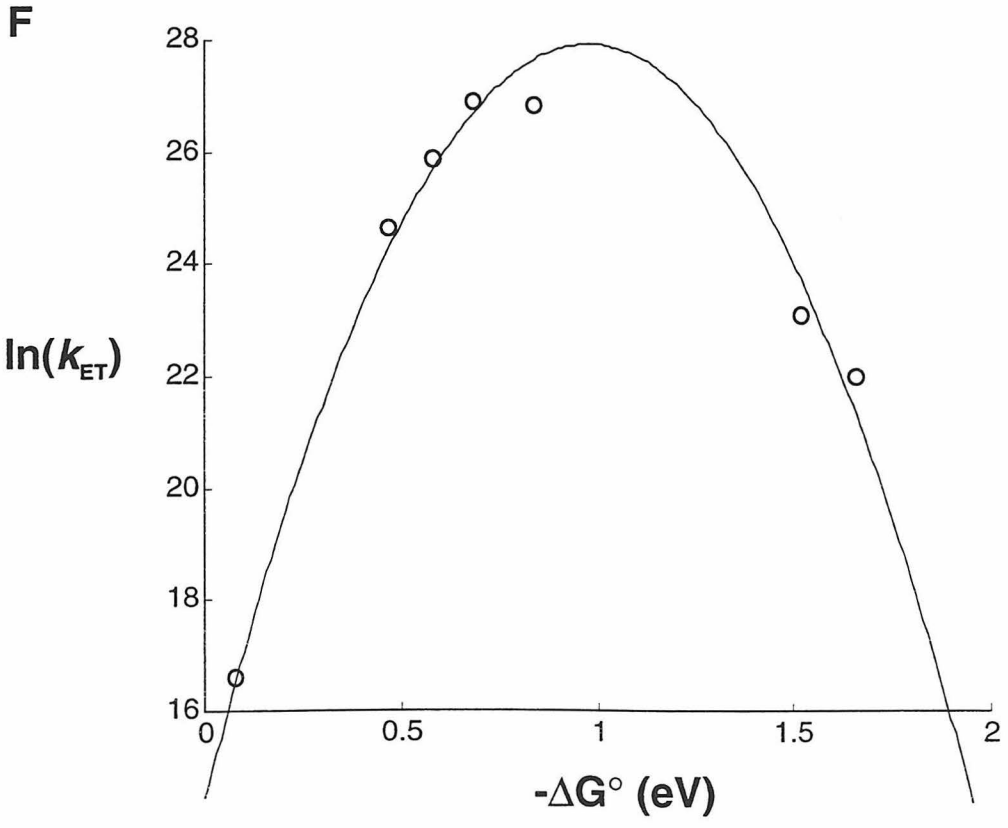
F
28
26
24
22
20
18
16
ln(k_{ET})
0
0.5
1
1.5
2
-ΔG° (eV)

G

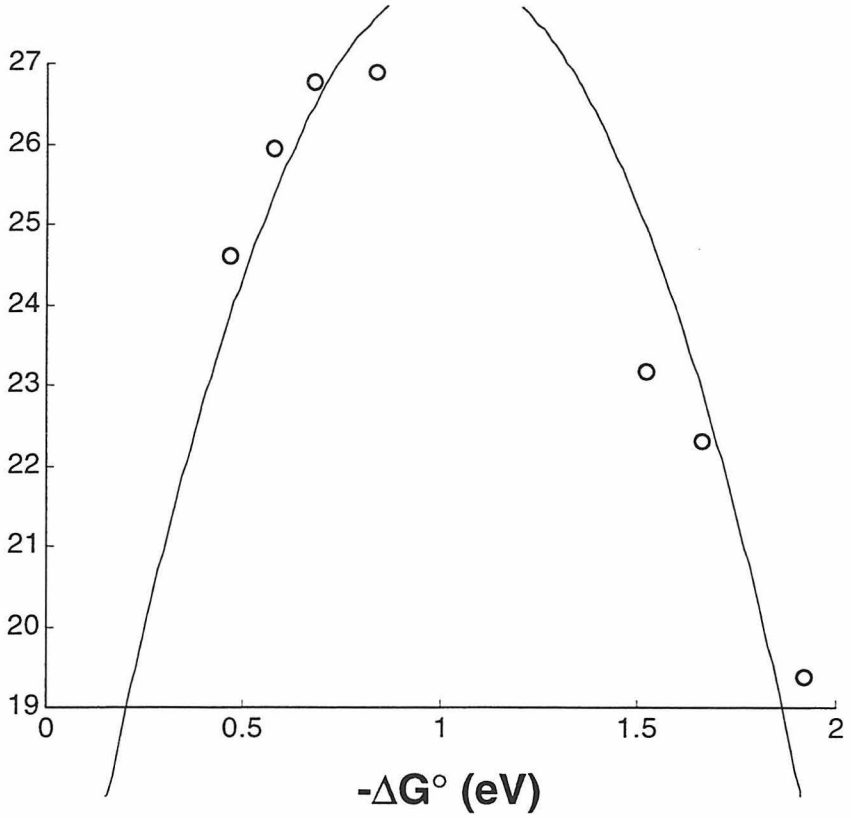
27
26
25
24
23
22
21
20
19
0
0.5
1
1.5
2
ln(k_{ET})
-ΔG° (eV)

H

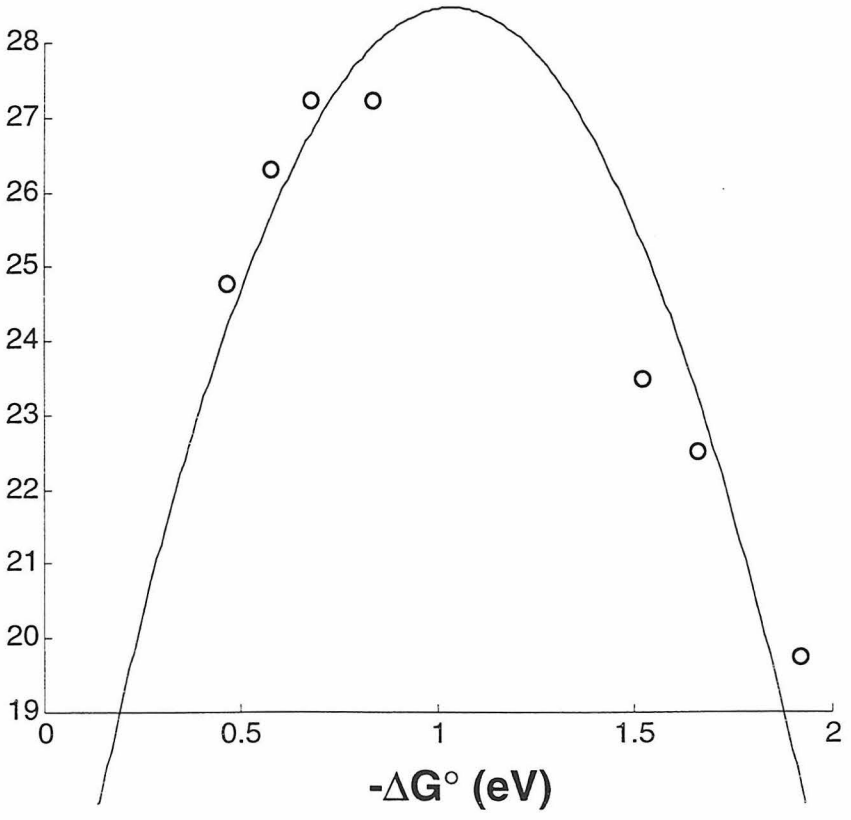
28
27
26
25
24
23
22
21
20
19
0
0.5
1
1.5
2
ln(k_{ET})
-ΔG° (eV)

I

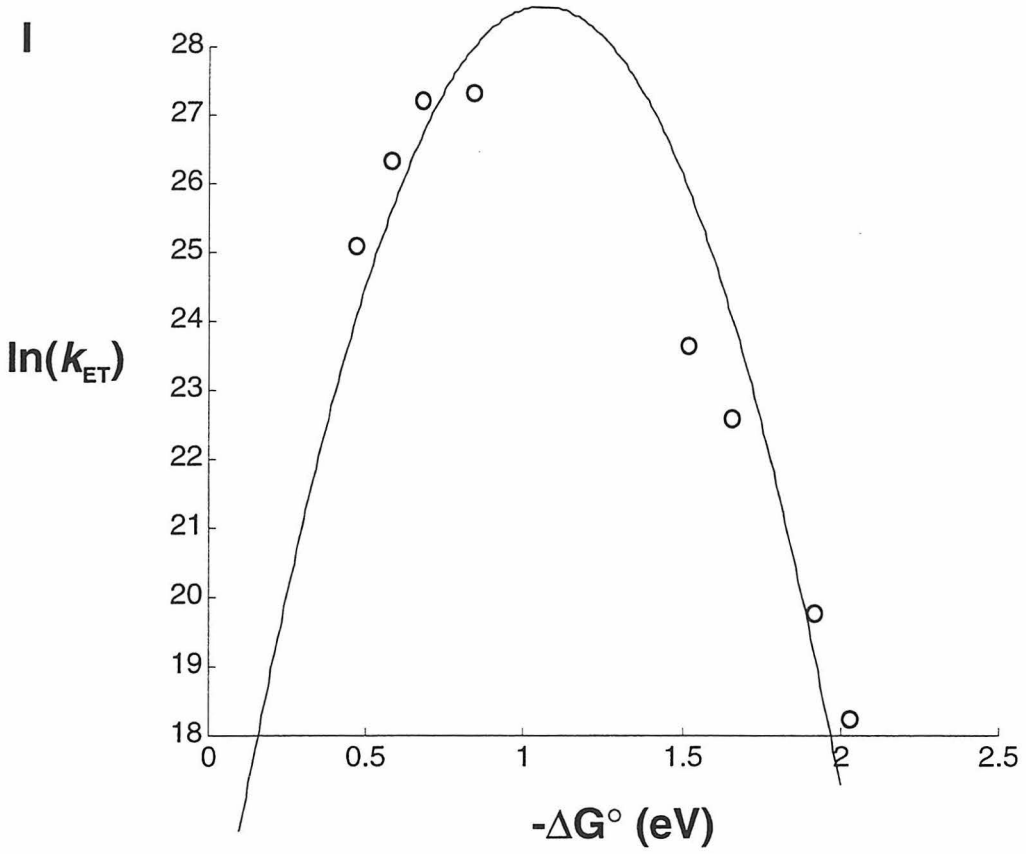

Table III.5 Values of H_{AB} and λ obtained from the best fits of all the photoinduced and thermal ET rates to Equation I.5 as a function of temperature.

Temperature (°K)	H_{AB} (cm^{-1})	λ (eV)
200	26	1.01
210	32	1.00
220	38	1.00
230	49	0.99
240	55	0.98
250	66	0.98
260	75	1.04
270	88	1.04
280	97	1.06

have different amounts of donor-acceptor coupling. This is certainly possible, since the electron is transferred from the pσ orbital of the iridium core through the bridge to the pyridinium, while the recombination reaction returns the electron to the core's dσ* orbital. In an attempt to discover if this is indeed the case, all the rates determined for every temperature were combined and then divided into two sets; one containing the rates of the forward reactions, and the other containing the rates of the recombination reactions. Each set was then fit to Equation I.5.

The two fits produce dramatically different results (Figure III.19). The best fit of the charge-separation reactions yields an H_{AB} of 175 cm^{-1} and a λ of 1.26 eV, while the best fit of the recombination reactions yields an H_{AB} of 10.6 cm^{-1} and a λ of 1.19 eV. As different as these numbers may be, they do yield good fits to the corresponding data sets at all the temperatures (Figure III.20). The large reorganization energies are difficult to accept, however, since the ^{1}ET photoinduced reduction of 4-phenylpyridinium -- which has been conclusively demonstrated[18] to result in the reduction of the cationic acceptor -- appears adiabatic. Consequently, while these global fits do yield results that conform to the data well, the results are unacceptable, and thus offer no evidence that H_{AB} is substantially different for the forward and reverse reactions.

It is apparent from a close analysis of the fits shown in Figure III.18 that as the temperature increases, their quality decreases. This may be the result of a weak inverted effect that is only apparent at temperatures for which more than two inverted region rates have been obtained. Consequently, the data might best be fit

Figure III.19 A global fit of all the charge-separation data results in parameters (H_{AB} = 175 cm^{-1} and λ = 1.26 eV) that yield a dramatically different $\ln(k_{ET})$ *vs.* $-\Delta G°$ curve than what is obtained from the results of a global fit of all the charge-recombination data (H_{AB} = 10.6 cm^{-1} and λ = 1.19 eV).

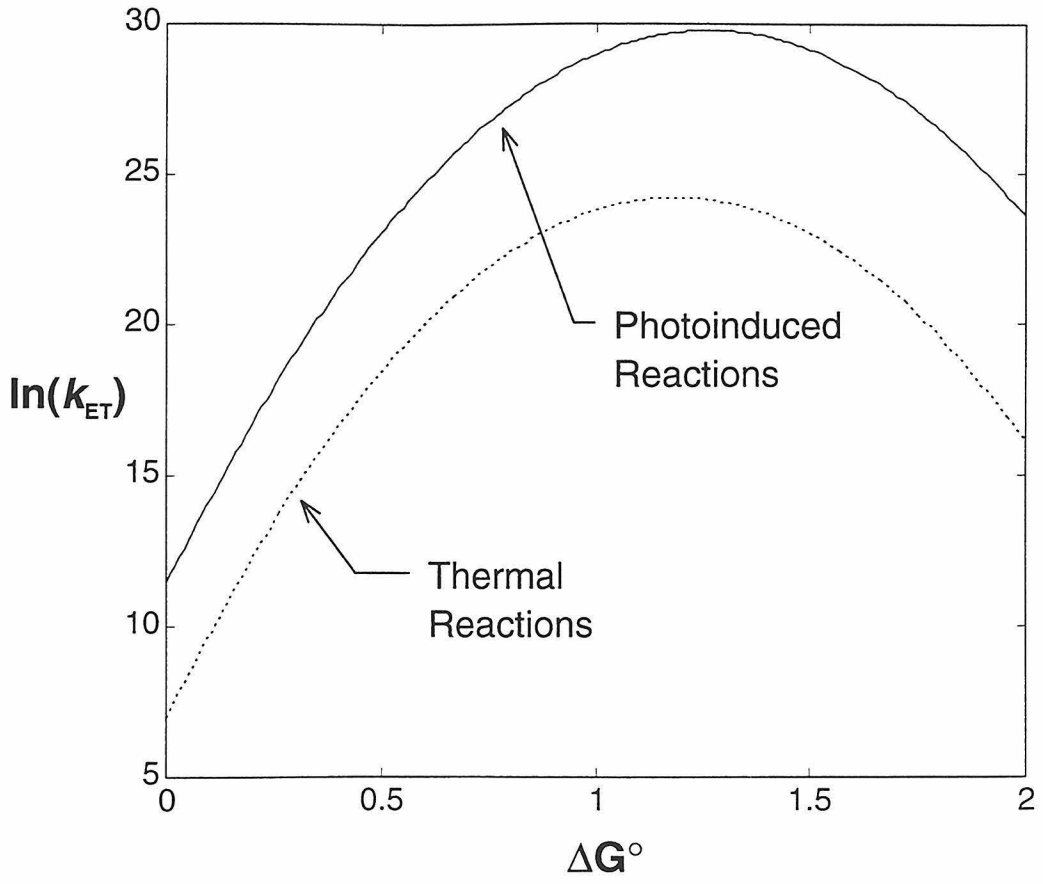
30
25
20
15
10
5
0
0.5
1
1.5
2
ln(k_{ET})
ΔG°
Photoinduced
Reactions
Thermal
Reactions

Figure III.20 By dividing the photoinduced and thermal ET data sets, global fits of each return values for H_{AB} and λ that fit the observed reaction rates well at every temperature.(**A**) shows the recombination fit with the data collected at 280° K; (**B**) shows the forward fit with the data collected at 200° K.

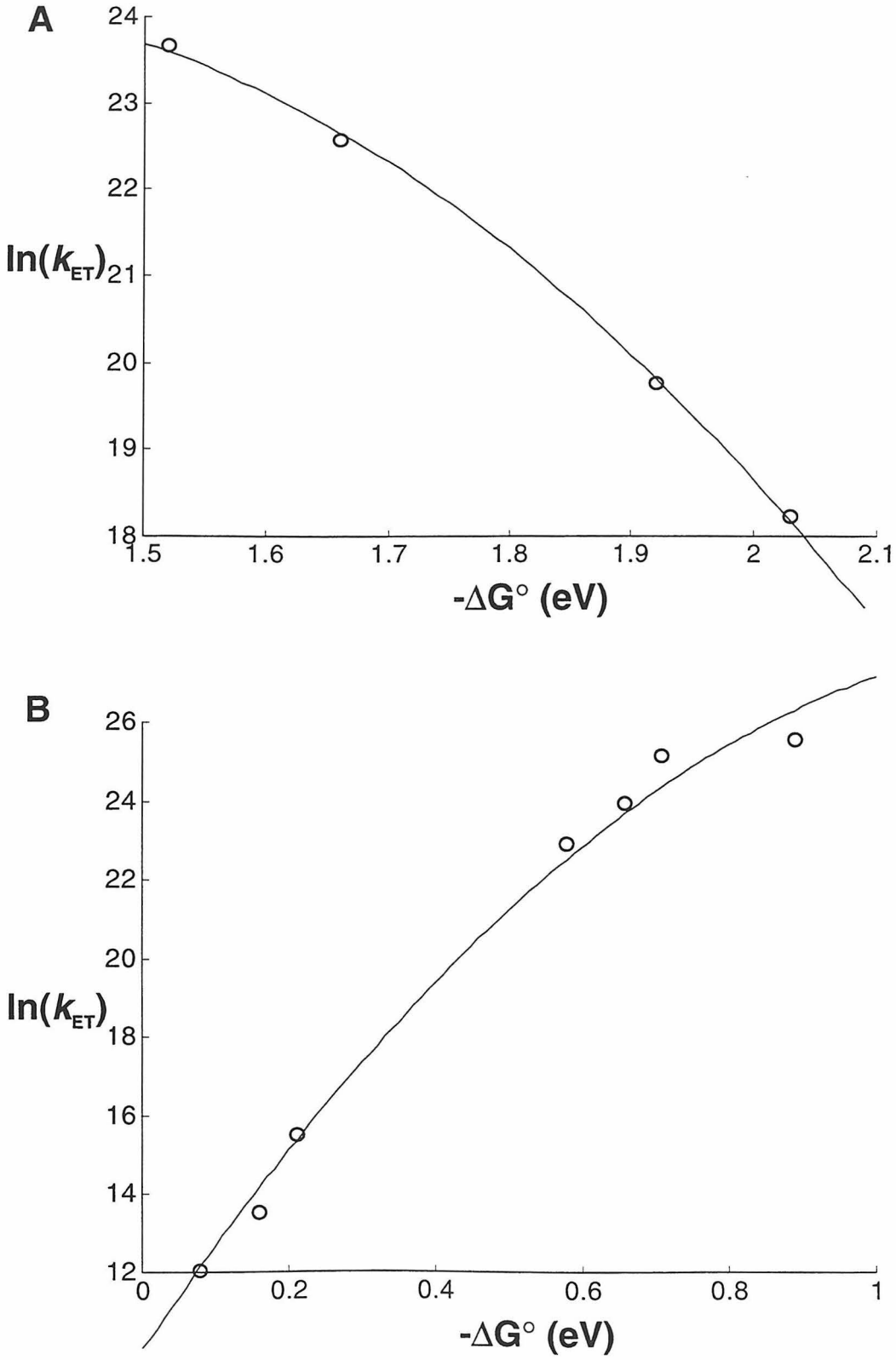
A
24
23
22
ln(k_{ET}) 21
20
19
18
1.5
1.6
1.7
1.8
1.9
2
2.1
-ΔG° (eV)
B
26
24
22
20
ln(k_{ET}) 18
16
14
12
0
0.2
0.4
0.6
0.8
1
-ΔG° (eV)

with a quantum-mechanical ET model that explicitly considers vibrational interactions between the donor and acceptor potential energy surfaces.

The resonance Raman spectrum obtained from excitation of the charge-transfer band of 4-phenylpyridinium iodide provides information about which high frequency vibrations may be responsible for such reactant-product coupling (Figure III.6). The spectrum of the salt shows at least five vibrations between 1100 cm^{-1} and 1700 cm^{-1} that are strongly coupled to the pyridinyl radical formation. Two weaker features in this region are also apparent. It is computationally prohibitive to fit the ET data to a model that explicitly considers all seven nuclear frequencies, but a rough approximation of such a fit is possible with a single-mode model that uses their average. Because some Raman modes are more strongly enhanced than others, the single-mode fits performed here used an average of their frequencies weighted by their intensities. With this value of ~1500 cm^{-1}, Equation I.6 yields noticeably better fits at every temperature than does Equation I.5, although the resulting values for H_{AB} and λ still increase with temperature.

Because the reorganization energies of these reactions should be insensitive to temperature, the best estimates for λ_{in} and λ_{out} are obtained from the data acquired at temperatures between 250° K and 280° K, which include more than just the rates of the high-driving force reactions within Ir_2(4-phenylpyridinium)$_2$ and Ir_2(pyridinium)$_2$, which can be measured at every temperature. As the temperature is increased to the point where the charge separated states of Ir_2(3,4-dimethylpyridinium)$_2$ and Ir_2(2,4,6-trimethylpyridinium)$_2$ are quickly formed, the rates of these more deeply inverted reactions can be measured. The best fits of data

collected between 250° and 280° K consistently yield values for λ_{in} of ~0.006 eV and λ_{out} of ~0.86 eV. These values have been used in fits of the data at each temperature in which only H_{AB} was allowed to float. Considering the uncertainties of the photoinduced reaction rates, which are never directly measured, the resulting fits are very good (Figure III.21). In a trend similar to that exhibited by the fits to classical ET theory, H_{AB} shows a consistent increase as the temperature of the sample is raised, although not as dramatic a one (Table III.6).

Conformation Considerations

These results raise two important questions. First, why does H_{AB} increase with temperature? Second, why, if $\lambda \approx 0.86$ eV, does Ir_2(4-phenylpyridinium)$_2$ show no emission at any temperature when the driving-force for its ^{1}ET reaction is -0.98 eV? The answers lie in an analysis of all the compounds' electron-transfer activation energies.

With values for $\Delta G°$ and λ, E_A for each reaction can be predicted using Equation I.5. When these theoretically determined numbers are compared to those determined from experiment for the normal region reactions, a consistent difference of approximately 0.119 eV is found (Table III.7). This suggests that an activated process occurs prior to photoinduced electron-transfer.

This is quite plausible. Molecular mechanics calculations on the free phosphonite ligand bound to a pyridinium show that it prefers to adopt two conformers in the gas phase that differ in energy by ~2 kcal/mol. One is highly twisted, while the other is linear (Figure III.22). The activation energy for

Figure III.21 For every temperature, the rates of charge-separation and recombination can be combined and fit to a quantum-mechanical single-mode ET model (ω = 1500 cm^{-1}, λ_{in} = 0.0057 eV, λ_{out} = 0.855 eV, and H_{AB} is allowed to float): (**A**) T = 200° K, (**B**) T = 210° K, (**C**) T = 220° K, (**D**) T = 230° K, (**E**) T = 240° K, (**F**) T = 250° K, (**G**) T = 260° K, (**H**) T = 270° K and (**I**) T = 280° K. The results of these fits are listed in Table III.6.

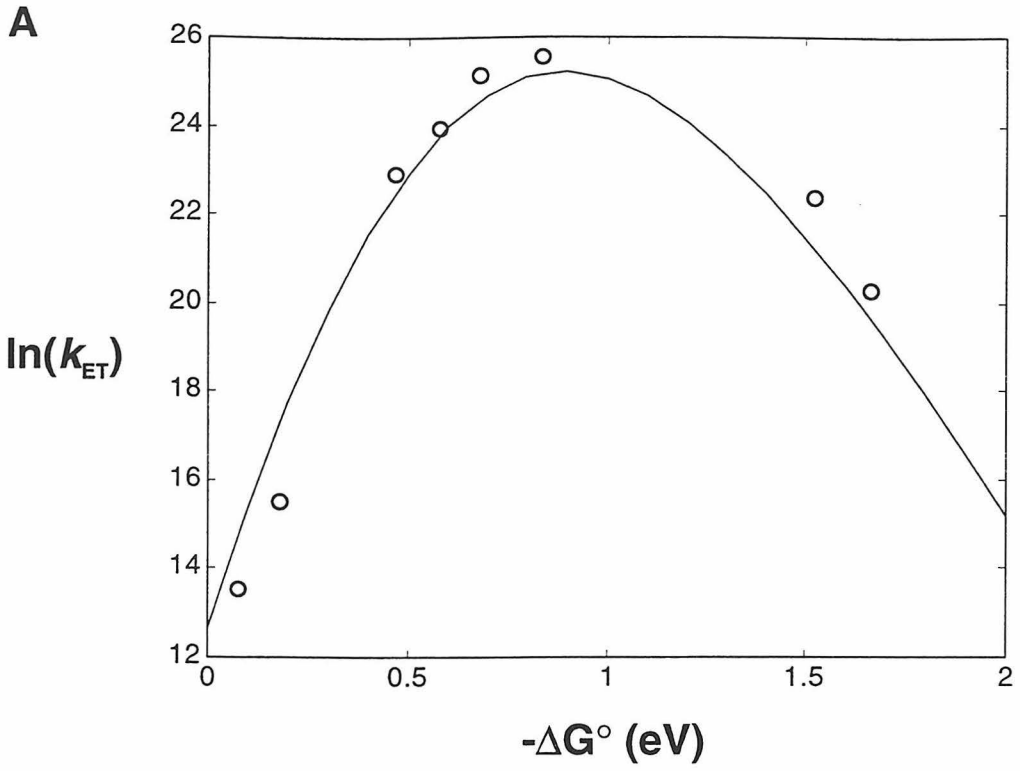
A
26
24
22
20
18
16
14
12
0
0.5
1
1.5
2
ln(k_{ET})
-ΔG° (eV)

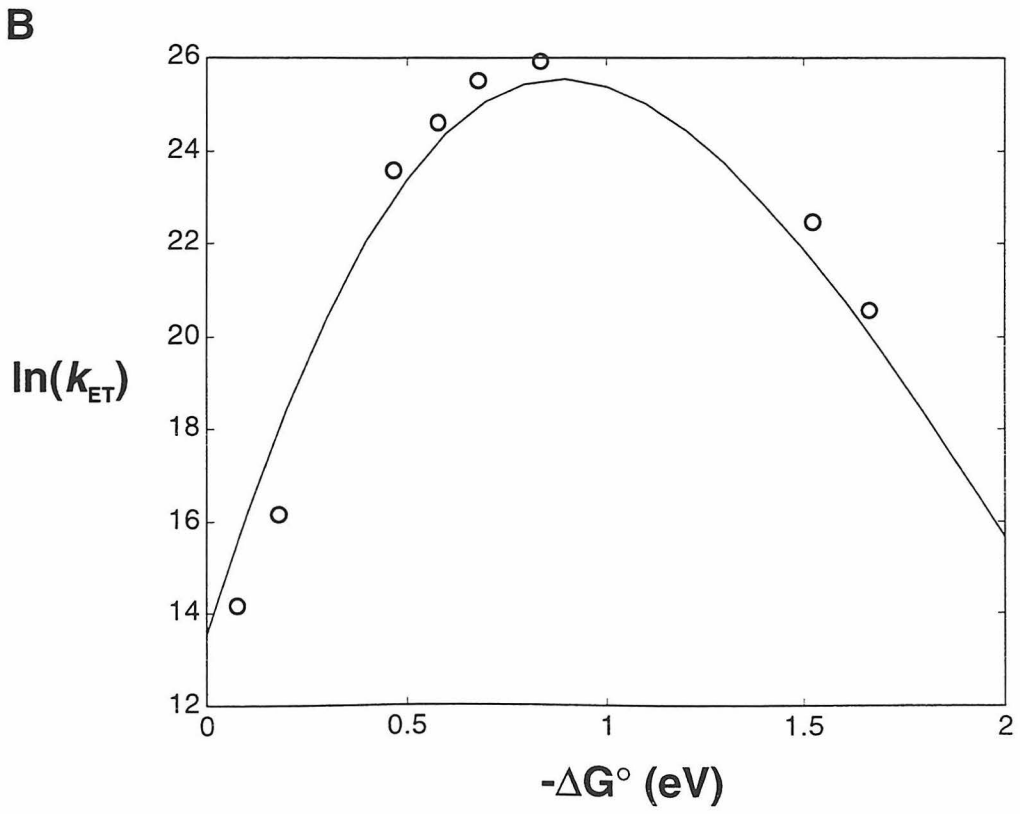
B
26
24
22
20
18
16
14
12
0
0.5
1
1.5
2
ln(k_{ET})
-ΔG° (eV)

C

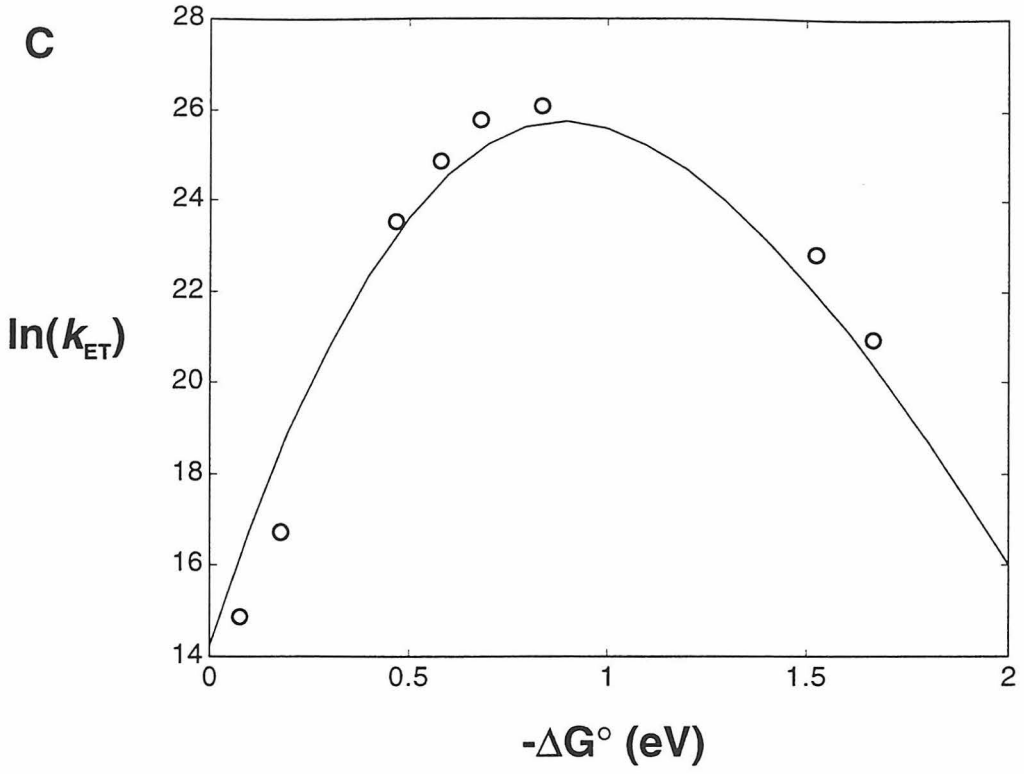
28
26
24
22
20
18
16
14
0
0.5
1
1.5
2
ln(k_{ET})
-ΔG° (eV)

D

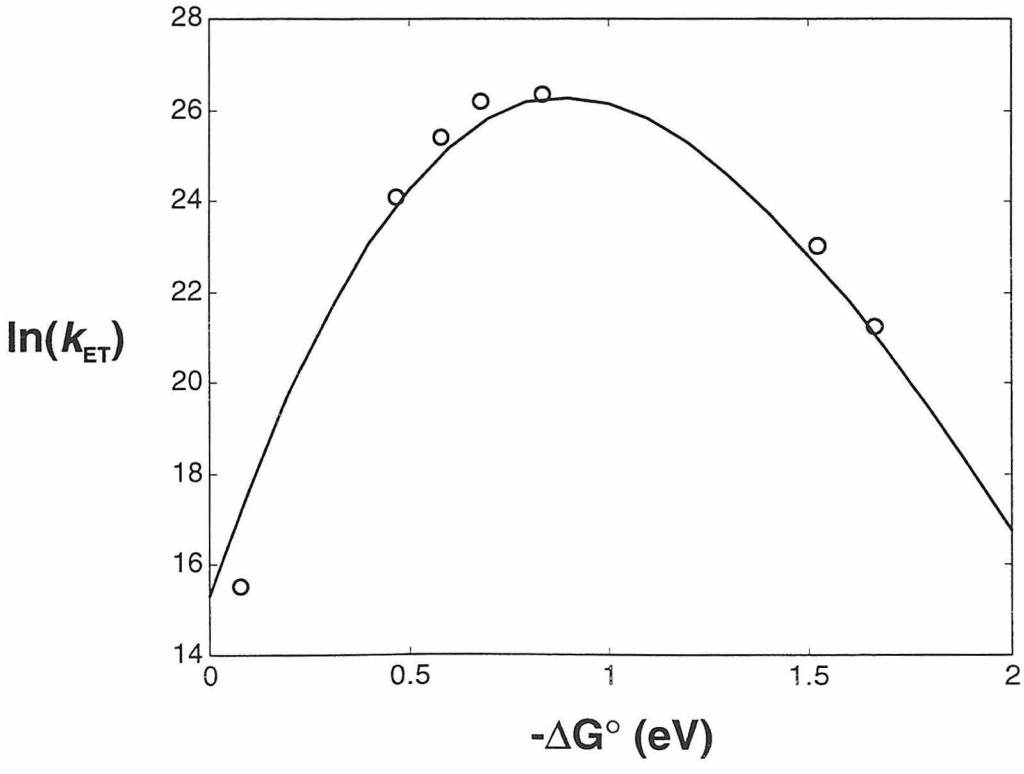
28
26
24
22
20
18
16
14
0
0.5
1
1.5
2
ln(k_{ET})
-ΔG° (eV)

E

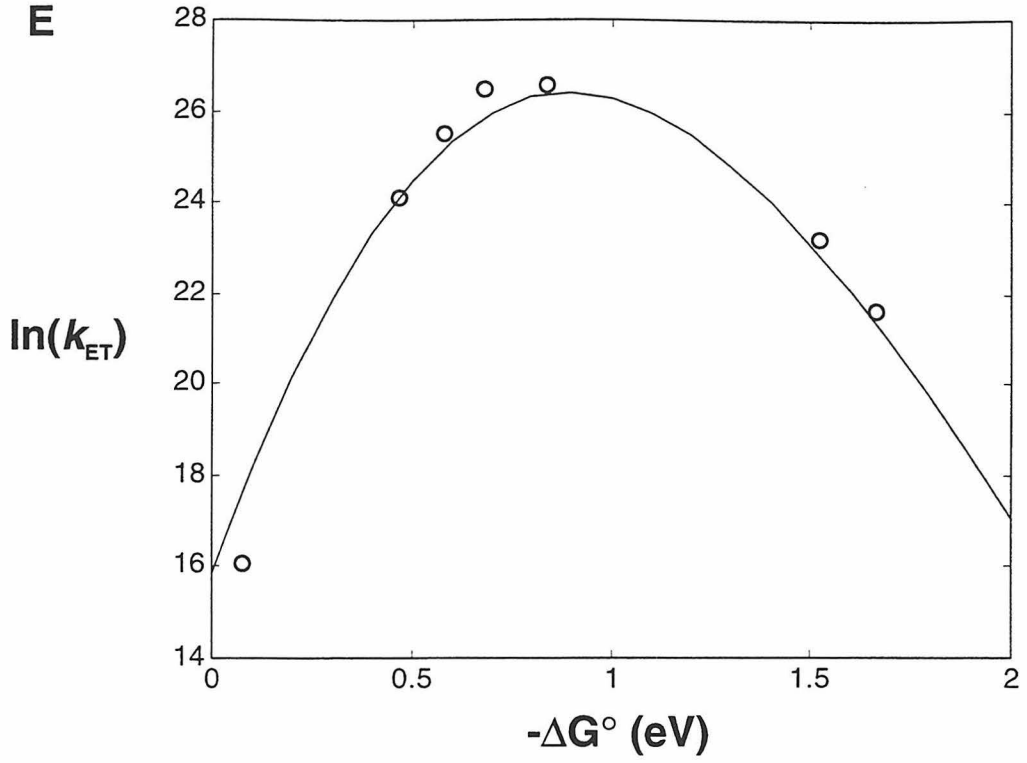
28
26
24
22
20
18
16
14
0
0.5
1
1.5
2
ln(k_{ET})
-ΔG° (eV)

F

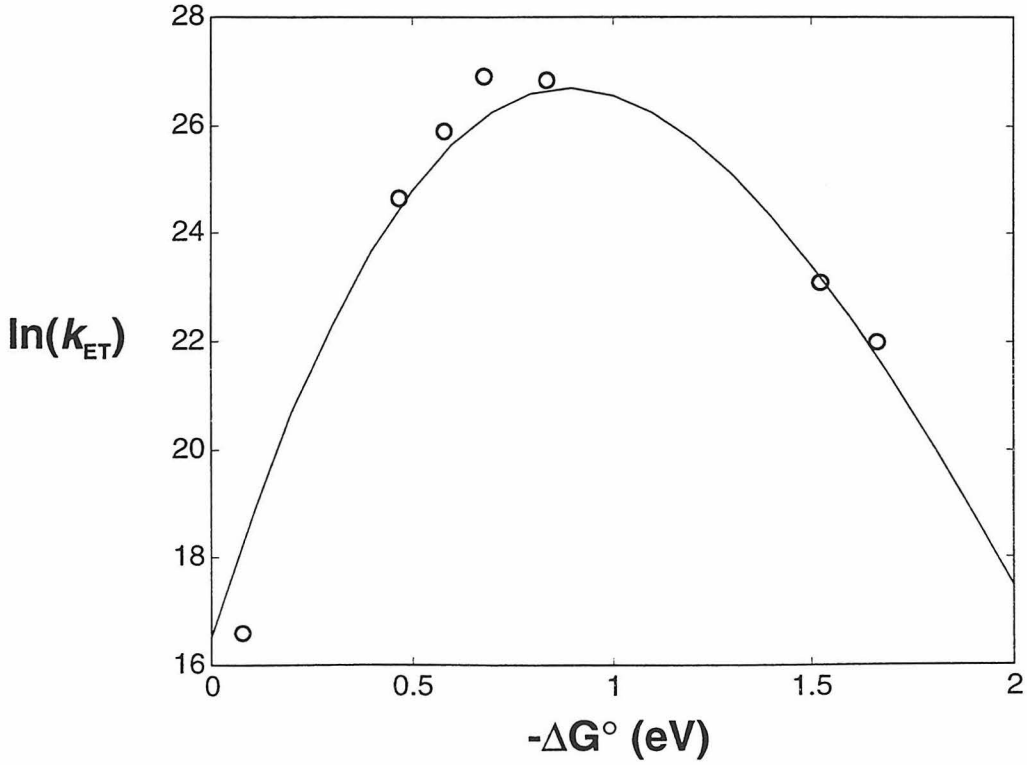
28
26
24
22
20
18
16
0
0.5
1
1.5
2
ln(k_{ET})
-ΔG° (eV)

G

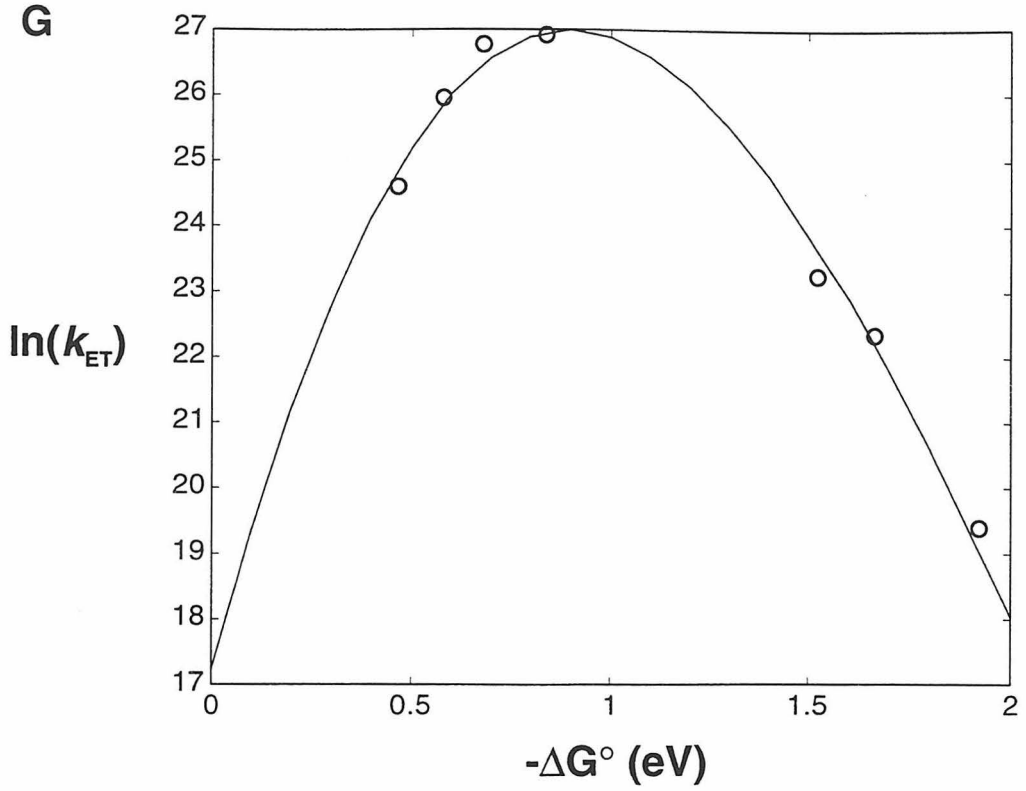
27
26
25
24
23
22
21
20
19
18
17
0
0.5
1
1.5
2
ln(k_{ET})
-ΔG° (eV)

H

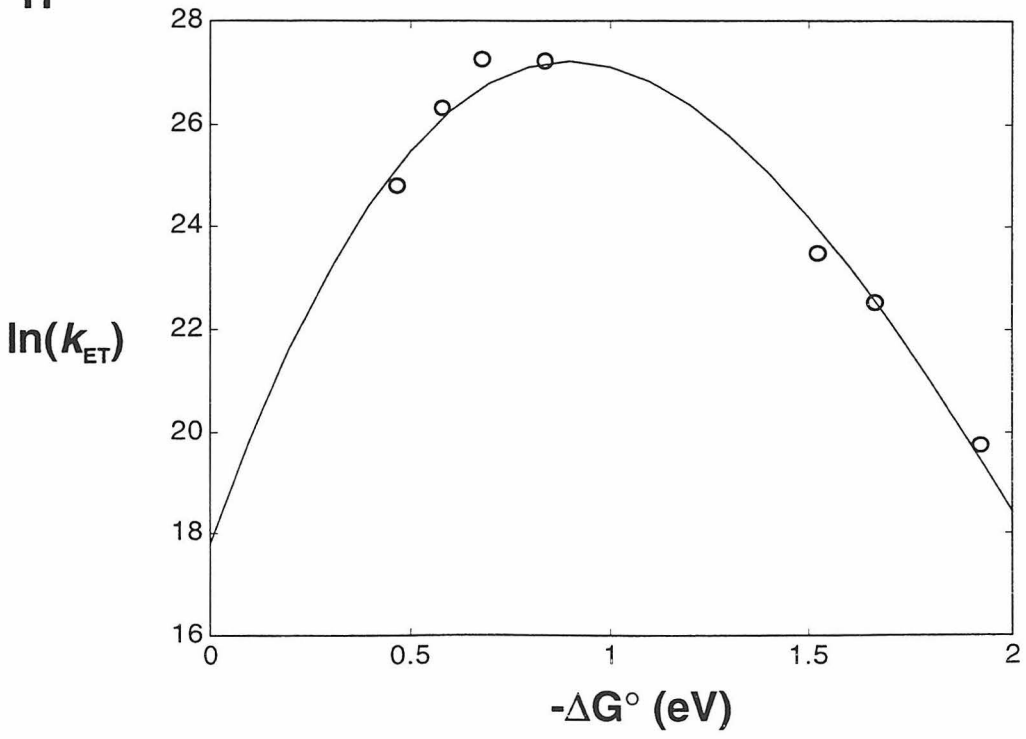
28
26
24
22
20
18
16
0
0.5
1
1.5
2
ln(k_{ET})
-ΔG° (eV)

I

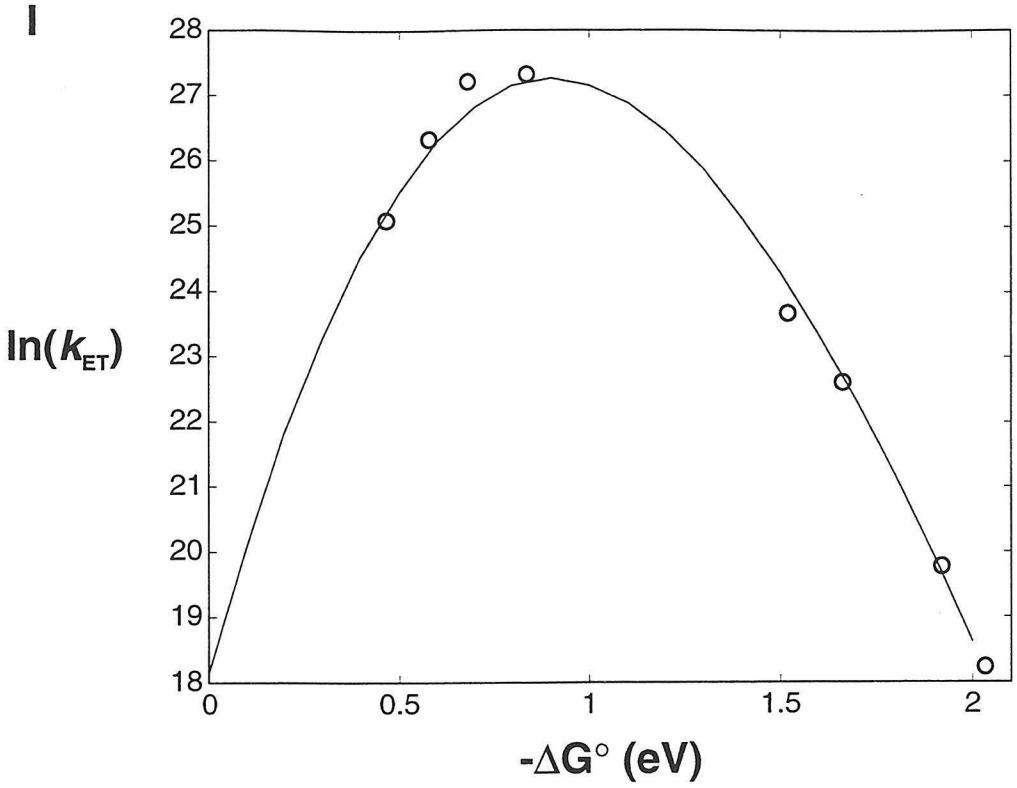

Table III.6 Results of a best fits to all the photoinduced and thermal ET rates to Equation I.6 (single high-frequency mode ω = 1500 cm^{-1}, λ_{in} = 0.0057 eV, λ_{out} = 0.885 eV). Solvent reorganization is treated classically. These results are compared to those listed in Table III.5.

Temperature (°K)	Classical H_{AB} (cm^{-1}) *	Quantum H_{AB} (cm^{-1}) †	ΔH_{AB} (cm^{-1})
200	26	18	8
210	32	21	11
220	38	23	15
230	49	31	18
240	55	34	21
250	66	40	26
260	75	48	27
270	88	56	32
280	97	58	39

* Determined from the best fits of the data in which both H_{AB} and λ were allowed to float.

† Determined from the best fits of the data in which only H_{AB} was allowed to float: λ_{out} = 0.855 eV, λ_{in} = 0.0057 eV, ω = 1500 cm^{-1}.

Table III.7 Summary of the activation energies determined for both the photoinduced and thermal electron-transfer reactions. They are compared with theoretical values determined from the reactions' driving-forces and reorganization energies with Equation I.5.

Donor	Acceptor	-ΔG° (eV)	Exp. E_A (eV)	Thr. E_A (eV)	ΔE_A (eV)
$^3Ir_2$*	3,4-Me_2py$^+$	0.08	0.294	0.177	0.117
$^3Ir_2$*	4-Mepy$^+$	0.18	0.244	0.135	0.109
$^1Ir_2$*	2,4,6-Me_3py$^+$	0.47	0.159	0.044	0.115
$^1Ir_2$*	3,4-Me_2py$^+$	0.58	0.151	0.023	0.128
$^1Ir_2$*	4-Mepy$^+$	0.68	0.136	0.001	0.127
$^1Ir_2$*	py$^+$	0.84	0.116	0.000	0.116
$^1Ir_2$*	4-Phpy$^+$	0.98	≈ 0 *	0.004	--
4-Phpy$^\bullet$	Ir_2^+	1.52	0.085	0.126	-0.041
py$^\bullet$	Ir_2^+	1.66	0.162	0.186	-0.024
4-Mepy$^\bullet$	Ir_2^+	1.82	‡	0.267	--
3,4-Me_2py$^\bullet$	Ir_2^+	1.92	0.104	0.326	-0.222
2,4,6-Me_3py$^\bullet$	Ir_2^+	2.03	§	0.397	--

* The $^1Ir_2$* state is completely quenched by the 4-phenyl pyridinium acceptor at all temperatures (200° to 300° K).

‡ Low solubility prevented measurement of the recombination rates.

§ At temperatures lower than 280° K, the transient spectrum is dominated by the ^{3}ET reaction.

Figure III.22 The minimized geometries of the two conformers adopted in the gas phase by the phosphonite and pyridinium acceptor. The phosphorous atom is on the left, and is bound to an aritifical hydrogen atom.

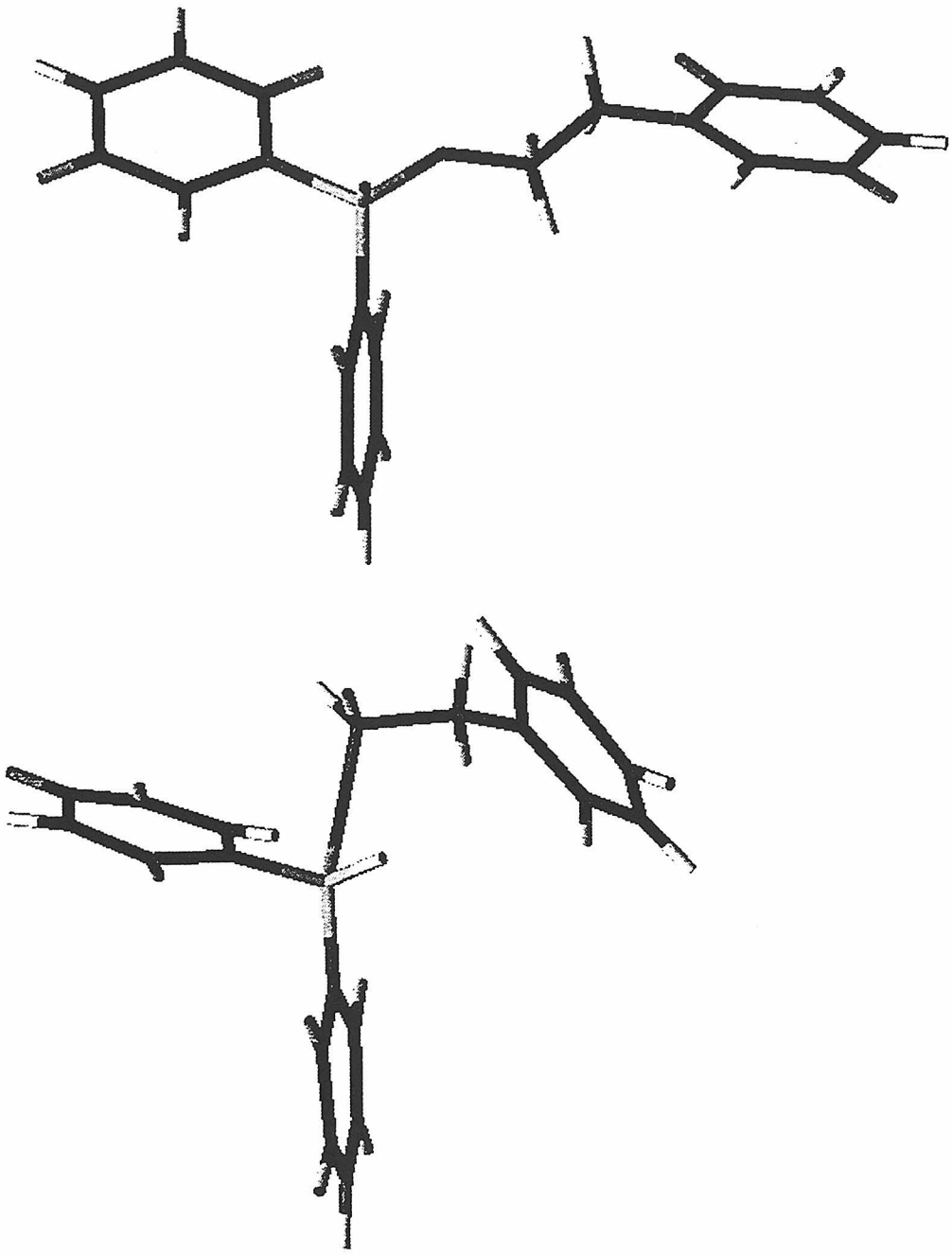

interconversion was not calculated, but energy minimizations of each will not lead the model to adopt the other conformer. The phosphorous-nitrogen distance in the linear configuration is 5.08 Å, and is 3.56 Å in the bent. These conformers will undoubtedly be different when the false hydrogen atoms on the phosphorous atoms are replaced with the iridium core, and the molecule is solvated. Still, these calculations suggest that the iridium complexes may adopt two general conformers in solution, and that the adoption of the thermodynamically less stable one is necessary for electron-transfer to occur. The single-photon counting experiments described above indicate that the bond rotations which could conceivably form the active geometry can occur faster than ET.

Previous work indicates that ET within the $Ir_2(A)_2$ complexes occurs through the donor-acceptor bridge, rather than through space.[41] This can be combined with large amounts of evidence that indicate electron-transfer is much more facile though bonds with *trans* geometries than through those with *cis*,[42] to lead to the conclusion that the phosphonite ligands must adopt geometries similar to that shown in the top half of Figure III.22 before ET can occur. The difference in the observed normal region activation energies from those predicted by theory indicates that the geometry change has an E_A of approximately 0.119 eV.

It is unclear why the ligands would prefer more twisted geometries to more linear ones, but the modeling suggests that for the pyridinium acceptor, steric interactions are not significant. In contrast, it is likely that the steric bulk of the 4-phenylpyridinium acceptor would prevent the adoption of this twisted state. If this is the case, and Ir_2(4-phenylpyridinium)$_2$ is forced to adopt a geometry that allows

large donor-acceptor coupling, then its apparent activationless behavior can be explained: While the ^{1}ET reaction in this compound actually lies within the Marcus inverted region, it always appears quenched simply because H_{AB} *in the linear configuration* is so large. This explains why H_{AB} appears to increase with temperature. The actual coupling between the iridium core and the pyridinium acceptors is highly dependent on the molecules' geometries, and is probably quite high for the linear configuration.

Examination of Table III.6 shows that the activation energies determined for the charge-recombination reactions do not deviate from theoretically calculated ones in the regular manner that the forward ones do. They are, however, consistently *less*. This adds to the evidence that nuclear tunneling does play a role in the inverted region ET within these complexes. The deviation of -0.222 eV shown by the Ir_2(3,4-dimethylpyridinium)$_2$ reaction emphasizes that as the reactant and product wells become more deeply nested, the overlap of their wavefunctions increases.

Isotope Effects

The rates of recombination reactions within Ir_2(pyridinium)$_2$ between 200° K and 280° K are consistently 1.2 times greater than those within the deuterated pyridinium isomer. This effect can be accounted for by reduction the mean high-temperature nuclear vibrational frequencies used in Equation I.6 to fit these data from 1500 cm^{-1} to approximately 1200 cm^{-1} (Figure III.23). Such a decrease is consistent with the resonance Raman spectra of the natural-

Figure III.23 The effect of frequency on a $\ln(k_{ET})$ *vs.* $-\Delta G°$ curve obtained using Equation I.6 is shown in (**A**): The arrow indicates the movement of the plot as ω is increased from 1000 cm^{-1} to 1250 cm^{-1} to 1500 cm^{-1} (λ_{in} = 0.006 eV, λ_{out} = 0.93 eV and H_{AB} = 24 cm^{-1}). The ratio of rates as a function of driving-force using the same parameters is shown in (**B**), in which k_H has been calculated with ω = 1500 cm^{-1} and k_D has been calculated with ω = 1000 cm^{-1} (solid line) and 1250 cm^{-1} (dashed line).

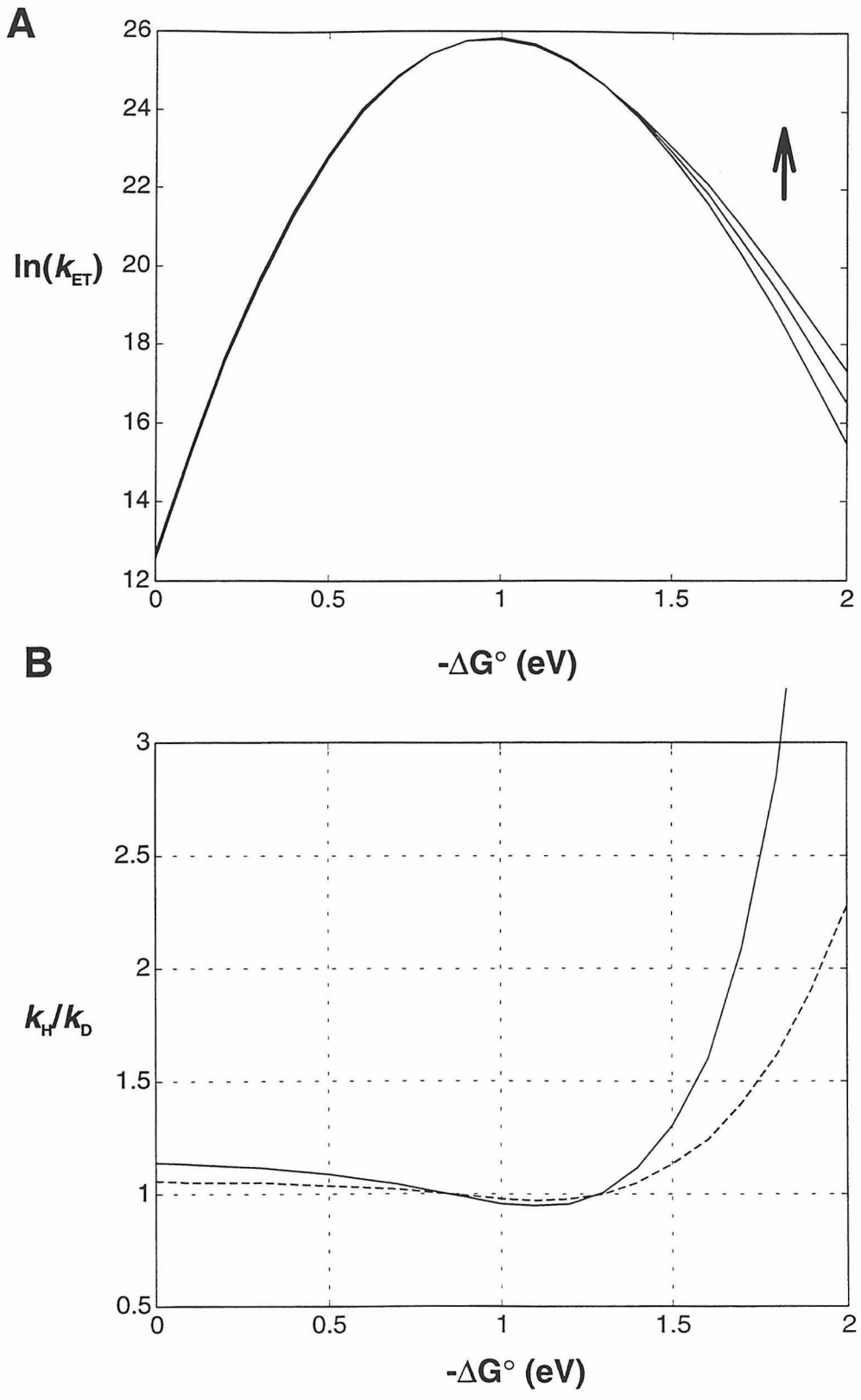
A
26
24
22
ln(k_{ET})
20
18
16
14
12
0
0.5
1
1.5
2
-ΔG° (eV)
B
3
2.5
2
k_H/k_D
1.5
1
0.5
0
0.5
1
1.5
2
-ΔG° (eV)

abundance and deuterated 4-phenylpyridinium iodide salts, which show the movement of several bands to lower energies (Figure III.8).

The isotope effects observed for the photoinduced reactions are much more difficult to explain. Their magnitudes simply do not agree with the single-mode quantum-mechanical ET model. Similar large effects have been observed by others, and have been explained in terms of reactant-product coupling *via* high energy, low nuclear distortion, vibrational modes.[43] It is possible, then, that by modeling the iridium complexes' behavior with a multimode quantum-mechanical model, all the observed isotope effects can be accounted for.

Summary

Revised electrochemical data, temperature-dependent kinetic measurements and isotope studies indicate that electron-transfer within the covalently-coupled iridium-pyridinium complexes does not behave classically, in contrast to earlier findings. Quantum effects are necessary to obtain good fits of the k_{ET} *vs.* $-\Delta G^\circ$ curves at higher temperatures, and are necessary to explain kinetic isotope effects in both the normal and inverted regions. Fits of the data indicate $\lambda_{out} \approx 0.855$ eV and $\lambda_{in} \approx 0.006$ eV in butyronitrile. The remarkably strong inverted behavior shown by the $Ir_2(A)_2$ system is due to the small amount of internal reorganization accompanying electron-transfer.

It has been hypothesized that the flexible bridge connecting these compounds' donors and acceptors can adopt two conformations, only one of which is suitable for fast ET. The barrier to adoption of the active conformer is

approximately 0.119 eV. It is argued that the steric bulk of the 4-phenylpyridinium acceptor forces Ir_2(4-phenylpyridinium)$_2$ to adopt this active conformer in solution. This geometry's large value of H_{AB} allows the singlet photoinduced ET reaction within this compound to appear activationless, when in fact it lies in the inverted region.

REFERENCES AND NOTES

[1] Lewis, N. S.; Mann, K. N.; Gordon, J. G. II; Gray, H. B. *J. Am. Chem. Soc.* 1976, 98, 7461.

[2] Smith, D. C.; Gray, H. B. *Coord. Chem. Rev.* **1990**, *100*, 169.

[3] Mann, K. R.; Gray, H. B. *Adv. Chem. Ser.* **1979**, *173*, 225: Rice, S. F.; Milder, S. J.; Goldbeck, R. A.; Kliger, D. S.; Gray, H. B. *Coord. Chem. Rev.* **1982**, *43*, 349.

[4] Rice, S. F.; Gray, H. B. *J. Am. Chem. Soc.* **1981**, *103*,1593.

[5] Casper, J. V.; Gray, H. B. *J. Am. Chem. Soc.* **1984**, *106*, 3029.

[6] Bushnell, G. W.; Fjeldsted, D. O. K.; Stobart, S. R.; Zaworotko, M. J.; Knox, S. A. R.; Macpherson, K. A. *Organometallics* **1985**, *4*, 1107: Beveridge, K. A.; Bushnell, G. W.; Stobart, S. R.; Atwood, J. L.; Zaworotko, M. J. *Organometallics* **1983**, *2*, 1447.

[7] Marshall, J. L. , *Ph.D. Dissertation*, California Institute of Technology, Pasadena, **1986**.

[8] Marshall, J. L.; Stobart, S. R.; Gray, H. B. *J. Am. Chem. Soc.* **1984**, *106*, 3027.

[9] Marshall, J. L.; Hopkins, M. D.; Miskowski, V. M.; Gray, H. B. *Inorg. Chem.* **1992**, *31*, 5034.

[10] Winkler, J. R.; Marshall, J. L.; Netzel, T. L.; Gray, H. B. *J. Am. Chem. Soc.* **1986**, *108*, 2263.

[11] Rehm, D.; Weller, A. *Isr. J. Chem.* **1970**, *8*, 259.

[12] McCleskey, T. M.; Winkler, J. R.; Gray, H. B. *J. Am. Chem. Soc.* **1992**, *114*, 6935.

[13] McCleskey, T. M.; Winkler, J. R.; Gray, H. B. *Inorg. Chim. Acta* **1994**, *225*, 319.

[14] The lowest lying excited state of the pyridinyl radical anion is 0.4 eV above the ground-state.[12]

[15] Mines, G. A.; Bjerrum, M. J.; Hill, M. G.; Casimiro, D. R.; Chang, I-J.; Winkler, J. R.; Gray, H. B. (submitted for publication, 1995).

[16] McCleskey, T. M. *Ph.D. Dissertation*, California Institute of Technology, Pasadena, **1994**.

[17] Fox, L. S.; Marshal, J. L.; Gray, H. B. *J. Am. Chem. Soc.* **1987**, *109*, 6901.

[18] Fox L. S., *Ph.D. Dissertation*, California Institute of Technology, Pasadena, **1989**.

[19] Fox L. S.; Kozik, M.; Winkler, J. R.; Gray, H. B. *Science* **1990**, *247*, 1069.

[20] Marcus, R. A. *Isr. J. Chem.* **1988**, *28*, 205.

[21] Liang, N.; Miller, J. R.; Closs, G. L. *J. Am. Chem. Soc.* **1990**, *112*, 5353: Kroon, J.; Oevering, H.; Verhoeven, J. W.; Warman, J. M.; Oliver, A. M.; Paddon-Row, M. N. *J. Phys. Chem.* **1993**, *97*, 5065: Heitele, H.; Pöllinger, F.; Häberle, T.; Michel-Beyerle, M. E.; Staab, H. A. *J. Phys. Chem.* **1994**, *98*, 7402.

[22] Taniguchi, V. T.; Sailasuta-Scott, N.; Anson, F. C.; Gray, H. B. *Pure Appl. Chem.* **1980**, *52*, 2275.

[23] Koepp, H. M.; Wendt, H.; Stehlow, H. Z. Z. *Elektrochem.* **1960**, *64*, 983.

[24] Gange, R. R.; Koval, C. A.; Lisensky, G. C. *Inorg. Chem.* **1980**, *19*, 2854.

[25] Howell, J. O.; Kuhr, W. G.; Enswan, R. E.; Wightman, R. M. *J. Electroanal. Chem.* **1986**, *209*, 77.

[26] Boyd, D. C.; Rodman, G. S.; Mann, K. R. *J. Am. Chem. Soc.* **1986**, *108*, 1779: Hill, M. G.; Mann, K. R. *Inorg. Chem.* **1991**, *30*, 1429.

[27] The disproportionation rate constant for $[Ir(COD)pz]_2^+$ has been measured: $k_d = 7 \times 10^6\ M^{-1}\ s^{-1}$ (Martyn, K.; Hill, M. G. unpublished data).

[28] Hill, M. G.; Lamanna W., Mann, K. R. *Inorg. Chem.* **1991**, *30*, 4687.

[29] Nicholson, R. S.; Shain, S. *Anal. Chem.* **1964**, *36*, 706.

[30] Webber, A.; Kirowa-Eisner, E.; Osteryoung, J.; Hermolin, J. *J. Electrochem. Soc.* **1982**, *129*, 2725.

[31] Andrieux, C. P.; Nadjo, N.; Saveant, J. M. *J. Electroanal. Chem.* **1970**, *26*, 147.

[32] Meyers, A. B.; Mathies, R. A. *Resonance Raman Intensities: A Probe of Excited-State Structure and Dynamics* in Biological Applications of Raman Spectroscopy vol. 2, Spiro, T. A. ed. John Wiley & Sons: New York. **1987**.

[33] Silverstein, R. M.; Bassler, G. C.; Morrill, T. C. Spectrometric Identification of Organic Compounds 4th ed. John Wiley & Sons: New York. **1981**.

[34] The unusually low solubility of Ir_2(4-methylpyridinium)$_2$ prevented measurement of its transient spectrum in short path-length cells.

[35] Isied, S. S.; Vasilian, A. *J. Am. Chem. Soc.* **1984**, *106*, 1732: Isied, S. S.; Vassilian, A.; Magnuson, R. H.; Schwartz, H. A. *J. Am. Chem. Soc.* **1985**, *107*, 7432.

[36] The melting point of butyronitrile is 181° K.

[37] Barbara, P.F.; Rand, S.D.; Rentzepis, P. M. *J. Am. Chem. Soc.* **1981**, *103*, 2156.

[38] Ma, J.; Dutt, G. B.; Waldeck, D. H.; Zimmt, M. B. *J. Am. Chem. Soc.* **1994**, *116*, 10619.

[39] Gegiou, D.; Muszkat, K. A.; Fischer, E. *J. Am. Chem. Soc.* **1968**, *90*, 3907: Bery, L. A.; Schuster, G. B.; Drickamer, H. G. *J. Am. Chem. Soc.* **1979**, *101*, 129: Chiang, W.-L.; Laane, J. *J. Chem. Phys.* **1994**, *100*, 8755.

[40] Todd, D. C.; Fleming, G. R. *J. Chem. Phys.* **1993**, *98*, 269: Saltiel, J.; Waller, A. S.; Sears, D. F. *J. Am. Chem. Soc.* **1993**, *115*, 2453; Mohrschladt, R.; Schroeder, J.; Schwarzer, D.; Troe, J.; Vöhringer, P. *J. Chem. Phys.* **1994**, *101*, 7566.

[41] Farid, R. S.; Chang, I-J.; Winkler, J. R.; Gray, H. B. *J. Phys. Chem.* **1994**, *98*, 5176.

[42] Closs, G. L.; Calcaterra, L. T.; Green, N. J.; Penfield, K. W.; Miller, J. R. *J. Phys. Chem.* **1986**, *90*, 3673.

[43] Gould, I. R.; Farid, S. *J. Am. Chem. Soc.* **1988**, *110*, 7883: Gould, I. R.; Ege, D.; Moser, J. E.; Farid, S. *J. Am. Chem. Soc.* **1990**, *112*, 4290: Meyers, A. B. *Chem. Phys.* **1994**, *180*, 215.

Chapter IV

Intramolecular Electron-Transfer in Strongly Coupled Bimetallic Donor-Acceptor Systems

Introduction

The properties of strongly coupled mixed-valence metal dimers have received extensive study for over 25 years.[1] During this time, the direct measurement of electron-transfer (ET) rates in an extraordinary number of weakly coupled donor-bridge-acceptor (D(br)A) systems has provided a detailed understanding of the nonadiabatic process.[2] In contrast, the adiabatic intramolecular ET within these molecules have, until recently, only been studied indirectly with the help of models developed by Mulliken[3] and Hush.[4] Consequently, their behavior is less well understood.

The optical spectra of strongly coupled mixed-valence bimetallic complexes often contain metal-metal charge-transfer (MMCT) absorption features at low energies. The reorganization energy λ and electronic coupling H_{AB} associated with the electron-transfer from one metal to the other can be determined from the analysis of these features. With the aid of Hush theory, Stein and Taube[5,6] first drew a correlation between metal-metal distance and coupling in a series of bis-ruthenium complexes. Since that time, numerous studies of strongly coupled dimers have appeared in the literature which use band-shape analysis to estimate rates of ET.[7] Only recently, however, has the technology become available for the direct measurement of these rates.

The strong coupling manifested by easily detectable MMCT absorption bands allows electron-transfer between the metals to occur on the picosecond or

subpicosecond timescales. Recently, Reid and coworkers found that the charge-recombination following excitation into the MMCT band of $(NH_3)_5Ru^{III}CNRu^{II}(CN)_5^-$ is coupled to the vibrational frequencies of the solvent in which it is dissolved, occurring in 85 fs in H_2O, and in 122 fs in D_2O.[8] This augments early transient infrared absorption studies of the same molecule. In addition to fast excited-state decay, Doorne and coworkers found that the initial charge-transfer places large amounts of energy directly into the RuC≡N stretching mode, so that photoinduced charge-transfer occurs between the reactant and a vibrationally excited product.[9] Both studies emphasize that, while band-shape analysis is useful for the qualitative study of ET within strongly coupled metal dimers, the rates such analyses provide are substantially different than those determined from measurements of excited-state decay. The differences emphasize that the behavior of these compounds is best described with quantum-mechanical electron-transfer models.

We have chosen a unique method of studying electron-transfer within strongly coupled D(br)A metal-metal dimers. Instead of exciting into their MMCT absorption bands, we have indirectly initiated ET with the local excitation of D or A. In the future, this technique will be extended to study the excited-state processes within symmetric and asymmetric metal dimers with a variety of bridging ligands. Here, the first results of these studies are reported: Both the symmetric and mixed-valence oxidation states of [(2,2'-bipyridine)(2,2',2"-terpyridine)$Ru^{II}CNRu^{II,III}(NH_3)_5]^{2+,3+}$ ($Ru_b^{II}CNRu_a^{II,III}$) have been studied and compared to the behavior of the monomer [(bpy)(tpy)RuCN](PF_6) (bpy = 2,2'-bipyridine; tpy = 2,2',2"-terpyridine).

Experimental

Reagent grade solvents were used without further purification for synthesis. UV-grade acetonitrile was distilled over CaH_2 prior to use for all spectroscopic measurements.

All compounds were prepared by Adrian Ponce by synthetic methods reported elsewhere.[10]

Steady-state Absorption and Emission Spectroscopy

UV-Vis NIR spectra were obtained using a modified Cary14 spectrometer (Olis) under IBM PC control.

Relative luminescence quantum yields were measured with a Hitachi 4500 fluorimeter under PC control. All samples were thoroughly degassed prior to data collection, and had an absorbance of approximately 0.1 at the excitation wavelength.

Electrochemistry and Spectroelectrochemistry

Electrochemical measurements were performed by Dr. Patrick J. Farmer.

Electrochemical data were measured with a Bioanalytical Systems 100 electrochemical analyzer. Cyclic voltammetry experiments were performed at room temperature in degassed acetonitrile containing 0.3 M tetrabutyl ammonium hexafluorophosphate (TBAH). A carbon electrode was used as the working electrode, a standard calomel electrode (SCE) was used as the reference electrode and ferrocene was used as an internal standard (Fe^{2+}/Fe^{3+} $E_{½}$ = 400 mV *vs.* NHE).[11]

Spectroelectrochemical measurements were made by coupling the electrochemical apparatus with a Hewlett Packard 8452A diode array UV-Vis spectrometer. The sample was dissolved in a 0.3 M TBAH/acetonitrile solution and degassed with N_2. Amorphous carbon was used as the working electrode to perform bulk electrolysis in a modified 1-cm quartz cuvette. Sample reduction was performed at -1600 mV *vs.* NHE.

Picosecond Transient Absorption

The experiment is described in Chapter II. Samples were flowed through a 1-mm path-length cell and excited at 532 nm, 416 nm or 683 nm.

Results

Steady-state Absorption and Emission Spectroscopy

The absorption spectra of the monomer (bpy)(tpy)RuCN$^+$ and the dimers $Ru_b^{II}CNRu_a^{II}$ and $Ru_b^{II}CNRu_a^{III}$ are shown in Figure IV.1 and summarized in Table IV.1. We have found that small amounts of impurities can alter the spectra of these compounds dramatically; consequently great care was taken to achieve a high degree of purity. The absorption spectrum of (bpy)(tpy)RuCN$^+$ is dominated by a combination of the metal-to-bpy and metal-to-tpy charge transfer bands with a maximum absorbance at 485 nm. Upon complexation with the ruthenium-pentaammine moiety to form $Ru_b^{II}CNRu_a^{II}$, this feature loses some intensity and shifts to the blue. Oxidation of this dimer to $Ru_b^{II}CNRu_a^{III}$ further attenuates this band's intensity, and shifts the maximum to slightly higher energy. A metal-metal

Figure IV.1 Absorption spectra of $[(bpy)(tpy)Ru^{II}(CN)]^{+}$ (--------), $[(bpy)(tpy)Ru^{II}(CN)Ru^{II}(NH_3)_5]^{3+}$ (———) and $[(bpy)(tpy)Ru^{II}(CN)Ru^{III}(NH_3)_5]^{4+}$ (— — —).

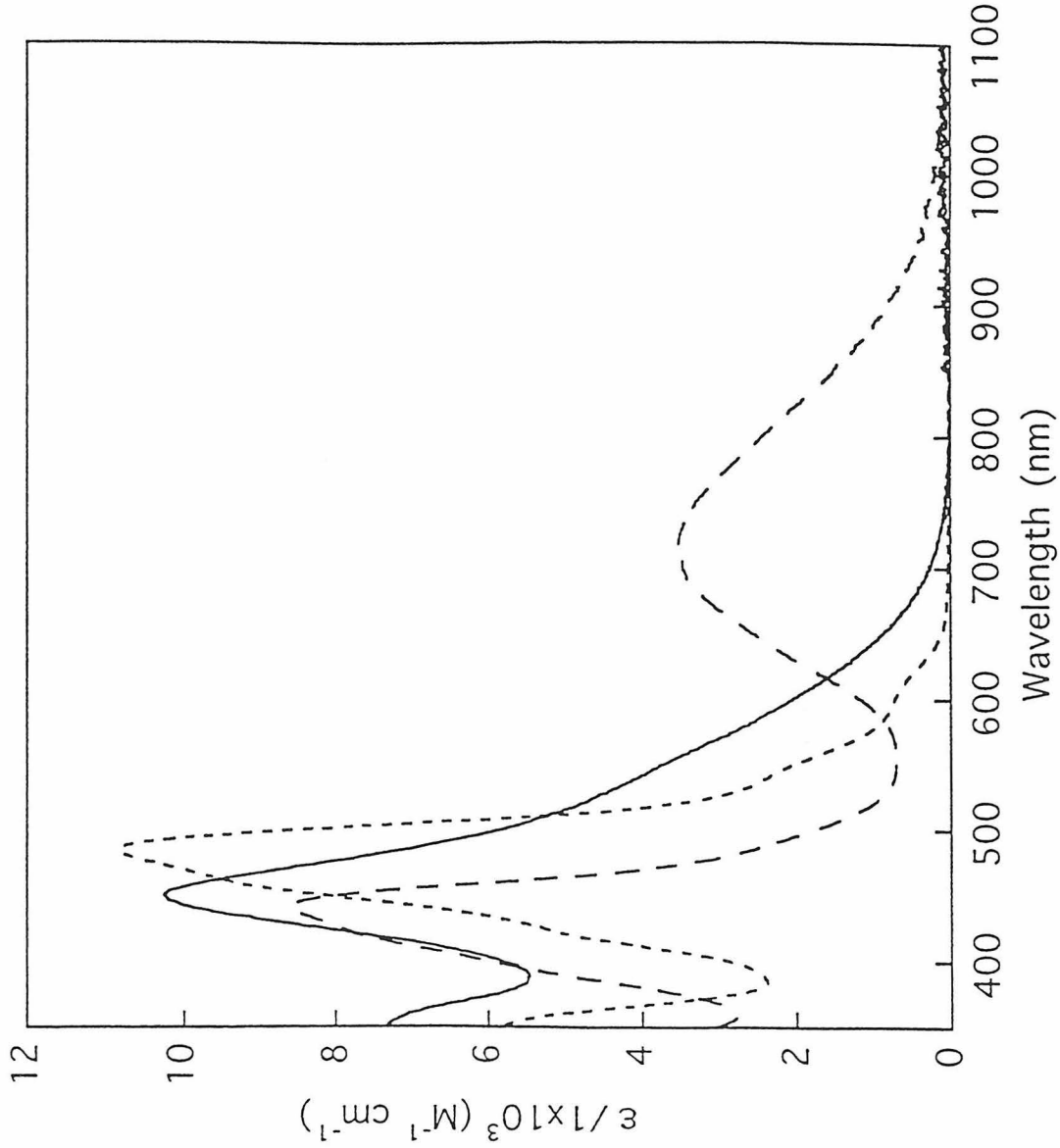
ε/1x10³ (M⁻¹ cm⁻¹)
0
2
4
6
8
10
12
400
500
600
700
800
900
1000
1100
Wavelength (nm)

Table IV.1 Spectroscopic Properties of $Ru_bCNRu_a^{3+/2+}$ Complexes.

Compound	MLCT λ_{max} (nm)	Emission λ_{max} (nm) §	Φ	k (s^{-1})
$[Ru(bpy)(tpy)CN](PF_6)$	485	651	$1.5(1) \times 10^{-4}$	$1.3(1) \times 10^{8}$
$[(bpy)(tpy)RuCNRu(NH_3)_5](PF_6)_3$	441	†	†	$1.2(2) \times 10^{10}$
$[(bpy)(tpy)RuCNRu(NH_3)_5](PF_6)_2$	451	†	†	‡

§ Using 450 nm excitation.
† Showed no emission at room temperature in acetonitrile.
‡ No transient optical density change was observed upon excitation at 416 nm or 683 nm.

charge-transfer absorption feature also appears, centered at 717 nm (ε = 3,500 $M^{-1}cm^{-1}$).

Excitation of the monomer (450 nm) in acetonitrile at room temperature produces MLCT luminescence. A quantum yield of 1.5×10^{-4} was determined using $[Ru(bpy)_3](PF_6)_2$ in acetonitrile as a reference.[12] Emission was not observed from either dimer in solution at room temperature.

Electrochemistry and Spectroelectrochemistry

The electrochemical data is summarized in Table IV.2. All reduction and oxidation values correspond to fully reversible, one-electron processes. Oxidation of the monomer at 1.68 V *vs.* NHE is assigned to the $Ru^{III/II}$ couple, while its reduction at -1.38 V is assigned to the formation of the tpy anion radical.[13] A second, reversible one-electron wave observed at -1.69 V can be attributed to the reduction of the neighboring bpy ligand. These ligand-based reductions occur at similar potentials of the dimer (-1.40 V and -1.67 V). In contrast, the monomer and dimer $Ru_b^{III/II}$-imine oxidation potentials differ substantially: the latter is 380 mV lower than the former. The $Ru_a^{III/II}$-ammine potential (0.09 V) is close to that of $Ru(NH_3)_6^{3+/2+}$ in water (0.10 V).[14]

Particularly relevant to these studies are the spectral changes accompanying the dimer's oxidation and reduction. Oxidation of Ru_b bleaches the MLCT absorption. Reduction of the terpyridine ligand causes an increase in absorbance from 340-470 nm, and a slight decrease and red-shifting of the $Ru_b \rightarrow$(tpy, bpy) MLCT maximum (Figure IV.2).

Table IV.2 Electrochemical Properties of $Ru_bCNRu_a^{3+/2+}$ Complexes. All redox couples are fully reversible, one-electron processes. Values given *vs.* NHE.

Compound	$\mathbf{E_{1/2}\ Ru_b^{III/II}}$ **(V)**	$\mathbf{E_{1/2}\ Ru_a^{III/II}}$ **(V)**	$\mathbf{E_{1/2}\ Ru_a^{II/I}}$ **(V)**
$[Ru_b(bpy)(tpy)CN](PF_6)$	1.69	--	-1.39
$[(bpy)(tpy)Ru_bCNRu_a(NH_3)_5]^{n+}(PF_6)_n$	1.30	0.09	-1.40

Figure IV.2 Spectral changes accompanying the reduction of $(tpy)(bpy)Ru^{II}CNRu^{II}(NH_3)_5$ in acetonitrile.

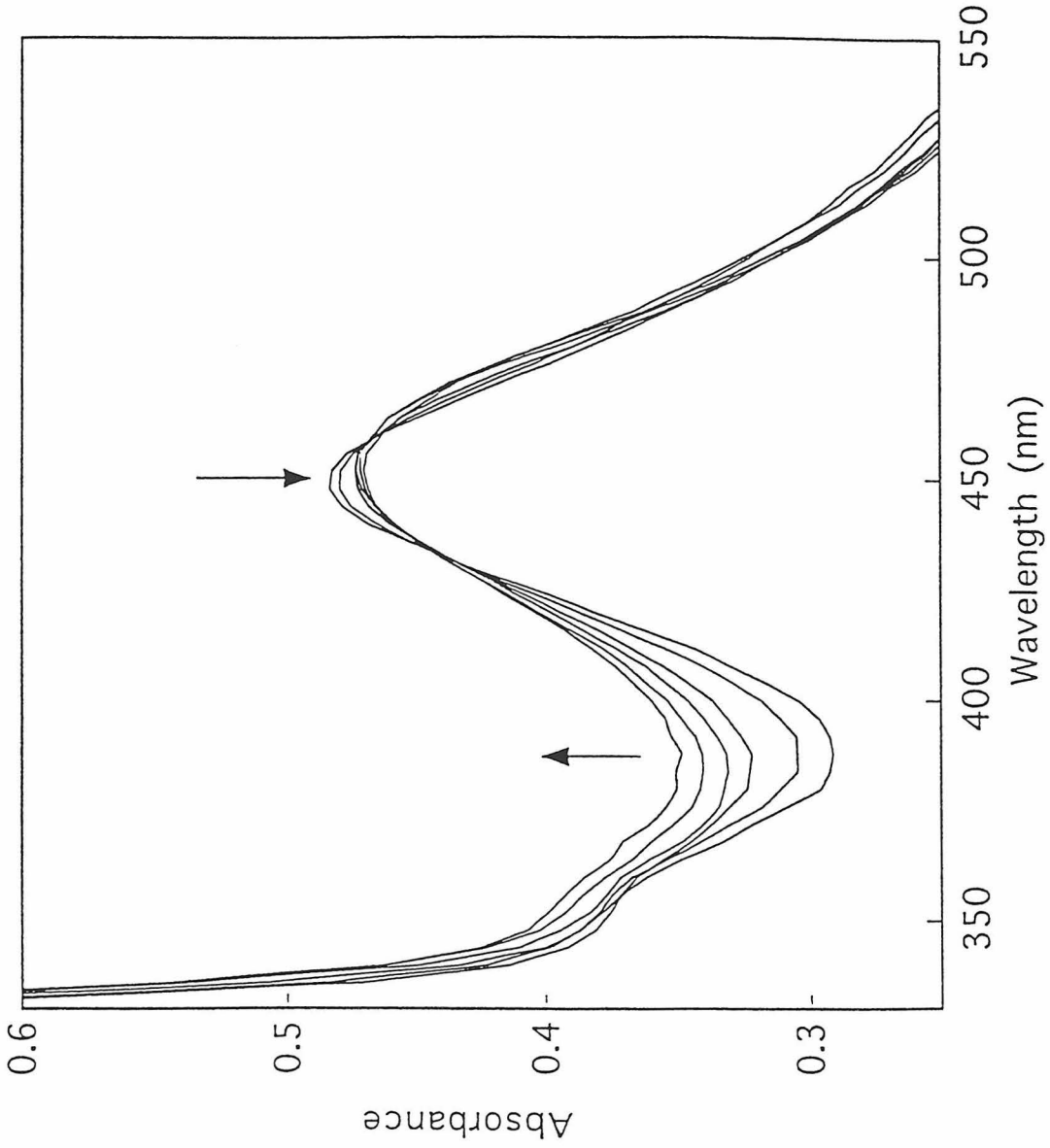
0.6
0.5
0.4
0.3
Absorbance
350
400
450
500
550
Wavelength (nm)

Picosecond Transient Absorption

Excitation of (bpy)(tpy)RuCN$^+$ at 532 nm in acetonitrile at room temperature causes bleaching of the MLCT transition and the growth of a new absorption feature that extends from 430 nm to higher energies (Figure IV.3). This is consistent with generation of a metal-to-ligand excited-state.[15] The bleach fits well to a single exponential function that decays with a lifetime of 7.7 ns, falling between the excited-state lifetimes of $Ru(bpy)_3^{2+}$ (600 ns)[12] and $Ru(tpy)_2^{2+}$ (0.25 ns).[16] The increase in optical density centered near 380 nm decays at the same rate.

Because of its weak absorbance at 532 nm, the mixed-valence dimer $Ru_b^{II}CNRu_a^{III}$ was excited at 416 nm, but no measurable optical density changes occurred. Excitation into the MMCT band at 683 nm also produced no measurable transient. Convolution of our instrument response (~18 ps FWHM using 416 nm pump light) with a single exponential decay function provides an estimate of 0.1 ps for the lower limit of the MLCT excited-state lifetime.[17]

Excitation of $Ru_b^{II}CNRu_a^{II}$ at 532 nm, however, does yield a transient that is detectable with this instrument. It includes an OD increase to the blue of 440 nm which reaches a maximum near 390 nm (Figure IV.4). This feature decays with a rate of 1.16×10^{10} s^{-1}. While this transient looks similar to that of (bpy)(tpy)RuCN$^+$, comparison of the two reveals differences do exists: The monomer's OD increase appears to extend to higher energies, and the bleach of the MLCT band is more pronounced (Figure IV.5).

Figure IV.3 Transient difference spectrum of (bpy)(tpy)RuCN$^+$ in acetonitrile immediately following excitation at 532 nm (**A**). The bleach at 480 nm can be fit to a single exponential decay function with τ = 7.7 ns (**B**).

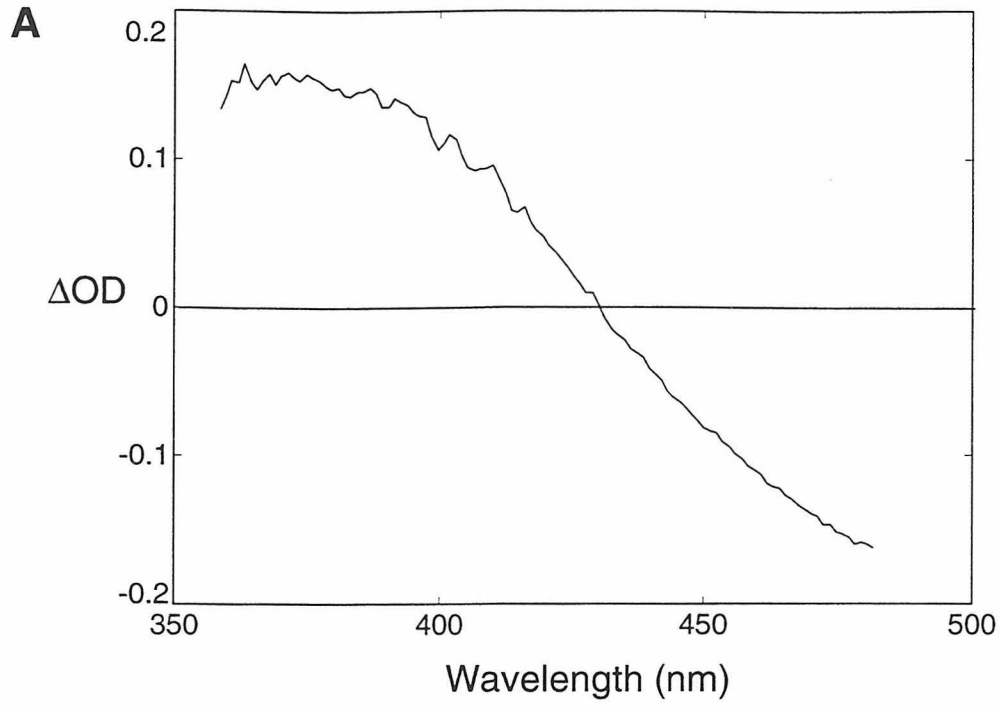
A
0.2
0.1
ΔOD
0
-0.1
-0.2
350
400
450
500
Wavelength (nm)

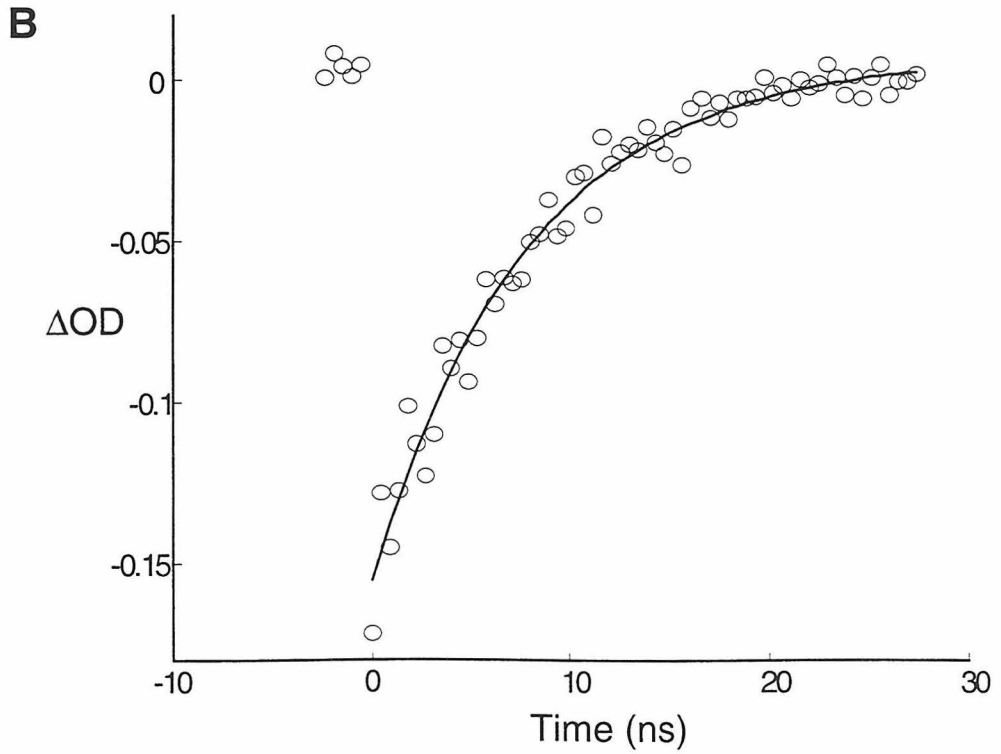
B
0
-0.05
ΔOD
-0.1
-0.15
-10
0
10
20
30
Time (ns)

Figure IV.4 Transient difference spectrum of $(tpy)(bpy)Ru^{II}CNRu^{II}(NH_3)_5]^{2+}$ in acetonitrile following excitation at 532 nm (**A**). Its decay can be fit (at 411 nm) to a single exponential function with $k = 1.16 \times 10^{10}$ s^{-1} (**B**). The offset baseline is due to monomer impurity.

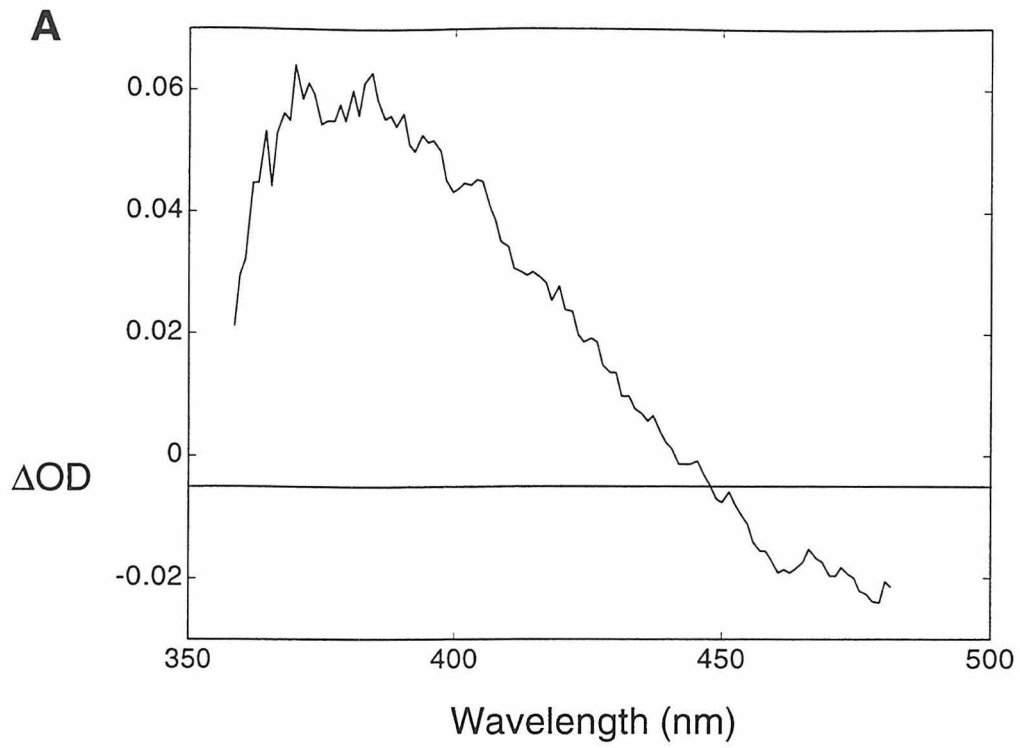
A
0.06
0.04
0.02
0
-0.02
ΔOD
350
400
450
500
Wavelength (nm)

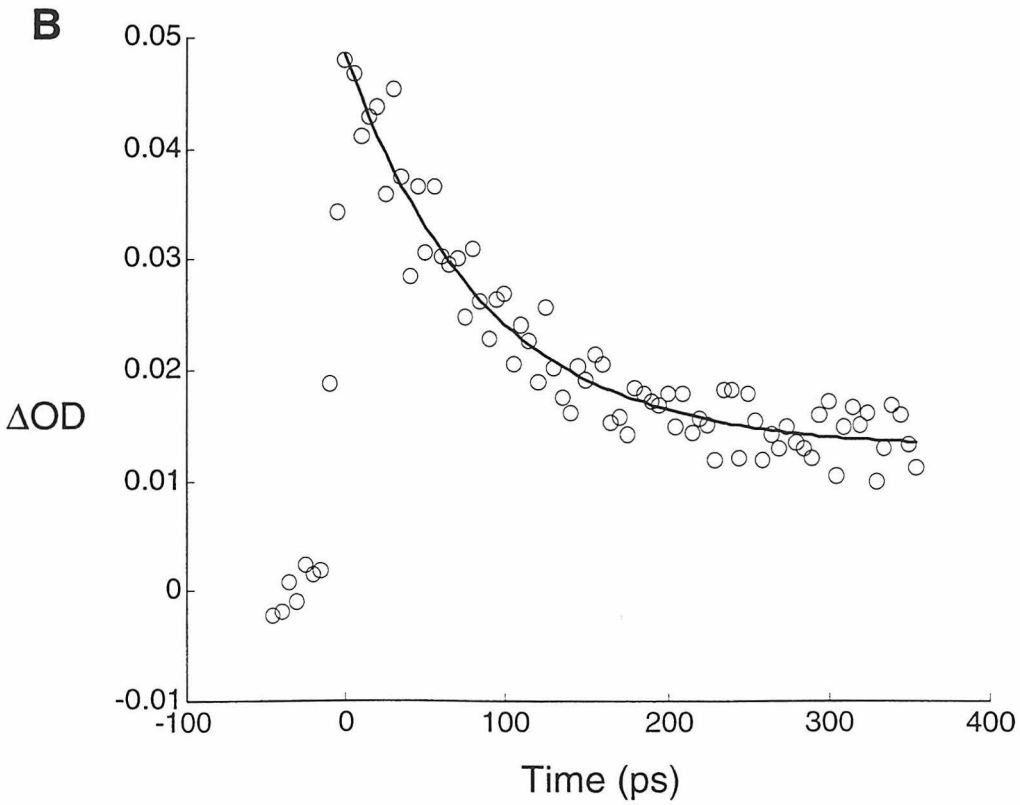
B
0.05
0.04
0.03
0.02
0.01
0
-0.01
ΔOD
-100
0
100
200
300
400
Time (ps)

Figure IV.5 A comparison of the normalized transient spectra of (bpy)(tpy)RuCN^{+} (———) and (tpy)(bpy)Ru^{II}CNRu^{II}(NH$_3$)$_5$]$^{2+}$ (------) in acetonitrile following 532 nm excitation.

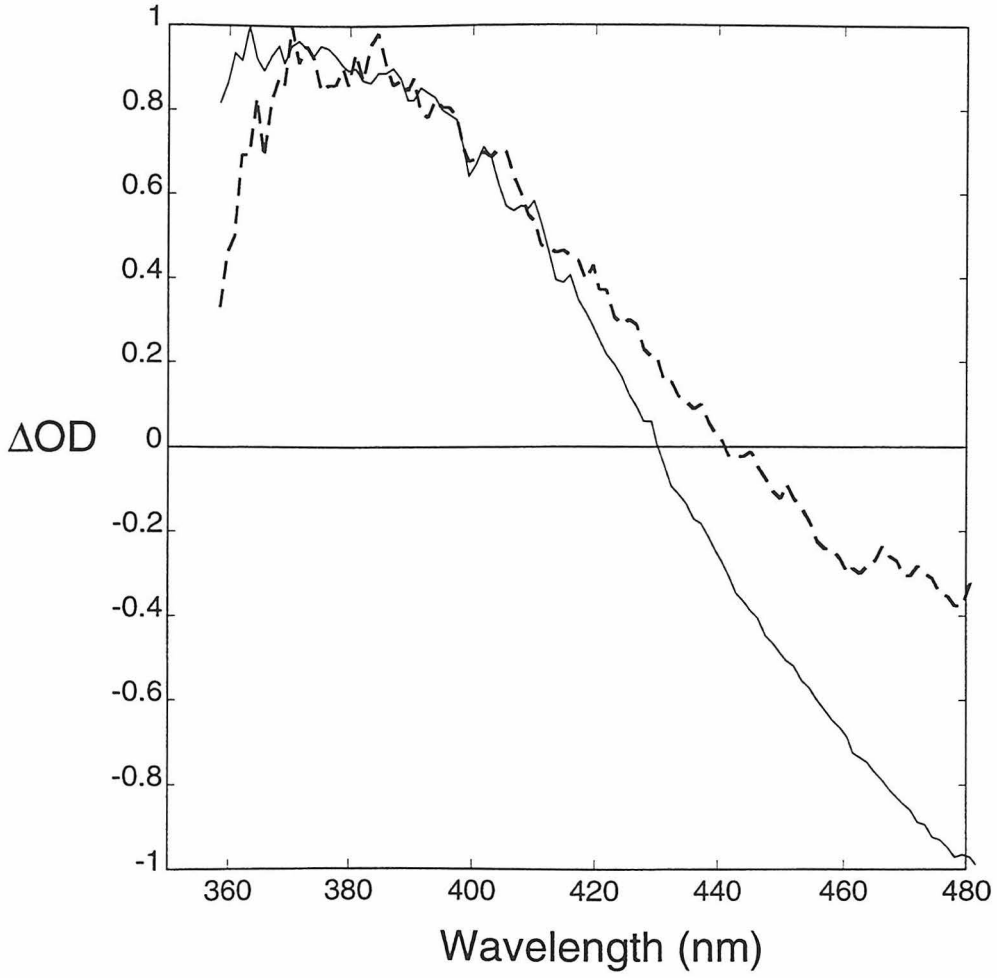
1
0.8
0.6
0.4
0.2
0
-0.2
-0.4
-0.6
-0.8
-1
ΔOD
360
380
400
420
440
460
480
Wavelength (nm)

Discussion

The broad 717 nm absorption feature in the ground-state spectrum of $[(tpy)(bpy)Ru^{II}CNRu^{III}(NH_3)_5]^{3+}$ has been assigned to the $Ru_b^{II} \rightarrow Ru_a^{III}$ charge-transfer band.[18] Its analysis provides information about the coupling strength and reorganization energy of this reaction. The energy of the MMCT absorption maximum is related to the energy difference between $Ru_b^{II}CNRu_a^{III}$ and $Ru_b^{III}CNRu_a^{II}$ by:[4]

Equation IV.1 $$E_{op} = \Delta E_0 + \lambda$$

The electochemical data provides an estimate for E_0 of 1.21 eV, so that $\lambda \approx 0.52$ eV. The inner sphere component can be estimated from studies of the electron self-exchange reactions of Ru-diimine and Ru-ammine complexes:[19] $\lambda_{in} \approx 0.8$ eV. Hush theory also provides an estimate for H_{AB}:

Equation IV.2 $$H_{AB} = \sqrt{\frac{E_{OP}\Delta\nu_{1/2}\varepsilon_{max}}{2380r^2}}$$

The crystal structure of the mixed-valence dimer provides a value for the metal-metal distance $r = 5.11$ Å (Figure IV.6). With the intensity ε_{max} and width $\Delta\nu_{1/2}$ of the charge-transfer band, an approximate electronic-coupling strength of 2000 cm^{-1} is obtained. This large value indicates electron-transfer reactions will occur in the adiabatic limit. Compounds with similar values of H_{AB} have been shown to be valence-trapped (Robin and Day class II) species.[20]

Figure IV.6 ORTEP of $(tpy)(bpy)Ru^{II}CNRu^{III}(NH_3)_5]^{3+}$.

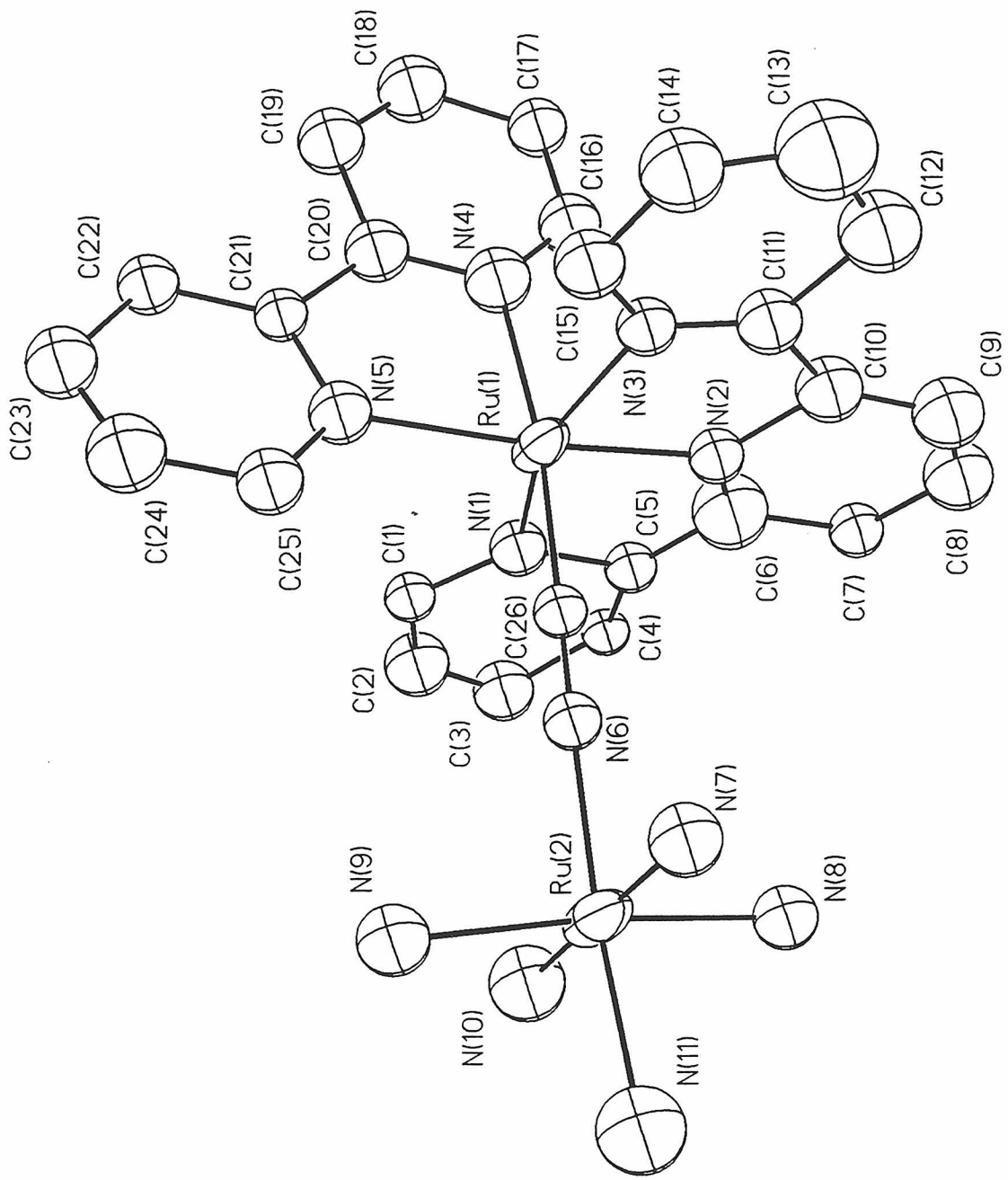
C(18)
C(19)
C(17)
C(14)
C(13)
C(16)
C(12)
C(22)
C(20)
N(4)
C(21)
C(11)
C(15)
C(10)
C(9)
C(23)
N(5)
Ru(1)
N(3)
N(2)
C(24)
C(25)
C(1)
N(1)
C(5)
C(6)
C(7)
C(8)
C(2)
C(26)
C(4)
C(3)
N(6)
N(7)
N(9)
Ru(2)
N(8)
N(10)
N(11)

Excitation of the $Ru_b^{II} \rightarrow$imine charge transfer within both $Ru_b^{II}CNRu_a^{III}$ and $Ru_b^{III}CNRu_a^{II}$ can initiate intramolecular ET reactions. Two of these involve $Ru^{II} \rightarrow Ru^{III}$ processes (**2** and **3** in Figure IV.7), and two can be described as tpy•- $\rightarrow Ru^{III}$ reactions (**1** and **4**). The rate constants for both **1** and **2** are probably greater than 1×10^{12} s^{-1}, since no transient were observed following excitation of the mixed-valence dimer. Excitation of $Ru_b^{II}CNRu_a^{II}$, however, produces a transient similar to the difference spectrum obtained from the compound's one-electron, tpy-based reduction (Figure IV.2). This most likely corresponds to the formation of $[(bpy)(tpy•-)Ru^{II}CNRu^{III}(NH_3)_5]^{2+}$. From this assignment, we can infer that reaction **3** has a rate constant of greater than 1×10^{12} s^{-1}, and that reaction **4** occurs at a rate of 1.16×10^{10} s^{-1}.

Both of the $Ru^{II} \rightarrow Ru^{III}$ reactions (**2** and **3**) lie deep within the Marcus inverted region ($-\Delta G° > \lambda \approx 0.60$ eV). The driving force for **2** is estimated to be 1.21 eV from the electrochemical data, while that for **3** is approximately 0.88 eV. Despite this value, the rates of these processes are too fast to measure with our experiment. Classical electron-transfer theory thus does not appear suitable for the modeling of their behavior, in agreement with the findings of others.[8,9] Calculations using Equation I.6, in which reactant/product coupling is allowed to occur *via* a high frequency C≡N stretching mode, do produce values greater than 1×10^{12} s^{-1}.[10]

The outer-sphere reorganization energy for the transfer of an electron from the tpy anion to Ru_a^{III} is certainly different from the value obtained from the MMCT absorption feature of $Ru_b^{II}CNRu_a^{III}$, as it occurs over a greater distance. Differences in λ_{in} are certain as well, since the tpy ring must undergo distortion upon reduction.

Figure IV.7 Kinetic schemes for intramolecular electron-transfer reactions within $(tpy)(bpy)Ru^{II}CNRu^{III}(NH_3)_5]^{2+}$ (**A**) and $(tpy)(bpy)Ru^{II}CNRu^{II}(NH_3)_5]^{3+}$ (**B**) following Ru→imine excitation.

A

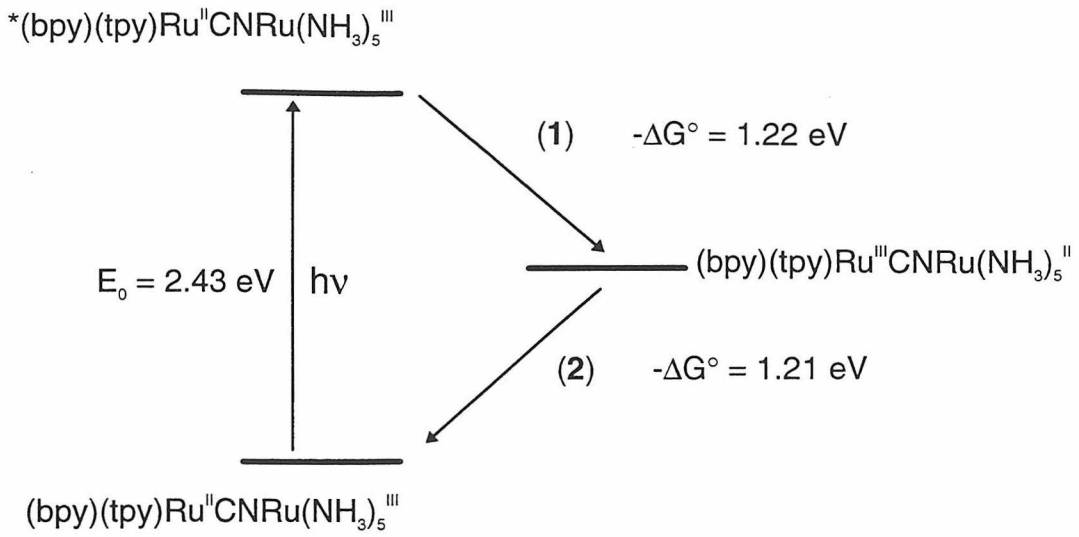
*(bpy)(tpy)Ru^{II}CNRu(NH$_3$)$_5^{III}$
(1) -ΔG° = 1.22 eV
E$_0$ = 2.43 eV
hν
(bpy)(tpy)Ru^{III}CNRu(NH$_3$)$_5^{II}$
(2) -ΔG° = 1.21 eV
(bpy)(tpy)Ru^{II}CNRu(NH$_3$)$_5^{III}$

B

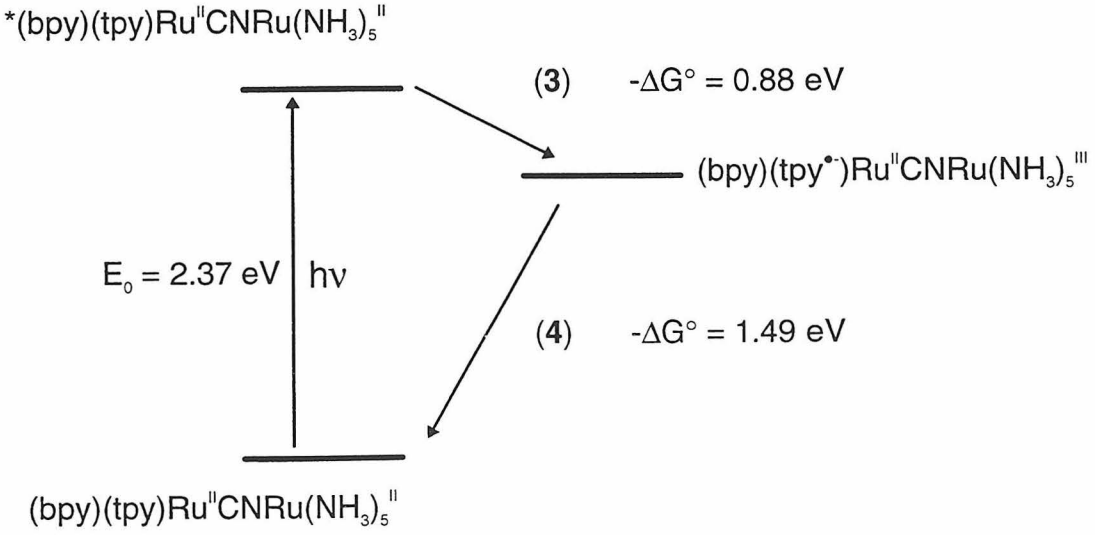
*(bpy)(tpy)Ru^{II}CNRu(NH$_3$)$_5^{II}$
(3) -ΔG° = 0.88 eV
(bpy)(tpy$^{\bullet-}$)Ru^{II}CNRu(NH$_3$)$_5^{III}$
E$_0$ = 2.37 eV
hν
(4) -ΔG° = 1.49 eV
(bpy)(tpy)Ru^{II}CNRu(NH$_3$)$_5^{II}$

This energy should be similar to that associated with the MLCT excited-state formation of $Ru(bpy)_3^{2+}$, which has been determined to be 0.17 eV.[21] Calculation of λ_{out} is difficult given the compound's irregular cavity shape, but if an increase of 0.2 eV is assumed, the total reorganization energy associated with ET from tpy•- to Ru_a^{III} is estimated to be approximately 0.89 eV. It is clear that reaction **4** in Figure IV.7 is still highly inverted.

With values for H_{AB} (2000 cm^{-1}), $\Delta G°$ (1.49 eV) and λ (0.89), classical electron-transfer theory predicts a rate of 4.8×10^{10} s^{-1} for the charge-recombination within $[(bpy)(tpy•-)Ru^{II}CNRu^{III}(NH_3)_5]^{2+}$. Consideration of the high frequency mode described above only increases this rate, which is already four times greater than the one which was measured. A plausible explanation for these differences may be that H_{AB} is significantly smaller for reaction **4** than it is for reactions **1-3**. At this time, it is unclear why this may be the case.

Conclusion

Although others have shown that ET following excitation of the metal-to-metal charge-transfer band in strongly coupled mixed-valence dimers occurs in femptoseconds, we have found that excitation of the $Ru_b^{II} \rightarrow$immine charge-transfer band of $[(tpy)(bpy)Ru^{II}CNRu^{II}(NH_3)_5]^{2+}$ forms an excited-state that decays on the picosecond timescale. An explanation for this may be that the electronic coupling between the terpyridinine anion and oxidized ammine-bound metal of the excited-state is much smaller than the metal-metal coupling in the mixed-valence analogue.

REFERENCES AND NOTES

[1] Creutz, C.; Taube, H. *J. Am. Chem. Soc.* **1969**, *91*, 3988.

[2] Marcus, R. A.; Sutin, N. *Biochim. Biophys. Acta* **1985**, *811*, 265: Closs, G. L.; Miller, J. R. *Science* **1988**, *240*, 440: Jordan, K. D.; Paddon-Row, M. N. *Chem. Rev.* **1992**, *92*, 395.

[3] Mulliken, R. S. *J. Am. Chem. Soc.* **1952**, *64*, 811: Mulliken, R. S.; Person, W. B. Molecular Complexes. Wiley: New York. **1969**.

[4] Hush, N. S. *Electrochim. Acta* **1968**, *13*, 1005.

[5] Stein, C. A. and Taube H. *J. Am. Chem. Soc.* **1970**, *103*, 615.

[6] Stein C. A.; Lewis N. A.; Seitz G. *J. Am. Chem. Soc.* **1982**, *104*, 2596.

[7] Sutton, J. E.; Taube, H. *Inorg. Chem.* **1981**, *20*, 3125: Yeh, A.; Haim, A. *Inorg. Chim. Acta* **1979**, *33*, 51: Aquino, M. A. S.; Lee, F. L.; Gabe, E. J.; Bensimon, C.; Greedan, J. E.; Crutchley, R. J. *J. Am. Chem. Soc.* **1992**, *114*, 5130.

[8] Reid, P. J.; Silva, C.; Barbara, P. F.; Karki, L.; Hupp, J. T. *J. Phys. Chem.* **1995**, *99*, 2609.

[9] Doorn, S. K.; Stoutland, P. O.; Dyer, R. B.; Woodruff, W. H. *J. Am. Chem. Soc.* **1992**, *114*, 3133.

[10] Ponce, A.; Bachrach, M.; Winkler, J. R. (submitted for publication, 1995).

[11] Gagne, R. R.; Kovaland, C. A.; Lisensky, G. C. *Inorg. Chem.* **1980**, *19*, 2855.

[12] Caspar, J. V. and Meyer, T. J. *J. Am. Chem. Soc.* **1983**, *105*, 5583.

[13] Belser, P.; Von-Zelewsky, A.; Juris, A.; Barigellettiand, F.; Balzani, V. *Gazz. Chim. Ital.* **1985**, *115*, 723.

[14] Ford, P. C. *Coord. Chem. Rev.* **1970**, *5*, 75.

[15] Sutin, N.; Creutz, C. in Inorganic and Organometallic Photochemistry, Wrighton, M. S. ed. American Chemical Society: Washington, D.C. **1978**.

[16] Blair, D. F.; Gellesand, J.; Chan, S. I. *Biophys. J.* **1986**, *50*, 713.

[17] This is assuming a 0.005 ΔOD detection limit.

[18] Altabef, A. B.; DeGallo, S. B. R.; Folquerand, M. E.; Katz, N. E. *Trans. Met. Chem.* **1993**, *18*, 319.

[19] Brown, G. M.; Sutin, N. *J. Am. Chem. Soc.* **1979**, *101*, 883.

[20] Katz, N. E.; Creutz, C.; Sutin, N. *Inorg. Chem.* **1988**, *27*, 1687.

[21] Sutin, N.; Brunschwig, B. S.; Creutz, C.; Winkler, J. R. *Pure Appl. Chem.* **1988**, *60*, 1817.

Chapter V

Intramolecular Electron-Transfer in Strongly Coupled Metallocene-Based Donor-Acceptor Systems

Introduction

Although there have been few detailed studies of electron-transfer within strongly coupled donor-acceptor complexes, tremendous effort has been directed at understanding what factors affect the nonlinear optical properties (NLO) of similar materials. NLO materials come in a variety of forms, including inorganic or organometallic crystals, semiconductors,[1] doped glasses,[2] polymers[3] or poled polymers.[4] The distribution of charge within these is sensitive to electromagnetic fields in such a way that they can become active in harmonic generation and frequency summing. While the effect light has on the charge distribution within many of these materials is best considered on a macroscopic level, some materials' NLO properties depend on the nonlinear properties of the individual molecules they contain. In particular, some contain molecules composed of covalently coupled electron donor-acceptor moieties. The higher order optical properties of these molecules have been shown to depend on the donors and acceptors, and the electronic coupling between them.

A great deal of work has attempted to quantitatively relate the polarizabilities of molecules to their NLO behavior, but no effort -- until now -- has been made to understand how nonlinear optical properties are affected by molecules' optically induced excited-states. Linear and nonlinear optical effects are considered by the same theory, summarized briefly here.

A low intensity electric field E induces a dipole μ in an atom or molecule by an amount dependent on its linear polarizability α:

Equation V.1 $\mu = \alpha E$

This varies with the electric field if the field oscillates. The polarization P of a bulk material in an electric field is similarly expressed in terms of its linear polarization susceptibility χ:[5]

Equation V.2 $P = \chi E$

When a molecule is exposed to very intense electric fields, such as those within laser pulses, its polarizability is no longer linearly dependent on E, and is expressed as:

Equation V.3 $P = \alpha E + \beta E^2 + \gamma E^3 + \cdots$

Now, in addition to its linear polarizability, the distribution of electrical charge within the molecule is a function of the first hyperpolarizability β, which leads to second order effects, the second hyperpolarizability γ, which leads to third order effects, and to even higher order terms. The optical properties of bulk materials are described by an analogous expression in which P_0 is the sample's static dipole:

Equation V.4 $P = P_0 + \chi^{(1)}E + \chi^{(2)}E^2 + \chi^{(3)}E^3 + \cdots$

The susceptibility of charge distribution to E is now described with the linear tensor $\chi^{(1)}$, quadratic tensor $\chi^{(2)}$, cubic tensor $\chi^{(3)}$, and so on. Whether or not a susceptibility is nonzero depends on the symmetry of the material, so that all even-order susceptibilities are zero for centrosymmetric materials.

The ramifications of Equation V.4 become clear when the electric field is expressed as a plane light wave, *i.e.*, $E = E_0\cos(\omega t)$:

Equation V.5 $$P = P_0 + \chi^{(1)}E_0\cos(\omega t) + \chi^{(2)}E_0^{\,2}\cos^2(\omega t) + \chi^{(3)}E_0^{\,3}\cos^3(\omega t) + \cdots$$

which can be expanded to yield:

Equation V.6 $$P = (P_0 + \tfrac{1}{2}\chi^{(2)}E_0^{\,2}) + \chi^{(1)}E_0\cos(\omega t) + \tfrac{1}{2}\chi^{(2)}E_0^{\,2}\cos^2(2\omega t) + \cdots$$

Now, it is clear that the polarization of the material consists of a frequency doubled component, meaning that two photons of frequencies ω can combine to generate one with a frequency 2ω. Similar effects occur at higher orders, so that light pulses with high intensities can be frequency doubled in materials with suitable values of $\chi^{(2)}$, tripled in materials with suitable values of $\chi^{(3)}$, and so on. Additional effects, such as frequency summing, are also possible.

Inorganic crystals such as $LiNbO_3$, $LiTaO_3$ and potassium titanyl phosphate are routinely used in laser experiments to generate harmonics and sums of laser pulses (see Chapter II). There is also great potential for the use of NLO materials in other, more common, applications.[6]

One example comes from optical communications.[7] Much of the electrical wire used in telecommunications is being replaced by fiber optics, which offer lower noise and substantially higher data transmission bandwidths. Currently, the control of optical signals is achieved with a combination of semiconductor lasers and electronic detectors, amplifiers and switches. Replacement of these electronic parts with materials that can act as switches by changing their optical characteristics

upon the absorption of light, or which can be used to amplify or change the frequencies of input light, would greatly increase communication speeds. Applications such as this continue to spur the development of new NLO materials. Desired are ones with large values of $\chi^{(2)}$ and $\chi^{(3)}$, and good mechanical properties.

To produce nonlinear optical materials with varied mechanical properties, research has turned from simple crystals and polymers to small synthetic molecules that can be embedded within polymers. Studies have focused on the factors that affect molecular hyperpolarizabilities which, in turn, affect bulk susceptibilities. For example, Marder and coworkers have established a relationship between α, β and γ, and the chemical and electronic structures of organic polymethine dyes.[8] These dyes are composed of an electron donating group covalently bound by a polyene bridge to an accepting group. Their study has shown that quantitative relationships between a molecule's structure and NLO properties can be drawn.

From this and other work, it is now accepted that in order for a material to have a large second-order hyperpolarizability, it must:[5] 1) be easily polarizable, 2) have an asymmetric charge distribution and 3) a π-conjugated electron pathway. Much of the work done to quantify these criteria has utilized organic molecules, but some organometallic complexes also have significant nonlinear properties. Of them, the iodide salt of (*E*)-1-ferrocenyl-2-(1-methyl-4-pyridinium)ethylene has the largest second harmonic generation value measured to date (Figure V.1).[9] This finding led to the synthesis and characterization of a wide variety of metallocene-based compounds, some containing chiral groups to ensure noncentrosymmetric crystallization.[10] It also prompted theoretical efforts to explain their behavior.[11,12]

Figure V.1 These metallocene compounds show large nonlinear optical susceptibilities.

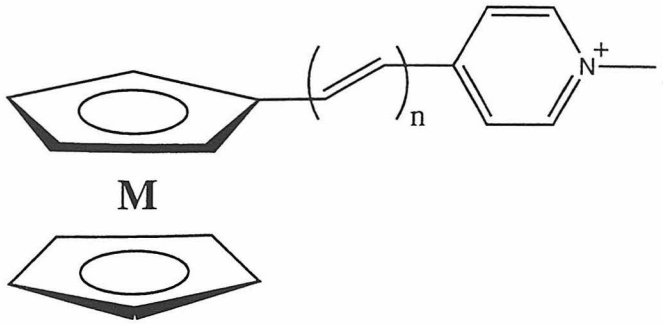
M
n
N+

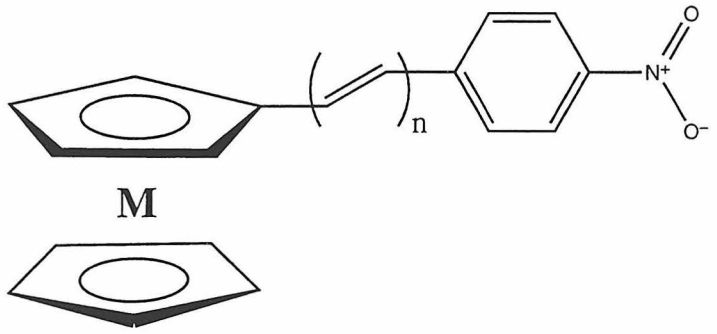
M
n
N+
O
O-

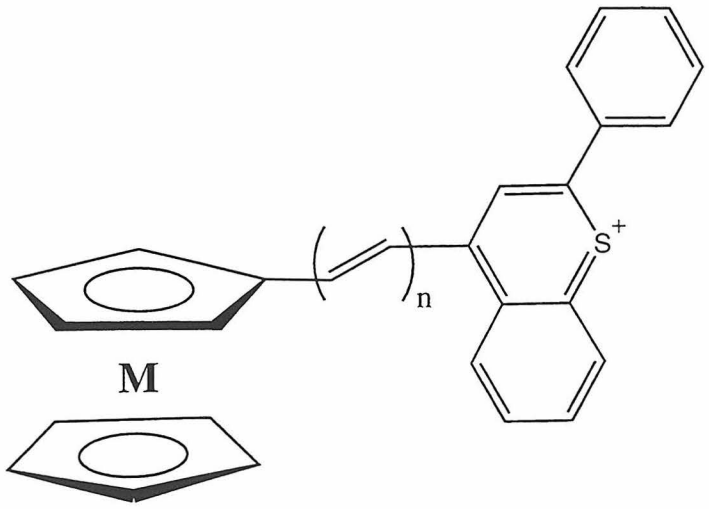
M
n
S+

In one notable attempt made by Kanis and coworkers, ZINDO calculations are used to explain both the linear and nonlinear optical properties of the organometallic chromophores.[12] Although the calculations provide estimates of NLO properties that are in reasonable agreement with those obtained by experiment, they fail to provide accurate values for the energies of the two major optical transitions characteristic of these compounds. In the ferrocene compound mentioned above, these features are found at approximately 375 nm ($\varepsilon \approx 22{,}000$ $M^{-1}cm^{-1}$) and 580 nm ($\varepsilon \approx 6{,}000$ $M^{-1}cm^{-1}$). Furthermore, the calculated oscillator strengths of the compounds' lower energy transition are in disagreement with experiment by over two orders of magnitude. Ignoring conventional wisdom, the authors assign the higher energy band to an MLCT transition, and the lower energy one to a ligand-field transition. They then continue to use the results of their calculations to draw a correlation between the molecules' structures and hyperpolarizabilities.

We have endeavored to prove the erroneous nature of their conclusions for two reasons. First, to simply provide an accurate understanding of these compounds, and second, to form a firm basis upon which studies of their excited-states can be conducted.

The metallocene compounds shown in Figure V.1 can be effective in the study of intramolecular electron-transfer. Both the metal and electron acceptor moieties can be altered to vary the driving force of the charge separation and recombination reactions that may occur upon optical excitation. The polyene bridge between then can be varied in a number of ways to affect the donor-acceptor

coupling. Several compounds with different isomers (*Z* and *E*) and lengths of polyene bridges have already been synthesized. Alkyne-based compounds have also been made. Approaches have been developed for the synthesis of other bridges, such as chalcones, allowing facile control over donor-acceptor coupling and detailed study of the regime between the weak and strong coupling limits.

Clearly, these molecules have great potential for the study of intramolecular charge-transfer reactions. Of equal interest, however, is that if electron-transfer does occur upon their optical excitation, ET theory can be used to help understand how such factors as H_{AB} and ΔG° affect α, β and γ. Work has addressed how the molecular hyperpolarizabilities are affected by a molecule's ground-state polarization: We have begun work that may eventually establish how molecular excited-state dynamics affect NLO properties. We have assigned the optical absorption features of these metallocenes, and then studied how they change upon the molecules' optical excitation.

Experimental

In the following text, the compounds will be abbreviated by D(n)(A) in which D = Fc (ferrocene) or Rc (ruthenacene), n is the number of ethylene groups in the spacer, and A is the acceptor. Unless noted, the compounds are all *E* isomers. So, Fc(1)(*N*-methylpyridinium) is short for (*E*)-1-ferrocenyl-2-(1-methyl-4-pyridinium)ethylene, and *cis*-Fc(1)(4-nitrophenyl) is short for (*Z*)-1-ferrocenyl-2-(4-nitrophenyl)ethylene.

Steady-state absorption spectra were obtained with the same equipment described in Chapter III, and electrochemical and spectroelectrochemical experiments were performed in a manner similar to that described in Chapter IV. The description of the transient absorption experiment is provided in Chapter II.

Synthesis

All the compounds were prepared in the labs of Dr. Seth Marder by Dr. Chin-Ti Chen. Their synthesis is based on previously published work.[9,13]

Resonance Raman

Resonance Raman experiments were conducted with the same apparatus described in Chapter III. Here, the samples were excited either with the 501.7 nm line of a Coherent Innova 70 argon ion laser, or with the 532 nm mode-locked output of a Coherent Antares 76 Nd:YAG laser. Non-resonance Raman experiments were conducted in the labs of Professor Giuseppe Zerbi at the Politecnico di Milano by Dr. Anna Gussoni.

Photolysis

The 514 nm line of a Coherent Innova 70 argon ion laser was used for the photolysis experiments. Samples were dissolved in either degassed spectroscopic grade methanol or degassed anhydrous ethanol.

Results

Steady-state Absorption

The absorption spectra of these metallocene compounds are dominated by two strong features. Their energies and intensities depend on the metal (iron or ruthenium), the electron acceptor, the length and type of spacer and the solvent in which the compounds are dissolved.

Shown in Figure V.2 are the spectra of the Fc(1)(A) compounds as a function of electron acceptor. As the acceptor becomes easier to reduce, the band in the red moves to lower energy and gains in intensity: In methylene chloride, Fc(1)(4-nitrophenyl) λ_{max} = 500 nm ($\varepsilon \approx 4{,}900\ M^{-1}cm^{-1}$), Fc(2)(*N*-methylpyridinium) λ_{max} = 580 nm ($\varepsilon \approx 6{,}000\ M^{-1}cm^{-1}$) and Fc(1)(2-phenylthioflavone) λ_{max} = 925 nm ($\varepsilon \approx 20{,}000\ M^{-1}cm^{-1}$). The higher energy band follows the same trend: Fc(1)(4-nitrophenyl) λ_{max} = 360 nm ($\varepsilon \approx 17{,}500\ M^{-1}cm^{-1}$), Fc(1)(*N*-methylpyridinium) λ_{max} = 375 nm ($\varepsilon \approx 22{,}000\ M^{-1}cm^{-1}$) and Fc(1)(2-phenylthioflavone) λ_{max} = 525 nm ($\varepsilon \approx 32{,}500\ M^{-1}cm^{-1}$). It should be noted that the feature in the absorption spectrum of the last compound centered near 385 nm ($\varepsilon \approx 16{,}000\ M^{-1}cm^{-1}$) is a localized 2-phenylthioflavone transition.

Changing the metal from iron to ruthenium also has a dramatic effect on the compounds' spectra, moving the blue band to higher energy and weakening its intensity (Figure V.3). In contrast, the energy of the red band increases substantially while gaining in intensity by close to a factor of two. The high and low energy bands almost appear as one in Rc(1)(4-nitrophenyl).

Figure V.2 The absorption spectra of the (*E*)-1-ferrocenyl-2-(A)ethylene compounds as a function of the acceptor in methylene chloride: (**A**) A = 2-phenylthioflavone and (**B**) A = 4-nitrophenyl.

A

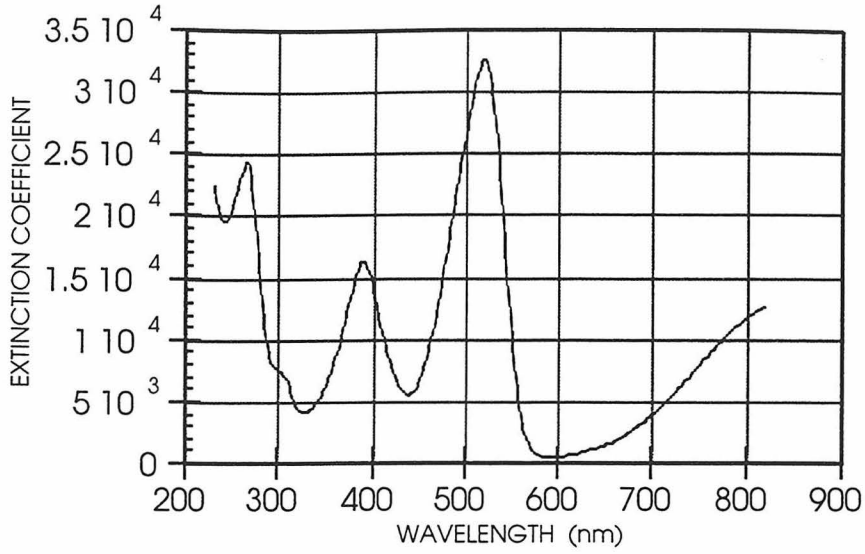
EXTINCTION COEFFICIENT
3.5 10 4
3 10 4
2.5 10 4
2 10 4
1.5 10 4
1 10 4
5 10 3
0
200
300
400
500
600
700
800
900
WAVELENGTH (nm)

B

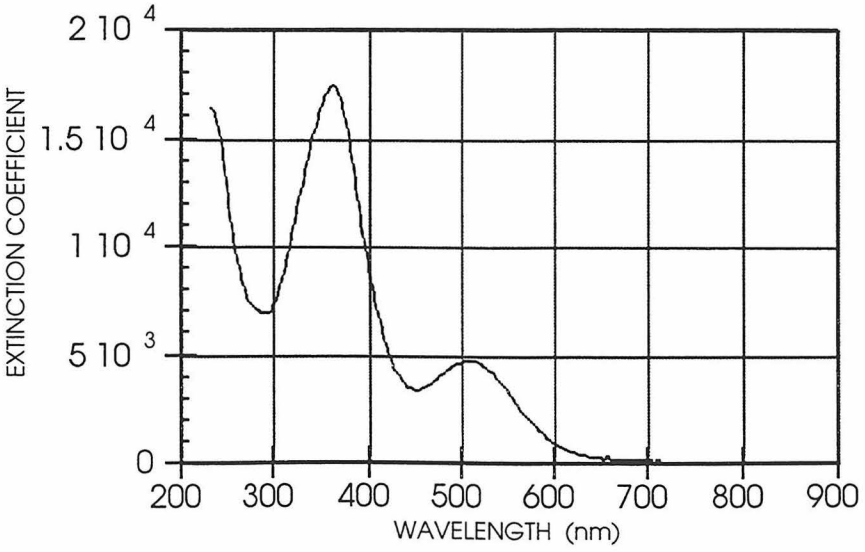
EXTINCTION COEFFICIENT
2 10 4
1.5 10 4
1 10 4
5 10 3
0
200
300
400
500
600
700
800
900
WAVELENGTH (nm)

Figure V.3 The absorption spectra of the (*E*)-1-D-2-(4-nitrophenyl)ethylene compounds in methylene chloride as a function of the donor D: (**A**) D = ruthenacene and (**B**) D = ferrocene.

A

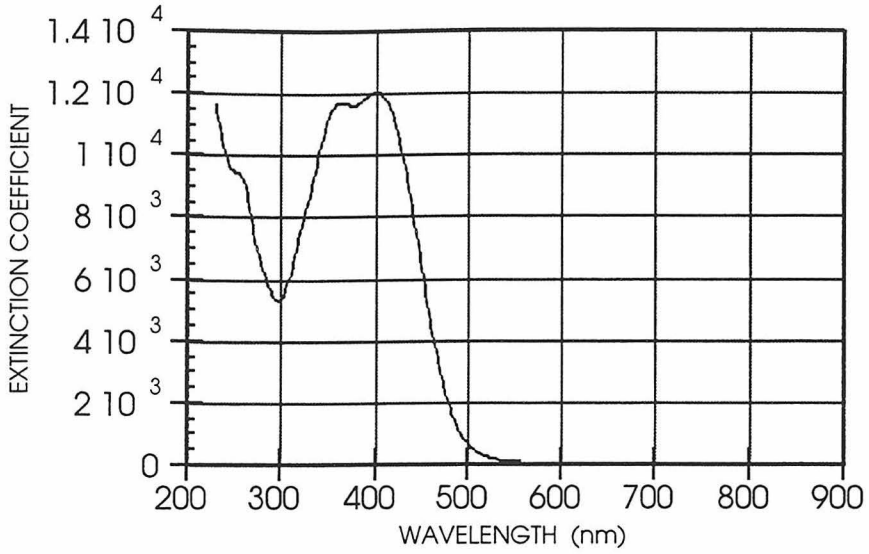
EXTINCTION COEFFICIENT
1.4 10 4
1.2 10 4
1 10 4
8 10 3
6 10 3
4 10 3
2 10 3
0
200
300
400
500
600
700
800
900
WAVELENGTH (nm)

B

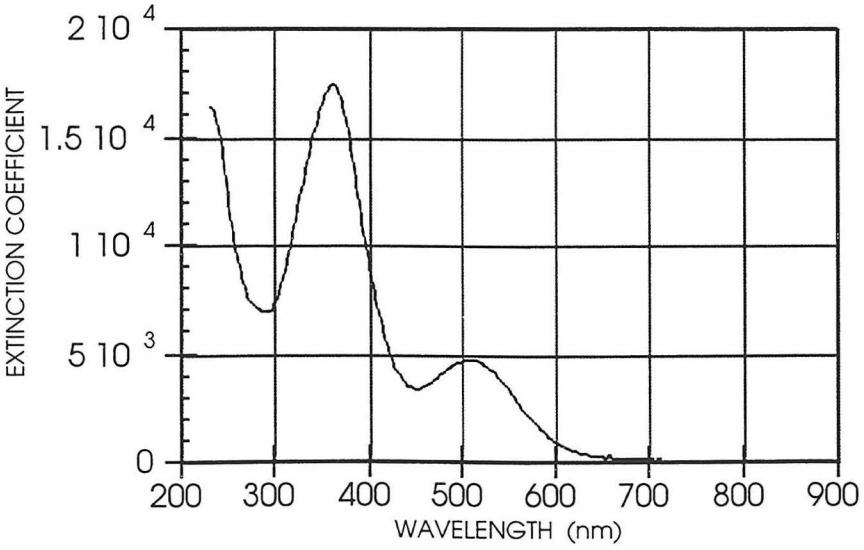
EXTINCTION COEFFICIENT
2 10 4
1.5 10 4
1 10 4
5 10 3
0
200
300
400
500
600
700
800
900
WAVELENGTH (nm)

A third spectroscopic trend is solvatochromism. Both bands shift to lower energy as the solvent polarity is increased (Figure V.4). On a wavelength scale, the red band appears to move more than the blue, but in fact the energy of the latter is more susceptible to the dielectric of its environment.

Finally, the compounds' spectra depend highly on the bridge connecting their donors and acceptors (Figure V.5). For example, as the number of ethylene groups *n* in Fc(*n*)(*N*-methylpyridinium) is increased from 1 to 3, the blue band moves to lower energies and gains intensity: λ_1 = 375 nm ($\varepsilon \approx$ 22,000 $M^{-1}cm^{-1}$), λ_2 = 410 nm ($\varepsilon \approx$ 23,000 $M^{-1}cm^{-1}$) and λ_3 = 430 nm ($\varepsilon \approx$ 33,000 $M^{-1}cm^{-1}$). The lower energy band also gains intensity, but its energy does not change.

Electrochemistry and Spectroelectrochemistry

The reduction potentials of the compounds are shown in Table V.1. All are characterized by an oxidation that can be assigned to the $Fe^{III/II}$ couple,[14] and a reduction probably due to that of the electron acceptor or the acceptor/bridge π system. Only the 4-nitrophenyl compounds undergo reversible reduction. The pyridinium complexes most likely undergo dimerization upon reduction,[15] and the same may occur to the 2-phenylthioflavone compounds.

Oxidation of Fc(1)(4-nitrophenyl) in acetonitrile appears to form a single product (Figure V.6). Its absorption at 355 nm bleaches, and two absorption bands in the visible form: The first has an extinction coefficient somewhat larger than the bleaching band, and is centered near 420 nm. The second is broader and weaker,

Figure V.4 The absorption features in the optical spectrum of (*E*)-1-ferrocenyl-2-(4-nitrophenyl)ethylene shift to lower energy as the dielectric of the solvent is increased (hexane *vs.* DMF). Similar behavior is observed for all the metallocene compounds.

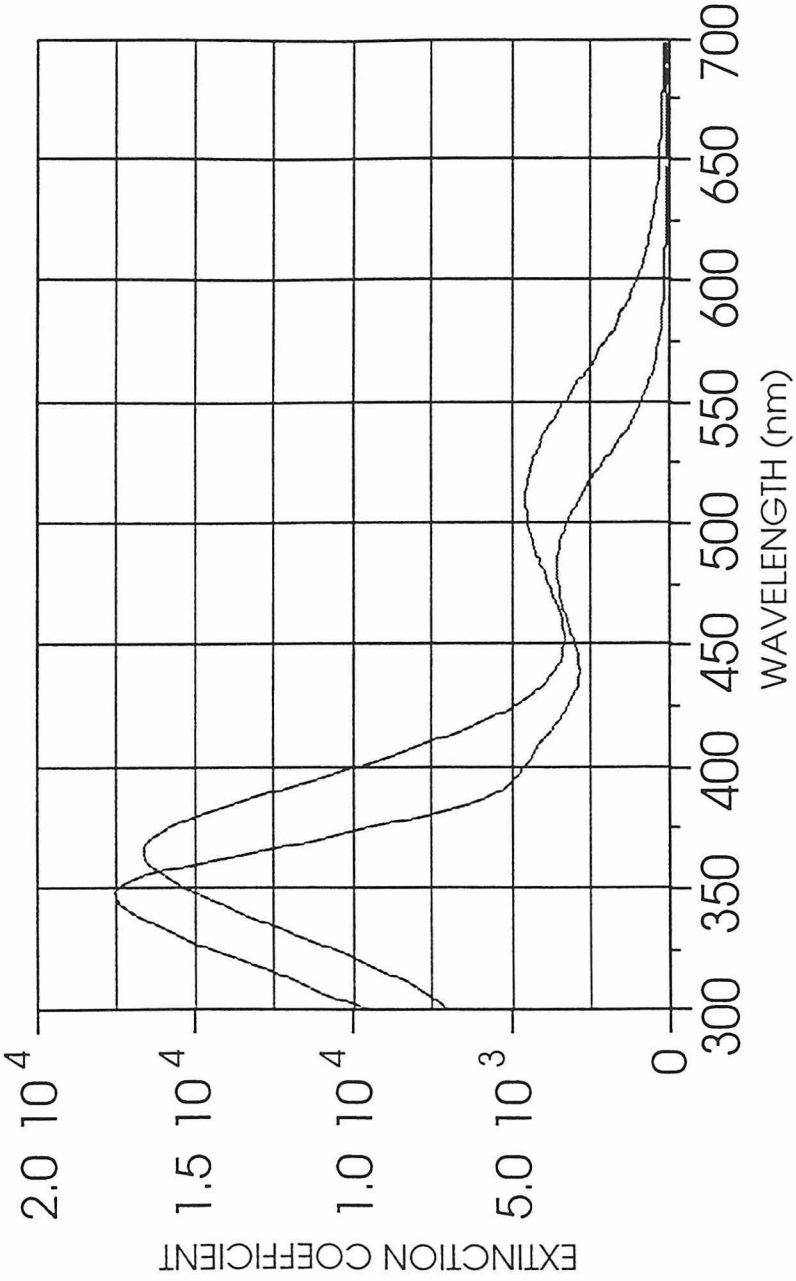
EXTINCTION COEFFICIENT
2.0 10^4
1.5 10^4
1.0 10^4
5.0 10^3
0
300
350
400
450
500
550
600
650
700
WAVELENGTH (nm)

Figure V.5 The absorption spectra of the ferrocene/*N*-methylpyridinium compounds change dramatically as the length of the polyene spacer increase from $n = 1$ (———) to $n = 2$ (— —) to $n = 3$ (---------).

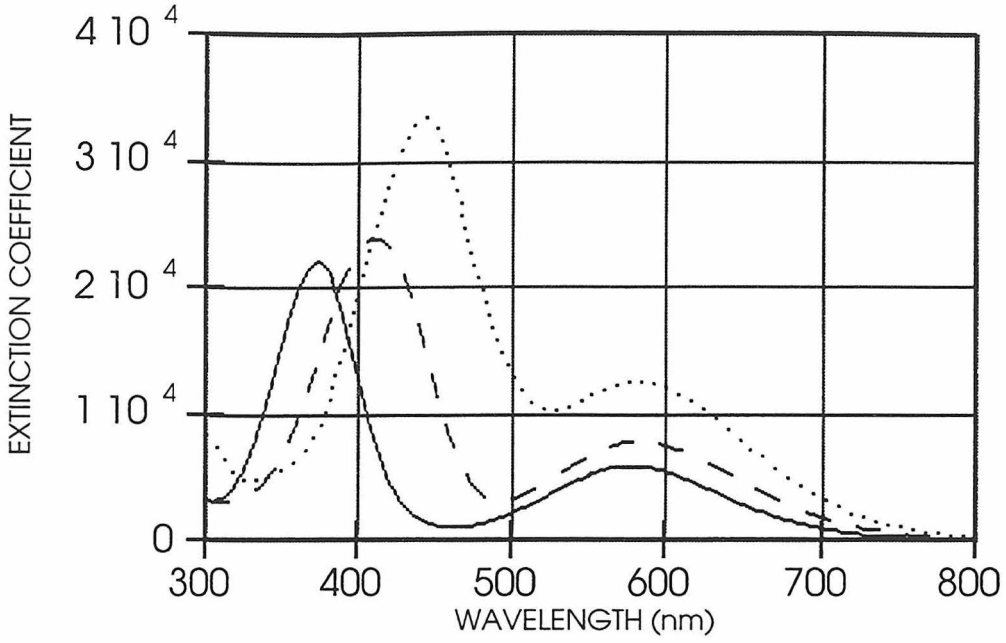
4 10 4
3 10 4
2 10 4
1 10 4
0
EXTINCTION COEFFICIENT
300
400
500
600
700
800
WAVELENGTH (nm)

Table V.1 Reduction potentials of the ferrocene-based compounds.

X	*n*	$Fe^{III/II}$ (V) [1]	Red 1 (V) 1	Red 2 (V) 1
N-Methyl Pyridinium	1	0.52	-1.15 [2]	--
"	2	0.39	-1.05 2	--
"	3	0.42	-0.98 2	--
4-Nitrophenyl	1	0.44	-1.12	-1.89 2
Thioflavin	1	0.63	-0.16	-2.16 2

[1] Versus SCE.

[2] Irreversable.

Figure V.6 Changes in the optical absorption spectrum of (*E*)-1-ferrocenyl-2-(4-nitrophenyl)ethylene in acetonitrile upon oxidation at +1 V *vs* SCE.

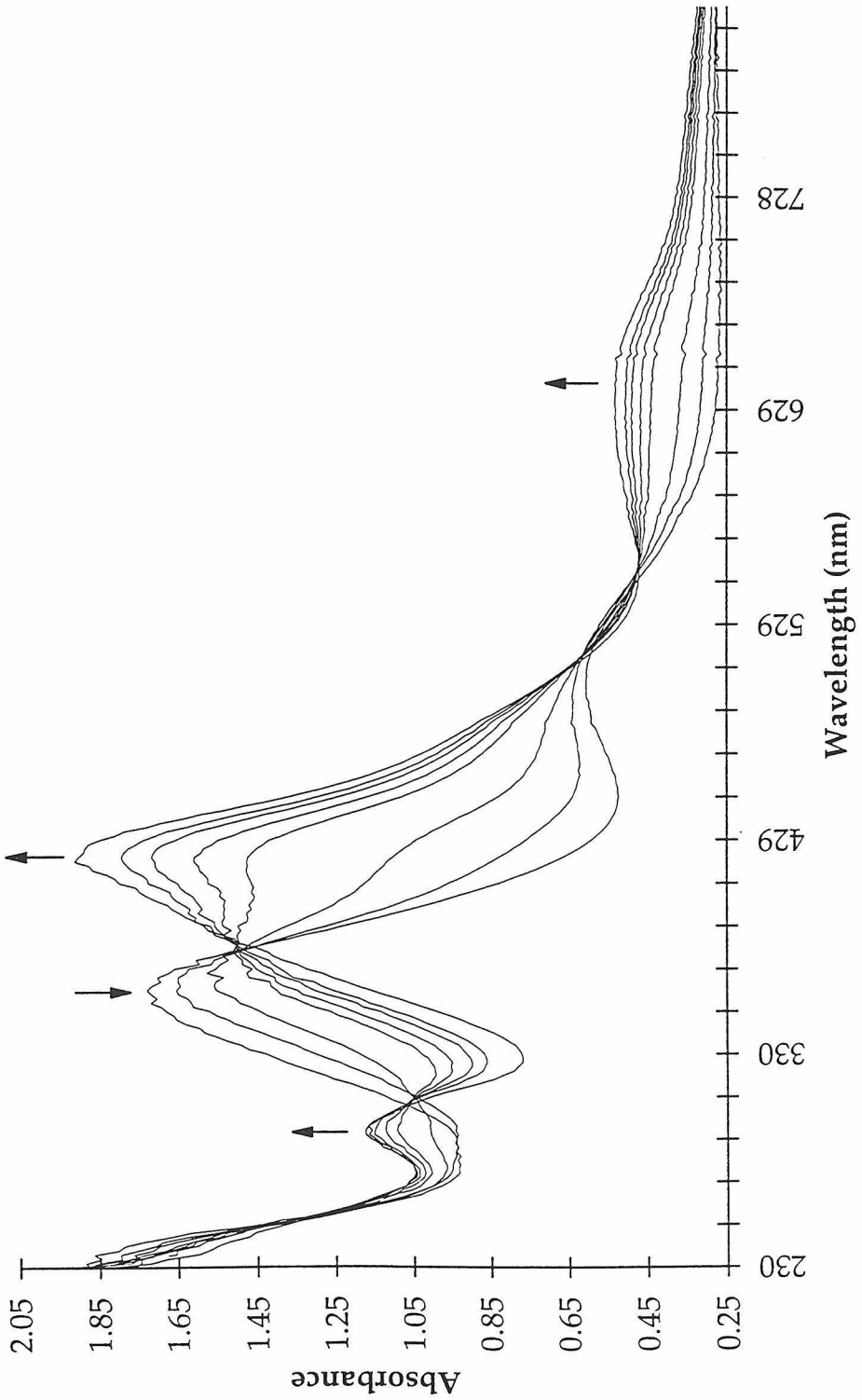
Absorbance
2.05
1.85
1.65
1.45
1.25
1.05
0.85
0.65
0.45
0.25
230
330
429
529
629
728
Wavelength (nm)

with a maximum near 640 nm. The latter can be assigned to the lower symmetry analogue of the ligand-to-metal $^2E_{2g} \rightarrow {}^2E_{1u}$ transition within ferrocinium.[16]

Resonance Raman

Numerous bands in the Raman spectrum of Fc(1)(*N*-methylpyridinium) are enhanced when it is excited at 532 nm. The resonance spectrum can be compared to that of *N*-ethyl 4-phenylpyridinium iodide (Figure V.7). The 441.6 nm excitation used to obtain the latter is in resonance with the iodide-to-pyridinium charge-transfer band, so that the spectrum provides information about changes in the cation's nuclear coordinates upon reduction.[17] It is of great interest to note that both share a feature at 1225 cm^{-1} and possibly at ~1525 cm^{-1}. In addition, the strong feature at 1296 cm^{-1} in the *N*-ethyl pyridinium spectrum may correspond to the one found at 1285 cm^{-1} in the ferrocene compound's, as some bands should shift due to differences between the two molecules' π systems (Table V.2). That their resonance spectra share features is strong evidence that the low energy optical transition in Fc(1)(*N*-methylpyridinium) has charge-transfer character. The dependence of the band's position on the metal indicates that the charge-transfer occurs from the metal to the pyridinium.

Excitation into the low energy band of Fc(1)(4-nitrophenyl) with 501.7 nm light also yields enhanced Raman scattering (Figure V.8). The small band at 1300 cm^{-1} corresponds to one of the most intense features in the compound's nonresonance Raman spectrum, which can be assigned to the symmetric N-O

Figure V.7 The resonance Raman spectrum of (*E*)-1-ferrocenyl-2-(*N*-methylpyridinium)ethylene in CH_3CN excited at 532 nm (**A**) can be compared to that of 4-phenylpyridinium iodide in CD_3CN excited at 441.6 nm (**B**).

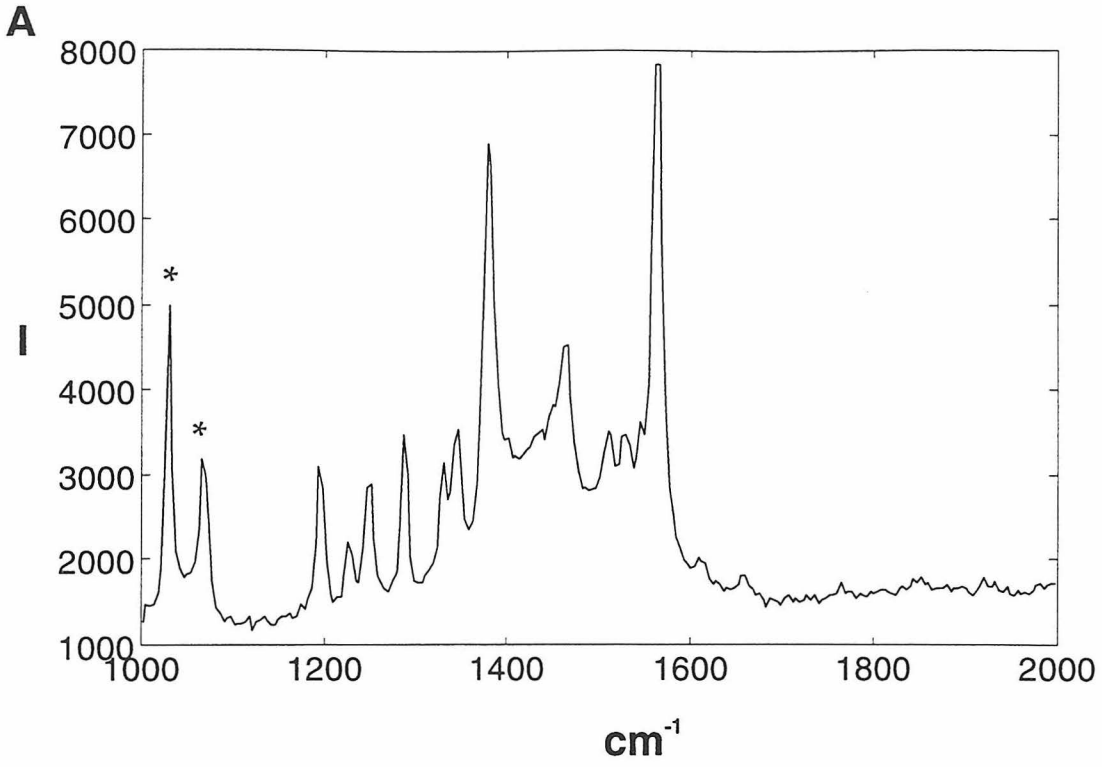
A
8000
7000
6000
5000
4000
3000
2000
1000
I
*
*
1000
1200
1400
1600
1800
2000
cm-1

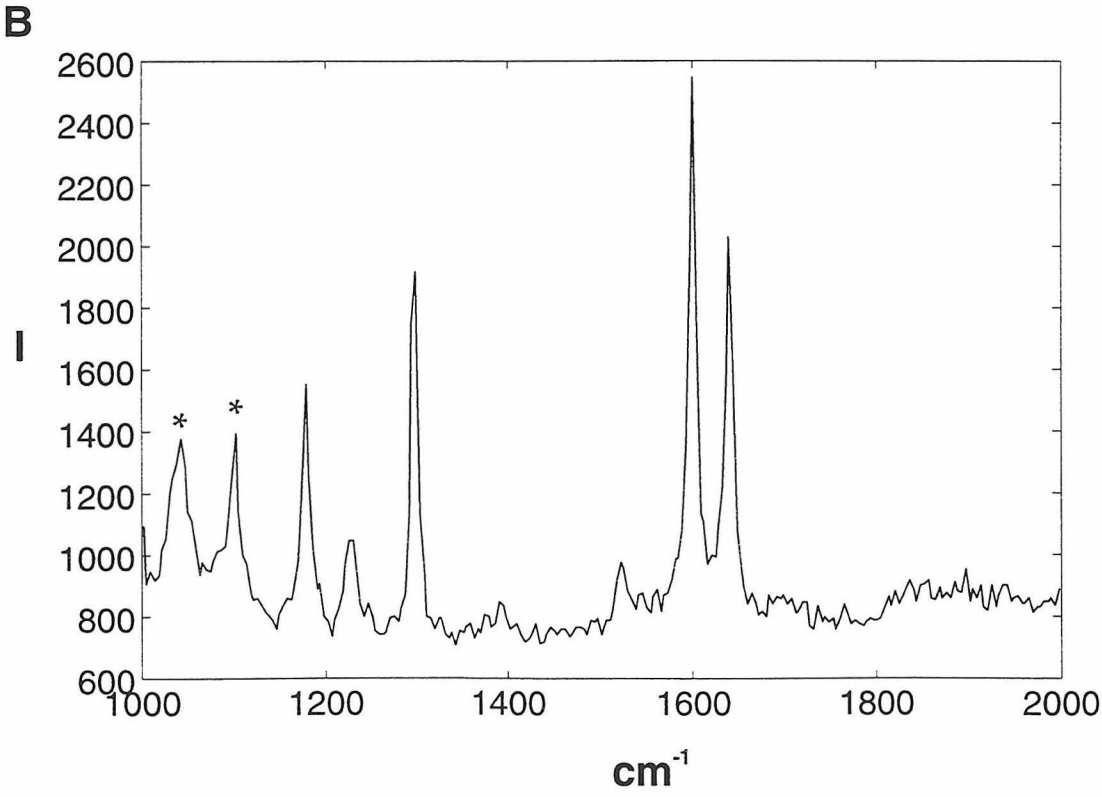
B
2600
2400
2200
2000
1800
1600
1400
1200
1000
800
600
I
*
*
1000
1200
1400
1600
1800
2000
cm-1

Table V.2 Fc(2)(*N*-methylpyridinium) in acetonitrile resonance Raman data (λ_{ex} = 532 nm).

Raman Shift (cm^{-1})	Approximate Intensity
1194	3000
1225	2050
1247	3000
1285	4000
1329	3050
1343	3500
1379	7000
1463	4500
1513	3500
1527	3500
1563	8000

Figure V.8 The resonance Raman spectrum of (*E*)-1-ferrocenyl-2-(4-nitrophenyl)ethylene in CH_3CN excited at 501.7 nm shows a feature at 1300 cm^{-1} that is one of the strongest of those within the compound's nonresonance spectrum.

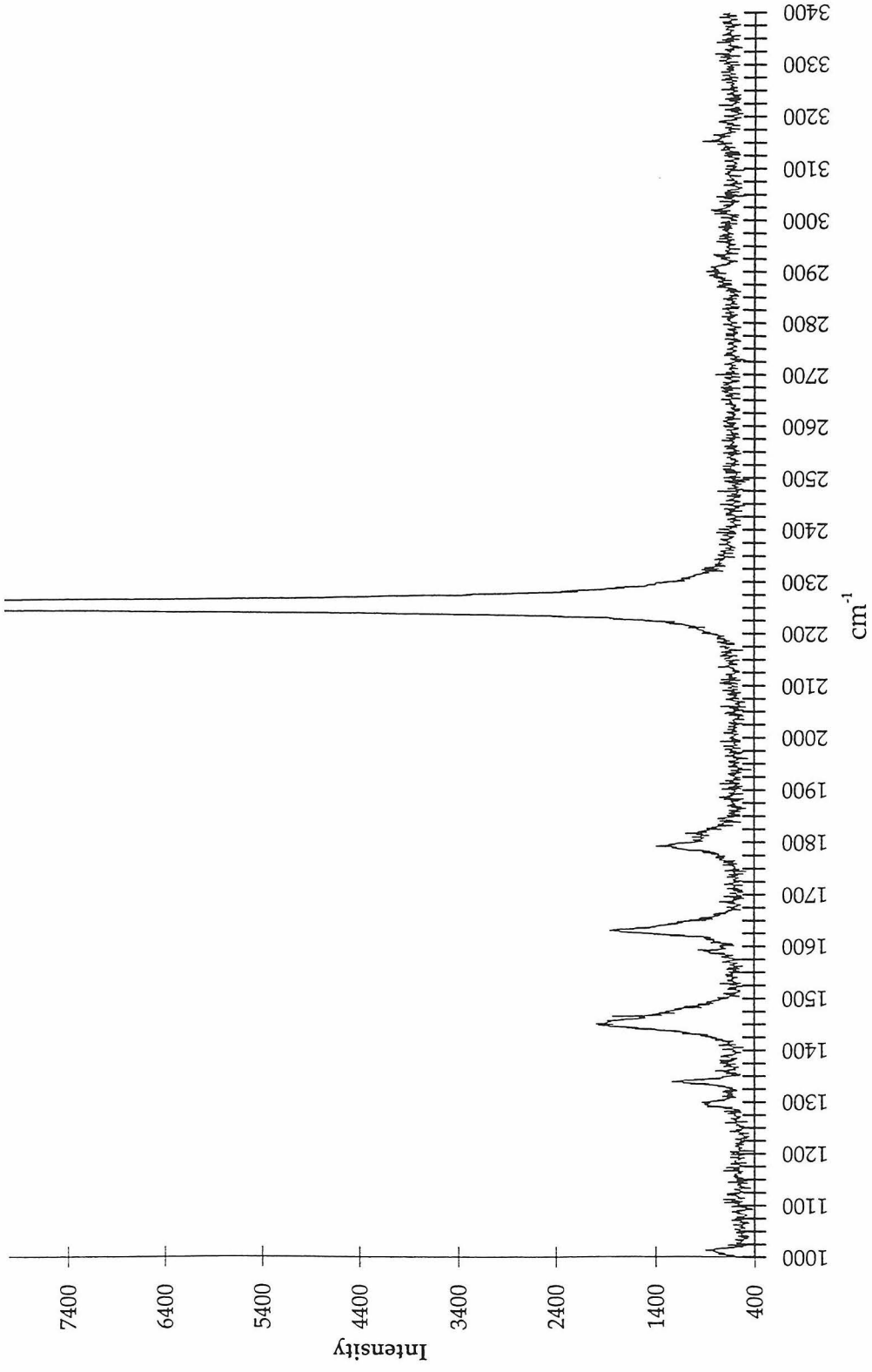
Intensity
7400
6400
5400
4400
3400
2400
1400
400
1000
1100
1200
1300
1400
1500
1600
1700
1800
1900
2000
2100
2200
2300
2400
2500
2600
2700
2800
2900
3000
3100
3200
3300
3400
cm-1

stretch (Table V.3).[18] It is very likely that this enhancement is due to the transfer of charge from the iron to the nitrophenyl moiety.

Photolysis

During an unsuccessful Raman experiment, it was found that room temperature irradiation of Fc(1)(*N*-methylpyridinium) at 514 nm in methanol or ethanol causes the compound's rapid and irreversible degradation. Spectra of the reaction mixture taken over the course of photolysis indicate that no long-lived intermediates are formed prior to product formation.

Although no attempt was made to characterize the product, two factors indicate it is a product of the complex and solvent molecules. First, its spectrum differs with the nature of the alcohol solvent (Figure V.9). Second, it does not form in acetonitrile. The Fc(1)4-nitrophenyl compound does not show any reactivity under the same conditions, indicating the reaction probably involves the highly reactive pyridinyl anion, instead of the cyclopentadienyl rings, which can react with alcohols under UV irradiation.[19] Photolyses of the longer polyene-bridged ferrocene/pyridinium complexes were not attempted.

Picosecond Transient Absorption

The excited-state decay kinetics of some of the ferrocene-based compounds have been measured. They can typically be fit to the sum of two exponentials, with rate constants that differ by close to one order of magnitude (Table V.4).

Both (*E*)-1-ferrocenyl-2-(4-nitrophenyl)ethylene and 1-ferrocenyl-2-(4-nitrophenyl)ethyne were excited at 355 nm. The blue absorption feature in the

Table V.3 Fc(2)(4-nitrophenyl) in acetonitrile resonance Raman data (λ_{ex} = 501.7 nm).

Raman Shift (cm^{-1})	**Approximate Intensity**
1300	900
1341	1200
1591	900
1792	1300
1810	1100

Figure V.9 Photolysis of (*E*)-1-ferrocenyl-2-(*N*-methylpyridinium)ethylene at 514 nm yields products with absorption spectra that depend on the solvent in which the reaction took place.

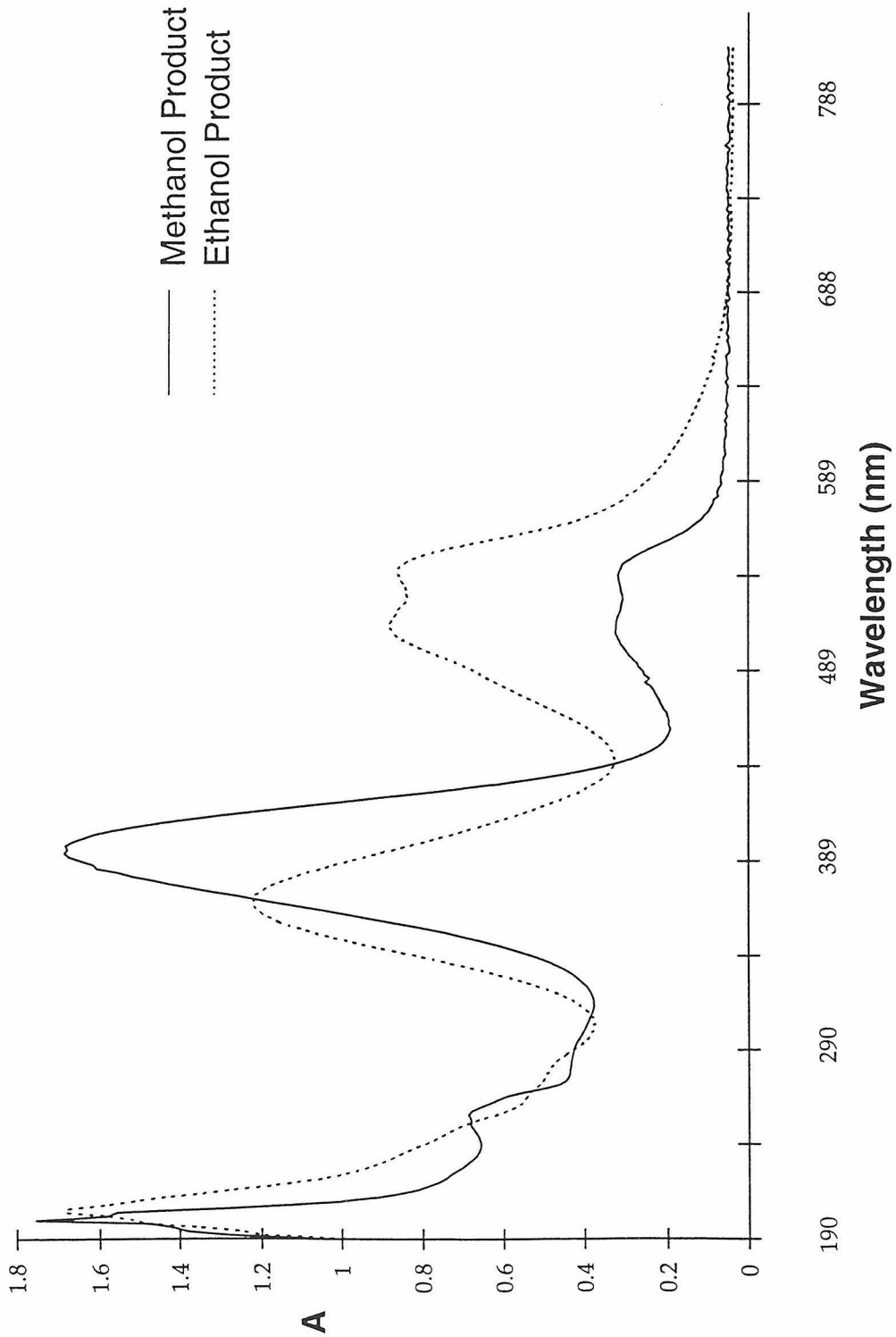
Methanol Product
Ethanol Product
A
1.8
1.6
1.4
1.2
1
0.8
0.6
0.4
0.2
0
190
290
389
489
589
688
788
Wavelength (nm)

Table V.4 Summary of transient absorption data.

Ferrocene Compound		Transient Absorption (nm)		Decay Rate / (1×10^{10} s)	
Acceptor	**Bridge**	**OD Bleach**	**OD Increase**	k_1	k_2
4-nitrophenyl *	*E*-ethylene	360	440	1.3	920
" *	ethylyne	-- †	450	-- ‡	21
N-methyl pyridinium §	*E*-ethylene	370	540	1.5	710
" §	*E,E*-1,3-butyadiene	400	650	3.1	26
" §	*E,E,E*-1,3,5-hexatriene	430	700	3.0	33

* Data acquired in acetonitrile.

† No bleach was apparent from 370 - 500 nm.

‡ Kinetics were best fit to a function containing only one exponential.

§ Data acquired in methanol.

ethylene compound's ground-state absorption spectrum bleaches upon excitation, while its optical density (OD) increases near 440 nm (Figure V.10). The decay of this feature can be fit to a biexponential function ($k_1 = 1.3 \times 10^{10}$ s^{-1} and $k_2 = 9.2 \times 10^8$ s^{-1}). By contrast, the ethyne-bridged compound shows only an OD increase between 380 nm and 500 nm, which disappears with a single rate of 2.1×10^9 s^{-1} (Figure V.11).

All three of the Fc(n)(*N*-methylpyridinium) complexes (n = 1-3) were excited at 532 nm, almost at the maximum of their red absorption features. Unfortunately, methanol solutions of the compounds were used for these experiments, as they were completed before the photochemical activity of Fc(1)(*N*-methylpyridinium) was observed. This means that while their kinetics, like the alkene-bridged 4-nitrophenyl complex, are best fit to a biexponential function, one -- or even both -- decay components may result from product formation, rather than simple non-radiative decay. Nevertheless, the transient spectra and their rates of decay are both strongly dependent on the length the polyene bridge separating the ferrocene and pyridinium moieties. The behavior of the alkene-bridged compound is particularly interesting.

Upon excitation of Fc(1)(*N*-methylpyridinium) at 532 nm, the absorption feature centered near 380 nm bleaches, and an OD increase appears to its red (Figure V.12). The exact position of its maximum is difficult to ascertain due to a lack of probe light between 500 nm and 550 nm, but it is probably close to 540 nm: The increased absorbance continues beyond 550 nm. A weak absorption feature also appears in the red: Centered near 650 nm, it decays while the stronger 540 nm

Figure V.10 Excitation of (*E*)-1-ferrocenyl-2-(4-nitrophenyl)ethylene at 355 nm yields a bleaching of its blue ground-state absorption feature and an optical-density increase centered near 440 nm (**A**). Decay of the feature monitored between 440 nm and 450 nm can be fit to a biexponential function with decay constants $k_1 = 1.3 \times 10^{10}$ s^{-1} and $k_2 = 9.2 \times 10^{8}$ s^{-1} (**B**).

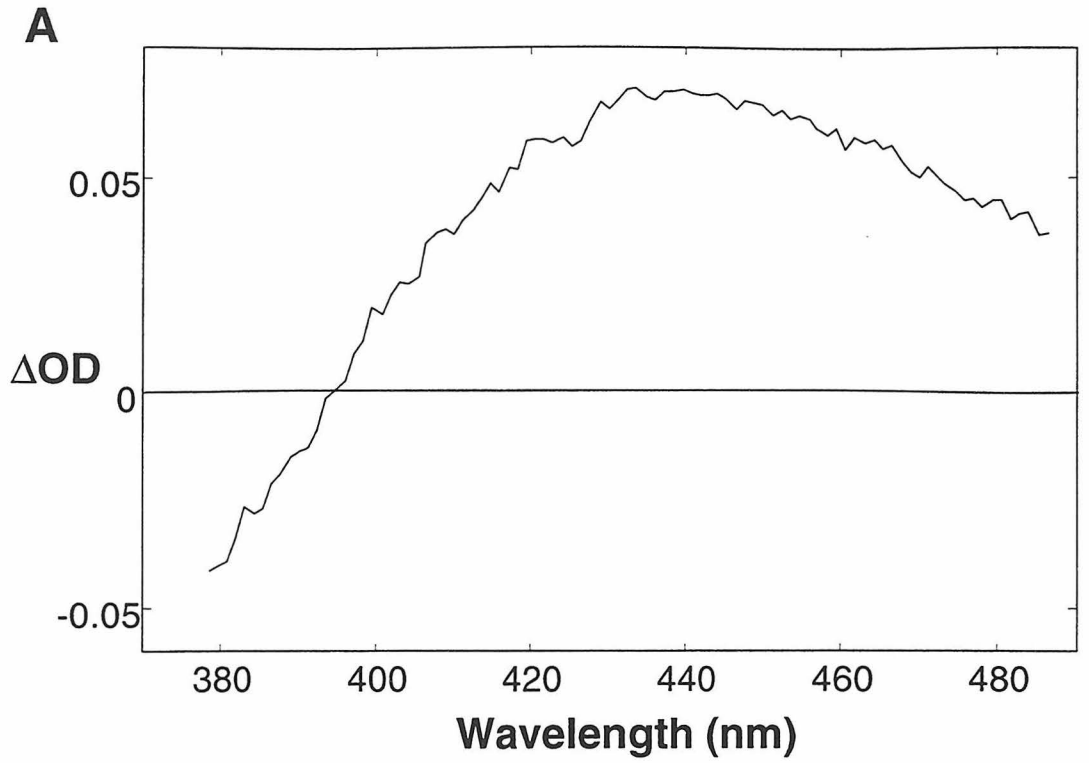
A
0.05
ΔOD
0
-0.05
380
400
420
440
460
480
Wavelength (nm)

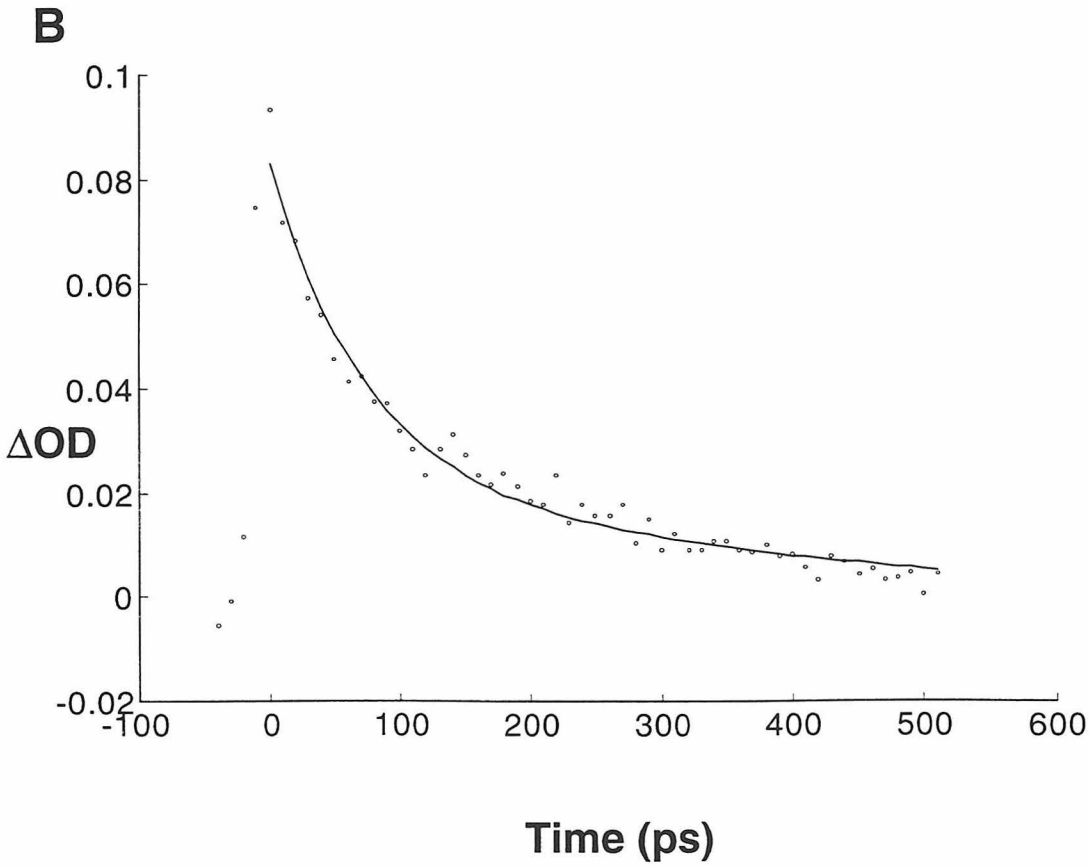
B
0.1
0.08
0.06
0.04
ΔOD
0.02
0
-0.02
-100
0
100
200
300
400
500
600
Time (ps)

Figure V.11 Excitation of 1-ferrocenyl-2-(4-nitrophenyl)ethyne at 355 nm yields an optical-density increase centered near 440 nm (**A**). Decay of the feature monitored between 440 nm and 450 nm can be fit to an exponential function with a decay constant $k = 2.1 \times 10^9\ s^{-1}$ (**B**).

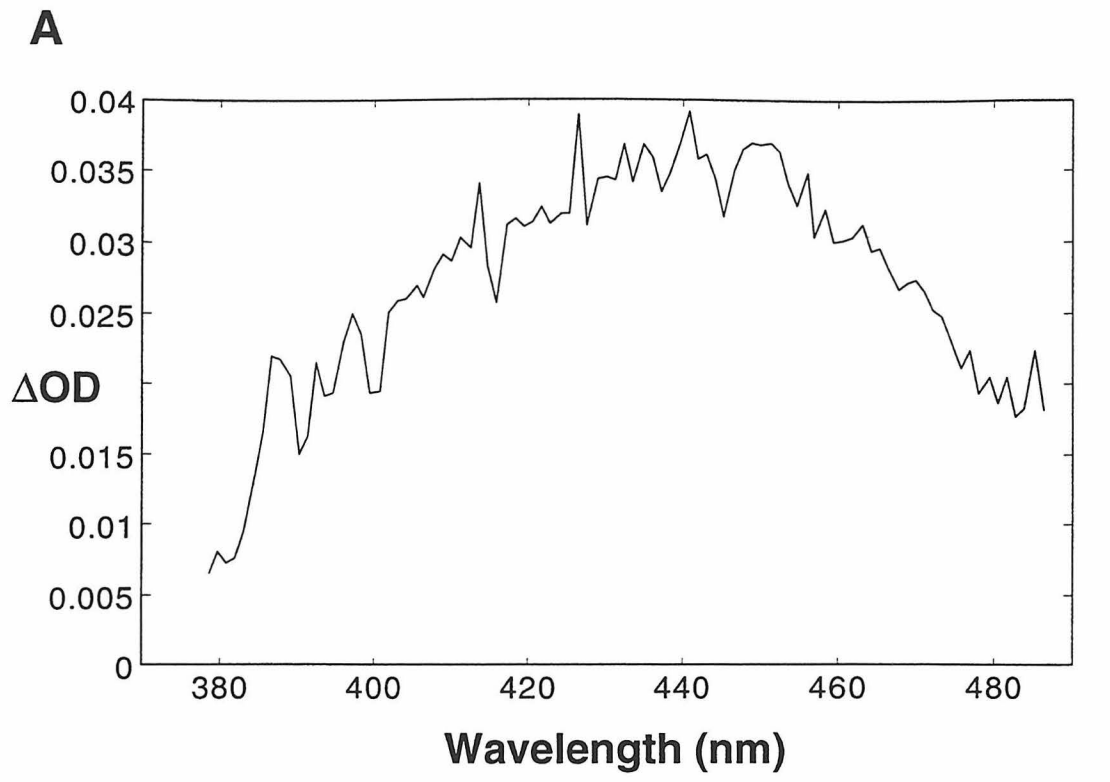
A
0.04
0.035
0.03
0.025
ΔOD
0.015
0.01
0.005
0
380
400
420
440
460
480
Wavelength (nm)

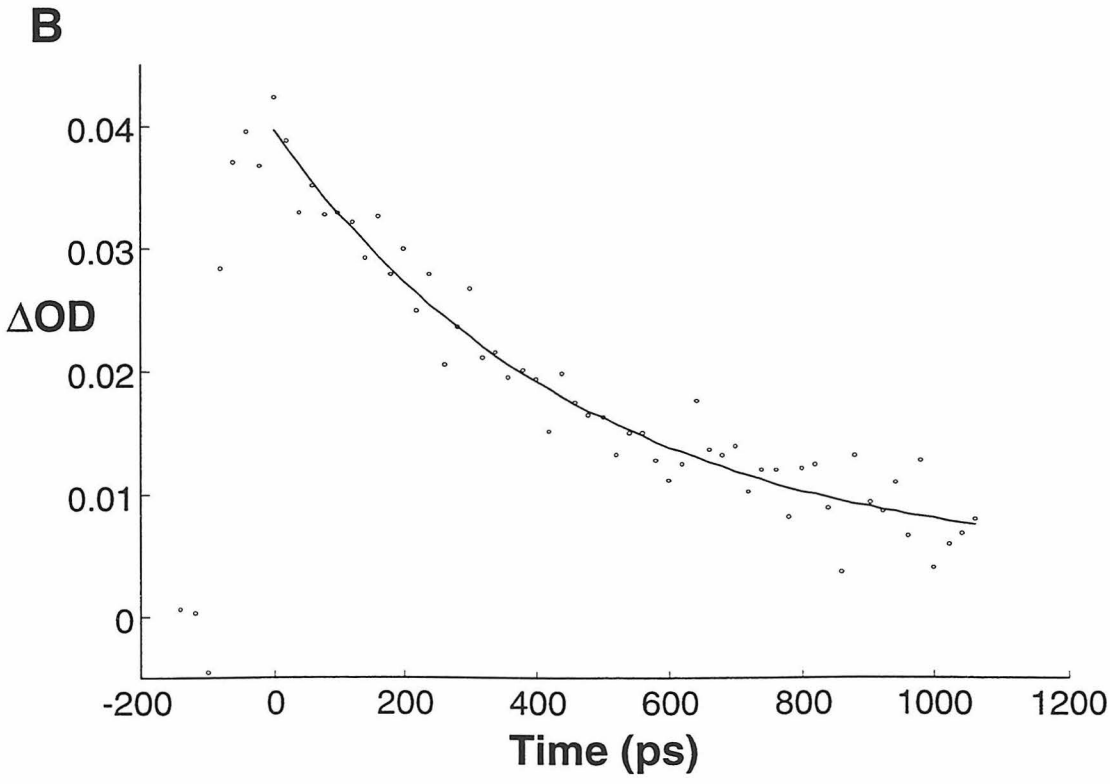
B
0.04
0.03
ΔOD
0.02
0.01
0
-200
0
200
400
600
800
1000
1200
Time (ps)

Figure V.12 Excitation of (*E*)-1-ferrocenyl-2-(*N*-methylpyridinium)ethylene at 532 nm yields a bleaching of its blue ground-state absorption feature and an optical-density increase centered near 520 nm (**A**). Decay of the feature monitored between 480 nm and 485 nm can be fit to an exponential function with a decay constant $k = 7.1 \times 10^8\ s^{-1}$ (**B**).

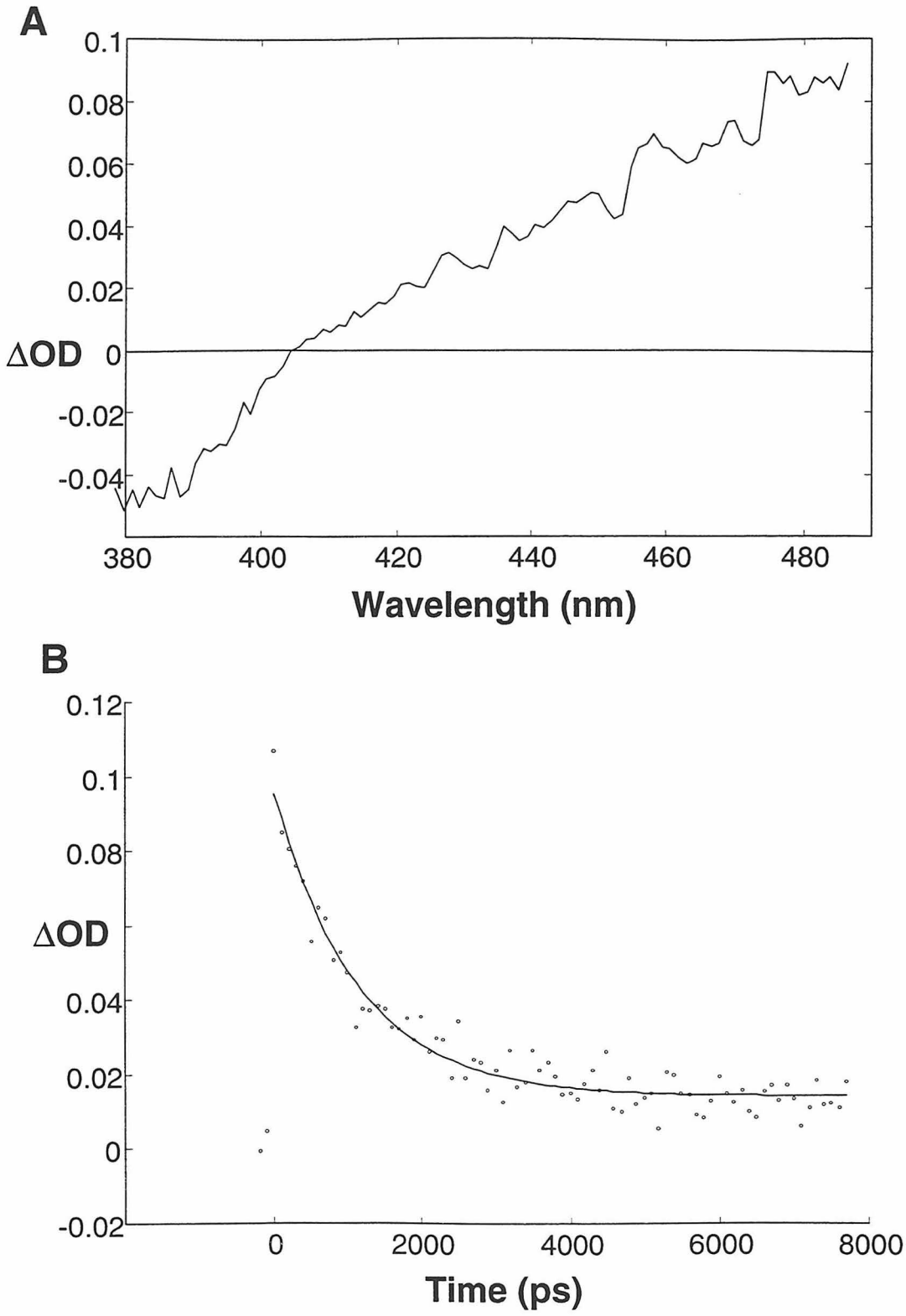
A
0.1
0.08
0.06
0.04
0.02
ΔOD 0
-0.02
-0.04
380
400
420
440
460
480
Wavelength (nm)
B
0.12
0.1
0.08
ΔOD
0.04
0.02
0
-0.02
0
2000
4000
6000
8000
Time (ps)

absorbance grows in strength, completely disappearing when the stronger absorption is at its maximum (Figure V.13). Both the growth and decay kinetics can be fit to a single exponential with a rate constant of 1.5×10^{10} s^{-1} (Figure V.14). The subsequent decay of the transient spectrum between 380 nm and 580 nm occurs at a rate of 7.1×10^{8} s^{-1}.

The n = 2 and 3 pyridinium compounds do not exhibit such complex excited-state behavior. Like its shorter counterpart, excitation of Fc(2)(*N*-methylpyridinium) at 532 nm causes a bleach of the band at 410 nm, and an OD increase to its red (Figure V.15). The bleach can be fit to a biexponential decay function. There is also a weaker absorption feature centered near 650 nm, which decays with the same rate constants ($k_1 = 3.0 \times 10^{10}$ s^{-1} and $k_2 = 2.6 \times 10^{9}$ s^{-1}) as the features in the blue (Figure V.16).

The same type of behavior is exhibited by the excited-state of Fc(3)(*N*-methylpyridinium). Its blue band bleaches (Figure V.17), while an increase in absorption centered near 700 nm appears (Figure V.18). There may be another OD increase somewhere near 530 nm, but the lack of probe light between 500 nm and 550 nm prevents its detection. Both transient features can be fit to biexponential functions with decay constants $k_1 = 3.2 \times 10^{10}$ s^{-1} and $k_2 = 2.2 \times 10^{9}$ s^{-1}.

A summary of these compounds' transient behavior highlights the apparent shift in their red absorbance to lower energy as the length of the polyene spacer is increased (Table V.4).

Figure V.13 Excitation of (*E*)-1-ferrocenyl-2-(*N*-methylpyridinium)ethylene at 532 nm causes the growth of two features in the red.

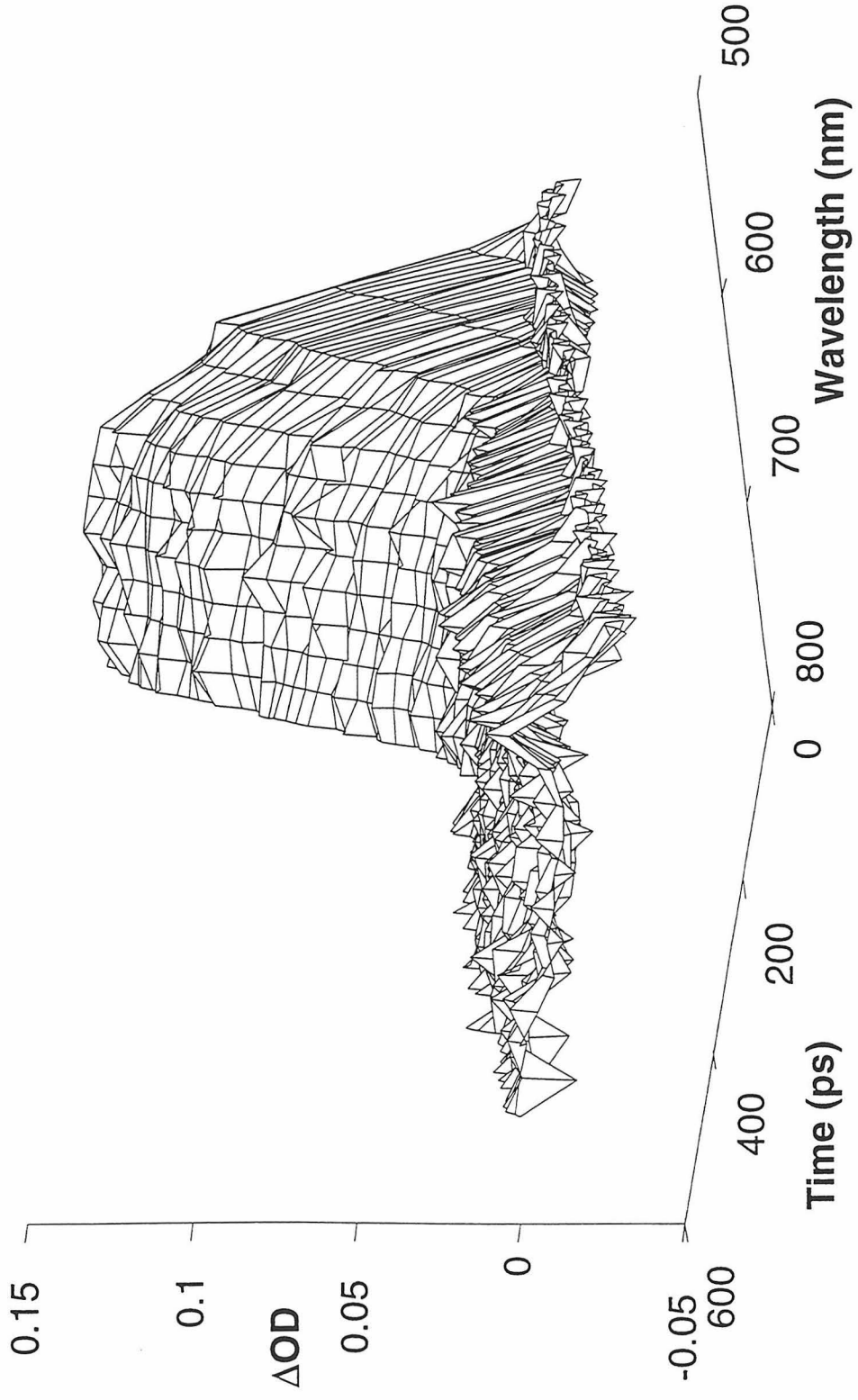
0.15
0.1
ΔOD
0.05
0
-0.05
600
400
200
0
800
700
600
500
Time (ps)
Wavelength (nm)

Figure V.14 Excitation of (*E*)-1-ferrocenyl-2-(*N*-methylpyridinium)ethylene at 532 nm yields an optical-density increase centered near 700 nm with kinetics that can be fit to an exponential function with a decay constant $k = 1.5 \times 10^{10}$ s^{-1} (**A**). At the same rate, the feature centered near 520 nm grows in intensity to then decay at a rate of 7.1×10^{8} s^{-1} (**B**).

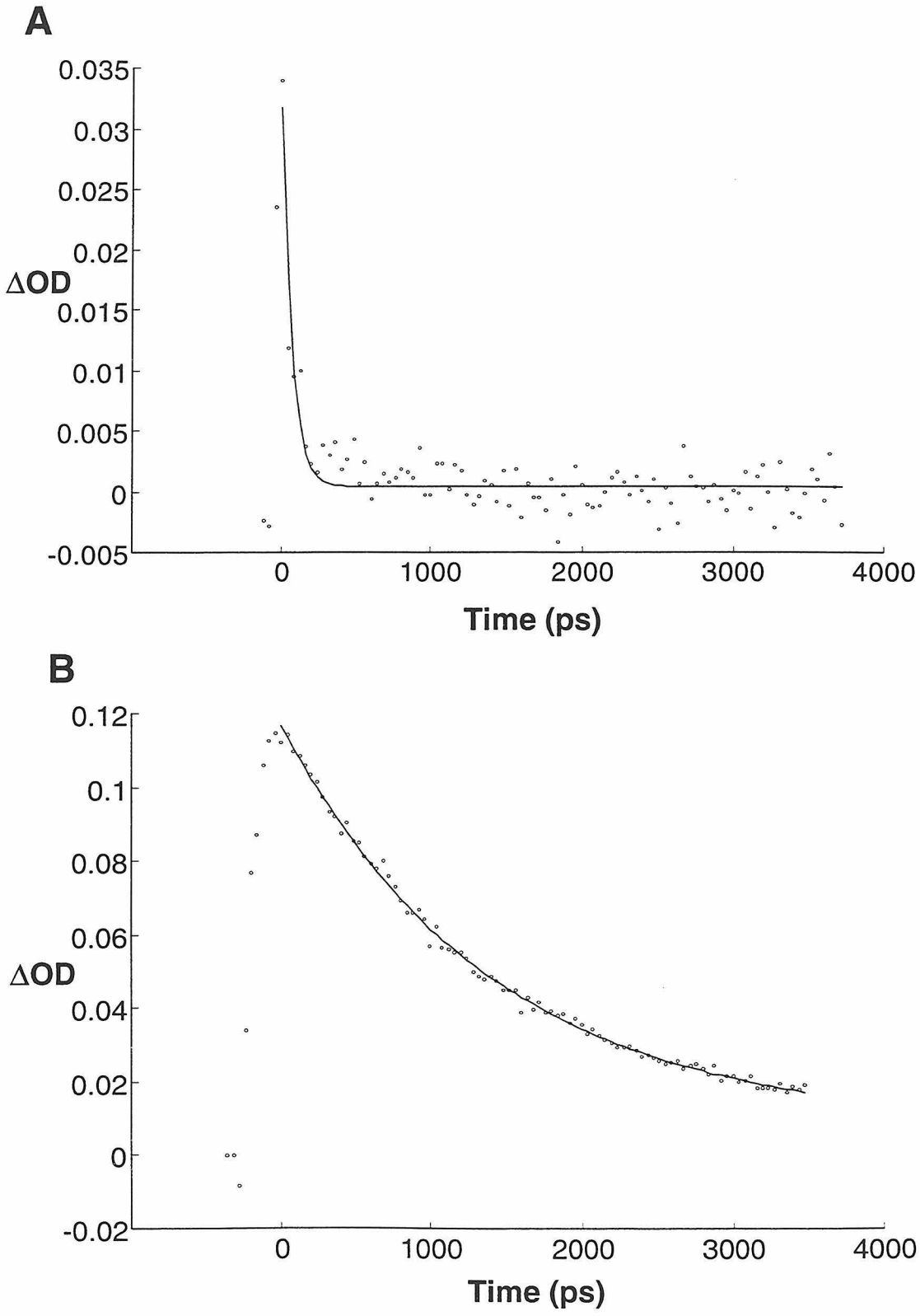
A
0.035
0.03
0.025
0.02
ΔOD
0.015
0.01
0.005
0
-0.005
0
1000
2000
3000
4000
Time (ps)
B
0.12
0.1
0.08
0.06
ΔOD
0.04
0.02
0
-0.02
0
1000
2000
3000
4000
Time (ps)

Figure V.15 Excitation of (*E,E*)-1-ferrocenyl-4-(*N*-methylpyridinium)propyldiene at 532 nm yields a bleaching of its blue ground-state absorption feature and an optical-density increase to the red (**A**). Decay of the bleach monitored between 400 nm and 410 nm can be fit to a biexponential function with decay constants $k_1 = 4.5 \times 10^{10}$ s^{-1} and $k_2 = 2.8 \times 10^{9}$ s^{-1} (**B**).

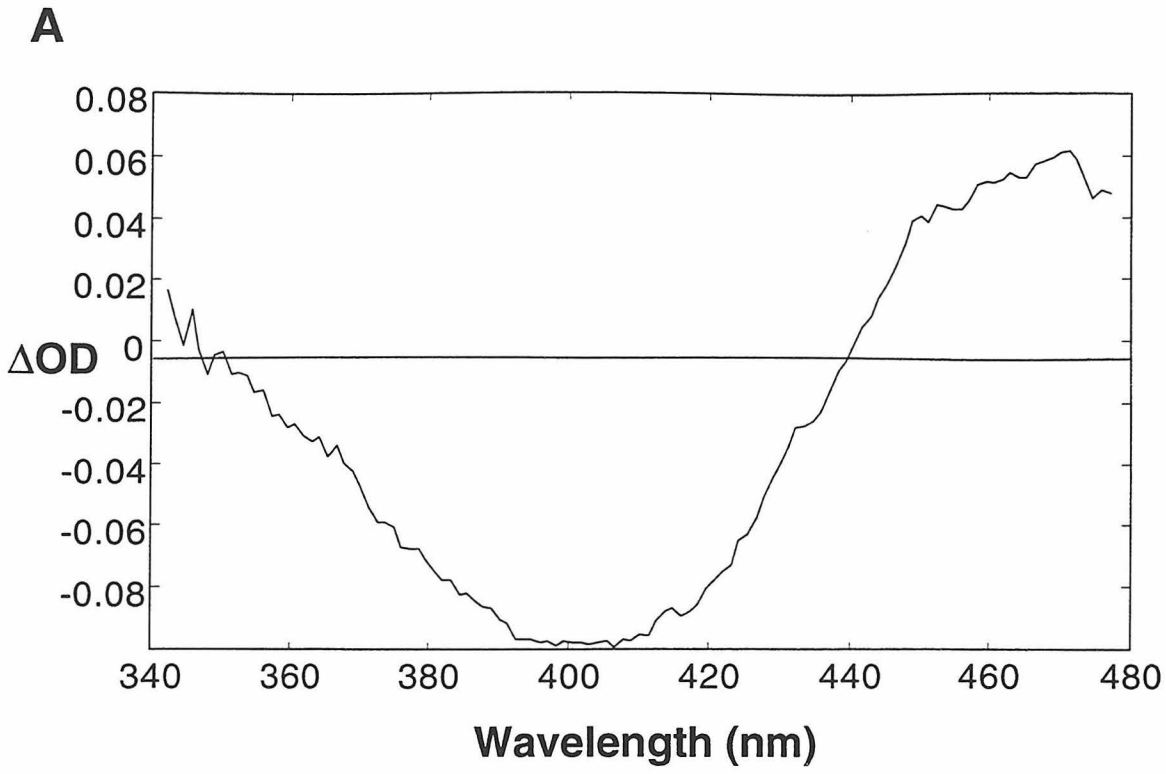
A
0.08
0.06
0.04
0.02
0
-0.02
-0.04
-0.06
-0.08
ΔOD
340
360
380
400
420
440
460
480
Wavelength (nm)

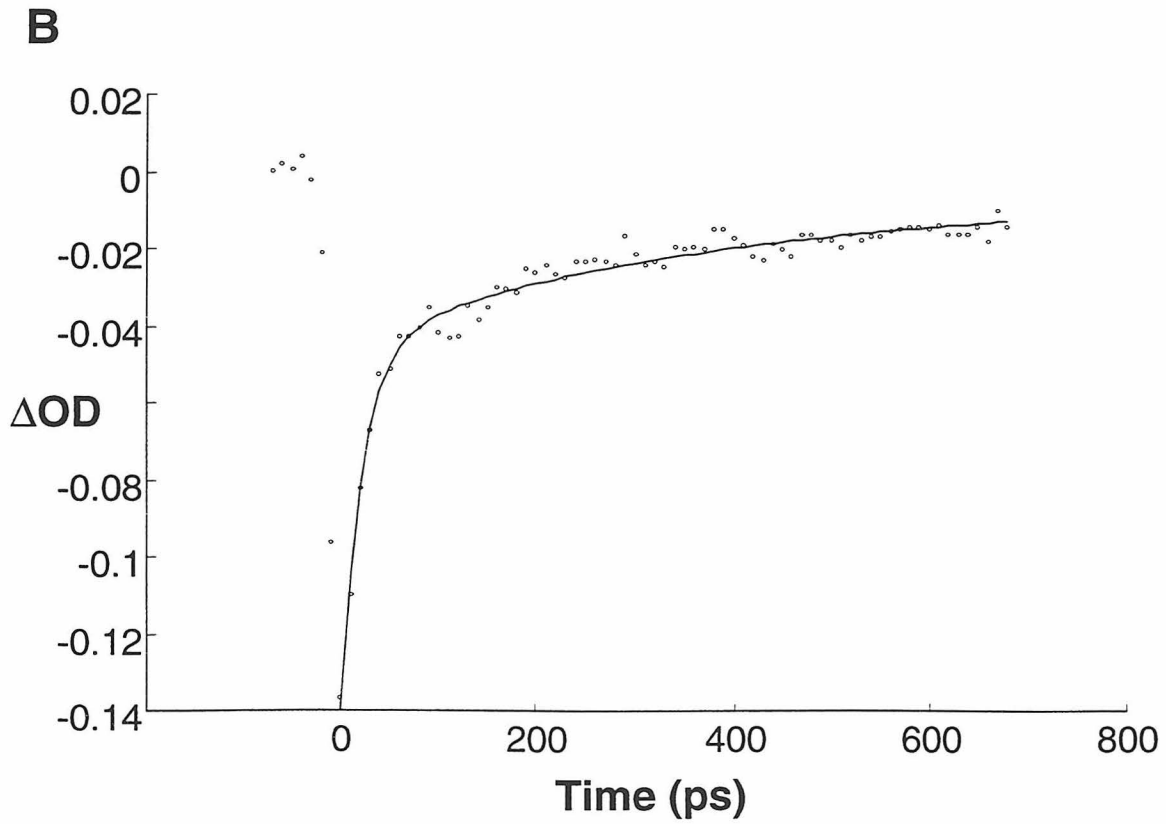
B
0.02
0
-0.02
-0.04
-0.08
-0.1
-0.12
-0.14
ΔOD
0
200
400
600
800
Time (ps)

Figure V.16 Excitation of (*E,E*)-1-ferrocenyl-4-(*N*-methylpyridinium)propyldiene at 532 nm yields an optical-density increase centered near 640 nm (**A**). Decay of the feature monitored between 640 nm and 650 nm can be fit to a biexponential function with decay constants $k_1 = 1.6 \times 10^{10}$ s^{-1} and $k_2 = 2.4 \times 10^{9}$ s^{-1} (**B**).

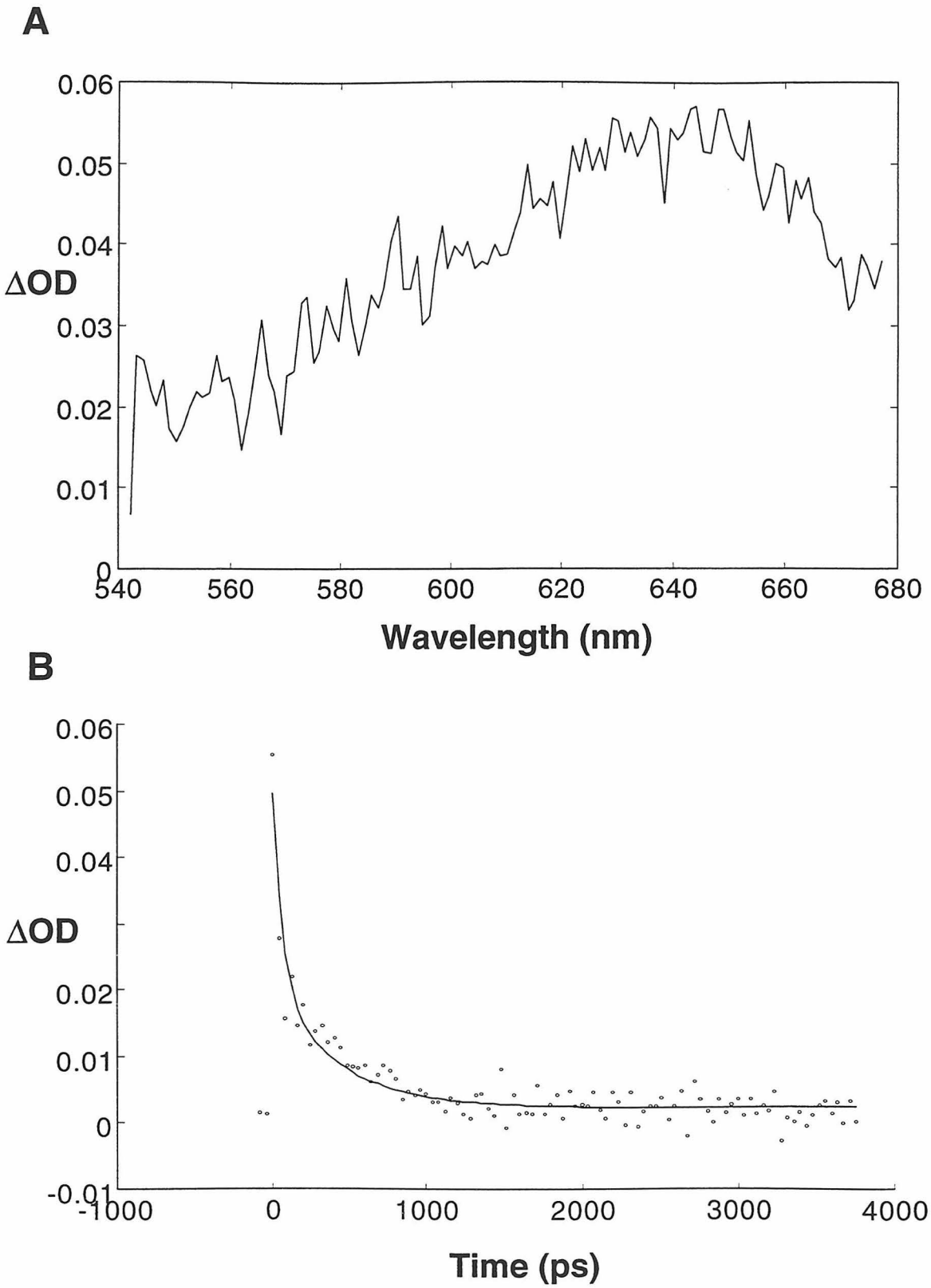
A
0.06
0.05
0.04
ΔOD
0.03
0.02
0.01
0
540
560
580
600
620
640
660
680
Wavelength (nm)
B
0.06
0.05
0.04
ΔOD
0.02
0.01
0
-0.01
-1000
0
1000
2000
3000
4000
Time (ps)

Figure V.17 Excitation of (*E,E*)-1-ferrocenyl-6-(*N*-methylpyridinium)hex-1,3,5-ene at 532 nm yields a bleaching of its blue ground-state absorption feature (**A**). Decay of the bleach monitored between 430 nm and 440 nm can be fit to a biexponential function with decay constants k_1 = 4.1×10^{10} s^{-1} and $k_2 = 5.5 \times 10^{9}$ s^{-1} (**B**).

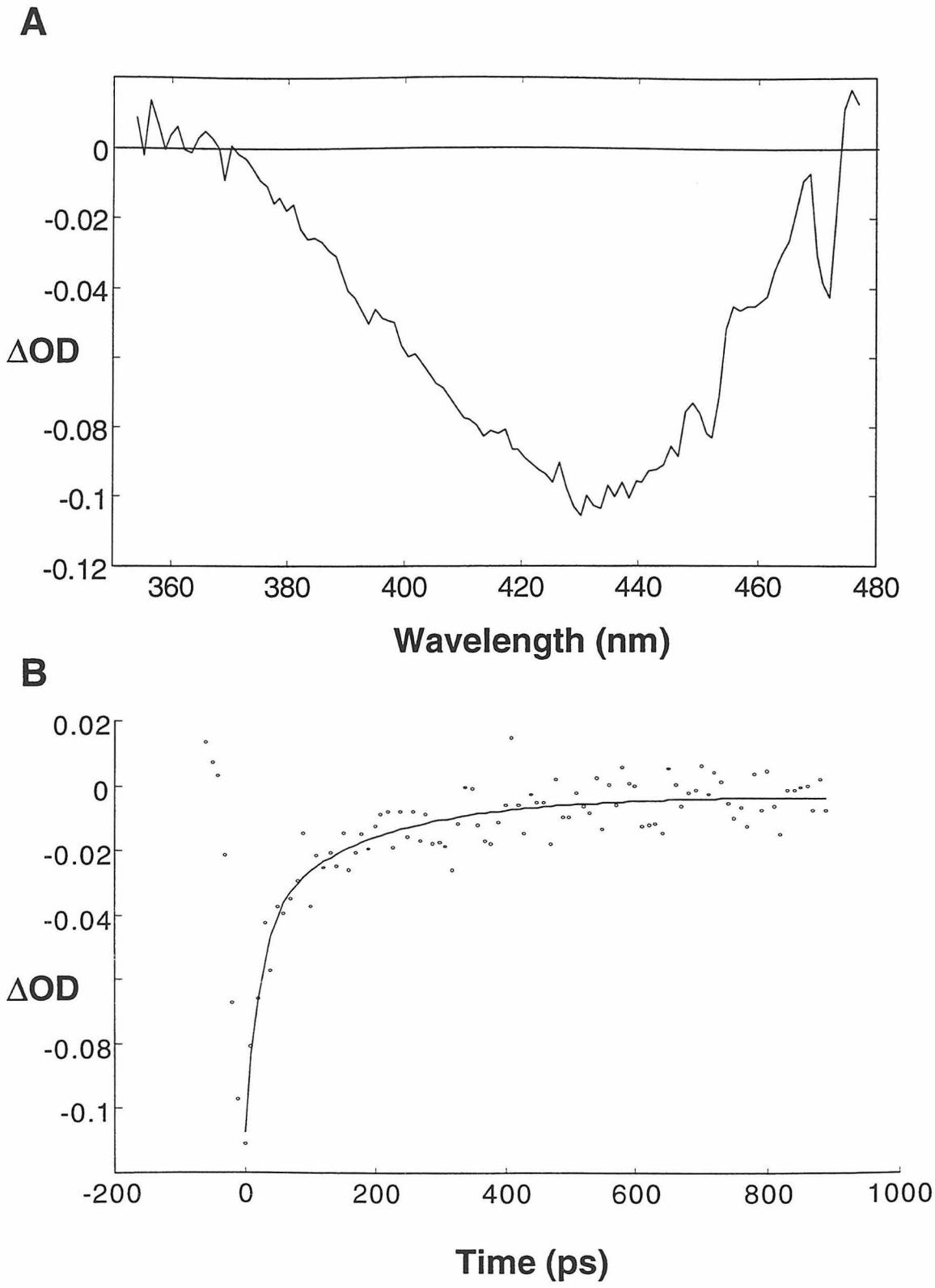
A
0
-0.02
-0.04
ΔOD
-0.08
-0.1
-0.12
360
380
400
420
440
460
480
Wavelength (nm)
B
0.02
0
-0.02
-0.04
ΔOD
-0.08
-0.1
-200
0
200
400
600
800
1000
Time (ps)

Figure V.18 Excitation of (*E,E*)-1-ferrocenyl-6-(*N*-methylpyridinium)hex-1,3,5-ene at 532 nm yields an optical-density increase centered near 700 nm (**A**). Decay of the feature monitored between 690 nm and 710 nm can be fit to a biexponential function with decay constants $k_1 = 1.9 \times 10^{10}$ s^{-1} and $k_2 = 1.1 \times 10^9$ s^{-1} (**B**).

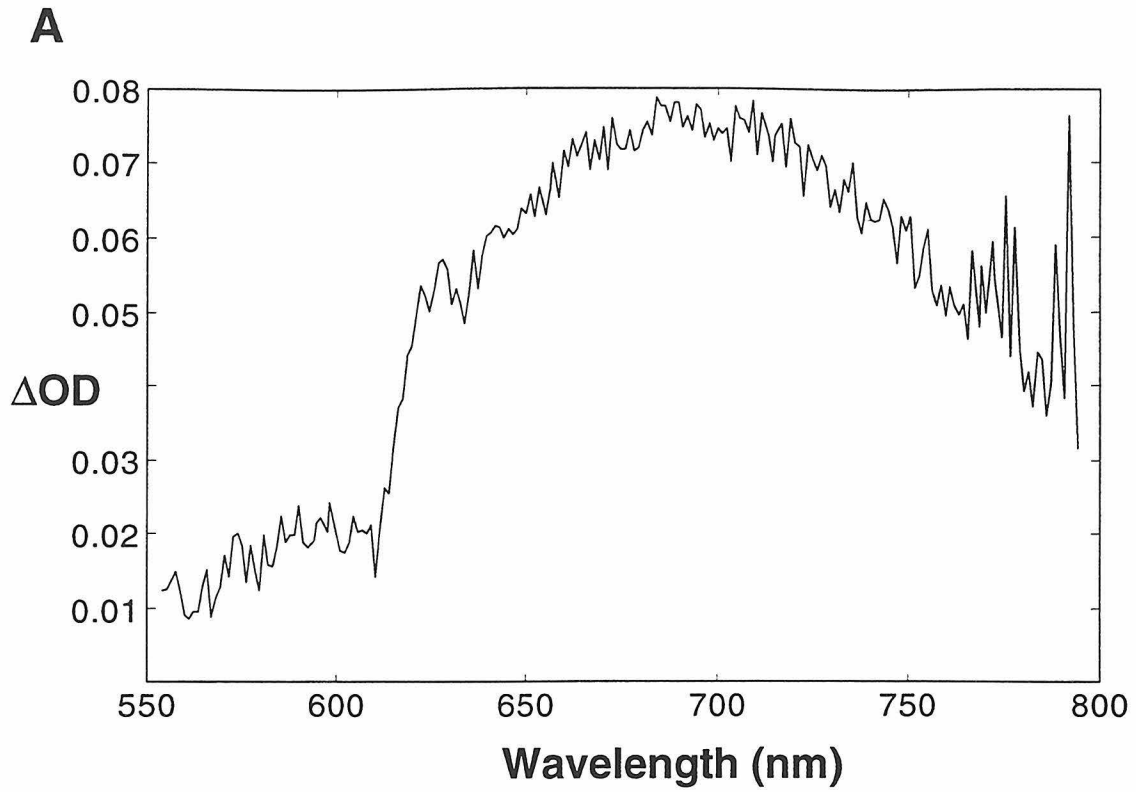
A
0.08
0.07
0.06
0.05
ΔOD
0.03
0.02
0.01
550
600
650
700
750
800
Wavelength (nm)

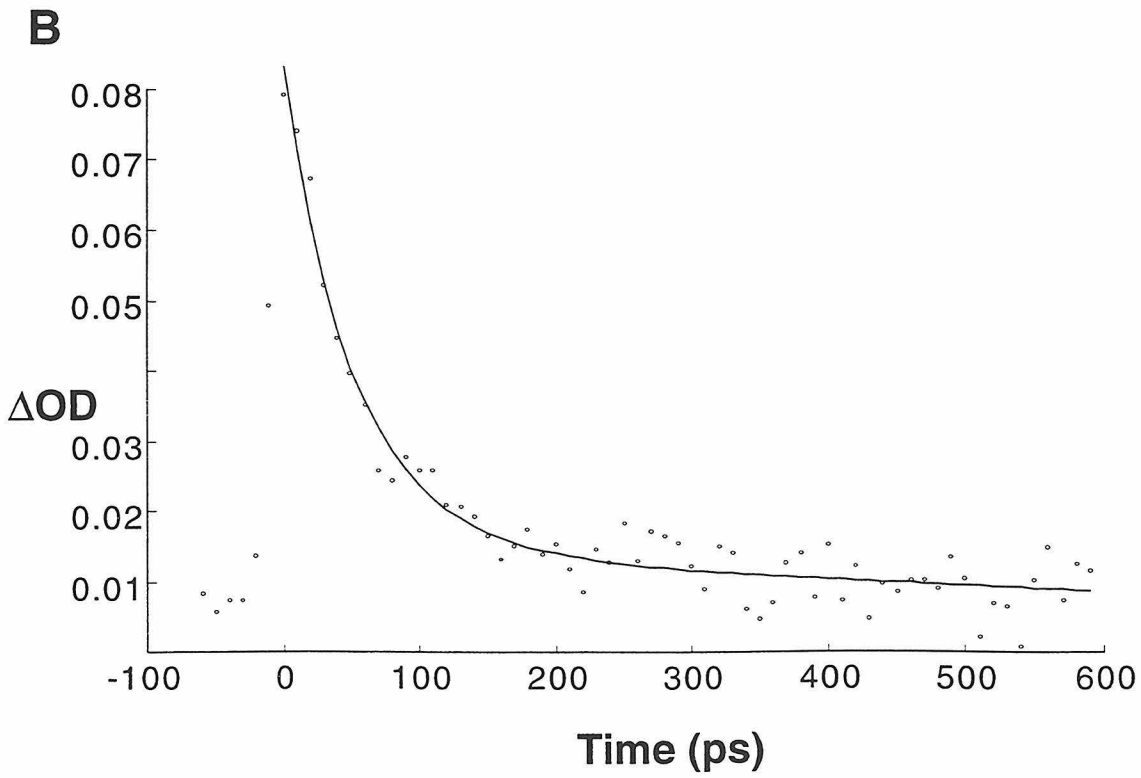
B
0.08
0.07
0.06
0.05
ΔOD
0.03
0.02
0.01
-100
0
100
200
300
400
500
600
Time (ps)

Discussion and Conclusion

Unlike the weakly coupled compounds discussed in Chapter III, the absorption spectra of these are substantially different from a superposition of their components' spectra. This is a clear indication that the donor and acceptor portions of these metallocene-based molecules are very strongly coupled. Little is known about the charge-transfer processes in molecules with donor-acceptor couplings of such magnitude. Before their excited-state behavior can be considered, however, the molecules' ground-state optical spectra must first be understood.

Assignment of Steady-State Absorption Features

The optical spectrum of each D(*n*)(A) compound is dominated by two strong absorption features. The higher energy one appears around 380 nm, and moves to lower energy as the length of the polyene spacer is increased. Its precise position varies little between the iron and ruthenium isomers of any given complex, but does shift as a function of solvent. As the solvent dielectric increases, this band moves to lower energy, a trait consistent with a charge-transfer transition. Its energy is also clearly a function of the acceptor group (Figure V.2). On the basis of their ZINDO calculations, Kanis *et al.* attribute this feature to photoinduced metal-to-ligand charge-transfer.[12] This appears unlikely in view of the band's insensitivity to the nature of the metal (Figure V.3). Further, photoelectron ionization spectroscopic (PES) measurements of the *cis*- and *trans*-D(1)(4-nitrophenyl) (D = $Fe(\eta\text{-}C_5H_5)_2$, $Ru(\eta\text{-}C_5H_5)_2$ or $Os(\eta\text{-}C_5H_5)_2$) compounds clearly indicate that the metals' d orbitals undergo no measurable perturbation upon complexation with the electron

acceptor.[20] It is clear from these data that the blue feature found in the optical absorption spectra of all the metallocene complexes is entirely ligand based. Extended Hückel calculations on Fc(1)(4-nitrophenyl) indicate that it results from charge-transfer from a molecular orbital based on the cyclopentadienyl ligand to one located almost entirely on the acceptor.[11]

To lower energy lies another absorption feature of lesser intensity. Unlike that of its counterpart, this band's energy is strongly dependent on the metal. Kanis *et al.* attribute the feature to a d-d transition, despite its large extinction coefficient. Their assignment is clearly incorrect. First, the band exhibits solvatochromism consistent with a charge-transfer transition (Figure V.4). Second, its energy varies as a function of the acceptor. Third, excitation into the low energy bands of both Fc(1)(4-nitrophenyl) and Fc(1)(*N*-methylpyridinium) generates resonance Raman spectra that are consistent with the reduction of each acceptor. Finally, the red absorption disappears upon the metal-based oxidation of all the ferrocene complexes. These data combine with PES results to suggest that this low energy absorption corresponds to charge-transfer from the metal donor to the polyene-coupled acceptor.

It follows from these assignments that intramolecular charge-transfer does occur upon optical excitation into these two bands. Their widths and intensities, however, suggest charge is not highly localized on the donor or acceptor. These are clearly Robin and Day class III compounds.[21] This makes analysis of their behavior difficult with electron-transfer theory that assumes the donor and acceptor moieties are not affected by the coupling between them. Nevertheless, it is still interesting

to estimate values for λ and H_{AB} with classical Hush theory (Equations IV.1 and IV.2).[22]

Equation IV.2 produces very large values of H_{AB} for these compounds: For example, inserting into the equation an approximate through-space iron-nitro distance[23] of 7.87 Å yields a value of 9,500 cm^{-1} for Fc(1)(4-nitrophenyl). The metal-pyridinium coupling in Fc(1)(*N*-methylpyridinium) is estimated to be 4,700 cm^{-1}.

The low-energy band deviates from Hush's correlation of band energy with band width:[24]

Equation V.7

$$\bar{\nu}_{max} = \frac{\bar{\nu}_{1/2}}{2310}$$

The widths of the low energy bands of both Fc(1)(4-nitrophenyl) and Fc(1)(*N*-methylpyridinium) are one-third narrower than the relationship predicts. Such deviations have been attributed to the inaccuracy of the theory's assumption of ET in the high-temperature limit.[25] As the resonance Raman data clearly shows, vibrations that couple the ground and charge-separated states have energies greater than kT. Accurate values for the reorganization energy associated with ET thus cannot be determined from bandshape analyses. It is possible, however, to get rough estimates of λ_{out} from solvent sphere calculations. These indicate that for the $n = 1$ compounds, $\lambda_{out} \approx 0.84$ eV for acetonitrile and 0.53 eV for methanol.[26]

Although neither H_{AB} nor λ can be accurately determined at this time, the excited-state behavior of the ferrocene compounds can be considered qualitatively.

Excited-State Behavior

The bleaching of the ligand-ligand charge-transfer band (LLCT) and the increased absorption immediately to its red following 355 nm excitation of Fc(1)(4-nitrophenyl) (Figure V.10) are in qualitative agreement with the changes in its absorption spectrum upon oxidation (Figure V.6). Spectroelectrochemistry also shows the compound's oxidation results in the growth of a broad absorption feature centered near 630 nm, but no transient spectral changes were detected further red than 550 nm. This is consistent with the movement of charge from different portions of the ligand bound to the iron, rather than oxidation of the metal.

The decay of the transient is presumably caused by charge-recombination, but why it does not fit to a single exponential function is unclear. One possibility is that the molecule quickly twists after charge separation, similar to the way stilbene isomerizes upon UV excitation.[27] It is possible that both charge-separation and geometric relaxation occur within the temporal width of the laser pulse, in which case the observed kinetics reflect both charge-recombination and the adoption of a geometry necessary for it to occur (Figure V.19). The activation energy necessary for the molecule to move from its twisted state to the planar one which allows ET must be very low: Isomerization products have not been observed at room temperature for any of the ferrocene alkene-bridged complexes upon long-term exposure to UV light.[28]

The comparison of this compound's excited-state behavior to that of its alkyne-bridged analogue lends support to this hypothesis: The latter does not exhibit biphasic decay kinetics when excited at 355 nm. The decay of the OD

Figure V.19 The two canonical forms of Fc(1)(4-nitrophenyl) give an indication of how isomerization about the bridge might occur following charge-transfer. A possible, qualitative, energy level diagram is offered to explain the excited-state decay kinetics of the alkene-bridged complexes.

M
M
M
k_1
k_2
hν

increase centered near 450 nm can be fit to a single exponential function with a rate constant of 2.1×10^9 s^{-1}. If optical excitation of these compounds reduces the bridge's bond order, the alkyne complex would still remain rigid in its excited-state. If this is the case, and the measured decay is due solely to back electron-transfer, then the difference between the nitrophenyl compounds' rates could be due to the different energies of their molecular orbitals that act as electron donors and acceptors.

The biphasic kinetics exhibited by the Fc(*n*)(*N*-methylpyridinium) compounds may also be due to the formation of a twisted excited-state: The rates of the fast kinetic components in all the pyridinium compounds are very close to that observed for the fast component of Fc(1)(4-nitrophenyl), and do not vary much among themselves (Table V.4). The anomalous behavior of Fc(1)(*N*-methylpyridinium) may be the result of its photochemical activity.

Oxidation of the iron in these compounds should also lead to an absorption increase in the red. Unfortunately, their instability to electrochemical oxidation makes analysis of spectroelectrochemical data of little use in addressing this point. Upon excitation into the ferrocene/pyridinium compounds' metal-to-ligand charge-transfer band at 532 nm, however, an increase in absorption does appear between 600 nm and 800 nm. It is likely that this is due to the ferrocenium ligand-to-metal charge-transfer band: Its movement to lower energies as the molecules' π-systems becomes more extended is consistent with the ligands' reduction potentials. Similar red-shifting has been observed upon substitution of the cyclopentadienyl rings of ferrocene.[16] The brief appearance of the low energy absorption in the transient spectrum of Fc(1)(*N*-methylpyridinium) thus indicates that, following charge-

transfer to form Fe^{3+} and a pyridinyl radical, the molecule reacts with solvent. In the other two pyridinium compounds, the red absorption decays at the same rate as do the higher energy OD changes.

If the slow components of the molecules' biphasic decays are due to charge-recombination, their dependence on the difference between the oxidation and reduction potentials of the compounds is consistent with inverted region reactions. The rates become faster as the value diminishes from 1.67 eV for n = 1, to 1.44 eV for n = 2, to 1.40 eV for n = 3. Although λ_{out} will increase as the distance between the donor and acceptor becomes larger, the total reorganization energies of these reactions are unlikely to be greater than 1 eV.

The pyridinium compounds' excited-states all decay faster than Fc(1)(4-nitrophenyl)'s. Two factors may account for this. First, the driving force of the intraligand nitrophenyl reaction may be larger than the driving forces of these. Another possible explanation for this discrepancy lies in the resonance Raman spectra of the different compounds. The spectrum of Fc(1)(*N*-methylpyridinium) shows a large number of vibrations coupled to the low energy charge-transfer band (Figure V.7). By contrast, the resonance spectrum of the nitrophenyl compound shows fewer vibrations which are of lower energies and intensities (Figure V.8). These differences indicate that nuclear tunneling may play a larger role in the metal-to-ligand electron-transfer reactions within the pyridinium complexes than it does within the nitrophenyl ones. It is possible that λ_{in} is equally small for the intraligand ET reactions within the nitrophenyl complexes.

Establishing a Relationship

It is clear that additional transient experiments need to be done before quantitative relationships between excited-state decay kinetics and molecular hyperpolarizabilities can be established. Three series of experiments need to be performed. First, the behavior of the Fc(*n*)(*N*-methylpyridinium) complexes needs to be determined in a solvent in which they are photochemically stable. It appears that only the excited-state of the $n = 1$ compounds does react with alcohols, since it is the only one of the three that shows complex behavior, but precautions must be taken to ensure that none of the decay processes observed are due to sample degradation.

Second, the excited-state behavior of all the complexes should be determined as a function of pump wavelength. Here, the nitrophenyl compounds were excited at 355 nm, into their high energy bands, while the pyridinium compounds were excited at 532 nm, close to the maximum of their low energy bands. By exciting the same bands, it may be possible to determine if the rates of the acceptor-to-metal charge-recombination reactions correlate with ΔG°.

Finally, temperature dependence studies should be performed for two reasons. First, if the fast decay component exhibited in the kinetics of the alkene-bridged compounds is indeed due to excited-state isomerization, then it stands to reason that at lower temperatures the twisted isomer could be frozen-out. In addition, the activation energies of this proposed isomerization, as well as the proposed electron-transfer, could be determined.

As this information is acquired, it may be possible to begin establishing a connection between rates of photoinduced and thermal electron-transfer reactions and molecular nonlinear optical susceptibilities β and γ.

REFERENCES AND NOTES

[1] Schmitt-Rink, S.; Chemla, D. S.; Miller, D. A. B. *Adv. Phys.* **1989**, *38*, 89: Tai, K.; Mysyrowicz, A.; Fischer, R. J.; Slusher, R. E.; Cho, A. Y. *Phys. Rev. Lett.* **1989**, *62*, 1784.

[2] Vogel, E. M. *J. Am. Ceram. Soc.* **1989**, *72*, 719: Lines, M. E. *J. Appl. Phys.* **1991**, *69*, 6876.

[3] Singer, K. D.; Sohn, J. E.; Lalama, *J. Appl. Phys. Lett.* **1986**, *49*, 248: Kajzar, F.; Messier, J.; Rosilio, C. *J. Appl. Phys.* **1986**, *60*, 3040.

[4] Marder, S. R.; Perry, J. W. *Science* **1994**, *263*, 1706.

[5] Long, N. J. *Angew. Chem. Int. Ed. Engl.* **1995**, *34*, 21.

[6] Nonlinear Optics: Materials and Devices. C. Flytzanis and J. L. Oudar eds. Springer-Verlag, New York: **1985**.

[7] Gibbs, H. M. Optical Bistability: Controlling Light with Light. Academic, New York: **1985**.

[8] Marder, S. R.; Gorman, C. B.; Meyers, F.; Perry, J. W.; Bourhill, G.; Brédas, J. L.; Pierce, B. M. *Science* **1994**, *265*, 632: Meyers, F.; Marder, S. R.; Pierce, B. M.; Brédas, J. L. *J. Am. Chem. Soc.* **1994**, *116*, 10703.

[9] Marder, S. R.; Perry, J. W.; Tiemann, B. G.; Schaefer, W. P. *Organometallics*, **1991**, *10*, 1896.

[10] Dias, A. R.; Garcia, M. H.; Robato, M. P.; Green, M. L. H.; Lai, K. K.; Pulham, A. J.; Klueber, S. M.; Galavoine, G. *J. Organomet. Chem.* **1993**, *453*, 241.

[11] Calabrese, J. C.; Cheng, L.-T.; Green, J. C.; Marder, S. R.; Tam, W. *J. Am. Chem. Soc.* **1991**, *113*, 7227: Waite, J.; Papadopoulos, M. G. *J. Phys. Chem.* **1991**, *95*, 5426.

[12] Kanis, D. R.; Ratner, M. A.; Marks, T. J. *J. Am. Chem. Soc.* **1992**, *114*, 10338.

[13] Green, M. L. H.; Marder, S. R.; Thompson, M. E.; Bandy, J. A.; Bloor, D.; Kolinsky, P. V.; Jones, R. J. *Nature* **1987**, *330*, 360.

[14] Gagne, R. R.; Kovaland, C. A.; Lisensky, G. C. *Inorg. Chem.* **1980**, *19*, 2855.

[15] Akiyama, K.; Tero-Kubota, S.; Ikegami, Y. *J. Am. Chem. Soc.* **1983**, *105*, 3601: Akiyama, K.; Tero-Kubota, S.; Ikegami, Y.; Ikenone, T. *J. Phys. Chem.* **1985**, *89*, 339.

[16] Sohn, Y. S.; Hendrickson, D. N.; Gray, H. B. *J. Am. Chem. Soc.* **1971**, *93*, 3603.

[17] Meyers, A. B.; Mathies, R. A. *Resonance Raman Intensities: A Probe of Excited-State Structure and Dynamics* in Biological Applications of Raman Spectroscopy vol. 2, Spiro, T. A. ed. John Wiley & Sons: New York. **1987**.

[18] Silverstein, R. M.; Bassler, G. C.; Morrill, T. C. Spectrometric Identification of Organic Compounds 4th ed. John Wiley & Sons: New York. **1981**.

[19] Geoffroy, G. and Wrighton, M. S. Organometallic Photochemistry **1979**, Academic: New York.

[20] Bunting, H. E.; Green, J. C.; Marder, S. R.; Ringham, C. manuscript in preparation.

[21] Robin, M. B.; Day P. *Adv. Inorg. Chem. Radiochem.* **1967**, *10*, 247.

[22] Hush, N. S. *Prog. Inorg. Chem.* **1967**, *8*, 391.

[23] Obtained by assuming the crystal structure of Fc(1)(4-nitrophenyl) is close to that of Fc(2)(4-nitrophenyl)[9].

[24] This is valid in the classical limit at room temperature.

[25] Creutz, C.; Taube, H. *J. Am. Chem. Soc.* **1973**, *95*, 1086.

[26] Using $\lambda_{solv} = (1/d)(1/n^2 - 1/D)e^2$ where d = 7.87 Å. For acetonitrile, the index of refraction n = 1.344 and the static dielectric constant D = 36.2. For methanol, n = 1.329 and D = 32.6.

[27] Saltiel, J.; Waller, A. S.; Sears, D. F. Jr. *J. Am. Chem. Soc.* **1993**, *115*, 2453.

[28] Marder, S. R. Personal Communication.